

Strength reliability of metallic components
fabricated by selective laser melting:
Application on non-combustible Mg-products

フロアニヨ, サラウズ, ブライアン, スティーブ

<https://hdl.handle.net/2324/5068224>

出版情報 : Kyushu University, 2022, 博士 (工学), 課程博士
バージョン :
権利関係 :

Doctorate Dissertation in September 2022

**Strength reliability of metallic components fabricated
by selective laser melting: Application on non-
combustible Mg-products**

Supervisor: *Prof. Shigeru HAMADA*

Submitted to Faculty of Engineering
Department of Hydrogen Energy Systems, Kyushu
University, Japan

Proaño Sarauz Bryan Steve

Table of Contents

CHAPTER 1.- GENERAL INTRODUCTION	4
1.1 Nomenclatures	4
1.2 Background	5
1.3 Review	6
1.4 Objective	9
1.5 Non-combustible Mg alloys	10
1.6 Contents	11
1.7 References	12
1.8 List of tables	23
1.9 List of figures	24
CHAPTER 2.- WEAKEST REGION ANALYSIS OF SLM PRODUCTS	25
2.1 Introduction	25
2.2 Experimental procedure	27
2.3 Results	29
<i>2.3.1 Tensile tests and fractography results</i>	29
<i>2.3.2 Microstructure observation and distribution</i>	29
<i>2.3.3 Micro-hardness tests results</i>	31
2.4 Discussion	31
2.5 Conclusions	34
2.6 References	35
2.7 List of tables	39
2.8 List of figures	40
CHAPTER 3.- PLASTIC STRAIN DISTRIBUTION THROUGH THE INNER MICROSTRUCTURE DUALITY OF SLM PRODUCTS	57
3.1 Introduction	57
3.2 Experimental procedure	59
3.3 Results	60
<i>3.3.1 Extreme value statistics of defects</i>	60
<i>3.3.2 Tensile tests and fractography results</i>	61
<i>3.3.3 EBSD analysis</i>	61
<i>3.3.4 Fracture toughness results</i>	62
3.4 Discussion	63
3.5 Conclusions	65
3.6 References	66
3.7 List of tables	70

3.8 List of figures	71
CHAPTER 4.- FRACTURE TOUGHNESS CALCULATION OF SLM PRODUCTS: MURAKAMI'S THEORY APPLICATION USING ARTIFICIALLY INTRODUCED DRILL HOLES	83
4.1 Introduction	83
4.2 Experimental procedure	85
4.3 Results	86
<i>4.3.1 Tensile tests results</i>	86
<i>4.3.2 Fractography results and determination of stable propagation area of the crack</i>	86
<i>4.3.3 Fracture toughness results</i>	87
4.4 Discussion	87
<i>4.4.1 Strength variation and constant fracture toughness</i>	87
<i>4.4.2 Influence of drill hole</i>	90
4.5 Conclusions	91
4.6 References	92
4.7 List of tables	94
4.8 List of figures	95
CHAPTER 5.- MICROSTRUCTURE HOMOGENIZATION VIA HEAT TREATMENT: THE INFLUENCE OF ANNEALING IN SLM PRODUCTS	108
5.1 Introduction	108
5.2 Experimental procedure	110
5.3 Results	112
<i>5.3.1 Surface roughness and microstructure observation</i>	112
<i>5.3.2 Micro-hardness results</i>	112
<i>5.3.3 Tensile tests results</i>	113
<i>5.3.4 Fractography results</i>	114
<i>5.3.5 EBSD analysis</i>	115
5.4 Discussion	115
<i>5.4.1 Impact of the microstructure homogenization on the fracture process</i>	115
<i>5.4.2 The R curve alternative</i>	117
5.5 Conclusions	118
5.6 References	119
5.7 List of figures	123
CHAPTER 6.- IDEAL TENSILE STRENGTH OF A METALLIC SLM PART: EXAMPLE OF A NON-COMBUSTIBLE MAGNESIUM ALLOY	136
6.1 Introduction	136

6.2 Method proposal for fabrication of the ideal SLM specimen	138
6.2.1 <i>Presence of geometrical defects</i>	138
6.2.2 <i>Mechanical removal of the outer surface</i>	138
6.2.3 <i>Flow chart of the proposed method</i>	139
6.3 Experimental procedure	139
6.4 Results	141
6.4.1 <i>Mechanical removal of the outer surface</i>	141
6.4.2 <i>Tensile tests results</i>	141
6.4.3 <i>Fractography results</i>	142
6.4.4 <i>Void formation and coalescence observation</i>	143
6.4.5 <i>EBSD analysis</i>	143
6.5 Discussion	143
6.5.1 <i>Fracture mechanism in small, ideal specimens</i>	143
6.5.2 <i>Microstructural factors that affect the UTS value and critical area size of the defect</i>	145
6.6 Conclusions	147
6.7 References	148
6.8 List of tables	153
6.9 List of figures	154
APPENDIX	172
A.1 Appendix A	172
A.1.1 <i>Plastic instability condition and ideal UTS determination of SLM products</i>	172
A.2 References	173
A.3 List of tables	175
A.4 List of figures	176
CHAPTER 7.- THEORETICAL EVALUATION OF MATERIAL INDEX FOR FRACTURE TOUGHNESS VARIATION IN SLM PRODUCTS	177
7.1 Introduction	177
7.2 Experimental procedure	178
7.3 Results	179
7.3.1 <i>Tensile tests and fractography results</i>	179
7.3.2 <i>Microstructure observation and distribution</i>	180
7.4 Discussion	180
7.5 Conclusions	182
7.6 List of figures	183
CHAPTER 8.- CONCLUDING REMARKS	192
ACKNOWLEDGEMENTS	194

CHAPTER 1.- GENERAL INTRODUCTION

1.1 Nomenclatures

E	Young's modulus
G	Shear modulus
L	Specimen length
L_0	Observed length from specimen
F	Cumulative distribution function
T	Return period
y_i	Standardized variable
y_{\max}	Maximum distribution line
K	Strength coefficient in Eq. (A.2)
K_I	Stress intensity factor
K_{IC}	Fracture toughness
φ	Energy release rate
φ_C	Critical energy release rate
R	Crack growth resistance
n	Number of inspection measurements
n	Strain-hardening exponent in Eq. (A.2)
a_1	Stable propagation area of the crack
a_0	Surface crack
Δa	Crack growth length
\sqrt{area}	Defect size: the square root of the area including abnormal structure and stable fracture regions projected on the plane perpendicular to a loading direction
$\sqrt{area_c}$	Critical and minimum size of defect which influences the UTS of SLM product
$\hat{\varepsilon}$	Total strain at plastic instability condition
ε_{el}	Elastic strain
ε_{pl}	Plastic strain

$\hat{\epsilon}_{pl}$	Plastic strain at plastic instability condition
$\hat{\epsilon}_{el}$	Elastic elongation at plastic instability condition
ν	Poisson's ratio
σ	Stress
σ_{∞}	Remote stress
σ_C	UTS
σ_{ci}	Ideal UTS with no defects
σ_Y	Yield strength

1.2 Background

Selective laser melting (SLM) technologies developed from an early stage as an idea of rapid prototyping using a controlled heat source approximately in the year 1995 [1, 2]. However, technological setbacks at the time prevented SLM from becoming a viable manufacturing process, where complex concepts such as Computer Assisted Design (CAD) models intertwined with laser irradiation technologies and a consecutive layer-by-layer sintering had not yet reached their scientific peak until recent years [2-4]. Currently, the SLM process is an Additive Manufacturing (AM) technique alternative that uses a laser beam as a heat source to melt a powder bed in narrow layers consecutively until a 3D CAD assisted model is obtained as a final product [5]. SLM uses the concept of solidification after melting to form the desired shape, resulting in a microstructure consisting of melt pool formations that form as soon as the laser moves away from the molten region. The concept has enabled SLM to be considered as a micro-welding and micro-casting process [6, 7], but with a wider range of advantages such as high-speed production of complex geometries with a high precision without requiring post-processing [2]. Furthermore, the industrial applications of SLM have provided a solution to bespoke difficult metallic components that would be exceedingly time and cost expensive if conventional manufacturing methods were used.

However, there are several problems that can be encountered in the fabrication of SLM products due to the intrinsic nature of the process. The high temperature gradients and solidification rates build up thermal residual stresses which are maximum at the top of the final product and if they are desirable or not depends, among other factors, in its geometry and applications [8-10]. In addition, possible segregation and non-equilibrium

phases can be formed depending on the scanning strategy used. Defects such as gas porosities and lack-of-fusion pores are likely to appear and are directly influenced by scanning parameters such as energy input and scanning speed [11-14]. Furthermore, the resultant microstructure is non-homogeneous [15-17], and the layer-by-layer scan strategy affects the surface roughness quality of the product [11, 18, 19]. Regardless of the metallic powder used, all the problems mentioned above have been pointed out and discussed in the engineering field across an abundant number of papers with a sole purpose in mind: enable SLM processes as a viable, reliable, and efficient manufacturing technique.

Nevertheless, there is an important characteristic that the mechanical engineer evaluates to determine if a specific metallic part can be used for design: the mechanical properties. Particularly in SLM products, mechanical properties such as tensile strength at failure are significantly attractive because they are considerably higher if compared to their casting counterparts [20, 21]. Although it is a positive characteristic, several attempts have tried to explain the real reason behind that phenomenon, without a clear conclusion. In addition, the mechanical properties of SLM products present a relatively high variation in the results, particularly in ductility values [22-24]. Thus, despite the attractive characteristics that can be achieved using SLM technologies, the reliability of the mechanical properties of SLM products is low. This leaves a space that only extended research can fill, and this thesis will do its best efforts to do so.

1.3 Review

Before addressing the purpose of this study, it is of great importance to point out a general overview of how the SLM process has attracted researchers throughout recent years. For instance, different studies focused on the influence of the sintering parameters in the mechanical properties. Leuders et. al studied fatigue resistance and crack growth performance of TiAl6V4 alloys [25], concluding that the fracture behavior of the material is directly linked to its microstructure and can be tailored by heat treatment. Spierings et. al found that SLM scan-speed influences the mechanical properties in modified Al-Mg alloys by altering the precipitation of nm-scaled particles [26]. Larimian et. al analyzed the effect of energy density and scanning strategy on mechanical properties of 316L

stainless steel [27], and found that alternating the hatches by rotating the scanning direction angle exhibit highest densification and better mechanical properties. Wei et. al determined the processing range of energy input to achieve AZ91D Mg alloy specimens without any obvious macro-defects [28]. Beevers et. al studied the effect of the contour parameter in surface roughness and fatigue properties [29], and found that the net shaped surface specimens are more tolerant to fracture compared to the milled specimens. Finally, Oliveira et. al concluded that scan speed, laser power and layer thickness are the three key parameters that determine the mechanical properties of SLM products [30].

Due to the flexibility of the powder materials that could be used for sintering, Gu et. al suggested as a future research interest the extension of additive manufacturing including Fe, Ni, Al, Cu and Mg based powders [5]. As a result, several studies have used different metallic powders such as Ti alloys [31-33], Al alloys [23, 34-37], stainless steel [27, 38, 39], Co alloys [40, 41], Fe high-entropy alloys [42], Ni alloys [21, 43], Mg alloys [44, 45], and even Mo alloys [46] to name a few. Other authors focused on the defect's formation mechanism [47, 48], finding that porosities are entrapped gas bubbles that form when the energy density is too high, while incomplete fusion holes are formed between layers owing to the overlap between them. Other studies determined the influence of defects [49, 50], concluding that the presence of defects does not alter the overall microstructure of SLM products, but does influence the mechanical properties greatly to an unacceptable quality when they are present at the level of 5%. Studies regarding defect population discovered a link between the energy density and the amount of gas porosities owing to the presence of gas that allows vacuum inside the chamber of SLM equipment [13, 51], and a balance between energy input and scan velocity was suggested to decrease their presence [36, 52].

Furthermore, other researchers focused on the resultant microstructure [15, 31, 53, 54]. It was concluded that the different local thermal histories between the melt pool center and boundary form different microstructures in a wide variety of materials. For example, finer dendrites were observed in the melt pool center and coarser columnar dendrites were observed in the melt pool boundary in AlSi10Mg alloys [54, 55]. Similar results were observed in 316L austenitic stainless steel, showing a fine cellular substructure in the melt pool center and an enlarged epitaxial grain at the melt pool

borders [38]. Finally, in Ti—6Al—7Nb alloys, columnar grains oriented towards the melt pool center were found at the melt pool boundaries, and thin martensite particles were found at the melt pool center [16].

Owing to the high gradient temperatures and solidification rates, several studies have measured and analyzed the influence of residual stresses [56-58], concluding that the magnitude of residual stresses is at its maximum value at the top of the product, but the influence can be clearly observed at the bottom where the solidified material is not thick enough to restrict deformation, particularly when the product has a large length. Moreover, Mercelis et. al found that the residual stress profile suffers a considerable decrease owing to the relaxation phenomenon when the SLM product is removed from the base plate [8]. At the same time, several studies also analyzed the influence of post-processing mechanisms such as heat treatments, stress relief, and aging [10, 59-64]. It was concluded that heat treatments coarsen the microstructure, and the ductility increases significantly while the strength at failure decreases considerably [59, 65]. Furthermore, fracture behavior changes depending on the stress relief treatments [62], and direct aging of AlSi10Mg alloy can increase the hardness by 5.2% and thus the yield strength was increased [63].

It is important to mention that despite there being a large spectrum of literature regarding SLM processes, only a few studies have performed crack growth behavior analysis in static and cyclic loading and stated that fracture was caused by both the presence of unavoidable defects formed during sintering and microstructure irregularities attributed to the high and low solidification rates of the molten powder [32, 66]. However, a common stress concentration source responsible for fracture in all materials fabricated by SLM products has not been determined to date, nor its exact size or how to evaluate it. Additionally, the state at which the products fabricated by SLM are evaluated in the literature ranges from as-built state, machined state, heat treated, stress relieved and/or aged. Although post-processing is required in accordance with certain needs and the results are deeply analyzed and compared with other post-processing results or manufacturing technologies, a consensus to reach a distinction between as-built conditions and post-processed has not been achieved to date. Such distinction is particularly necessary because the results that cover mechanical properties, defect

formation and population, residual stresses, fracture mechanism, etc. change from an as-built state to any other post-processing state. For example, Baek et. al determined that a T6 heat treated AlSi10Mg flat specimen shows the poorest mechanical properties due to Si particles that enable dislocation emission, whilst maintaining the same ductility as the as-built state [60]. Then, Li et. al obtained much larger ductility results compared to the as-built state after testing AlSi10Mg flat specimens submitted to a conventional T6 heat treatment [65], while Aboulkhair et. al obtained similar results but on a round bar specimen without post-machining [53]. On the other hand, Casati et. al concluded that the fracture mechanism of a round bar machined specimen is void coalescence [38], similarly to Paul et. al, where void formation was verified at the melt pool borders [35]. However, results obtained by Wycisk et. al seem to contradict those affirmations by sustaining that defects located at the outer surface of Ti-6Al-4V alloy round bar machined specimens are responsible for fracture [67], similarly to Masuo et. al [11], and Qian et. al with machined AlSi10Mg alloys [68]. Furthermore, Aboulkhair et. al attributed the fracture of specimens in as-built state to the surface roughness of the final product [53], similarly to Vayssette et. al in as-built round bar Ti-6Al-4V specimens [69]. By analyzing the fracture mechanism if the as-built state, heat treated, and machined state separately, the critical factor before unstable fracture occurs can be reached. Thus, leaving a blank research space that this study will try to fulfill.

1.4 Objective

Simply put, the purpose of this study is to increase the reliability of the mechanical properties of SLM products. Despite its apparent simplicity, the large number of parameters that can be controlled and/or changed during sintering are known to influence the mechanical properties [30, 52, 70]. In consequence, it is difficult to determine a link between input sintering parameters and reliability if they are extremely variable. Moreover, output characteristics such as microstructure distribution cannot be controlled directly. Therefore, the starting point of this study is to determine a feature that can be controlled regardless of the amount of input variables and output characteristics that cannot, such as a fracture mechanism.

Using fracture mechanics concepts such as crack propagation and plastic deformation,

factors as to what are the critical concentration sources and the fracture process that SLM products undergo, can be determined. Then, these factors can be addressed specifically to control the ultimate tensile strength (UTS) of SLM products, thus being able to predict it before a tensile test is performed and in turn, increase the overall reliability of the process.

Finally, the author will try to focus on common factors that are present in all SLM products regardless of the material powder and the laser sintering parameters that were used. Then, a link between those common factors and the fracture mechanism can be determined to subsequently enable the extrapolation of the experimental results presented in this dissertation's case study and make them useful in the mechanical engineering society. For instance, one known common factor mentioned in SLM related literature is the microstructure duality, which will be analyzed in detail in Chapter 2. In addition, the reason why non-combustible Mg alloys were chosen for this study will be explained in Section 1.5.

1.5 Non-combustible Mg alloys

One of the advantages of SLM technologies is the wide range of metallic materials that can be used for the sintered products. In principle, if an alloy can be processed into metallic powder, it can work as a raw material for SLM [71]. The large flexibility of materials has allowed research with different metallic powders. Amongst the most common are Al [53, 72-76], 316L Stainless steel [27, 38, 39, 77, 78], Ti [79-83], Co [41, 84] and Ni [21, 43]. However, throughout the years Mg alloys have gained considerable attention within multiple areas, particularly due to its attractive properties such as high strength, durability and ductility obtained in relation to its significant low weight [85, 86]. As a result, Mg alloys have been used in orthopedics as a promising biodegradable material [87-89], in electronics devices such as notebooks and PCs as an alternative to plastic owing to the higher heat and electric conduction without being magnetic [90-92], and in the automotive and aero-space industry [85, 93].

Nevertheless, one of the intrinsic characteristics of Mg that is considered as a disadvantage is its flammable nature. Specifically, Mg alloys have a high volatility when submitted to high temperatures, disabling its use in traditional engineering manufacturing techniques and applications such as welding, casting or heat treatment applications [85,

86]. Thus, considering Mg based alloys for SLM processes could be a hazardous risk [44, 45]. To circumvent this problem, several researchers have intended to modify the chemical composition of the Mg alloys by adding elements such as Ca and Sr, which reduces the oxidation of Mg at high temperatures [94-96]. As a result, a patent was developed in Japan that enables the production of Mg alloy powder for SLM processes [97]. However, this study did not choose Mg alloys only for their recent scientific interest in diverse applications. A specific non-combustible Mg alloy was chosen to prove the flexibility of the SLM process with new powdered materials, and also to verify that the mechanical concepts used in this study can be applied in unexplored materials. In this manner, those same mechanical concepts can be extrapolated to materials that are currently popular amongst SLM processes and other materials that could be used in the future.

The metallic powder used in the entirety of this study for the fabrication of the specimens was Argon gas disk atomized AZX912 Mg alloy powder, where “X” stands for calcium. The chemical composition of the powdered material is shown in Table 1-1. The particle size distributions were $d_{10} = 31.3 \mu\text{m}$, $d_{50} = 47.1 \mu\text{m}$ and $d_{90} = 70.8 \mu\text{m}$, with an average particle size of $49.7 \mu\text{m}$.

1.6 Contents

The starting point of this study is the background and the contents of previous research that are relevant for this context. Chapter 2 analyses the weakest region of round bar tensile test specimens. This chapter briefly explains the formation mechanism of coarse microstructure and fine microstructure in SLM products, as well as their distribution rate and their role in the fracture mechanism considering the defect responsible for fracture under as-built conditions. Here the hypothesis and its originality are presented as a basis for the subsequent chapters.

Chapter 3 is focused on the verification of the hypothesis established in the previous chapter and analyzes the plastic strain distribution in a non-homogeneous microstructure. Also, the interaction of the microstructure duality between coarse and fine particles is discussed to propose the evaluation of the fracture mechanism quantitatively using Murakami’s Theory by using the size of the defect to calculate fracture toughness.

Chapter 4 presents the quantitative evaluation of the fracture mechanism proposed in Chapter 2 using the method proposed in Chapter 3 with artificially introduced defects to predict the UTS value of SLM products and increase the reliability of the process. In addition, the calculated fracture toughness for specimens in as-built conditions is compared to the results of specimens where a visible artificial defect is inserted.

Chapter 5 introduces the importance of a non-homogeneous microstructure compared to a homogeneous microstructure. Since traditional fracture mechanics needs a homogeneous material for engineering applications and purposes, it makes sense that the mechanical engineer would consider the homogenization of the SLM product via heat treatment. The impact of thermal post-processing on microstructure and the fracture mechanism is analyzed and discussed.

Chapter 6 discusses the true potential of SLM products by reducing the number of defects to a minimum and considers plastic instability theory to calculate a critical UTS value with its correspondent critical defect size by using a Mg alloy as an example. This concept allows the mechanical engineer to determine realistically the maximum UTS of SLM products achievable.

Chapter 7 evaluates theoretically the microstructure duality distribution of the plastic zone before unstable fracture occurs and its influence on the fracture process. As a result, a valid explanation for the variation of certain mechanical properties of SLM products, such as elongation, can be determined.

Chapter 8 includes the summary of this study and the conclusions relevant to the mechanical engineering community. In addition, the extension of the topics that could be researched in the future is proposed. The workflow covered in this Thesis is shown in Fig. 1-1.

1.7 References

- [1] J.P. Kruth, Material Incess Manufacturing by Rapid Prototyping Techniques, CIRP Annals, 40 (1991) 603-614. [https://doi.org/10.1016/S0007-8506\(07\)61136-6](https://doi.org/10.1016/S0007-8506(07)61136-6).
- [2] J.P. Kruth, M.C. Leu, T. Nakagawa, Progress in Additive Manufacturing and Rapid Prototyping, CIRP Annals, 47 (1998) 525-540. [https://doi.org/10.1016/S0007-8506\(07\)63240-5](https://doi.org/10.1016/S0007-8506(07)63240-5).
- [3] R. Tandon, J. Johnson, Powder Metal Technologies and Applications, Materials Park

- (OH): ASM International, 1998.
- [4] H.J. Niu, I.T.H. Chang, Instability of scan tracks of selective laser sintering of high speed steel powder, *Scripta Materialia*, 41 (1999) 1229-1234.
- [5] D. D Gu, W. Meiners, K. Wissenbach, R. Poprawe, Laser additive manufacturing of metallic components: Materials, processes and mechanisms, *International Materials Reviews*, 57 (2012) 133-164. [10.1179/1743280411Y.0000000014](https://doi.org/10.1179/1743280411Y.0000000014).
- [6] E.O. Olakanmi, R.F. Cochrane, K.W. Dalgarno, A review on selective laser sintering/melting (SLS/SLM) of aluminium alloy powders: Processing, microstructure, and properties, *Progress in Materials Science*, 74 (2015) 401-477. <https://doi.org/10.1016/j.pmatsci.2015.03.002>.
- [7] L.E. Murr, S.M. Gaytan, D.A. Ramirez, E. Martinez, J. Hernandez, K.N. Amato, P.W. Shindo, F.R. Medina, R.B. Wicker, Metal Fabrication by Additive Manufacturing Using Laser and Electron Beam Melting Technologies, *Journal of Materials Science & Technology*, 28 (2012) 1-14. [https://doi.org/10.1016/S1005-0302\(12\)60016-4](https://doi.org/10.1016/S1005-0302(12)60016-4).
- [8] P. Mercelis, J.P. Kruth, Residual stresses in selective laser sintering and selective laser melting, *Rapid Prototyping Journal*, 12 (2006) 254-265. [10.1108/13552540610707013](https://doi.org/10.1108/13552540610707013).
- [9] S. Marola, S. Bosia, A. Veltro, G. Fiore, D. Manfredi, M. Lombardi, G. Amato, M. Baricco, L. Battezzati, Residual stresses in additively manufactured AlSi10Mg: Raman spectroscopy and X-ray diffraction analysis, *Materials & Design*, 202 (2021) 109550. <https://doi.org/10.1016/j.matdes.2021.109550>.
- [10] Y. Liu, Y. Yang, D. Wang, A study on the residual stress during selective laser melting (SLM) of metallic powder, *The International Journal of Advanced Manufacturing Technology*, 87 (2016) 647-656. [10.1007/s00170-016-8466-y](https://doi.org/10.1007/s00170-016-8466-y).
- [11] H. Masuo, Y. Tanaka, S. Morokoshi, H. Yagura, T. Uchida, Y. Yamamoto, Y. Murakami, Effects of Defects, Surface Roughness and HIP on Fatigue Strength of Ti-6Al-4V manufactured by Additive Manufacturing, *Procedia Structural Integrity*, 7 (2017) 19-26. <https://doi.org/10.1016/j.prostr.2017.11.055>.
- [12] A. Bauereiß, T. Scharowsky, C. Körner, Defect generation and propagation mechanism during additive manufacturing by selective beam melting, *Journal of Materials Processing Technology*, 214 (2014) 2522-2528. <https://doi.org/10.1016/j.jmatprotec.2014.05.002>.
- [13] S. Tammas-Williams, H. Zhao, F. Léonard, F. Derguti, I. Todd, P.B. Prangnell, XCT analysis of the influence of melt strategies on defect population in Ti-6Al-4V components manufactured by Selective Electron Beam Melting, *Materials Characterization*, 102 (2015) 47-61. <https://doi.org/10.1016/j.matchar.2015.02.008>.
- [14] J.C. Hastie, M.E. Kartal, L.N. Carter, M.M. Attallah, D.M. Mulvihill, Classifying

- shape of internal pores within AlSi10Mg alloy manufactured by laser powder bed fusion using 3D X-ray micro computed tomography: Influence of processing parameters and heat treatment, *Materials Characterization*, 163 (2020) 110225. <https://doi.org/10.1016/j.matchar.2020.110225>.
- [15] M. Fousová, D. Dvorský, A. Michalcová, D. Vojtěch, Changes in the microstructure and mechanical properties of additively manufactured AlSi10Mg alloy after exposure to elevated temperatures, *Materials Characterization*, 137 (2018) 119-126. <https://doi.org/10.1016/j.matchar.2018.01.028>.
- [16] E. Chlebus, B. Kuźnicka, T. Kurzynowski, B. Dybała, Microstructure and mechanical behaviour of Ti—6Al—7Nb alloy produced by selective laser melting, *Materials Characterization*, 62 (2011) 488-495. <https://doi.org/10.1016/j.matchar.2011.03.006>.
- [17] L. Thijs, F. Verhaeghe, T. Craeghs, J.V. Humbeeck, J.-P. Kruth, A study of the microstructural evolution during selective laser melting of Ti—6Al—4V, *Acta Materialia*, 58 (2010) 3303-3312. <https://doi.org/10.1016/j.actamat.2010.02.004>.
- [18] J.G. Santos Macías, T. Douillard, L. Zhao, E. Maire, G. Pyka, A. Simar, Influence on microstructure, strength and ductility of build platform temperature during laser powder bed fusion of AlSi10Mg, *Acta Materialia*, 201 (2020) 231-243. <https://doi.org/10.1016/j.actamat.2020.10.001>.
- [19] G. Strano, L. Hao, R.M. Everson, K.E. Evans, Surface roughness analysis, modelling and prediction in selective laser melting, *Journal of Materials Processing Technology*, 213 (2013) 589-597. <https://doi.org/10.1016/j.jmatprotec.2012.11.011>.
- [20] Q. Yan, B. Song, Y. Shi, Comparative study of performance comparison of AlSi10Mg alloy prepared by selective laser melting and casting, *Journal of Materials Science & Technology*, 41 (2020) 199-208. <https://doi.org/10.1016/j.jmst.2019.08.049>.
- [21] D. Zhang, Z. Feng, C. Wang, W. Wang, Z. Liu, W. Niu, Comparison of microstructures and mechanical properties of Inconel 718 alloy processed by selective laser melting and casting, *Materials Science and Engineering: A*, 724 (2018) 357-367. <https://doi.org/10.1016/j.msea.2018.03.073>.
- [22] L.F. Wang, J. Sun, X.L. Yu, Y. Shi, X.G. Zhu, L.Y. Cheng, H.H. Liang, B. Yan, L.J. Guo, Enhancement in mechanical properties of selectively laser-melted AlSi10Mg aluminum alloys by T6-like heat treatment, *Materials Science and Engineering: A*, 734 (2018) 299-310. <https://doi.org/10.1016/j.msea.2018.07.103>.
- [23] P. Wang, J.F. Qi, Z.W. Chen, C.S. Lao, T.B. He, T.W. Lu, P. Gargarella, S. Scudino, Microstructure and mechanical properties of novel high-entropy alloy particle reinforced aluminum matrix composites fabricated by selective laser melting, *Journal*

- of Alloys and Compounds, 868 (2021) 159197. <https://doi.org/10.1016/j.jallcom.2021.159197>.
- [24] I. Tolosa, F. Garciandía, F. Zubiri, F. Zapirain, A. Esnaola, Study of mechanical properties of AISI 316 stainless steel processed by “selective laser melting”, following different manufacturing strategies, *The International Journal of Advanced Manufacturing Technology*, 51 (2010) 639-647. [10.1007/s00170-010-2631-5](https://doi.org/10.1007/s00170-010-2631-5).
- [25] S. Leuders, M. Vollmer, F. Brenne, T. Tröster, T. Niendorf, Fatigue Strength Prediction for Titanium Alloy TiAl6V4 Manufactured by Selective Laser Melting, *Metallurgical and Materials Transactions A*, 46 (2015) 3816-3823. [10.1007/s11661-015-2864-x](https://doi.org/10.1007/s11661-015-2864-x).
- [26] A.B. Spierings, K. Dawson, P.J. Uggowitzer, K. Wegener, Influence of SLM scan-speed on microstructure, precipitation of Al3Sc particles and mechanical properties in Sc- and Zr-modified Al-Mg alloys, *Materials & Design*, 140 (2018) 134-143. <https://doi.org/10.1016/j.matdes.2017.11.053>.
- [27] T. Larimian, M. Kannan, D. Grzesiak, B. AlMangour, T. Borkar, Effect of energy density and scanning strategy on densification, microstructure and mechanical properties of 316L stainless steel processed via selective laser melting, *Materials Science and Engineering: A*, 770 (2020) 138455. <https://doi.org/10.1016/j.msea.2019.138455>.
- [28] K. Wei, M. Gao, Z. Wang, X. Zeng, Effect of energy input on formability, microstructure and mechanical properties of selective laser melted AZ91D magnesium alloy, *Materials Science and Engineering: A*, 611 (2014) 212-222. <https://doi.org/10.1016/j.msea.2014.05.092>.
- [29] E. Beevers, A.D. Brandão, J. Gumpinger, M. Gschweitl, C. Seyfert, P. Hofbauer, T. Rohr, T. Ghidini, Fatigue properties and material characteristics of additively manufactured AlSi10Mg – Effect of the contour parameter on the microstructure, density, residual stress, roughness and mechanical properties, *International Journal of Fatigue*, 117 (2018) 148-162. <https://doi.org/10.1016/j.ijfatigue.2018.08.023>.
- [30] J.P. Oliveira, A.D. LaLonde, J. Ma, Processing parameters in laser powder bed fusion metal additive manufacturing, *Materials & Design*, 193 (2020) 108762. <https://doi.org/10.1016/j.matdes.2020.108762>.
- [31] A.A. Antonysamy, Microstructure, Texture and Mechanical Property Evolution During Additive Manufacture of Ti6Al4V Alloy Using Laser, Electron Beam, and Arc Melting Techniques for Aerospace Applications., in: *Faculty of Engineering and Physical Sciences, The University of Manchester*, 2012.
- [32] V. Cain, L. Thijs, J. Humbeeck, B. Hooreweder, R. Knutsen, Crack propagation and

- fracture toughness of Ti6Al4 V alloy produced by selective laser melting, 5 (2014) 68-76. [10.1016/j.addma.2014.12.006](https://doi.org/10.1016/j.addma.2014.12.006).
- [33] J. Karimi, C. Suryanarayana, I. Okulov, K.G. Prashanth, Selective laser melting of Ti6Al4V: Effect of laser re-melting, *Materials Science and Engineering: A*, 805 (2021) 140558. <https://doi.org/10.1016/j.msea.2020.140558>.
- [34] J. Zhang, B. Song, Q. Wei, D. Bourell, Y. Shi, A review of selective laser melting of aluminum alloys: Processing, microstructure, property and developing trends, *Journal of Materials Science & Technology*, 35 (2019) 270-284. <https://doi.org/10.1016/j.jmst.2018.09.004>.
- [35] M.J. Paul, Q. Liu, J.P. Best, X. Li, J.J. Kruzic, U. Ramamurty, B. Gludovatz, Fracture resistance of AlSi10Mg fabricated by laser powder bed fusion, *Acta Materialia*, 211 (2021) 116869. <https://doi.org/10.1016/j.actamat.2021.116869>.
- [36] N. Read, W. Wang, K. Essa, M.M. Attallah, Selective laser melting of AlSi10Mg alloy: Process optimisation and mechanical properties development, *Materials & Design (1980-2015)*, 65 (2015) 417-424. <https://doi.org/10.1016/j.matdes.2014.09.044>.
- [37] J. Suryawanshi, K.G. Prashanth, S. Scudino, J. Eckert, O. Prakash, U. Ramamurty, Simultaneous enhancements of strength and toughness in an Al-12Si alloy synthesized using selective laser melting, *Acta Materialia*, 115 (2016) 285-294. <https://doi.org/10.1016/j.actamat.2016.06.009>.
- [38] R. Casati, J. Lemke, M. Vedani, Microstructure and Fracture Behavior of 316L Austenitic Stainless Steel Produced by Selective Laser Melting, *Journal of Materials Science & Technology*, 32 (2016) 738-744. <https://doi.org/10.1016/j.jmst.2016.06.016>.
- [39] K. Solberg, S. Guan, S.M.J. Razavi, T. Welo, K.C. Chan, F. Berto, Fatigue of additively manufactured 316L stainless steel: The influence of porosity and surface roughness, *Fatigue & Fracture of Engineering Materials & Structures*, 0 (2019). [10.1111/ffe.13077](https://doi.org/10.1111/ffe.13077).
- [40] Z.W. Chen, T. Guraya, K. Darvish, M.A.L. Phan, T. Pasang, Solidification During Selective Laser Melting of Co-29Cr-6Mo Alloy, *JOM*, 71 (2019) 691-696. [10.1007/s11837-018-3264-7](https://doi.org/10.1007/s11837-018-3264-7).
- [41] K.C. Yung, T.Y. Xiao, H.S. Choy, W.J. Wang, Z.X. Cai, Laser polishing of additive manufactured CoCr alloy components with complex surface geometry, *Journal of Materials Processing Technology*, 262 (2018) 53-64. [10.1016/j.jmatprotec.2018.06.019](https://doi.org/10.1016/j.jmatprotec.2018.06.019).
- [42] D. Lin, L. Xu, Y. Han, Y. Zhang, H. Jing, L. Zhao, F. Minami, Structure and mechanical properties of a FeCoCrNi high-entropy alloy fabricated via selective laser melting, *Intermetallics*, 127 (2020) 106963.

- <https://doi.org/10.1016/j.intermet.2020.106963>.
- [43] Y. Zhao, K. Aoyagi, Y. Daino, K. Yamanaka, A. Chiba, Significance of powder feedstock characteristics in defect suppression of additively manufactured Inconel 718, *Additive Manufacturing*, 34 (2020) 101277. <https://doi.org/10.1016/j.addma.2020.101277>.
- [44] R. Karunakaran, S. Ortgies, A. Tamayol, F. Bobaru, M.P. Sealy, Additive manufacturing of magnesium alloys, *Bioactive Materials*, 5 (2020) 44-54. <https://doi.org/10.1016/j.bioactmat.2019.12.004>.
- [45] V. Manakari, G. Parande, M. Gupta, Selective Laser Melting of Magnesium and Magnesium Alloy Powders: A Review, 7 (2016) 2. [10.3390/met7010002](https://doi.org/10.3390/met7010002).
- [46] L. Kaserer, J. Braun, J. Stajkovic, K.H. Leitz, B. Tabernig, P. Singer, I. Letofsky-Papst, H. Kestler, G. Leichtfried, Fully dense and crack free molybdenum manufactured by Selective Laser Melting through alloying with carbon, *International Journal of Refractory Metals and Hard Materials*, (2019) 105000. <https://doi.org/10.1016/j.ijrmhm.2019.105000>.
- [47] B. Zhang, Y. Li, Q. Bai, Defect Formation Mechanisms in Selective Laser Melting: A Review, *Chinese Journal of Mechanical Engineering*, 30 (2017) 515-527. [10.1007/s10033-017-0121-5](https://doi.org/10.1007/s10033-017-0121-5).
- [48] C. Tang, J.L. Tan, C.H. Wong, A numerical investigation on the physical mechanisms of single track defects in selective laser melting, *International Journal of Heat and Mass Transfer*, 126 (2018) 957-968. <https://doi.org/10.1016/j.ijheatmasstransfer.2018.06.073>.
- [49] H. Gong, K. Rafi, H. Gu, G.D. Janaki Ram, T. Starr, B. Stucker, Influence of defects on mechanical properties of Ti-6Al-4V components produced by selective laser melting and electron beam melting, *Materials & Design*, 86 (2015) 545-554. <https://doi.org/10.1016/j.matdes.2015.07.147>.
- [50] M. Dallago, B. Winiarski, F. Zanini, S. Carmignato, M. Benedetti, On the effect of geometrical imperfections and defects on the fatigue strength of cellular lattice structures additively manufactured via Selective Laser Melting, *International Journal of Fatigue*, 124 (2019) 348-360. <https://doi.org/10.1016/j.ijfatigue.2019.03.019>.
- [51] H. Kyogoku, T.-T. Ikeshoji, A review of metal additive manufacturing technologies: Mechanism of defects formation and simulation of melting and solidification phenomena in laser powder bed fusion process, *Mechanical Engineering Reviews*, 7 (2020) 19-00182-00119-00182. [10.1299/mer.19-00182](https://doi.org/10.1299/mer.19-00182).
- [52] H. Shipley, D. McDonnell, M. Culleton, R. Coull, R. Lupoi, G. O'Donnell, D. Trimble, Optimisation of process parameters to address fundamental challenges during

- selective laser melting of Ti-6Al-4V: A review, *International Journal of Machine Tools and Manufacture*, 128 (2018) 1-20. <https://doi.org/10.1016/j.ijmachtools.2018.01.003>.
- [53] N.T. Aboulkhair, I. Maskery, C. Tuck, I. Ashcroft, N.M. Everitt, The microstructure and mechanical properties of selectively laser melted AlSi10Mg: The effect of a conventional T6-like heat treatment, *Materials Science and Engineering: A*, 667 (2016) 139-146. <https://doi.org/10.1016/j.msea.2016.04.092>.
- [54] X. Liu, C. Zhao, X. Zhou, Z. Shen, W. Liu, Microstructure of selective laser melted AlSi10Mg alloy, *Materials & Design*, 168 (2019) 107677. <https://doi.org/10.1016/j.matdes.2019.107677>.
- [55] Y. Cao, X. Lin, Q.Z. Wang, S.Q. Shi, L. Ma, N. Kang, W.D. Huang, Microstructure evolution and mechanical properties at high temperature of selective laser melted AlSi10Mg, *Journal of Materials Science & Technology*, 62 (2021) 162-172. <https://doi.org/10.1016/j.jmst.2020.04.066>.
- [56] M. Shiomi, K. Osakada, K. Nakamura, T. Yamashita, F. Abe, Residual Stress within Metallic Model Made by Selective Laser Melting Process, *CIRP Annals*, 53 (2004) 195-198. [https://doi.org/10.1016/S0007-8506\(07\)60677-5](https://doi.org/10.1016/S0007-8506(07)60677-5).
- [57] C.R. Knowles, T.H. Becker, R.B. Tait, RESIDUAL STRESS MEASUREMENTS AND STRUCTURAL INTEGRITY IMPLICATIONS FOR SELECTIVE LASER MELTED TI-6AL-4V, *The South African Journal of Industrial Engineering*; Vol 23, No 3 (2012), (2012). [10.7166/23-3-515](https://doi.org/10.7166/23-3-515).
- [58] K.-H.k.-d.A.a. Kouadri, J.-E. Masse, L. Barrallier, Residual stress characterisation by X-ray diffraction of AZ91 magnesium alloy welded by laser processing, 2005.
- [59] F. Alghamdi, X. Song, A. Hadadzadeh, B. Shalchi-Amirkhiz, M. Mohammadi, M. Haghshenas, Post heat treatment of additive manufactured AlSi10Mg: On silicon morphology, texture and small-scale properties, *Materials Science and Engineering: A*, 783 (2020) 139296. <https://doi.org/10.1016/j.msea.2020.139296>.
- [60] M.-S. Baek, R. Kreethi, T.-H. Park, Y. Sohn, K.-A. Lee, Influence of heat treatment on the high-cycle fatigue properties and fatigue damage mechanism of selective laser melted AlSi10Mg alloy, *Materials Science and Engineering: A*, 819 (2021) 141486. <https://doi.org/10.1016/j.msea.2021.141486>.
- [61] L. Girelli, M. Tocci, M. Gelfi, A. Pola, Study of heat treatment parameters for additively manufactured AlSi10Mg in comparison with corresponding cast alloy, *Materials Science and Engineering: A*, 739 (2019) 317-328. <https://doi.org/10.1016/j.msea.2018.10.026>.
- [62] B. Amir, E. Grinberg, Y. Gale, O. Sadot, S. Samuha, Influences of platform heating and post-processing stress relief treatment on the mechanical properties and

- microstructure of selective-laser-melted AlSi10Mg alloys, *Materials Science and Engineering: A*, 822 (2021) 141612. <https://doi.org/10.1016/j.msea.2021.141612>.
- [63] T.-H. Park, M.-S. Baek, H. Hyer, Y. Sohn, K.-A. Lee, Effect of direct aging on the microstructure and tensile properties of AlSi10Mg alloy manufactured by selective laser melting process, *Materials Characterization*, 176 (2021) 111113. <https://doi.org/10.1016/j.matchar.2021.111113>.
- [64] Z. Li, Z. Li, Z. Tan, D.-B. Xiong, Q. Guo, Stress relaxation and the cellular structure-dependence of plastic deformation in additively manufactured AlSi10Mg alloys, *International Journal of Plasticity*, 127 (2020) 102640. <https://doi.org/10.1016/j.ijplas.2019.12.003>.
- [65] W. Li, S. Li, J. Liu, A. Zhang, Y. Zhou, Q. Wei, C. Yan, Y. Shi, Effect of heat treatment on AlSi10Mg alloy fabricated by selective laser melting: Microstructure evolution, mechanical properties and fracture mechanism, *Materials Science and Engineering: A*, 663 (2016) 116-125. <https://doi.org/10.1016/j.msea.2016.03.088>.
- [66] P.D. Nezhadfar, E. Burford, K. Anderson-Wedge, B. Zhang, S. Shao, S.R. Daniewicz, N. Shamsaei, Fatigue crack growth behavior of additively manufactured 17-4 PH stainless steel: Effects of build orientation and microstructure, *International Journal of Fatigue*, 123 (2019) 168-179. [10.1016/j.ijfatigue.2019.02.015](https://doi.org/10.1016/j.ijfatigue.2019.02.015).
- [67] E. Wycisk, A. Solbach, S. Siddique, D. Herzog, F. Walther, C. Emmelmann, Effects of Defects in Laser Additive Manufactured Ti-6Al-4V on Fatigue Properties, *Physics Procedia*, 56 (2014) 371-378. <https://doi.org/10.1016/j.phpro.2014.08.120>.
- [68] W. Qian, S. Wu, Z. Wu, S. Ahmed, W. Zhang, G. Qian, P.J. Withers, In situ X-ray imaging of fatigue crack growth from multiple defects in additively manufactured AlSi10Mg alloy, *International Journal of Fatigue*, 155 (2022) 106616. <https://doi.org/10.1016/j.ijfatigue.2021.106616>.
- [69] B. Vayssette, N. Saintier, C. Brugger, M. Elmay, E. Pessard, Surface roughness of Ti-6Al-4V parts obtained by SLM and EBM: Effect on the High Cycle Fatigue life, *Procedia Engineering*, 213 (2018) 89-97. <https://doi.org/10.1016/j.proeng.2018.02.010>.
- [70] B. Song, S. Dong, B. Zhang, H. Liao, C. Coddet, Effects of processing parameters on microstructure and mechanical property of selective laser melted Ti6Al4V, *Materials & Design*, 35 (2012) 120-125. <https://doi.org/10.1016/j.matdes.2011.09.051>.
- [71] A. Popovich, V. Sufiiarov, Metal Powder Additive Manufacturing, *New Trends in 3D Printing*, (2016) 215-236. [10.5772/63337](https://doi.org/10.5772/63337).
- [72] S. Beretta, M. Gargourimotlagh, S. Foletti, A. du Plessis, M. Riccio, Fatigue strength assessment of “as built” AlSi10Mg manufactured by SLM with different build orientations, *International Journal of Fatigue*, 139 (2020) 105737.

- <https://doi.org/10.1016/j.ijfatigue.2020.105737>.
- [73] S.R. Ch, A. Raja, R. Jayaganthan, N.J. Vasa, M. Raghunandan, Study on the fatigue behaviour of selective laser melted AlSi10Mg alloy, *Materials Science and Engineering: A*, 781 (2020) 139180. <https://doi.org/10.1016/j.msea.2020.139180>.
- [74] A. Hadadzadeh, C. Baxter, B.S. Amirkhiz, M. Mohammadi, Strengthening mechanisms in direct metal laser sintered AlSi10Mg: Comparison between virgin and recycled powders, *Additive Manufacturing*, 23 (2018) 108-120. <https://doi.org/10.1016/j.addma.2018.07.014>.
- [75] K. Kempen, L. Thijs, J. Van Humbeeck, J.P. Kruth, Mechanical Properties of AlSi10Mg Produced by Selective Laser Melting, *Physics Procedia*, 39 (2012) 439-446. <https://doi.org/10.1016/j.phpro.2012.10.059>.
- [76] M. Schuch, T. Hahn, M. Bleckmann, The mechanical behavior and microstructure of additively manufactured AlSi10Mg for different material states and loading conditions, *Materials Science and Engineering: A*, 813 (2021) 141134. <https://doi.org/10.1016/j.msea.2021.141134>.
- [77] A. Leicht, M. Fischer, U. Klement, L. Nyborg, E. Hryha, Increasing the Productivity of Laser Powder Bed Fusion for Stainless Steel 316L through Increased Layer Thickness, *Journal of Materials Engineering and Performance*, 30 (2021) 575-584. [10.1007/s11665-020-05334-3](https://doi.org/10.1007/s11665-020-05334-3).
- [78] M. Yakout, M.A. Elbestawi, S.C. Veldhuis, Density and mechanical properties in selective laser melting of Invar 36 and stainless steel 316L, *Journal of Materials Processing Technology*, 266 (2019) 397-420. <https://doi.org/10.1016/j.jmatprotec.2018.11.006>.
- [79] H. Attar, M. Calin, L.C. Zhang, S. Scudino, J. Eckert, Manufacture by selective laser melting and mechanical behavior of commercially pure titanium, *Materials Science and Engineering: A*, 593 (2014) 170-177. <https://doi.org/10.1016/j.msea.2013.11.038>.
- [80] J. Cao, K. Kou, C. Lam, Crack propagation analysis of 3D printed functionally graded titanium alloy components, *Theoretical and Applied Fracture Mechanics*, 111 (2021) 102865. <https://doi.org/10.1016/j.tafmec.2020.102865>.
- [81] E.R. Denlinger, J.C. Heigel, P. Michaleris, T.A. Palmer, Effect of inter-layer dwell time on distortion and residual stress in additive manufacturing of titanium and nickel alloys, *Journal of Materials Processing Technology*, 215 (2015) 123-131. <https://doi.org/10.1016/j.jmatprotec.2014.07.030>.
- [82] S. Leuders, M. Thöne, A. Riemer, T. Niendorf, T. Tröster, H.A. Richard, H.J. Maier, On the mechanical behaviour of titanium alloy TiAl6V4 manufactured by selective laser melting: Fatigue resistance and crack growth performance, *International Journal*

- of Fatigue, 48 (2013) 300-307. <https://doi.org/10.1016/j.ijfatigue.2012.11.011>.
- [83] E. Pessard, M. Laviolle, P. Laheurte, P. Didier, M. Brochu, High-cycle fatigue behavior of a laser powder bed fusion additive manufactured Ti-6Al-4V titanium: Effect of pores and tested volume size, *International Journal of Fatigue*, 149 (2021) 106206. <https://doi.org/10.1016/j.ijfatigue.2021.106206>.
- [84] K. Darvish, Z.W. Chen, T. Pasang, Reducing lack of fusion during selective laser melting of CoCrMo alloy: Effect of laser power on geometrical features of tracks, *Materials & Design*, 112 (2016) 357-366. [10.1016/j.matdes.2016.09.086](https://doi.org/10.1016/j.matdes.2016.09.086).
- [85] M.K. Kulekci, Magnesium and its alloys applications in automotive industry, *The International Journal of Advanced Manufacturing Technology*, 39 (2008) 851-865. [10.1007/s00170-007-1279-2](https://doi.org/10.1007/s00170-007-1279-2).
- [86] B.L. Mordike, T. Ebert, Magnesium: Properties — applications — potential, *Materials Science and Engineering: A*, 302 (2001) 37-45. [https://doi.org/10.1016/S0921-5093\(00\)01351-4](https://doi.org/10.1016/S0921-5093(00)01351-4).
- [87] Y. Chen, Z. Xu, C. Smith, J. Sankar, Recent advances on the development of magnesium alloys for biodegradable implants, *Acta Biomaterialia*, 10 (2014) 4561-4573. <https://doi.org/10.1016/j.actbio.2014.07.005>.
- [88] L.E. Murr, S.A. Quinones, S.M. Gaytan, M.I. Lopez, A. Rodela, E.Y. Martinez, D.H. Hernandez, E. Martinez, F. Medina, R.B. Wicker, Microstructure and mechanical behavior of Ti-6Al-4V produced by rapid-layer manufacturing, for biomedical applications, *Journal of the Mechanical Behavior of Biomedical Materials*, 2 (2009) 20-32. <https://doi.org/10.1016/j.jmbbm.2008.05.004>.
- [89] M.P. Staiger, A.M. Pietak, J. Huadmai, G. Dias, Magnesium and its alloys as orthopedic biomaterials: A review, *Biomaterials*, 27 (2006) 1728-1734. <https://doi.org/10.1016/j.biomaterials.2005.10.003>.
- [90] H. Watarai, Chapter 7: Trend of Research and Development for Magnesium Alloys, in: P.D.U. Kainer (Ed.) *Science & Technology Trends*, 2006, pp. 84-97.
- [91] J. Song, J. Chen, X. Xiong, X. Peng, D. Chen, F. Pan, Research advances of magnesium and magnesium alloys worldwide in 2021, *Journal of Magnesium and Alloys*, 10 (2022) 863-898. <https://doi.org/10.1016/j.jma.2022.04.001>.
- [92] Y. Yang, X. Xiong, J. Chen, X. Peng, D. Chen, F. Pan, Research advances in magnesium and magnesium alloys worldwide in 2020, *Journal of Magnesium and Alloys*, 9 (2021) 705-747. <https://doi.org/10.1016/j.jma.2021.04.001>.
- [93] H. Furuya, N. Kogiso, S. Matunaga, K. Senda, Applications of Magnesium Alloys for Aerospace Structure Systems, *Materials Science Forum - MATER SCI FORUM*, 350 (2000) 341-348. [10.4028/www.scientific.net/MSF.350-351.341](https://doi.org/10.4028/www.scientific.net/MSF.350-351.341).

- [94] B.S. You, W.W. Park, I.S. Chung, Effect of calcium additions on the oxidation behavior in magnesium alloys, *Scripta Materialia*, 42 (2000) 1089-1094. [10.1016/S1359-6462\(00\)00344-4](https://doi.org/10.1016/S1359-6462(00)00344-4).
- [95] K. Hirai, H. Somekawa, Y. Takigawa, K. Higashi, Effects of Ca and Sr addition on mechanical properties of a cast AZ91 magnesium alloy at room and elevated temperature, *Materials Science and Engineering: A*, 403 (2005) 276-280. <https://doi.org/10.1016/j.msea.2005.05.028>.
- [96] S. Akiyama, Flame-Resistant Magnesium Alloys by Calcium (Text in Japanese), *THE JOURNAL OF THE JAPAN FOUNDRYMEN'S SOCIETY*, 66 (1994) 38-42. [10.11279/imon.66.1_38](https://doi.org/10.11279/imon.66.1_38).
- [97] T. Matsumoto, F. Kido, H. Miyahara, Magnesium alloy powder (Text in Japanese), in: *Japan Patent Application No. 2017-180871*, 2017.

1.8 List of tables

Table 1-1 Chemical composition (wt%) of AZX912 Mg alloy.

Al	Zn	Ca	Mn	Si	Cu	Fe	Ni
8.55	0.64	1.81	0.18	0.034	0.001	0.003	0.001

1.9 List of figures

Strength reliability of SLM products

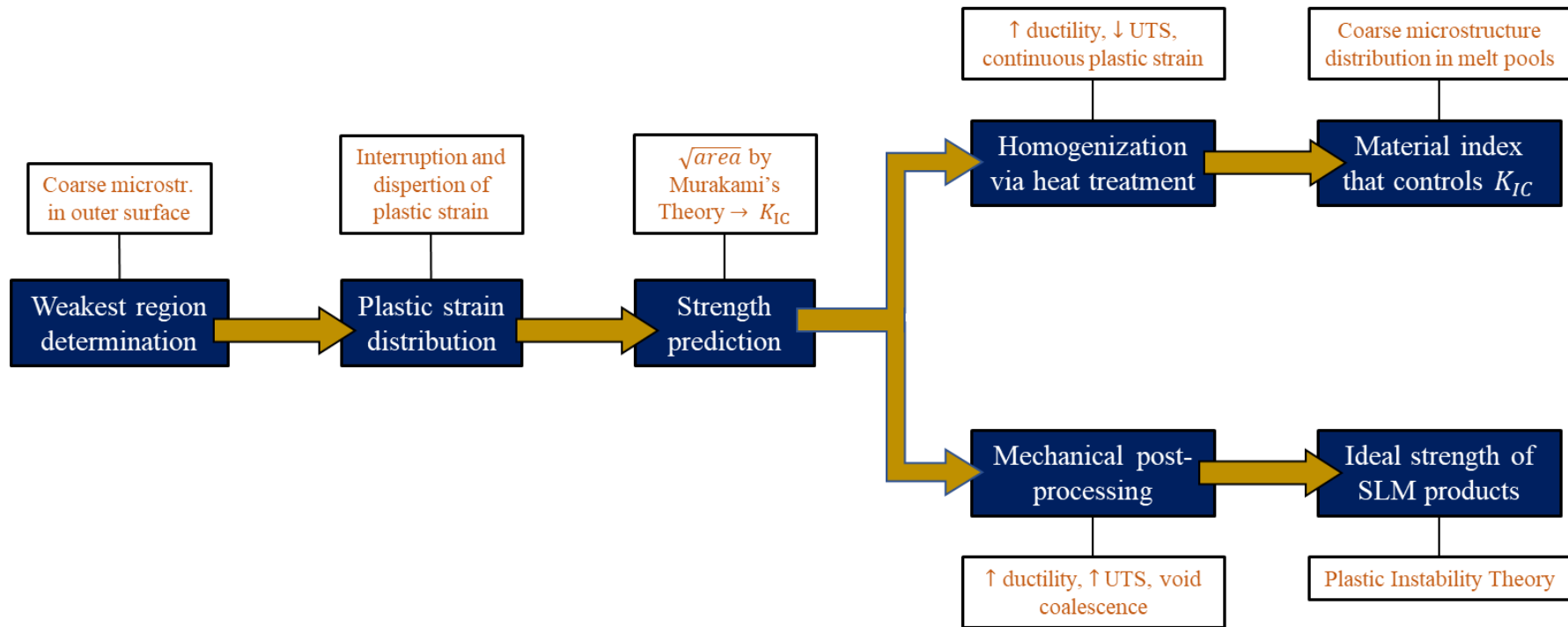


Fig. 1-1 Workflow chart of the present Dissertation.

CHAPTER 2.- WEAKEST REGION ANALYSIS OF SLM PRODUCTS

2.1 Introduction

SLM has gained considerable attention in recent years and several studies have analyzed its advantages as a viable manufacturing technique focusing on its mechanical properties [1-5]. Since the basis of this study will begin by determining a fracture mechanism, it makes sense to start analyzing the fracture characteristics of tensile test specimens in a controlled environment to further derive a general fracture process of SLM products. For this purpose, the present study will make a distinction in the literature that evaluates mechanical properties of SLM specimens in as-built state and after post-processing conditions. The former condition is achieved when the specimens fabricated in an SLM machine have not undergone any processing in the area where fracture is expected to occur and the latter condition is reached when the specimens are either mechanically machined, polished or heat treated, etc. in the area where fracture is expected to occur. For instance, in a round bar tensile test specimen, fracture will occur somewhere within the gauge length. Therefore, if the gauge length is in the same state as it was when removed from the SLM machine, it is considered “as-built”. However, if the gauge length is mechanically processed or heat treated, then the specimen will be considered as “post-processed”.

Currently, UTS values of specimens in as-built conditions are attractive to the mechanical engineer because they are considerably higher if compared to the traditional manufacturing counterparts. For example, Song et. al found that Ti-6Al-4V specimens fabricated by SLM show a 20% increase in UTS value compared to wrought specimens, 16% increase for Ni alloys compared to wrought specimens and 17% increase for 316L stainless steel compared to forged specimens [6], and Roth et. al found that the UTS value of AlSi10Mg increases by about 20% compared to the same alloy manufactured by casting [7]. To present the viability of SLM specimens using Mg alloys, this study uses AZX912 Mg alloy, where “X” stands for Calcium, which helps to undermine the natural volatility of Mg when exposed to high temperatures. The exact same Mg alloy fabricated

by casting was analyzed by Ochi et. al where the UTS value was 101 MPa [8]. Therefore, if the same pattern is to be continued, AZX912 Mg alloys should show an increase in the UTS value when fabricated by SLM.

Nevertheless, the reasoning behind the UTS value of SLM products in as-built conditions is attributed to several factors. Aboulkhair et. al noticed that fracture initiates at the fracture surface and attributed it to the poor surface roughness quality and presence of defects [9]. Rafi et. al established void formation and attributed the higher UTS of Ti64 alloy to the harder microstructure formed by SLM [10], and Olakanmi et. al also noticed that fracture always started from the imperfections at the surface, behaving as a surface-notch of AlSi10Mg alloys [11]. The criteria that a small defect located in the outer surface would be responsible for fracture is correct from a stress concentration perspective, but it is important to notice that SLM occasionally produces a large population of gas porosities and large sized lack-of-fusion pores throughout the sintered product [9, 12, 13], not only at the outer surface. Furthermore, XCT analyses have shown that defect population tends to concentrate towards the center instead of the outer surface [14, 15]. However, despite the presence of those large defects that cause large stress concentrations, as-built specimens still fractured from the outer surface. Therefore, the exact phenomenon that causes fracture to start at the outer surface remains unclear.

From a microstructure perspective, a large number of studies agree that SLM products present a microstructure duality regardless of the metallic powder used. For instance, Aboulkhair et. al [16], Cao et. al [1], Dong et. al [2], and Hadadzadeh et. al [17], have reported that in AlSi10Mg there are hard fine particles in the microstructure inside the melt pool and coarse particles at the melt pool borders. Similarly, Chlebus et. al [18], Murr et. al [19], and Rafi et. al [10] concluded that Ti alloys have martensitic microstructure with columnar grain boundaries at the melt pool boundaries owing to the different cooling rates. Finally, Casati et. al [20], Larimian et. al [21], and Yakout et. al [22] determined that melt pool boundaries include cellular substructures, and the melt pool center has refined microstructure in 316L stainless steel. In SLM products, the melt pool center has long, equiaxed refined microstructure owing to the concentrated cooling rate and the melt pool boundaries have columnar, coarsened microstructure owing to the solidification rate always directed towards the center of the melt pool in accordance to

heat transfer mechanisms [23]. Then, according to the Hall-Petch relation, hardness should be higher at the melt pool center where the microstructure is refined compared to the melt pool boundary where the microstructure is coarsened. Moreover, coarsened microstructure at the melt pool boundary is a result of a slow solidification rate [1, 9]. Therefore, the beginning of the scan track is of particular interest, due to its proximity to the unmolten powder. Considering that metallic powder has a lower heat transfer coefficient in comparison to the solidified material [24], then the beginning of the scan track of each layer undergoes a slower cooling rate in comparison with the remaining surface of the layer. As a result, the outer surface of the SLM product where the beginning of the scan track took place should present a soft, coarsened microstructure. If the coarsened microstructure has a lower hardness, stable crack propagation is enabled from the outer surface until it reaches the harder, refined microstructure at the center of the specimen. Thus, stable crack propagation is interrupted, inducing a larger stress concentration source than the visible defects and at the same time the fracture initiation point always being located at the outer surface is explained.

In this chapter, 6 round-bar specimens for tensile testing and 2 round-bar specimens for microstructure observation were fabricated by selective laser melting. The fractured specimens were submitted to scanning electron microscope (SEM) observation for fractography analyses. The microstructure distribution at the outer surface was determined via extreme value statistics and the microhardness of the microstructure was measured. The results of this study can provide a foundation for determining the defects responsible for fracture in SLM products and obtain methods to enhance the reliability of the process in as-built conditions.

2.2 Experimental procedure

The entirety of the specimens used in this study were carried out using an EOS M100 SLM machine, which is shown in Fig. 2-1. First, the specimens were 3D-modeled in Autodesk Inventor® and subsequently exported to an STL (stereolithography) format. Then, supports of the specimens were added using another 3D-CAD assisted software named Materialise Magics®. Afterwards, the specimens and the supports were added to the EOSPRINT® 3D Printing Software Data, where the laser irradiation parameters were

set. Then, the specimens, supports and parameters were exported to the EOS M100 SLM machine, which was finally set with the metallic powder as a raw material before sintering began.

The laser irradiation parameters were the same for all specimens and geometries shown in this study, and they are shown in Table 2-1. The scanning strategy for all the specimens and different geometries in this study can be observed in Fig. 2-2. Once the sintering was finished, the specimens were retrieved from the base plate using a Mitsubishi BA8 electrical discharge machine (EDM).

The metal powder used for the fabrication of the specimens was Argon gas disk atomized AZX912 Mg alloy powder. The chemical composition of the powdered material is shown in Table 1-1. The particle size distributions were $d_{10} = 31.3 \mu\text{m}$, $d_{50} = 47.1 \mu\text{m}$ and $d_{90} = 70.8 \mu\text{m}$, with an average particle size of $49.7 \mu\text{m}$, same results as shown in Section 1.4. The round bar specimens used in this study were carried out using the EOS M100 SLM machine shown in Fig. 2-1.

Four 4-mm and 6-mm round bar specimens were fabricated using a constant printing strategy: arranging the scanning direction in one layer parallel to the base plate, rotating 67° on the subsequent layer and repeating the process by applying successive layers in the building direction, as shown in Fig. 2-2 a). Three specimens for each diameter were submitted to tensile testing. The geometry of the specimens can be seen in Fig. 2-3. Tensile tests were performed using a Shimadzu AG-50kNXD universal electromechanical testing machine set at a strain rate of 0.0011 s^{-1} in conformance with the Japanese Industrial Standard JIS Z 2241:2011 (Method of Tensile Test for Metallic Materials). Tensile testing was performed along the building direction of the round-bar specimens at a room temperature range of 21-22 °C. All tests were performed using a screw-type grip set with spherical bearings to ensure that no misalignment or bending occurred during testing. Elongation was measured using a Shimadzu SG25-100 extensometer with a gauge length of 25 mm. Fracture surfaces were observed using a JEOL JSM-IT300 scanning electron microscope. The remaining specimens were submitted to microstructure observation.

For microstructure observation, a section from the gauge length of the round bar specimens was cut in horizontal and longitudinal cross sections as shown in Fig. 2-4, and

the inner surfaces were polished until a diamond-finish roughness was obtained; next, the polished segment was treated by the etchant (1 g picric acid, 10 ml acetic acid and 90 ml ethyl alcohol) to clarify the SEM images. The microstructure was observed using a Hitachi High-Tech Low Vacuum Analysis SU6600 scanning electron microscope, and it was measured using a Nikon Eclipse L150 optical microscope. Micro-hardness testing was performed using an HMV-FA Series Shimadzu Micro-Hardness Tester at a force of 10 g.

2.3 Results

2.3.1 Tensile tests and fractography results

Tensile tests for a total of six specimens were performed. Three specimens had a diameter of 4-mm, and three specimens had a diameter of 6-mm. All the S-S diagrams are shown in Fig. 2-5. The fractured specimens under as-built conditions yielded the following mean values: an ultimate strength of 340 MPa, a yield strength of 255 MPa (0.2% proof strength), and an elongation of 3.6%. These results are consistent with the results obtained in other previous studies that used similar alloys [25, 26]. Similar to other materials where mechanical properties obtained by SLM and casting processes were compared [27, 28], the UTS results of an AZX912 Mg alloy fabricated by SLM in as-built conditions are much higher compared to the same alloy fabricated by casting [8].

The fracture surfaces of a 4-mm and 6-mm round bar specimen are shown in Figs. 2-6 and 2-7 respectively. For both cases, the fracture initiation point and the area of the stable crack propagation are marked in accordance with hole-hole or peak-peak morphology for ductile fracture and peak-hole morphology for brittle fracture. It is important to note that there is not a visible defect where the fracture initiation point is located.

2.3.2 Microstructure observation and distribution

Figure 2-8 shows the microstructure observation results from a single melt pool located at the center of the specimens, while Fig. 2-9 shows the microstructure observed in the outer surface of the specimens. Figure 2-10 shows the microstructure distribution in a long section of the outer surface for 4-mm and 6-mm round bar specimens, showing

chunks of large and irregular coarsened grains. It is revealed in Fig. 2-8 that the fine dendrite-like α phase (gray area) and the Al_2Ca eutectic phase (white area) between dendrite are crystalized in the grain. Additionally, Fig. 2-8 also shows that dendrite is columnar and much more coarsened at the melt pool border compared to the center, where dendrite is refined. Microstructure results are consistent with those of other materials used in SLM.

To quantitatively evaluate the microstructure distribution at the outer surface of as-built SLM specimens, extreme value statistical analysis was performed. This method enables us to estimate the largest dimension of macrostructure that possibly exists in the whole sample. The whole specimen length and the observed length were defined as L (6 mm for the 6-mm round bar specimen) and L_0 (0.5 mm), respectively. The solidified structures were observed at a depth of 1000 μm from the side surface and at intervals of 100 μm without overlap. The cumulative distribution function F was calculated from the distribution of the maximum values obtained. Then, the extreme statistical graph was created with the standardized variable (y_i) according to the following equations:

$$F = \frac{i}{n + 1} \quad (2 - 1)$$

$$y_i = -\ln\{-\ln(F)\} \quad (2 - 2)$$

The maximum width of coarse grain area at each depth was estimated for the entire observation by the relationship between the obtained extreme statistical graph, the return period (T), and the maximum distribution line (y_{max}) shown in the following equations:

$$T = \frac{L_0 + L}{L_0} \quad (2 - 3)$$

$$y_{max} = -\ln\left\{-\ln\left(\frac{T - 1}{T}\right)\right\} \quad (2 - 4)$$

The area fraction of coarse microstructure compared to the entire specimen was measured for a certain depth from the outer surface in the vertical cross-sectional structure. Figure 2-11 shows an example of how the maximum width of coarse microstructure was measured for each depth range. From the relationship between the obtained extremum statistical graph which can be observed in Fig. 2-12, the return period (T) and the maximum distribution line (y_{max}), approximately 700 μm of length at the outer surface was evaluated at steps of 100 μm for both specimens. The analyses were performed up

until a depth of 1000 μm , and the distribution results of coarse microstructure at the outer surface can be observed in Fig. 2-13. For AZX912 Mg alloys, the coarse microstructure width stabilizes at a depth of approximately 430 μm and 600 μm for a 4-mm and 6-mm round bar specimen, respectively.

2.3.3 Micro-hardness tests results

Several microhardness measurements were performed at 10 g force at the center and boundaries of the melt pool formations in both 4-mm and 6-mm specimens. A schematic of the measurement setup is shown in Fig. 2-14. For as-built state, the average hardness of the melt pool center (fine microstructure) was 116 *HV* and that at the melt pool boundaries (coarse microstructure) was 84 *HV*. All microhardness measurements for all the specimens are depicted in Fig. 2-15.

2.4 Discussion

Starting from the microstructure observation, results were expected to show two types of microstructures owing to the different cooling rates at the melt pool center and boundary, as observed with different materials. As shown in Fig. 2-8, coarsened microstructure is located at the melt pool boundaries and refined microstructure is located at the melt pool center. Although the different microstructure between melt pool center and boundary can be distinguished visually, a concise definition of what is “coarse” and “fine” microstructure has not been defined yet, especially when microstructure covers crystallized grains, particles and precipitates. For instance, all the studies focused on microstructure rely on solidification rates and heat transfer mechanisms to describe the regions of the melt pool. It was previously stated that coarsened microstructure is a result of slow cooldown towards the melt pool center, which has refined microstructure due to the concentrated cooldown. However, from a heat transfer perspective, the melt pool border is the first to solidify towards the direction of the heat flow. Thus, the melt pool borders have thin, elongated grains (coarse microstructure). On the contrary, since the heat is concentrated in the melt pool center, grains are equiaxed (fine microstructure). Both types of grains can be seen in the EBSD analysis shown in Fig. 2-16 a). The elongated and equiaxed grains can be observed in Fig. 2-16 b) and c). A schematic of the

coarse and fine microstructure definition can be observed in Fig. 2-16 d).

It is important to note that fine microstructure has equiaxed grains, and coarse microstructure has thin, elongated grains. From a fracture mechanics perspective, grain size is of particular interest because an equiaxed grain enables dislocation movement while smaller grains block it. Nevertheless, coarse microstructure has a lower micro-hardness compared to the fine microstructure, which seems to contradict the general consensus of grain size and hardness. However, the micro-hardness results can be explained due to the presence of dendrite. Coarse microstructure is formed by columnar dendrite, and fine microstructure is formed by equiaxed dendrite. Dendrite formation in Mg alloys is critical because dendrite shows impurities within its branches, which are often of higher hardness [29]. This is true in non-combustible Mg alloys since the branches are most likely formed of Al_2Ca owing to the presence of Ca as a flame retardant in non-combustible Mg alloys [30]. Additionally, Al has a higher Young Modulus and hardness than Mg, thus making the dendrite branches harder than the body. The dendrite branches composed of Al_2Ca can be observed in Figs. 2-8 and 2-16, as the white lines that enclosed the darker areas. Therefore, since the center of the melt pool shows a much larger presence of dendrite branches it makes sense that the micro-hardness results are higher compared to the melt pool border, where the dendrite is much coarser. In addition, considering that SLM products show a non-homogeneous microstructure, it is possible that different solidification rates of the melt pool regions induce a different solidification density, thus making the melt pool center a dense region while the melt pool border can be considered as a diluted region. Regardless of the validity of these assumptions, a specific definition of the coarse and fine microstructures has not been achieved to date. As a result, columnar and elongated grains composed of coarse dendrite at the melt pool borders will be named as coarse microstructure and equiaxed grains composed of refined dendrite will be named as fine microstructure for simplicity.

Furthermore, Fig. 2-9 shows an irregular distribution of coarse microstructure located at several points in the outer surface. This phenomenon can be explained with the scanning strategy. As explained in the introduction, the microstructure coarsens when the solidification rate is slow towards the heat flow direction, and the beginning of the scan track does not allow heat to flow because it is surrounded by metallic powder, which has

a low heat transfer coefficient. Thus, it makes sense that the microstructure coarsens at the beginning of each scanning track of each layer. In addition, the 67° layer-by-layer rotation of the laser parameters shown in Table 2-1 means that when the specimen is observed from a cross-section point of view, the beginning of the scan track, and therefore the coarse microstructure, will appear every so often, which can be verified for both the 4-mm and 6-mm specimens in Fig. 2-10.

The micro-hardness results indicate that the melt pool boundary has a lower hardness compared to the melt pool center. Therefore, the fine microstructure is harder than the coarse microstructure. Further, since the coarse microstructure at the outer surface is large and irregular, stable crack propagation is enabled from the outer surface, thus explaining the fracture surface morphology of ductile fracture at the outer surface.

However, the most critical results for this chapter are the extreme statistics analyses. This is because the hypothesis presented assumes that the stable crack propagation is interrupted at the length where the irregular coarse microstructure is finished, and the microstructure distribution results using extreme statistics is a useful tool that determines such length. For this purpose, extreme value statistics of the 4-mm round bar specimen in Fig. 2-13 show that the coarse microstructure width stabilizes at approximately $430\ \mu\text{m}$ from the outer surface, meaning that the stable crack propagation is interrupted at approximately $430\ \mu\text{m}$. To confirm this statement, the stable fracture region from the fracture surface in Fig. 2-6 is measured, and it gives an approximate length of $430\ \mu\text{m}$. Accordingly, extreme statistics analysis of the 6-mm round bar specimen in Fig. 2-13 show an irregular coarse microstructure length of approximately $600\ \mu\text{m}$, and a similar length can be verified in the stable fracture morphology of the fracture surface shown in Fig. 2-7. Extreme statistics analysis of Fig. 2-13 show a maximum decrease in the maximum coarse grain width from $100\ \mu\text{m}$ to $60\ \mu\text{m}$ in a 4-mm round bar specimen, and a decrease from $140\ \mu\text{m}$ to $60\ \mu\text{m}$ in a 6-mm round bar specimen. Although that decrease can appear neglectable at first glance, they are results of extreme value statistics analyses, meaning that the results are the maximum size of the coarse microstructure possible and a smaller width is plausible. Additionally, the width at the outer surface covers a much larger area compared to the width towards the center, where the coarse microstructure width is large but the length is thin as can be seen in Fig. 2-11 b), c) and d).

Owing to the complex microstructure distribution and different definitions used in this discussion, the author will define several concepts that will be referenced in this study from this point forward. The length where the irregular coarse microstructure stabilizes in width determined by extreme statistics analysis will be referred to as outer microstructure. After such length, the region will be referred to as inner microstructure, where fine and coarse microstructure (mostly fine) are distributed regularly in the form of melt pool formations. Owing to the high surface roughness of SLM products, the outer surface presents small cracks that form between the unmolten powder particles that attach irregularly to the specimen during sintering. Once a stress σ is applied, a small crack with length a_0 propagates stably from the outer surface, leaving a continuous plastic deformation through the outer microstructure until it transitions into inner microstructure, where the stable propagation is suddenly interrupted, and unstable fracture occurs. The length of the stable propagation of the crack until it is interrupted will be referred to as stable propagation area of the crack a_1 , and it is the defect responsible for fracture in SLM products. This affirmation also explains why there is not a visible defect where the fracture initiation point is in the fracture surface. All defined concepts are shown in the fracture mechanism depicted in Fig. 2-17. The potential advantages of this original concept and its use will be discussed in the following chapter.

2.5 Conclusions

After analyzing the results of the tensile tests and microstructure observation of non-combustible Mg alloy specimen fabricated by SLM, the following conclusions were obtained:

- SLM products have a microstructure duality consisting of coarse microstructure and fine microstructure. Coarse microstructure is composed of thin, elongated dendrite towards the direction of the heat flow owing to the slow solidification rate and are located at the melt pool borders, while fine microstructure is composed of equiaxed dendrite owing to the concentrated solidification rate at the melt pool center.
- There are two microstructure regions present in SLM products under as-built conditions: outer microstructure and inner microstructure. The former consists

mostly of irregular chunks of coarse microstructure and the latter consists of a regular distribution of mostly fine microstructure in the form of melt pool formations.

- The point where the outer microstructure transitions into inner microstructure is determined by extreme statistics analysis, and it is approximately 430 μm and 600 μm for a 4-mm and 6-mm non-combustible Mg alloy round bar specimen fabricated by SLM, respectively. It is expected that when the diameter of the specimen increases, the extreme statistics result will also increase.
- In non-combustible Mg alloys fabricated by SLM, fine microstructure has an average hardness of 115 *HV* and coarse microstructure has an average hardness of 80 *HV*. Therefore, plastic deformation from a crack tip is more likely to propagate stably throughout the coarse microstructure.
- The length where the stable crack propagation is interrupted is where the largest stress concentration source is located, and it is the defect responsible for fracture in SLM products known as the stable propagation area of the crack.

2.6 References

- [1] Y. Cao, X. Lin, Q.Z. Wang, S.Q. Shi, L. Ma, N. Kang, W.D. Huang, Microstructure evolution and mechanical properties at high temperature of selective laser melted AlSi10Mg, *Journal of Materials Science & Technology*, 62 (2021) 162-172. <https://doi.org/10.1016/j.jmst.2020.04.066>.
- [2] Z. Dong, X. Zhang, W. Shi, H. Zhou, H. Lei, J. Liang, Study of Size Effect on Microstructure and Mechanical Properties of AlSi10Mg Samples Made by Selective Laser Melting, *Materials (Basel)*, 11 (2018) 2463. [10.3390/ma11122463](https://doi.org/10.3390/ma11122463).
- [3] M. Fousová, D. Dvorský, A. Michalcová, D. Vojtěch, Changes in the microstructure and mechanical properties of additively manufactured AlSi10Mg alloy after exposure to elevated temperatures, *Materials Characterization*, 137 (2018) 119-126. <https://doi.org/10.1016/j.matchar.2018.01.028>.
- [4] K. Kempen, L. Thijs, J. Van Humbeeck, J.P. Kruth, Mechanical Properties of AlSi10Mg Produced by Selective Laser Melting, *Physics Procedia*, 39 (2012) 439-446. <https://doi.org/10.1016/j.phpro.2012.10.059>.
- [5] D. Lin, L. Xu, Y. Han, Y. Zhang, H. Jing, L. Zhao, F. Minami, Structure and mechanical properties of a FeCoCrNi high-entropy alloy fabricated via selective laser melting, *Intermetallics*, 127 (2020) 106963. <https://doi.org/10.1016/j.intermet.2020.106963>.

- [6] B. Song, S. Dong, B. Zhang, H. Liao, C. Coddet, Effects of processing parameters on microstructure and mechanical property of selective laser melted Ti6Al4V, *Materials & Design*, 35 (2012) 120-125. <https://doi.org/10.1016/j.matdes.2011.09.051>.
- [7] C.C. Roth, T. Tancogne-Dejean, D. Mohr, Plasticity and fracture of cast and SLM AlSi10Mg: High-throughput testing and modeling, *Additive Manufacturing*, 43 (2021) 101998. <https://doi.org/10.1016/j.addma.2021.101998>.
- [8] N. Ochi, Y.-k. Higuchi, I. Narita, H. Miyahara, T. Matsumoto, H. Noguchi, Identification method of fracture mode based on measurement of microscopic plastic deformation in a Mg cast alloy, *Materials Science and Engineering: A*, 642 (2015) 113-116. <https://doi.org/10.1016/j.msea.2015.06.067>.
- [9] N.T. Aboulkhair, M. Simonelli, L. Parry, I. Ashcroft, C. Tuck, R. Hague, 3D printing of Aluminium alloys: Additive Manufacturing of Aluminium alloys using selective laser melting, *Progress in Materials Science*, 106 (2019) 100578. <https://doi.org/10.1016/j.pmatsci.2019.100578>.
- [10] H.K. Rafi, N.V. Karthik, H. Gong, T.L. Starr, B.E. Stucker, Microstructures and Mechanical Properties of Ti6Al4V Parts Fabricated by Selective Laser Melting and Electron Beam Melting, *Journal of Materials Engineering and Performance*, 22 (2013) 3872-3883. [10.1007/s11665-013-0658-0](https://doi.org/10.1007/s11665-013-0658-0).
- [11] E.O. Olakanmi, R.F. Cochrane, K.W. Dalgarno, A review on selective laser sintering/melting (SLS/SLM) of aluminium alloy powders: Processing, microstructure, and properties, *Progress in Materials Science*, 74 (2015) 401-477. <https://doi.org/10.1016/j.pmatsci.2015.03.002>.
- [12] N.T. Aboulkhair, N.M. Everitt, I. Ashcroft, C. Tuck, Reducing porosity in AlSi10Mg parts processed by selective laser melting, *Additive Manufacturing*, 1-4 (2014) 77-86. <https://doi.org/10.1016/j.addma.2014.08.001>.
- [13] B. Zhang, Y. Li, Q. Bai, Defect Formation Mechanisms in Selective Laser Melting: A Review, *Chinese Journal of Mechanical Engineering*, 30 (2017) 515-527. [10.1007/s10033-017-0121-5](https://doi.org/10.1007/s10033-017-0121-5).
- [14] S. Tammam-Williams, H. Zhao, F. Léonard, F. Derguti, I. Todd, P.B. Prangnell, XCT analysis of the influence of melt strategies on defect population in Ti-6Al-4V components manufactured by Selective Electron Beam Melting, *Materials Characterization*, 102 (2015) 47-61. <https://doi.org/10.1016/j.matchar.2015.02.008>.
- [15] W. Qian, S. Wu, Z. Wu, S. Ahmed, W. Zhang, G. Qian, P.J. Withers, In situ X-ray imaging of fatigue crack growth from multiple defects in additively manufactured AlSi10Mg alloy, *International Journal of Fatigue*, 155 (2022) 106616. <https://doi.org/10.1016/j.ijfatigue.2021.106616>.

- [16] N.T. Aboulkhair, I. Maskery, C. Tuck, I. Ashcroft, N.M. Everitt, The microstructure and mechanical properties of selectively laser melted AlSi10Mg: The effect of a conventional T6-like heat treatment, *Materials Science and Engineering: A*, 667 (2016) 139-146. <https://doi.org/10.1016/j.msea.2016.04.092>.
- [17] A. Hadadzadeh, B.S. Amirkhiz, S. Shakerin, J. Kelly, J. Li, M. Mohammadi, Microstructural investigation and mechanical behavior of a two-material component fabricated through selective laser melting of AlSi10Mg on an Al-Cu-Ni-Fe-Mg cast alloy substrate, *Additive Manufacturing*, 31 (2020) 100937. <https://doi.org/10.1016/j.addma.2019.100937>.
- [18] E. Chlebus, B. Kuźnicka, T. Kurzynowski, B. Dybała, Microstructure and mechanical behaviour of Ti—6Al—7Nb alloy produced by selective laser melting, *Materials Characterization*, 62 (2011) 488-495. <https://doi.org/10.1016/j.matchar.2011.03.006>.
- [19] L.E. Murr, S.A. Quinones, S.M. Gaytan, M.I. Lopez, A. Rodela, E.Y. Martinez, D.H. Hernandez, E. Martinez, F. Medina, R.B. Wicker, Microstructure and mechanical behavior of Ti—6Al—4V produced by rapid-layer manufacturing, for biomedical applications, *Journal of the Mechanical Behavior of Biomedical Materials*, 2 (2009) 20-32. <https://doi.org/10.1016/j.jmbbm.2008.05.004>.
- [20] R. Casati, J. Lemke, M. Vedani, Microstructure and Fracture Behavior of 316L Austenitic Stainless Steel Produced by Selective Laser Melting, *Journal of Materials Science & Technology*, 32 (2016) 738-744. <https://doi.org/10.1016/j.jmst.2016.06.016>.
- [21] T. Larimian, M. Kannan, D. Grzesiak, B. AlMangour, T. Borkar, Effect of energy density and scanning strategy on densification, microstructure and mechanical properties of 316L stainless steel processed via selective laser melting, *Materials Science and Engineering: A*, 770 (2020) 138455. <https://doi.org/10.1016/j.msea.2019.138455>.
- [22] M. Yakout, M.A. Elbestawi, S.C. Veldhuis, Density and mechanical properties in selective laser melting of Invar 36 and stainless steel 316L, *Journal of Materials Processing Technology*, 266 (2019) 397-420. <https://doi.org/10.1016/j.jmatprotec.2018.11.006>.
- [23] L. Thijs, F. Verhaeghe, T. Craeghs, J.V. Humbeeck, J.-P. Kruth, A study of the microstructural evolution during selective laser melting of Ti—6Al—4V, *Acta Materialia*, 58 (2010) 3303-3312. <https://doi.org/10.1016/j.actamat.2010.02.004>.
- [24] S. Aoyama, K. Sakamoto, T. Umemura, The Effect of Powder Coating on the Heat Transfer Coefficient of Molten Metal in the Shot Sleeve during Aluminum Alloy Die Casting, *THE JOURNAL OF THE JAPAN FOUNDRYMEN'S SOCIETY*, 64 (1992)

- 383-387. [10.11279/imonono.64.6_383](https://doi.org/10.11279/imonono.64.6_383).
- [25] R. Karunakaran, S. Ortgies, A. Tamayol, F. Bobaru, M.P. Sealy, Additive manufacturing of magnesium alloys, *Bioactive Materials*, 5 (2020) 44-54. <https://doi.org/10.1016/j.bioactmat.2019.12.004>.
- [26] T. Kimura, T. Nakamoto, T. Ozaki, K. Sugita, M. Mizuno, H. Araki, Microstructural formation and characterization mechanisms of selective laser melted Al–Si–Mg alloys with increasing magnesium content, *Materials Science and Engineering: A*, 754 (2019) 786-798. <https://doi.org/10.1016/j.msea.2019.02.015>.
- [27] Q. Yan, B. Song, Y. Shi, Comparative study of performance comparison of AlSi10Mg alloy prepared by selective laser melting and casting, *Journal of Materials Science & Technology*, 41 (2020) 199-208. <https://doi.org/10.1016/j.jmst.2019.08.049>.
- [28] D. Zhang, Z. Feng, C. Wang, W. Wang, Z. Liu, W. Niu, Comparison of microstructures and mechanical properties of Inconel 718 alloy processed by selective laser melting and casting, *Materials Science and Engineering: A*, 724 (2018) 357-367. <https://doi.org/10.1016/j.msea.2018.03.073>.
- [29] B. Song, S. Wen, C. Yan, Q. Wei, Y. Shi, Chapter 4 - Preparation and processing of metal matrix composites, in: B. Song, S. Wen, C. Yan, Q. Wei, Y. Shi (Eds.) *Selective Laser Melting for Metal and Metal Matrix Composites*, Academic Press, 2021, pp. 89-208.
- [30] H. Xie, L. Jia, J. Zhang, Z. Wang, Z. Lü, Formation of Al₂Ca Phase in as-Extruded X20 Magnesium Alloy by Solution Treatment, *Rare Metal Materials and Engineering*, 41 (2012) 958-961. [https://doi.org/10.1016/S1875-5372\(12\)60052-6](https://doi.org/10.1016/S1875-5372(12)60052-6).

2.7 List of tables

Table 2-1 Laser irradiation conditions.

Layer thickness (μm)	20
Laser power (W)	47.5
Scan speed (mm/s)	700
Scan spacing (mm)	0.08

2.8 List of figures



Fig. 2-1 EOS M100 SLM Machine

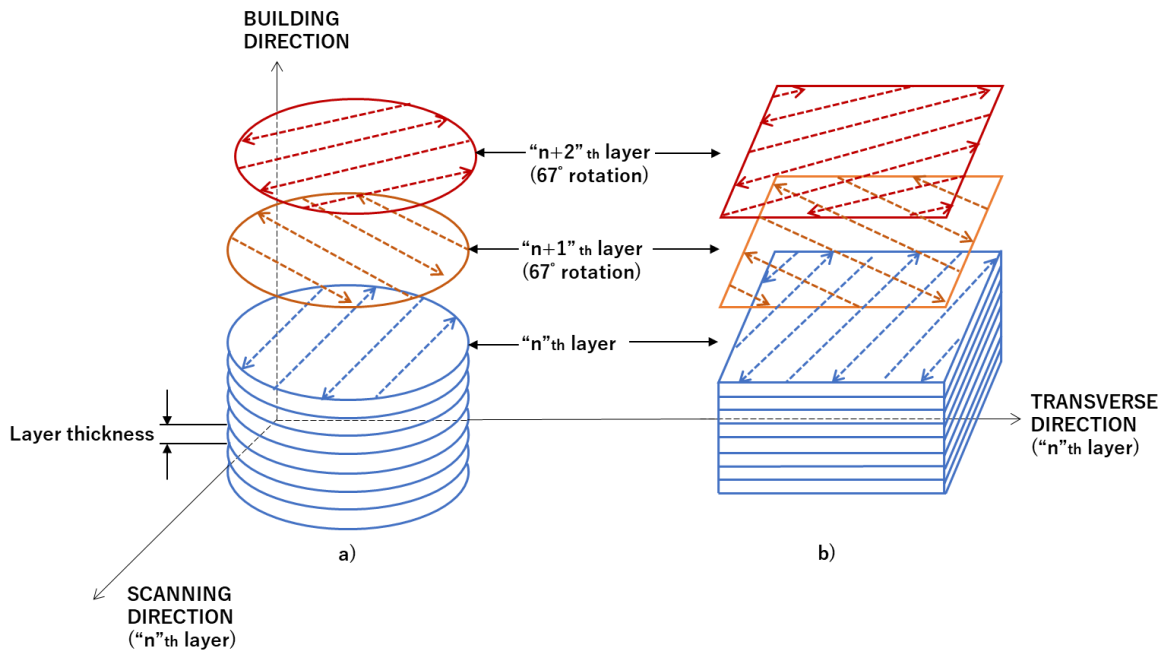


Fig. 2-2 Scanning strategy used for: a) round-bar specimens, and b) cubic specimens.

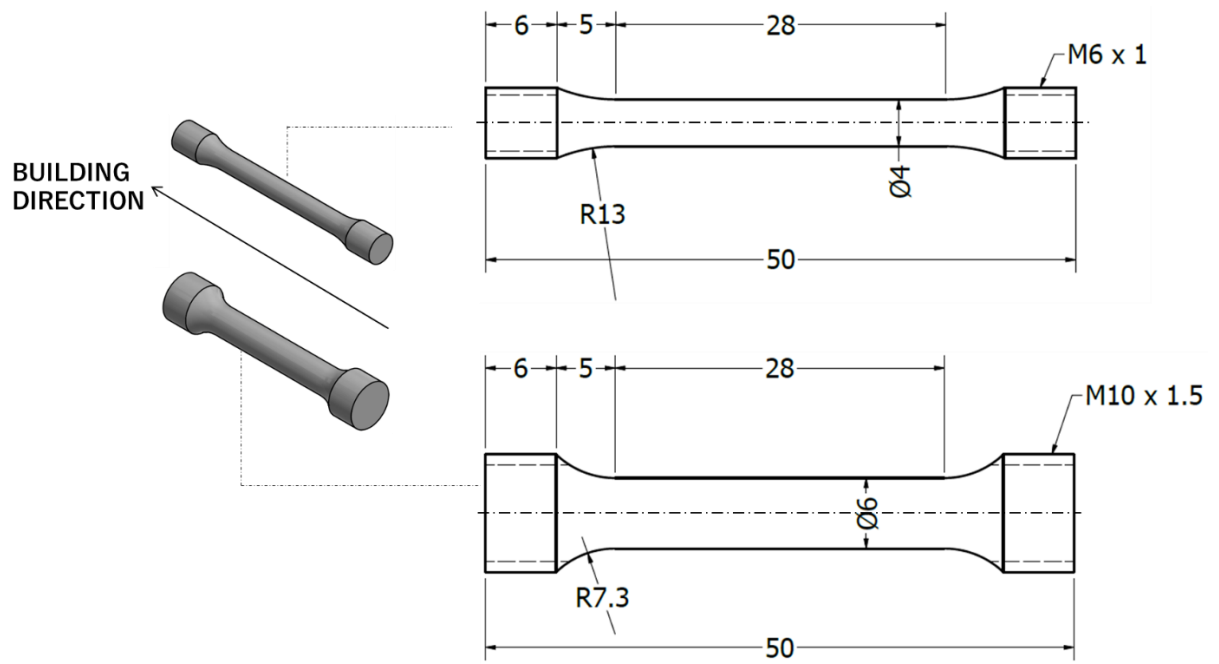


Fig. 2-3 Shapes and dimensions of the 4-mm round bar (up) and 5-mm round bar (down) tensile test specimens (Unit: mm).

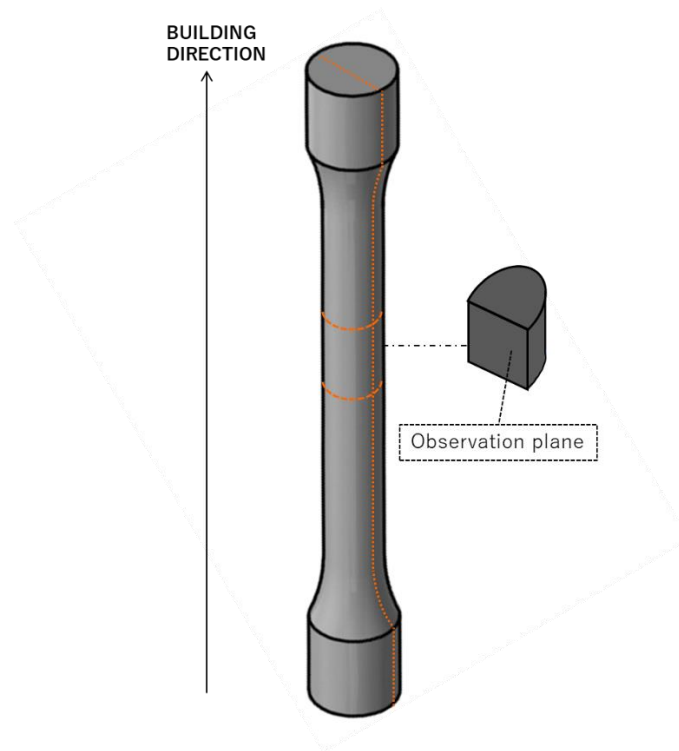


Fig. 2-4 Schematic of the cuts performed to the specimens for microstructure observation and distribution measurement.

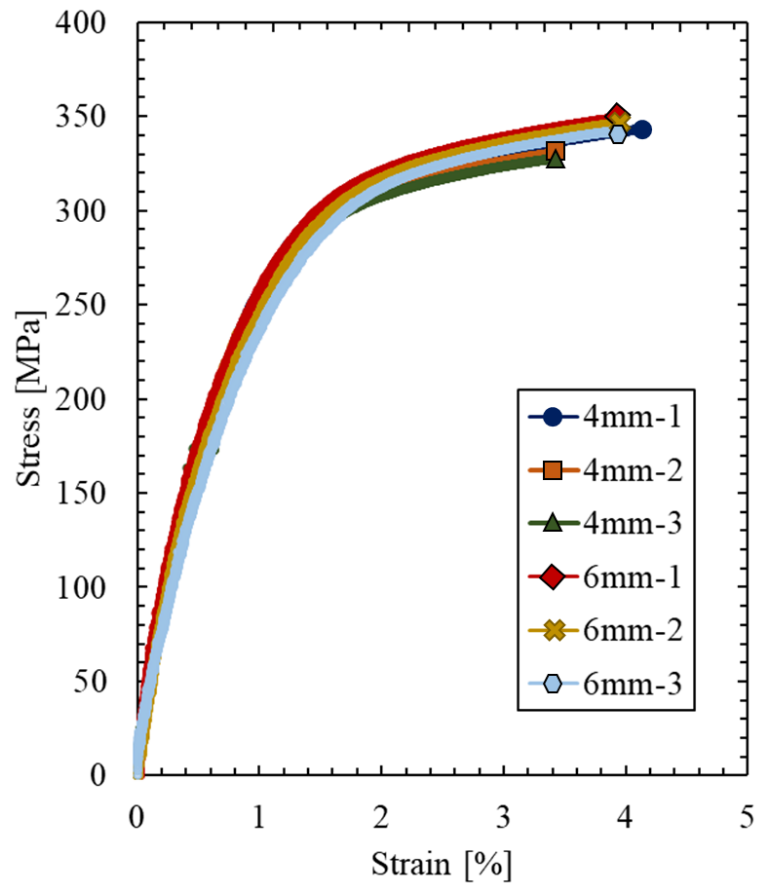


Fig. 2-5 Stress-strain diagrams of the 4 and 6-mm round bar specimens in as-built conditions.

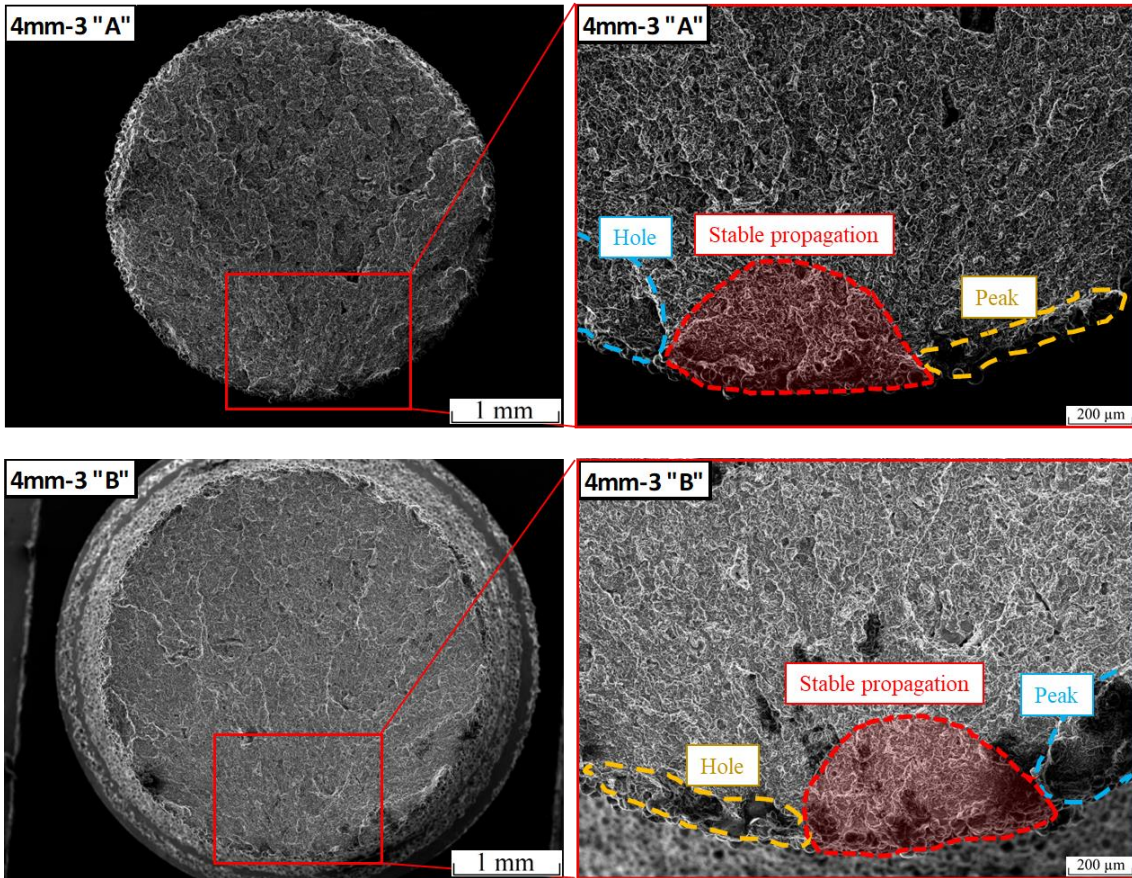


Fig. 2-6 SEM images of the fracture surfaces of the 4-mm round bar specimen showing the definition of the stable propagation area of the crack (red) by peak-hole fracture surface morphology.

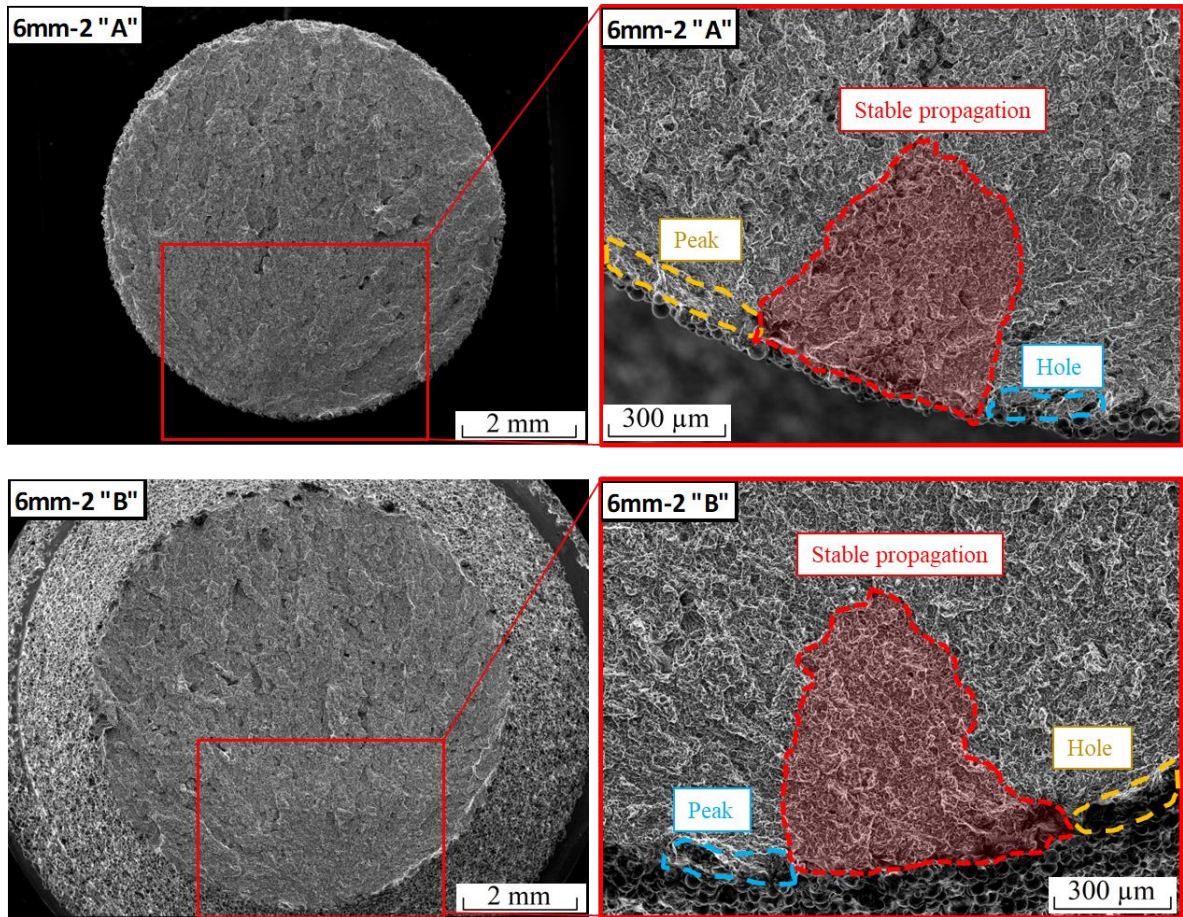


Fig. 2-7 SEM images of the fracture surfaces of the 6-mm round bar specimen showing the definition of the stable propagation area of the crack (red) by peak-hole fracture surface morphology.

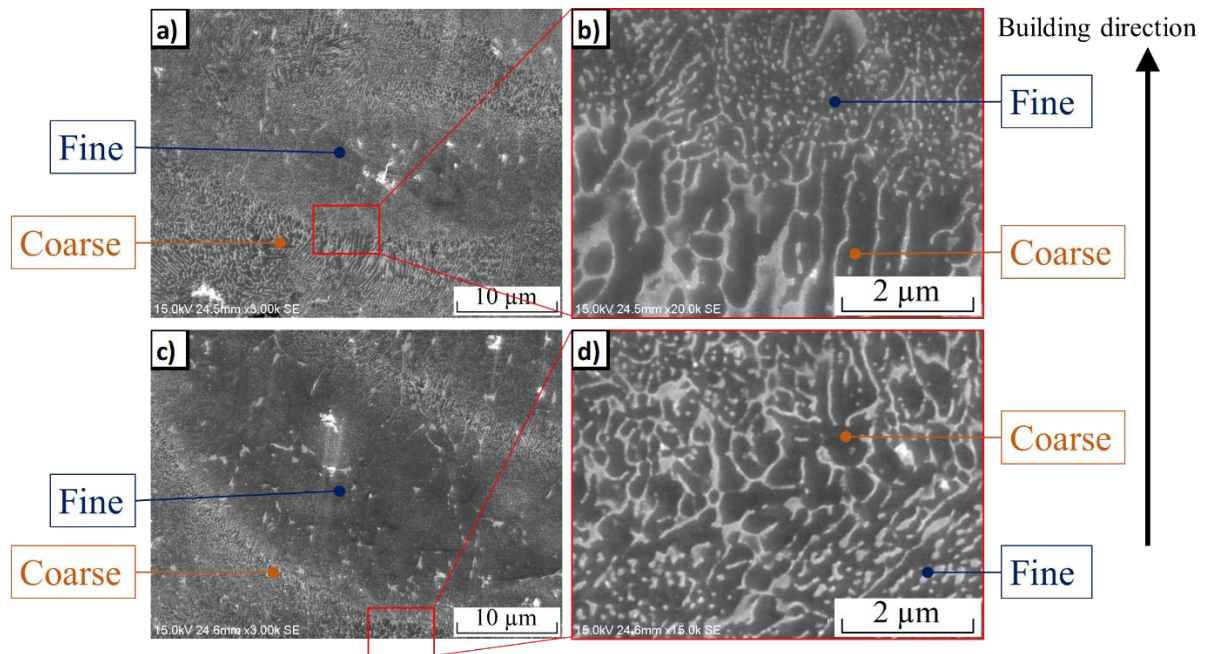


Fig. 2-8 SEM images showing fine and coarse microstructure in: a) Melt pool formation in 4-mm round bar, b) melt pool boundary in 4-mm round bar, c) melt pool formation in 6-mm round bar and d) melt pool boundary in 6-mm round bar.

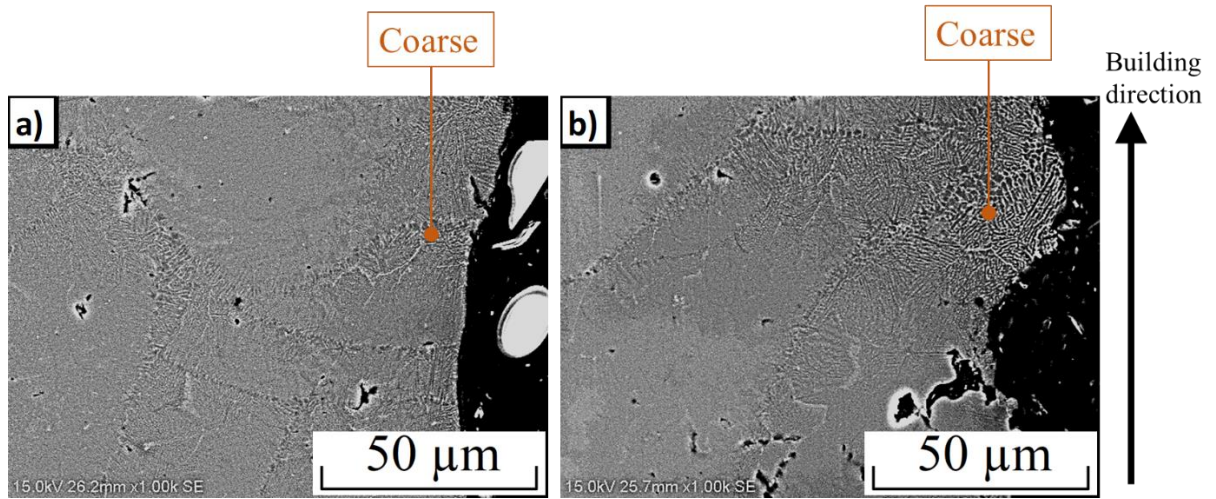


Fig. 2-9 SEM images showing the irregular chunks of coarse microstructure at the outer surface in: a) 4-mm round bar specimen and b) 6-mm round bar specimen.

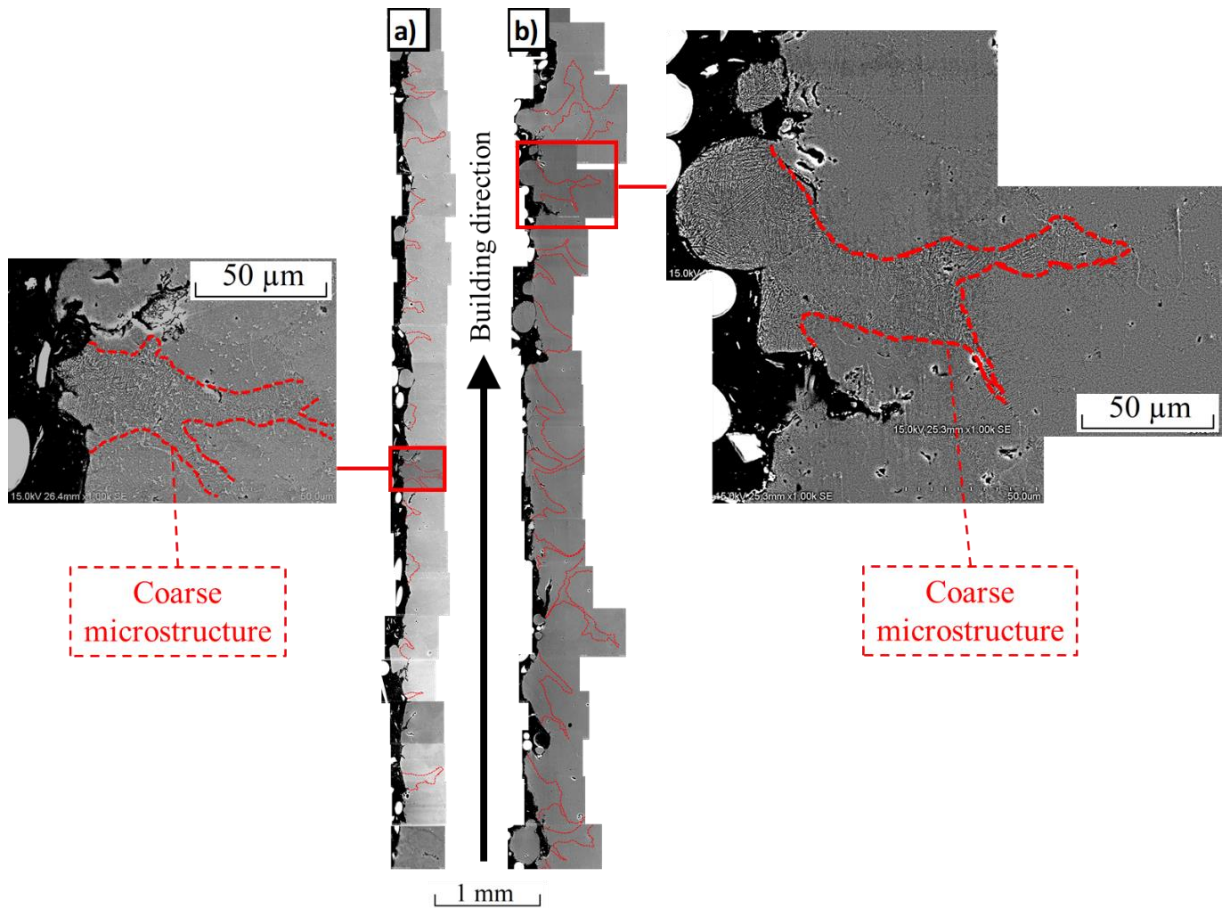


Fig. 2-10 SEM image compilation of the coarse microstructure at the outer surface (red) from the cross-section plane in: a) 4-mm round bar specimen and b) 6-mm round bar specimen.

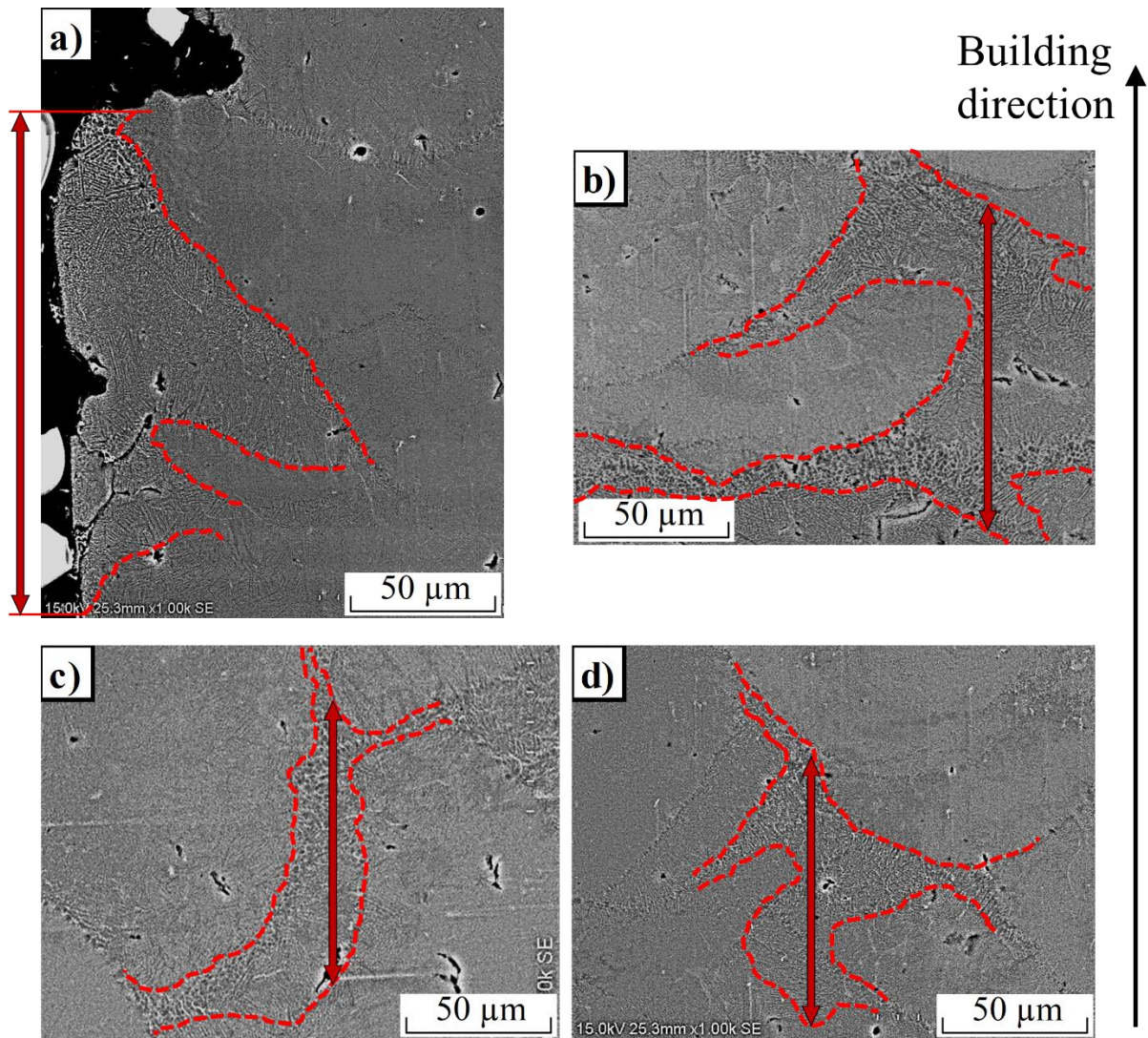


Fig. 2-11 SEM images of the width measurement of the coarse microstructure in the 6-mm round bar specimen at the following depth ranges: a) 0-100 μm ; b) 100-200 μm ; c) 200-300 μm ; and d) 400-500 μm .

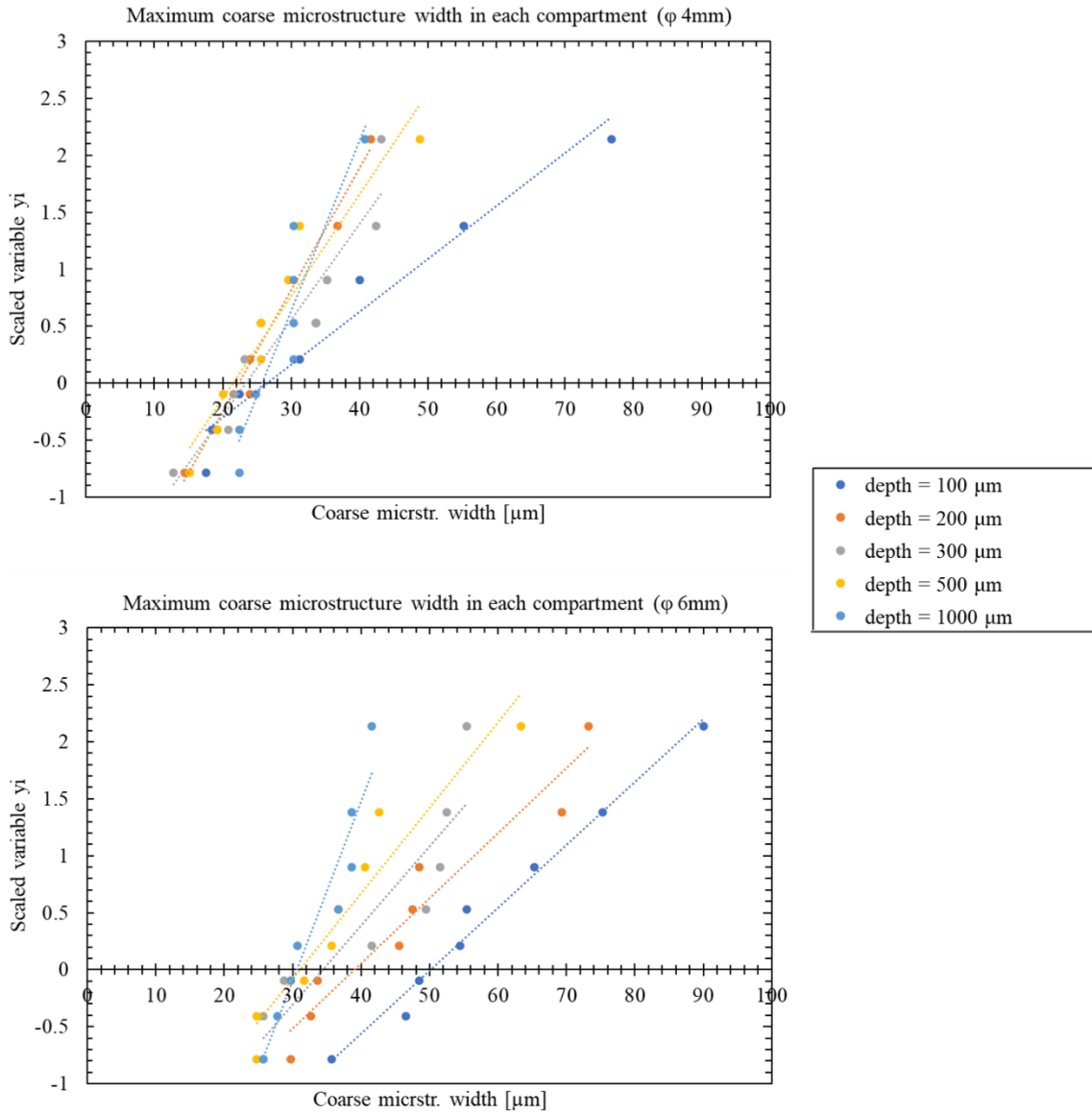


Fig. 2-12 Graph of statistics of extremes ($n = 40$ measurements across all depths) of the width of the coarse microstructure in the round bar specimens with diameters: 4-mm (up) and 6-mm (down).

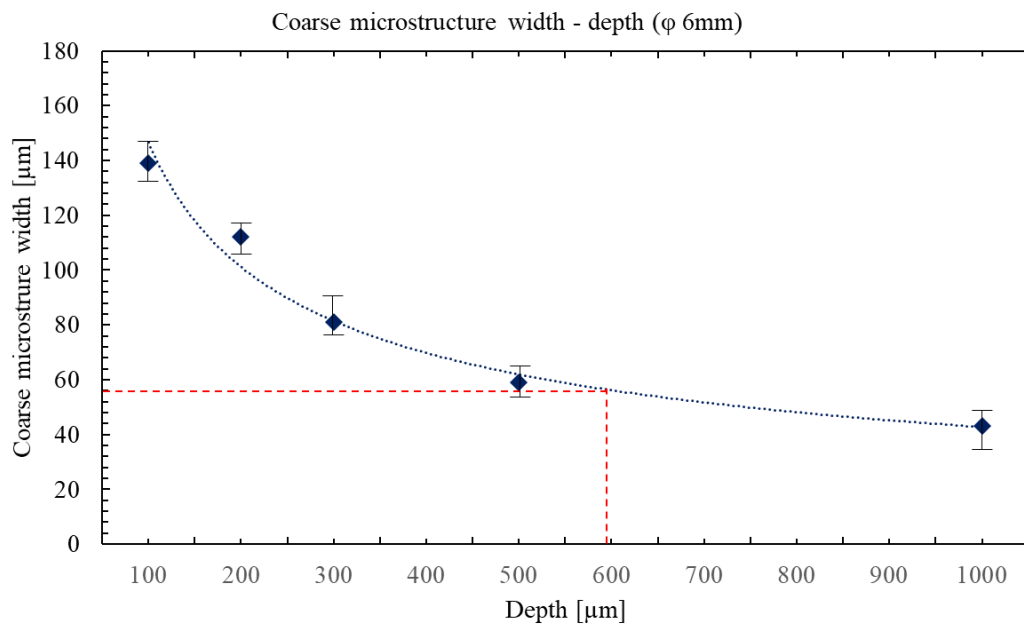
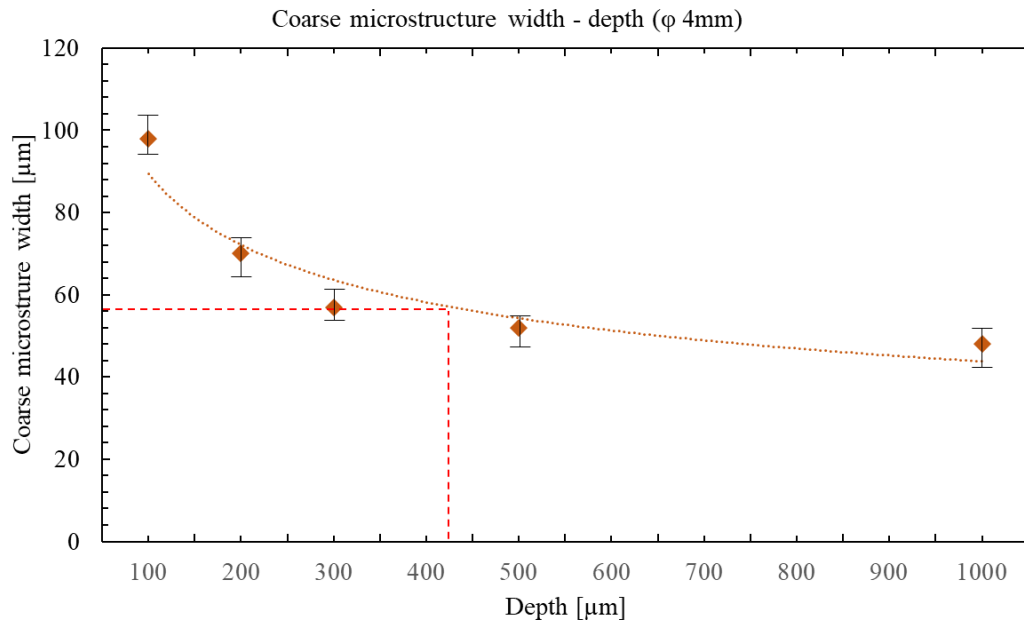


Fig. 2-13 Graphs showing the average width of the coarse microstructure in a specific depth of a 4-mm (up) and a 6-mm (down) round bar specimen, with standard error bars. The error bars are an indicator of the possible range where the results can be located. The width stabilizes at approximately 430 and 600 μm , respectively.

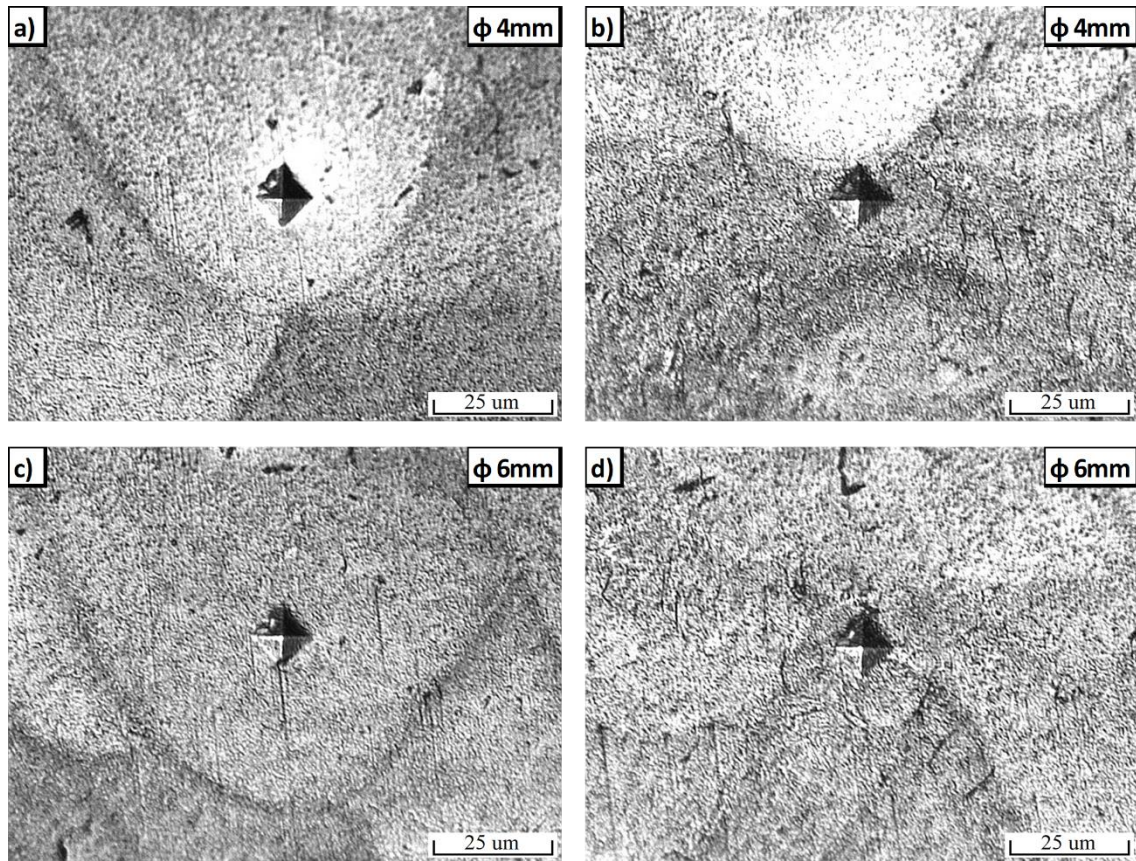


Fig. 2-14 Images of the micro-hardness test results of the 4-mm (up) and 6-mm round bar specimens. Measurements were taken at: the melt pool center in a) and c); and the melt pool boundary in b) and d).

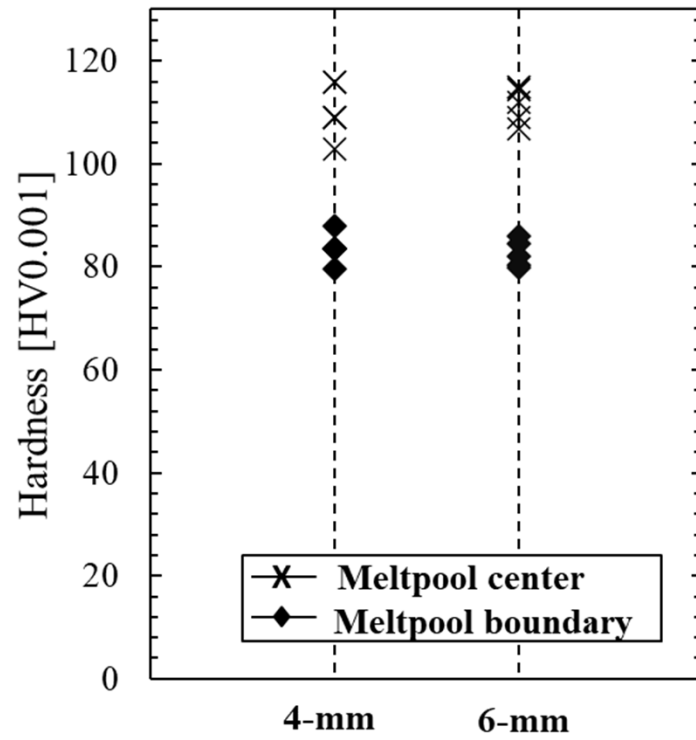


Fig. 2-15 Micro-hardness results at the center and the boundary of the melt pool formations in 4 and 6-mm round bar specimens.

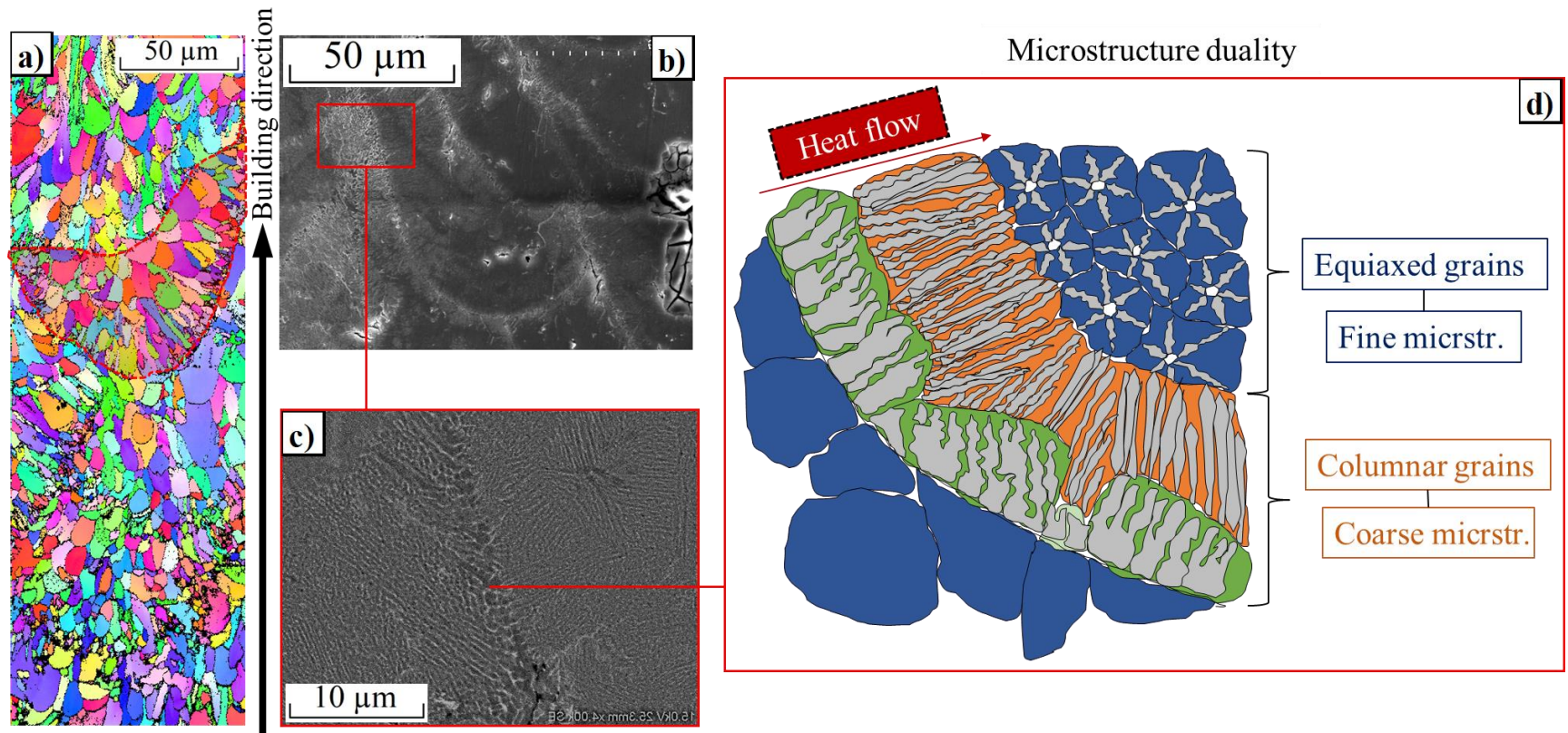


Fig. 2-16 Melt pool formations shown by: a) EBSD analysis; b) SEM image; c) SEM magnification of the melt pool border; and d) definition of fine and coarse microstructure.

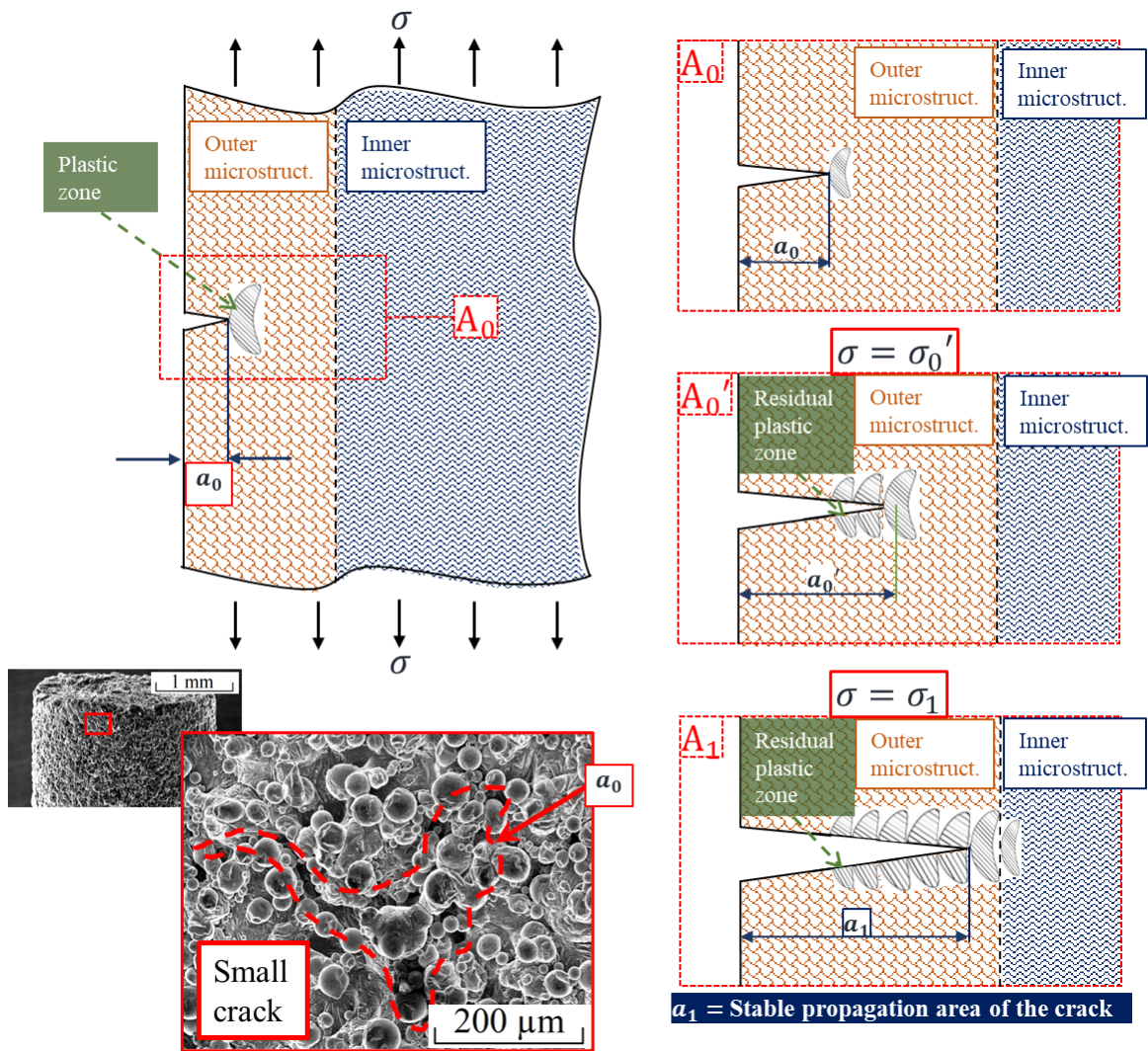


Fig. 2-17 Schematic of the fracture mechanism of SLM products under as-built conditions. The stable propagation area of the crack (a_1) is the defect responsible for fracture.

CHAPTER 3.- PLASTIC STRAIN DISTRIBUTION THROUGH THE INNER MICROSTRUCTURE DUALITY OF SLM PRODUCTS

3.1 Introduction

Now that the defect responsible for fracture in SLM products has been determined and with it a fracture mechanism, this chapter will focus on two factors. First, the influence of the geometrical, visible defects such as gas porosities and lack-of-fusion pores that are present in the specimen. Second, the plastic strain distribution at the crack tip when the crack has reached the inner microstructure as shown in Fig. 2-14.

Since defects are large stress concentration sources and can be critically damaging to the integrity of a metallic structure, it makes sense that the mechanical engineer would like to analyze its presence and determine the conditions where a visible defect can influence the fracture mechanism and, consequentially, alter the mechanical properties. As a result of this affirmation, several papers have analyzed the defect formation mechanisms [1, 2], their impact on mechanical properties [3-5], and evaluated a range of techniques to decrease defect population in SLM products [6, 7]. For instance, Dallago et. al [8], Masuo et. al [9], Qian et. al [10], and Qin et. al [4] have concluded that large defects, such as lack-of-fusion pores located on the surface or sub-surface, are critical factors that directly influence the fatigue strength of SLM products. In addition, studies performed by Attar et. al [11], Cao et. al [12], Gong et. al [13], Li et. al [14], Lin et. al [15], Mower et. al [16], and Schuch et. al [17], have established that the presence of defects cannot be neglected in the analysis of the fracture mechanism of SLM products. Although the conclusions are similar for many research authors, they seem to contradict the idea that fracture starts from the outer surface where no visible defects can be observed and can be verified with Figs. 2-4 and 2-5. However, there is a step that has been widely ignored, and that is the fact that defects seem to become relevant to the fracture process when the specimen fabricated by SLM is mechanically post-processed, as opposed to the specimen in as-built conditions, where visible defects do not influence on the fracture.

Since the introduction stipulated that a distinction between as-built and post-processed conditions has to be made due to the result variation of the literature in each state, the current chapter will focus on the as-built state. The role of defects where the specimen has been machined will be discussed in Chapter 6. However, the current chapter will discuss the relevance of visible defects and when they become influential to the fracture mechanism in SLM products under as-built conditions.

In addition, if the assumed fracture mechanism presented in Fig. 2-14 is correct, the plastic strain at the crack tip once it reaches the inner microstructure is yet to be explained. According to traditional fracture mechanics, if the material is homogeneous enough, the plastic zone at the crack tip is small enough to be neglected, satisfying the small-scale yielding (SSY) conditions. However, as was verified in section 2.3.3 and discussed in the previous chapter, the inner microstructure consists of melt pool formations with coarse microstructure in the borders and fine microstructure in the center. In short, it is not homogeneous. Therefore, the plastic strain distribution to form the plastic zone through the microstructure duality of the inner section of the specimen still needs an explanation that this chapter will try to provide.

To circumvent these problems, it would be extremely convenient if the largest defect present in a 6-mm round bar specimen could be determined. This is possible by extreme value statistics analysis. Then, a simple analogy can be made. If the maximum defect is larger than the stable propagation area of the crack, then the latter is responsible for fracture. However, if it is smaller than the stable propagation area of the crack, then the former will be responsible for fracture. Finally, the results are validated by establishing a mechanical equivalency between a visible stress concentration source, such as an artificial drill hole, and the stable propagation of the crack, which will be analyzed in the next chapter.

In addition, defect population and distribution can also play a role in the fracture process. For this purpose, by increasing the specimen size, the number of defects is expected to increase by using the same parameters [18, 19]. Subsequently, defects can coalesce with each other to form a stress concentration source larger than the stable propagation area of the crack, thus decreasing drastically the UTS value of SLM products.

Further, it was proven in section 2.3.3 that the fine microstructure is harder than the

coarse microstructure. Therefore, it makes sense that plastic strain will localize in the points where microstructure is softer, thus distributing deformation along the melt pool borders in the inner microstructure, resulting in a disperse plastic deformation. If plastic strain is not continuous through the inner microstructure, the stable propagation area of the crack can be considered an intrinsic defect of SLM products. And, if the size of this intrinsic defect is known before fracture in accordance with Murakami's Theory [20], then the UTS value can be predicted by using the concept of fracture toughness (K_{IC}) of a metallic body with a surface crack.

In this chapter, three round bar specimens of 9-mm and 16-mm respectively were fabricated and submitted to tensile testing. The increase in diameter size was selected to purposely increase the defect population and size and induce a defect responsible for fracture consisting of coalesced defects that is larger than the stable propagation area of the crack. Subsequently, fractography analysis was performed. Additionally, a fractured 6-mm round bar specimen was cut and submitted to extreme value statistics of defects and electron backscatter diffraction (EBSD) analysis for plastic strain observation. The results of this study can consolidate the stable propagation area of the crack as the defect responsible for fracture in SLM products and its size can be a critical factor to predict strength and increase the reliability of the process.

3.2 Experimental procedure

The raw material was AZX912 Mg alloy powder with the same composition as in Table 1-1. The particle size distributions were the same as shown in Section 1.4. Laser irradiation parameters are shown in Table 2-1. The round bar specimens were carried out using the EOS M100 SLM machine shown in Fig. 2-1.

Three round bar tensile test specimens for each diameter of 9 and 16 mm were built for this research. The specimens were fabricated using the same printing strategy shown in Fig. 2-2 a). The final geometry of the specimens is shown in Fig. 3-1. Tensile tests were performed using a Shimadzu AG-50kNXD universal electromechanical testing machine set at a strain rate of 0.0011 s^{-1} in conformance with the Japanese Industrial Standard JIS Z 2241:2011 (Method of Tensile Test for Metallic Materials). Tensile testing was performed along the building direction of the round-bar specimens at a room temperature

range of 21-22 °C. All tests were performed using a screw-type grip set with spherical bearings to ensure that no misalignment or bending occurred during testing. Elongation was measured using a Shimadzu SG25-100 extensometer with a gauge length of 25 mm. After tensile testing, the fractured specimens were destined to fracture surface observation using a JEOL JSM-IT300 scanning electron microscope.

For extreme value statistics of defects and EBSD analysis, a section from the fractured piece of a 6-mm round bar specimen from the previous chapter was cut in horizontal and longitudinal cross-sections as shown in Fig. 3-2. The lower horizontal cut plane was destined for extreme value statistics of defects while the cross-sectional cut plane was destined for EBSD analysis. The measuring of defects for extreme value statistics analysis was measured using a Nikon Eclipse L150 optical microscope. For EBSD analysis, a Hitachi-High Tech Low Vacuum Analysis Scanning Electron Microscope (SEM) SU6600 machine was used. The inner surfaces of the cross-sectional cut of the specimens were polished until a mirror-finish roughness was obtained. Polishing of the cut surfaces was done mechanically in addition to ion milling, as the mirror finish pass was performed with a Hitachi High-Tech IM-3000 machine at 2 kV.

3.3 Results

3.3.1 Extreme value statistics of defects

To consolidate the stable propagation area of the crack as a defect, the largest possible defect in the specimen must be determined. For this purpose, a fracture 6-mm round bar specimen from the previous chapter was cut horizontally below the fracture plane. Using the approach for extreme statistics of defects of Murakami [21], the largest inclusion size in a material is predicted by measuring the area of the largest defect in different sections of the gauge length, as is shown in Fig. 3-3. Results shown in Fig. 3-4 reveal that the biggest defect (e.g., porosity) present in a 6-mm round bar specimen has a \sqrt{area} of 67 μm . Accordingly, the biggest defect present in a 9-mm and 16-mm round bar specimens have a \sqrt{area} of 130 μm and 210 μm respectively. Despite the fact that a defect with a maximum size of 210 μm is still smaller than the stable propagation of the crack, it is important to mention that in this analysis the maximum size of a single defect is taken into consideration, not defect population. Defect population influences the fracture

mechanism when the defects are close enough to coalesce between each other, thus it is possible that a larger defect population forms a \sqrt{area} larger than the stable propagation area of the crack. If this affirmation is true or not will be analyzed with the S-S diagrams and fractography results.

3.3.2 Tensile tests and fractography results

Tensile tests for a total of six specimens were performed. Three specimens had a diameter of 9-mm, and three specimens had a diameter of 16-mm. All the S-S diagrams are shown in Fig. 3-5, which also includes one diagram from the previous chapter for a 4 and 6-mm specimen respectively for comparison purposes. The fractured specimens under as-built conditions yielded the following mean values for 9-mm and 16-mm respectively: an ultimate strength of 180 MPa and 130 MPa, and an elongation of 0.2% for both. The results show a similar trend of the Young's Modulus for all diameters involved.

The fracture surfaces of a 9-mm and 16-mm round bar specimen are shown in Figs. 3-6 and 3-7 respectively. For both cases, the fracture initiation points cannot be easily determined. Additionally, the population of defects has drastically increased in the fracture surface if compared to the 4-mm and 6-mm fracture surfaces of Figs. 2-4 and 2-5. Whether if the low quality of the specimen is related to the diameter or not will be analyzed in the discussion.

3.3.3 EBSD analysis

For EBSD analysis, the cross-sectional cut and molding was performed as shown in Fig. 3-8, where the fracture initiation point, and the stable propagation area of the crack can be observed. EBSD analysis for plastic strain observation can be quite deceptive when the grain size of a specimen is small, which is the case for SLM products and can be easily verified in Fig. 2-8. Thus, a magnification of x1000 was used for plastic strain observation. However, high magnification means that an analysis in a continuous extensive area can be extremely time consuming. Therefore, a single analysis was performed within the stable crack propagation area of the crack (outer microstructure) and then another analysis was performed further from the stable propagation area of the crack (inner microstructure).

The coarse and fine grain microstructures can be observed by Image Quality (IQ) maps, the crystal orientation, and twinning deformations by Inverse Pole Figure (IPF) maps, and plastic strain can be observed by Kernel Average Misorientation (KAM) maps. Analysis within the stable propagation area of the crack can be observed in Fig. 3-9, where a continuous plastic strain marked by deformation twinning characteristic of hexagonal closest packed (HCP) structures can be identified. Figure 3-10 shows the same maps further from the stable propagation area of the crack, where a more dispersed plastic strain concentrated in the outer areas of the melt pool formations can be observed. It is worth noticing that the outside regions of the melt pool formations are composed of coarse microstructure due to the longer cooldowns after solidification [22-25]. These results verify the sudden interruption of the stable propagation area of the crack and corroborates it as a defect responsible for fracture. Therefore, fracture toughness can be used for strength prediction.

3.3.4 Fracture toughness results

To determine a reliable material strength value, the capacity of a material to contain a fracture upon initiation, known as the fracture toughness (K_{IC}), must be considered. Once the fracture toughness is known, a reliable structural strength can be estimated by predicting the size of the defect that initiates crack propagation. If the stable propagation area of the crack is considered an intrinsic defect, the following equation proposed by Murakami et al. [26] can be used:

$$K_{IC} = 0.65\sigma_C\sqrt{\pi\sqrt{area}} \quad (3 - 1)$$

where σ_C is the strength at failure and \sqrt{area} is the square root of the stable propagation area of the crack. The strength at failure σ_C is a result from the tensile tests performed in section 2.3.1 and \sqrt{area} can be calculated by performing the square root of the area of stable fracture by fracture morphology as can be seen in Fig. 3-11, which was based on the stable fracture regions as shown in Figs. 2-4 and 2-5 from the previous chapter. All σ_C , \sqrt{area} and K_{IC} results for the 4 and 6-mm round bar specimens are presented in Table 3-1. The average fracture toughness for non-combustible Mg alloys is approximately $10.8 \text{ MPa}\sqrt{\text{m}}$.

To further consolidate the \sqrt{area} of the critical defect as a viable parameter, the

same concept should be used when the geometrical, observable defect is larger than the stable propagation area of the crack. Such is the case with Fig. 3-6, where the fracture surface contains a very large area responsible for fracture. According to the fracture surface observation, the \sqrt{area} size marked in Fig. 3-6 is approximately 3900 μm , and $\sigma_C = 140 \text{ MPa}$ according to Fig. 3-5. Thus, K_{IC} for the 9-mm round bar specimen is $10.1 \text{ MPa}\sqrt{\text{m}}$, which is a similar results obtained for the 4-mm and 6-mm round bar specimens.

3.4 Discussion

The starting point of the discussion is the extreme value statistics of defects. The results are a valid quantitative evaluation of the largest defect size that can be present in a 6-mm round bar non-combustible Mg alloy fabricated by SLM, and by extension, on a 4-mm round bar as well. Since the largest defect results shows a maximum \sqrt{area} value of 67.2 μm , which is roughly a circle-shaped gas pore with 76 μm of diameter, and the average \sqrt{area} of the stable propagation area of the crack shown in Table 3-1 is much larger with 571 μm , it makes sense that the defect responsible for fracture will be the latter.

Additionally, once the defect population is increased with the 9 and 16-mm round bar specimens, they form a much larger stress concentration source than the stable propagation area of the crack via coalescence of defects. This affirmation can be evidenced in Figs. 3-6 and 3-7, where a large population of defects is evidently present in the fracture surfaces of the broken specimens. The increase in defect population can be explained due to the specimen size. A larger diameter means that the scanning track for a single layer will take a longer amount of time, which in turn makes the layer cooler when a new layer is formed. Thus, re-melting of the previous layer is more difficult to achieve, which in turn means more irregular surfaces between the two layers and that means a larger amount of lack-fusion pores present in the specimen [1, 5, 27]. As a result, a large defect population as shown in Fig. 3-6 means that defects can coalesce with each other to form a larger area than the stable propagation of the crack (approximately 2 mm of depth formed by lack-of-fusion pores). However, the exact size of the \sqrt{area} parameter is difficult to determine because an analysis that determines which defects coalesce with each other is difficult to perform, thus, K_{IC} for these specimens cannot be calculated.

Moreover, the fracture surface of the 9-mm round bar specimen shown in Fig. 3-6 corresponds to the 9mm-1 specimen, which has the lowest UTS value (140 MPa) amongst the 9-mm round bar specimens shown in Fig. 3-5. Although the specimen has an unacceptable quality, it is worth mentioning that all the specimens were fabricated in bulk with the same fabrication parameters, which makes the result of such large defect population a rare encounter. However, a larger defect population is expected when the size of the specimen increases and the same fabrication parameters are used, thus leaving a blank space between fabrication parameter variation and specimen size that future research could fulfill. Nevertheless, with this result it is safe to conclude that if the defects do not coalesce with each other due to the increased population and are smaller than the stable propagation area of the crack, the fracture mechanism of SLM products in as-built conditions is the same as stipulated in Fig. 2-16. Furthermore, a defect size smaller than the stable propagation area of the crack enabled by microstructural differences can establish an aim indicator for industrial applications in the future.

However, the clearest evidence of a stable crack propagation is shown in Fig. 3-9, where plastic strain can be observed immediately below the fracture surface. Once the stable crack propagation reaches the limit between outer microstructure and inner microstructure, EBSD results shown in Fig. 3-10 present a plastic strain that, if compared to the plastic strain in Fig. 3-9, is more irregular and dispersed. Particularly, plastic strain seems to localize in the melt pool borders. This result makes sense since it was previously established that the melt pool borders consist of coarse microstructure, which has a lower hardness than the fine microstructure located in the melt pool center, thus enabling plastic strain to disperse. Nevertheless, the contrast of the plastic strain between the KAM maps of Figs. 3-9 and 3-10 are clear enough to safely state that the plastic strain is more homogeneous inside the stable propagation area of the crack in Fig. 3-9 compared to the plastic strain outside of the stable propagation area of the crack in Fig. 3-10. This result is critical for the current analysis because it serves as evidence that, in fact, the crack propagation is interrupted, further inducing a large stress concentration source that causes fracture in SLM products. The fracture mechanism, including the plastic strain dispersion, can be seen in Fig 3-12.

Since the stable propagation area of the crack was validated as an intrinsic, invisible

defect of specimens fabricated by SLM in as-built conditions, it can be used according to Murakami's Theory [26]. This theory establishes that if a surface crack size is known, then fracture toughness can be a tool to predict the strength at failure of a material if equation (3 – 1) is used. In accordance with this theory, the average fracture toughness calculated was approximately $10.8 \text{ MPa}\sqrt{\text{m}}$, a result consistent with other studies considering that larger K_{IC} values are expected for different Mg alloys with homogeneous microstructure owing to their high ductility [28-30]. Therefore, it makes sense to conclude that the average fracture toughness for AZX912 Mg alloys fabricated by SLM is $10.8 \text{ MPa}\sqrt{\text{m}}$ in as-built conditions.

3.5 Conclusions

The major goals of this chapter were to determine the conditions where the defects of SLM products have a role in the fracture mechanism and the validation of the stable propagation area of the crack as an intrinsic defect. With these goals achieved, fracture toughness can be used to predict the strength of SLM products, thus increasing the reliability of the process. The findings presented in this study have led to the following conclusions:

- If the parameters remain unchanged, by increasing the size of the specimen, the defect population is increased owing to the longer time required to sinter a single layer, thus affecting re-melting when a new layer is added and increasing the number of lack-of-fusion pores.
- A defect or coalescence of defects with a \sqrt{area} smaller than the square root of the stable propagation area of the crack will not influence in the fracture mechanism of SLM products in as-built conditions and will not alter their mechanical properties.
- The stable propagation area of the crack has a continuous plastic strain manifestation until it reaches the inner microstructure of the specimen, where the propagation is interrupted, and the plastic strain disperses.
- The fracture toughness for SLM products can be used to predict the strength of the material in accordance with using the \sqrt{area} parameter from Murakami's Theory and enhance process reliability. In non-combustible Mg alloys, the average fracture

toughness is $10.8 \text{ MPa}\sqrt{\text{m}}$.

3.6 References

- [1] A. Bauereiß, T. Scharowsky, C. Körner, Defect generation and propagation mechanism during additive manufacturing by selective beam melting, *Journal of Materials Processing Technology*, 214 (2014) 2522-2528. <https://doi.org/10.1016/j.jmatprotec.2014.05.002>.
- [2] B. Zhang, Y. Li, Q. Bai, Defect Formation Mechanisms in Selective Laser Melting: A Review, *Chinese Journal of Mechanical Engineering*, 30 (2017) 515-527. [10.1007/s10033-017-0121-5](https://doi.org/10.1007/s10033-017-0121-5).
- [3] S.R. Yeratapally, C.G. Lang, A.R. Cerrone, G.L. Niebur, K. Cronberger, Effect of defects on the constant-amplitude fatigue behavior of as-built Ti-6Al-4V alloy produced by laser powder bed fusion process: Assessing performance with metallographic analysis and micromechanical simulations, *Additive Manufacturing*, 52 (2022) 102639. <https://doi.org/10.1016/j.addma.2022.102639>.
- [4] Z. Qin, N. Kang, F. Zhang, Z. Wang, Q. Wang, J. Chen, X. Lin, W. Huang, Role of defects on the high cycle fatigue behavior of selective laser melted Al–Mg–Sc–Zr alloy, *International Journal of Fracture*, (2021). [10.1007/s10704-021-00593-0](https://doi.org/10.1007/s10704-021-00593-0).
- [5] N. Sanaei, A. Fatemi, Defects in additive manufactured metals and their effect on fatigue performance: A state-of-the-art review, *Progress in Materials Science*, 117 (2021) 100724. <https://doi.org/10.1016/j.pmatsci.2020.100724>.
- [6] S. Tammis-Williams, H. Zhao, F. Léonard, F. Derguti, I. Todd, P.B. Prangnell, XCT analysis of the influence of melt strategies on defect population in Ti–6Al–4V components manufactured by Selective Electron Beam Melting, *Materials Characterization*, 102 (2015) 47-61. <https://doi.org/10.1016/j.matchar.2015.02.008>.
- [7] N. Read, W. Wang, K. Essa, M.M. Attallah, Selective laser melting of AlSi10Mg alloy: Process optimisation and mechanical properties development, *Materials & Design* (1980-2015), 65 (2015) 417-424. <https://doi.org/10.1016/j.matdes.2014.09.044>.
- [8] M. Dallago, B. Winiarski, F. Zanini, S. Carmignato, M. Benedetti, On the effect of geometrical imperfections and defects on the fatigue strength of cellular lattice structures additively manufactured via Selective Laser Melting, *International Journal of Fatigue*, 124 (2019) 348-360. <https://doi.org/10.1016/j.ijfatigue.2019.03.019>.
- [9] H. Masuo, Y. Tanaka, S. Morokoshi, H. Yagura, T. Uchida, Y. Yamamoto, Y. Murakami, Effects of Defects, Surface Roughness and HIP on Fatigue Strength of Ti-6Al-4V manufactured by Additive Manufacturing, *Procedia Structural Integrity*, 7 (2017) 19-26. <https://doi.org/10.1016/j.prostr.2017.11.055>.

- [10] W. Qian, S. Wu, Z. Wu, S. Ahmed, W. Zhang, G. Qian, P.J. Withers, In situ X-ray imaging of fatigue crack growth from multiple defects in additively manufactured AlSi10Mg alloy, *International Journal of Fatigue*, 155 (2022) 106616. <https://doi.org/10.1016/j.ijfatigue.2021.106616>.
- [11] H. Attar, M. Calin, L.C. Zhang, S. Scudino, J. Eckert, Manufacture by selective laser melting and mechanical behavior of commercially pure titanium, *Materials Science and Engineering: A*, 593 (2014) 170-177. <https://doi.org/10.1016/j.msea.2013.11.038>.
- [12] Y. Cao, X. Lin, Q.Z. Wang, S.Q. Shi, L. Ma, N. Kang, W.D. Huang, Microstructure evolution and mechanical properties at high temperature of selective laser melted AlSi10Mg, *Journal of Materials Science & Technology*, 62 (2021) 162-172. <https://doi.org/10.1016/j.jmst.2020.04.066>.
- [13] H. Gong, K. Rafi, H. Gu, G.D. Janaki Ram, T. Starr, B. Stucker, Influence of defects on mechanical properties of Ti-6Al-4V components produced by selective laser melting and electron beam melting, *Materials & Design*, 86 (2015) 545-554. <https://doi.org/10.1016/j.matdes.2015.07.147>.
- [14] Z. Li, Z. Li, Z. Tan, D.-B. Xiong, Q. Guo, Stress relaxation and the cellular structure-dependence of plastic deformation in additively manufactured AlSi10Mg alloys, *International Journal of Plasticity*, 127 (2020) 102640. <https://doi.org/10.1016/j.ijplas.2019.12.003>.
- [15] D. Lin, L. Xu, Y. Han, Y. Zhang, H. Jing, L. Zhao, F. Minami, Structure and mechanical properties of a FeCoCrNi high-entropy alloy fabricated via selective laser melting, *Intermetallics*, 127 (2020) 106963. <https://doi.org/10.1016/j.intermet.2020.106963>.
- [16] T.M. Mower, M.J. Long, Mechanical behavior of additive manufactured, powder-bed laser-fused materials, *Materials Science and Engineering: A*, 651 (2016) 198-213. <https://doi.org/10.1016/j.msea.2015.10.068>.
- [17] M. Schuch, T. Hahn, M. Bleckmann, The mechanical behavior and microstructure of additively manufactured AlSi10Mg for different material states and loading conditions, *Materials Science and Engineering: A*, 813 (2021) 141134. <https://doi.org/10.1016/j.msea.2021.141134>.
- [18] E. Pessard, M. Laviolle, P. Laheurte, P. Didier, M. Brochu, High-cycle fatigue behavior of a laser powder bed fusion additive manufactured Ti-6Al-4V titanium: Effect of pores and tested volume size, *International Journal of Fatigue*, 149 (2021) 106206. <https://doi.org/10.1016/j.ijfatigue.2021.106206>.
- [19] X.-P. Niu, S.-P. Zhu, J.-C. He, D. Liao, J.A.F.O. Correia, F. Berto, Q. Wang, Defect tolerant fatigue assessment of AM materials: Size effect and probabilistic prospects,

- International Journal of Fatigue, (2022) 106884.
<https://doi.org/10.1016/j.ijfatigue.2022.106884>.
- [20] Y. Murakami, S. Kodama, S. Konuma, Quantitative evaluation of effects of non-metallic inclusions on fatigue strength of high strength steels. I: Basic fatigue mechanism and evaluation of correlation between the fatigue fracture stress and the size and location of non-metallic inclusions, *International Journal of Fatigue*, 11 (1989) 291-298. [https://doi.org/10.1016/0142-1123\(89\)90054-6](https://doi.org/10.1016/0142-1123(89)90054-6).
- [21] Y. Murakami, Appendix A: Instructions for a New Method of Inclusion Rating and Correlations with the Fatigue Limit, in: E.S. Ltd. (Ed.) *Metal Fatigue: Effects of Small Defects and Nonmetallic Inclusions*, 2002, pp. 321-350.
- [22] N.T. Aboulkhair, I. Maskery, C. Tuck, I. Ashcroft, N.M. Everitt, The microstructure and mechanical properties of selectively laser melted AlSi10Mg: The effect of a conventional T6-like heat treatment, *Materials Science and Engineering: A*, 667 (2016) 139-146. <https://doi.org/10.1016/j.msea.2016.04.092>.
- [23] R. Casati, J. Lemke, M. Vedani, Microstructure and Fracture Behavior of 316L Austenitic Stainless Steel Produced by Selective Laser Melting, *Journal of Materials Science & Technology*, 32 (2016) 738-744. <https://doi.org/10.1016/j.jmst.2016.06.016>.
- [24] A.B. Spierings, K. Dawson, P.J. Uggowitzer, K. Wegener, Influence of SLM scan-speed on microstructure, precipitation of Al₃Sc particles and mechanical properties in Sc- and Zr-modified Al-Mg alloys, *Materials & Design*, 140 (2018) 134-143. <https://doi.org/10.1016/j.matdes.2017.11.053>.
- [25] J. Wu, X.Q. Wang, W. Wang, M.M. Attallah, M.H. Loretto, Microstructure and strength of selectively laser melted AlSi10Mg, *Acta Materialia*, 117 (2016) 311-320. <https://doi.org/10.1016/j.actamat.2016.07.012>.
- [26] Y. Murakami, Analysis of stress intensity factors of modes I, II and III for inclined surface cracks of arbitrary shape, *Engineering Fracture Mechanics*, 22 (1985) 101-114. [https://doi.org/10.1016/0013-7944\(85\)90163-8](https://doi.org/10.1016/0013-7944(85)90163-8).
- [27] M.J. Matthews, G. Guss, S.A. Khairallah, A.M. Rubenchik, P.J. Depond, W.E. King, Denudation of metal powder layers in laser powder bed fusion processes, *Acta Materialia*, 114 (2016) 33-42. [10.1016/j.actamat.2016.05.017](https://doi.org/10.1016/j.actamat.2016.05.017).
- [28] H. Somekawa, T. Mukai, Fracture toughness in a rolled AZ31 magnesium alloy, *Journal of Alloys and Compounds*, 417 (2006) 209-213. <https://doi.org/10.1016/j.jallcom.2005.07.073>.
- [29] H. Somekawa, T. Mukai, Fracture Toughness in an Extruded ZK60 Magnesium Alloy, *MATERIALS TRANSACTIONS*, 47 (2006) 995-998. [10.2320/matertrans.47.995](https://doi.org/10.2320/matertrans.47.995).
- [30] M. Deng, H.-z. Li, S.-N. Tang, H.-J. Liao, X.-p. Liang, R.-M. Liu, Effect of Heat

Treatment on Fracture Toughness of As-Forged AZ80 Magnesium Alloy, Journal of Materials Engineering and Performance, 24 (2015) 1953-1960. [10.1007/s11665-015-1490-5](https://doi.org/10.1007/s11665-015-1490-5).

3.7 List of tables

Table 3-1 Average mechanical properties, \sqrt{area} parameter and K_{IC} values.

Diameter	Specimen	Strength [MPa]	area [mm²]	\sqrt{area} [mm]	K_{IC} [MPa\sqrt{m}]
4-mm	4mm-1	343	0.51	0.71	10.5
	4mm-2	331	0.53	0.73	10.3
	4mm-3	328	0.61	0.78	10.6
6-mm	6mm-1	350	0.61	0.78	11.3
	6mm-2	347	0.59	0.77	11.1
	6mm-3	343	0.58	0.76	10.9
Avg		340	0.57	0.76	10.8

3.8 List of figures

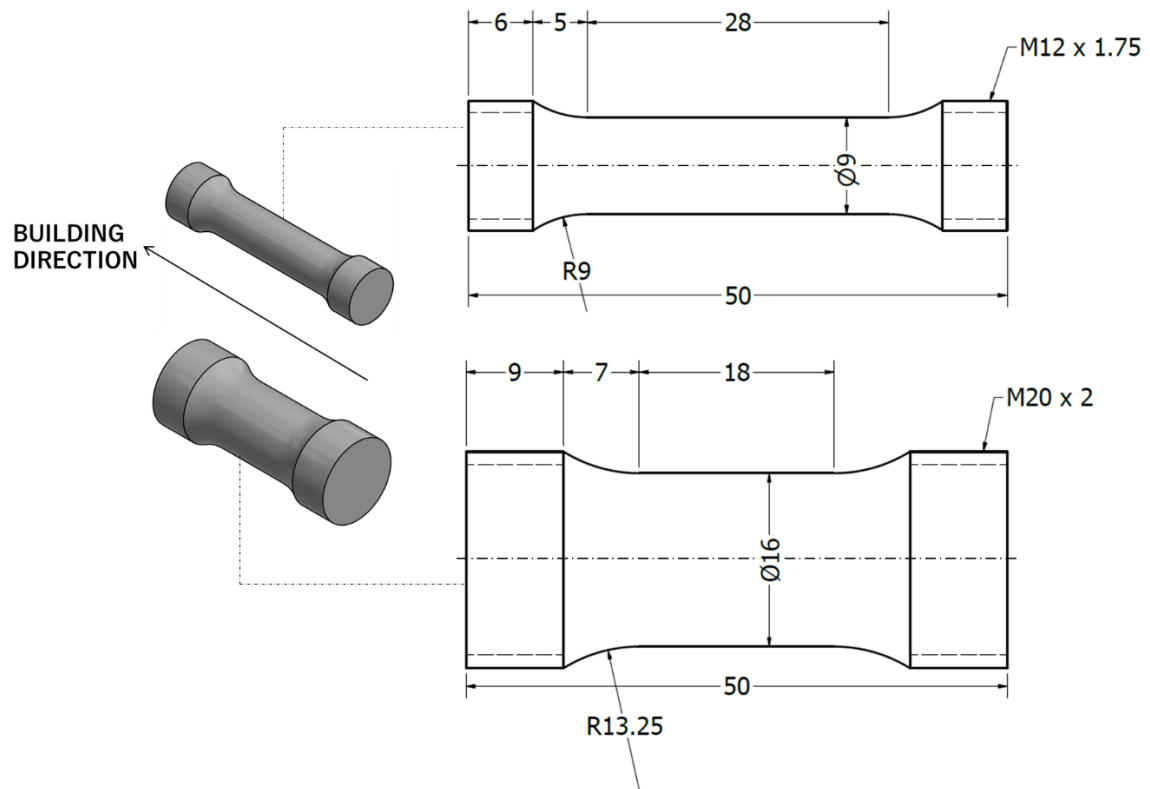


Fig. 3-1 Shapes and dimensions of the 9-mm round bar (up) and 16-mm round bar (down) tensile test specimens (Unit: mm).

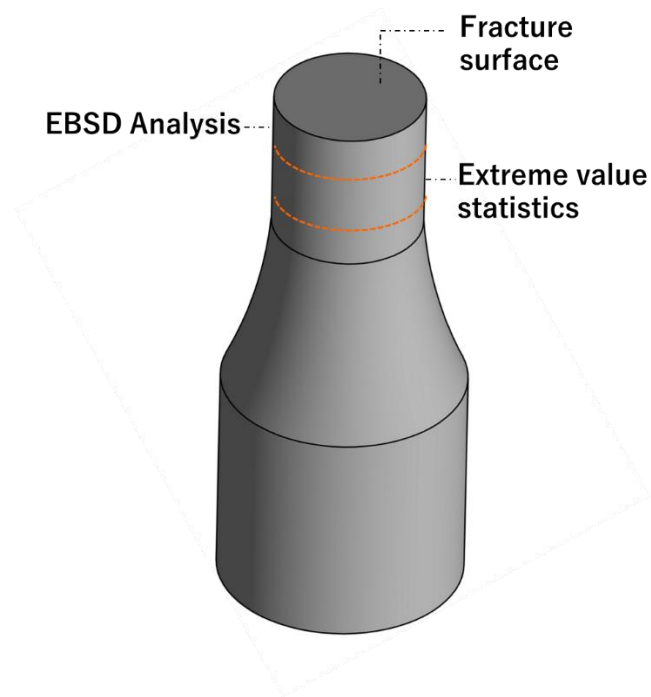


Fig. 3-2 Schematic of the cuts performed to the fractured specimen for EBSD analysis and extreme value statistics of defects.

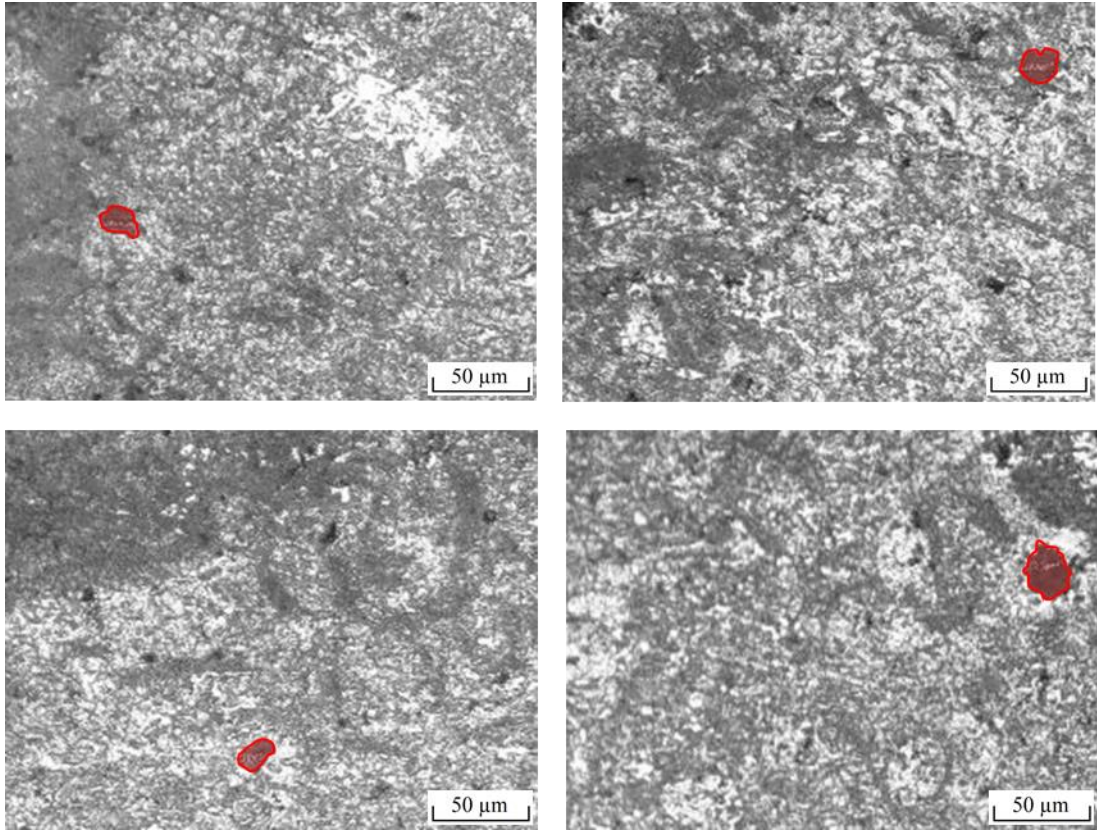


Fig. 3-3 Microscopic views of the largest defect for each image marked in red for extreme value statistics of defects.

$$V_o(\text{Control Volume}) = 0.00094 \text{ mm}^3 = 940000 \mu\text{m}^3$$

$$V(\text{Specimen Volume}) = 173 \text{ mm}^3$$

$$n = 40$$

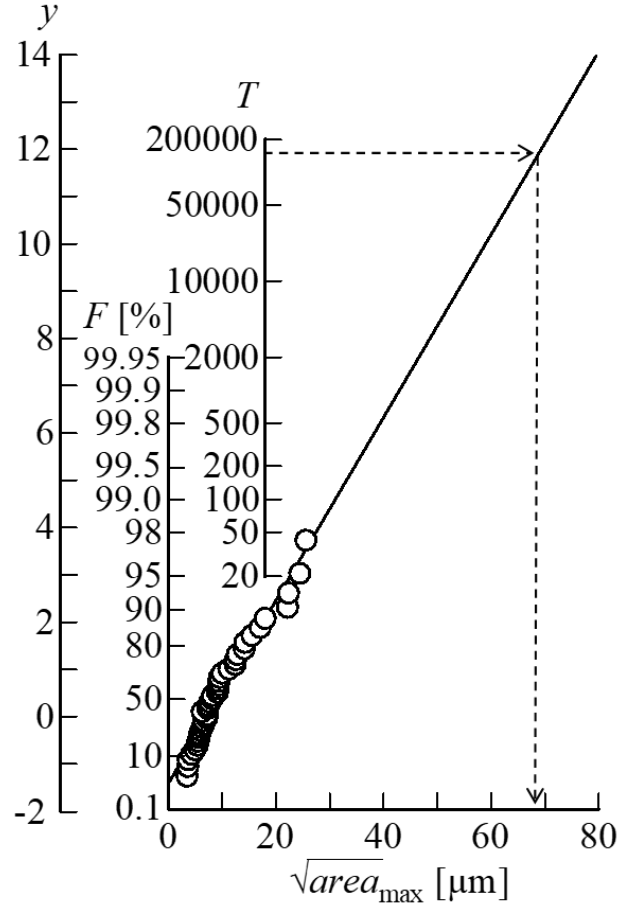


Fig. 3-4 Statistics of extremes distribution of AZX912 Mg alloy defects contained in a 6-mm round bar tensile test specimen fabricated by SLM.

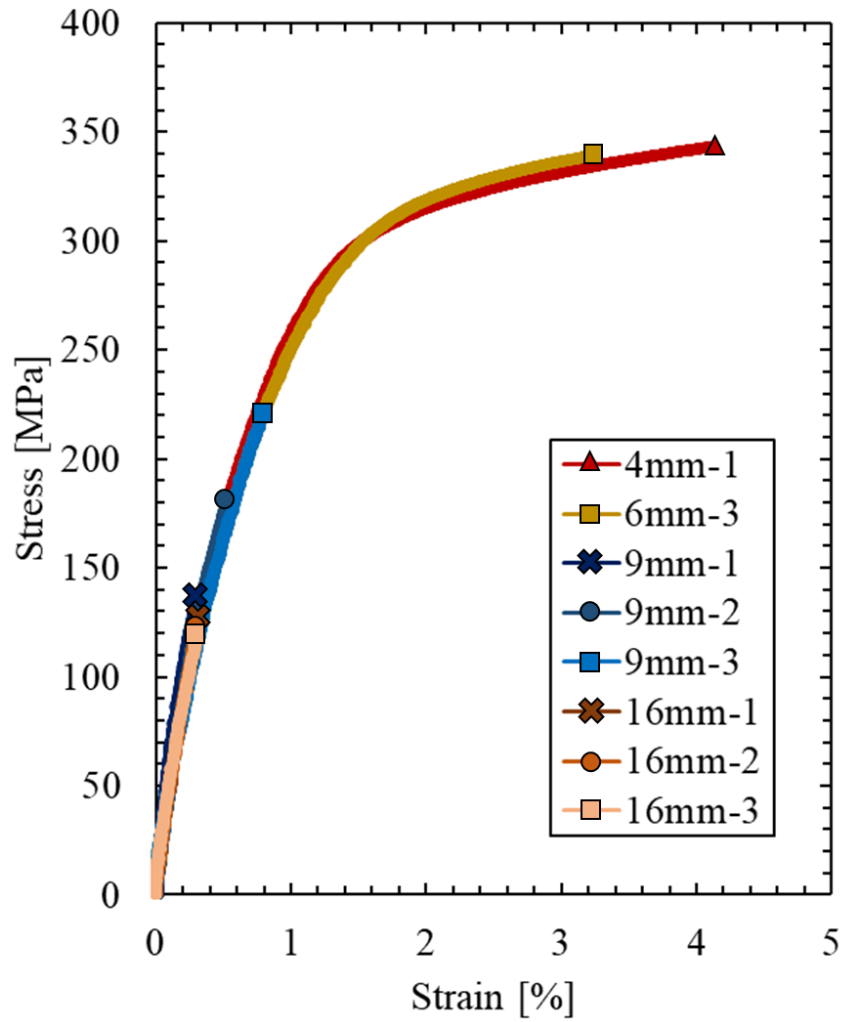


Fig. 3-5 Stress-strain diagrams of the 9 and 16-mm round bar specimens in as-built conditions. Diagrams for 4 and 6-mm are included for comparison

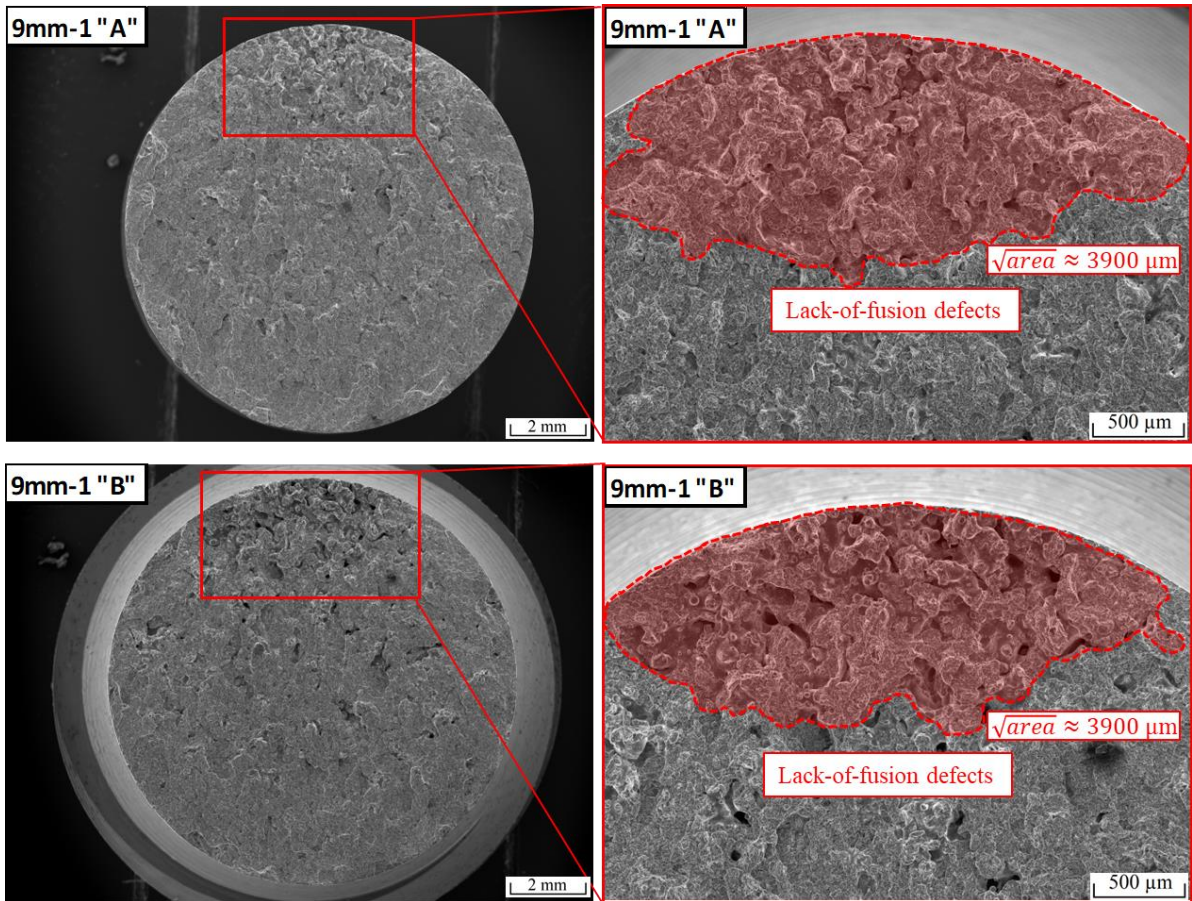


Fig. 3-6 SEM images of the fracture surfaces of the 9-mm round bar specimen showing the lack-of-fusion defects that caused fracture.

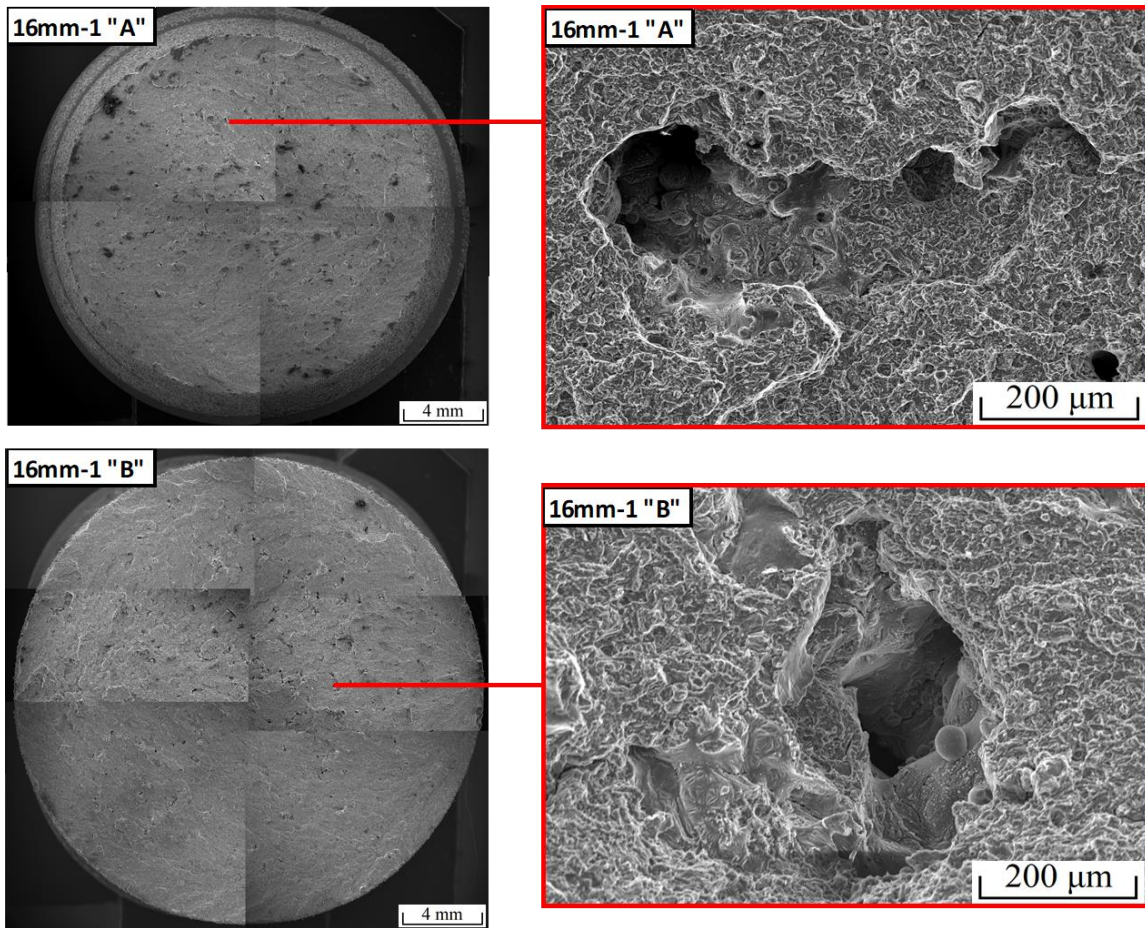


Fig. 3-7 SEM images of the fracture surfaces of the 16-mm round bar specimen showing the lack-of-fusion defects present in the fracture surface.

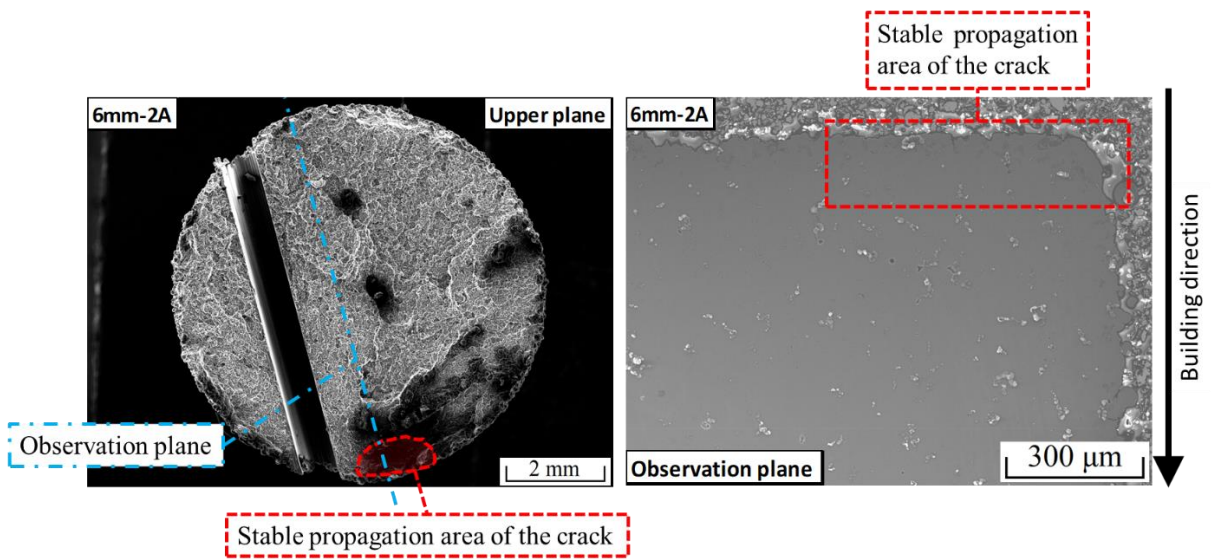


Fig. 3-8 SEM image of the cut and polish steps of the 6-mm round bar fractured specimen for EBSD observation (left), and the SEM image of the observation plane (right) marking the stable propagation area of the crack.

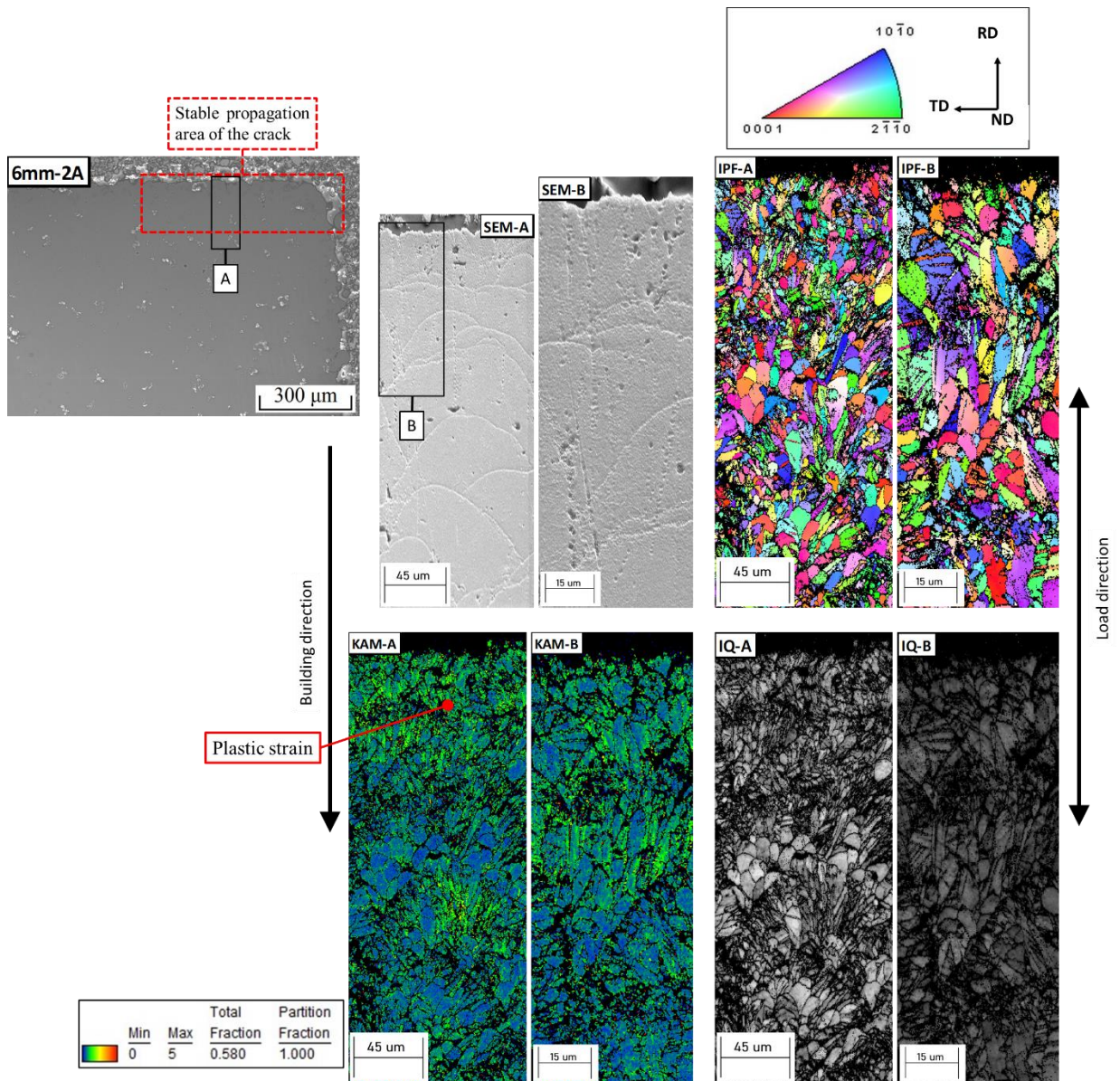


Fig. 3-9 EBSD analysis inside of the stable propagation area of the crack in a fractured specimen showing SEM imaging (Upper left), IQ map (Upper right), IPF map (Lower left) and KAM map (Lower right). Twinning deformation characteristic of Mg alloys (HCP crystalline structure) can be seen in the IPF map. Coarse microstructure is located near the crack front. Light green areas in the KAM map show a continuous plastic deformation.

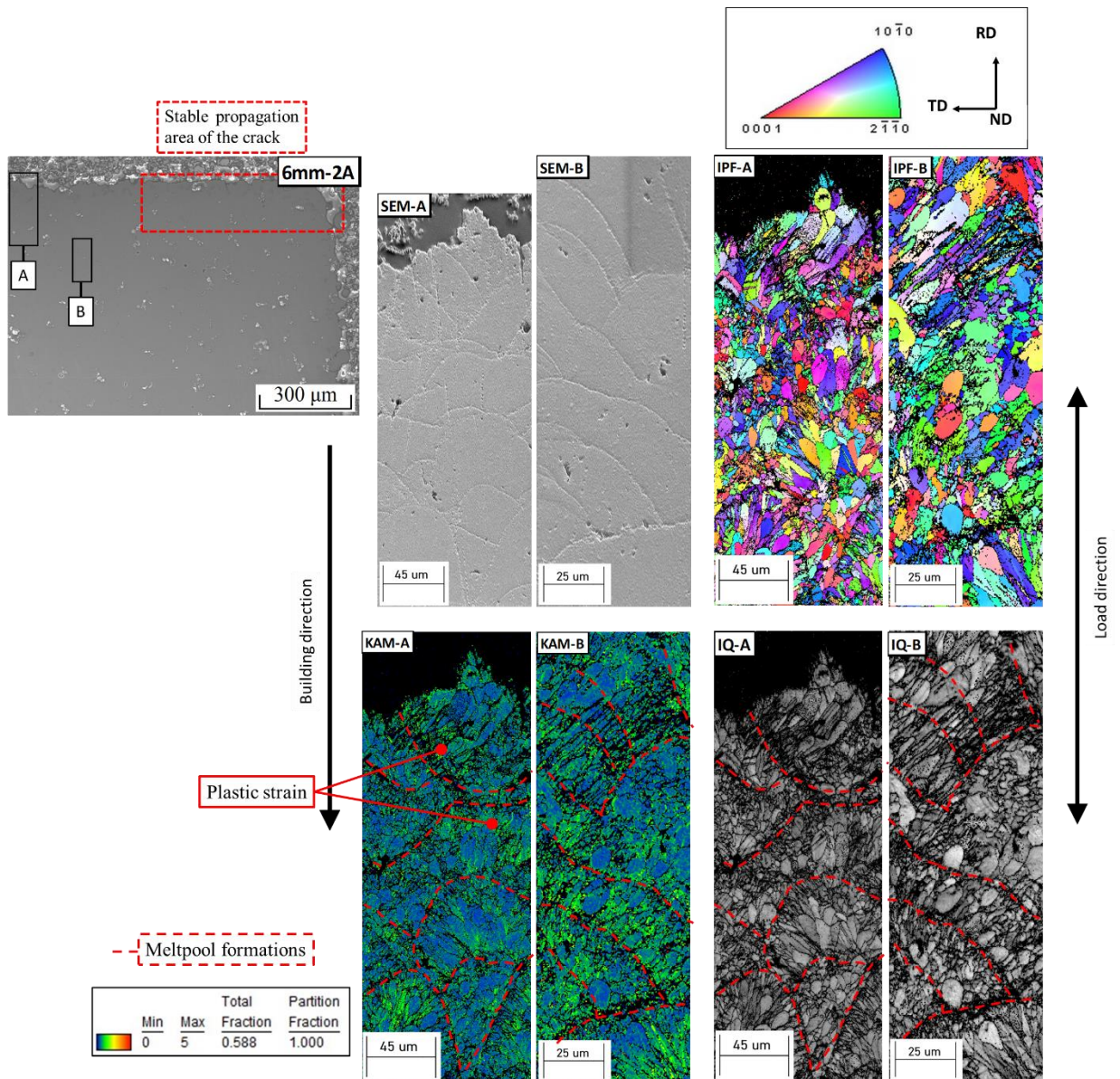


Fig. 3-10 EBSD analysis outside of the stable propagation area of the crack of a fractured specimen showing SEM imaging (Upper left), IQ map (Upper right), IPF map (Lower left) and KAM map (Lower right). Coarse microstructure is located at the borders of the melt pool formations. Light green areas in the KAM map show a disperse plastic deformation concentrating in the melt pool borders.

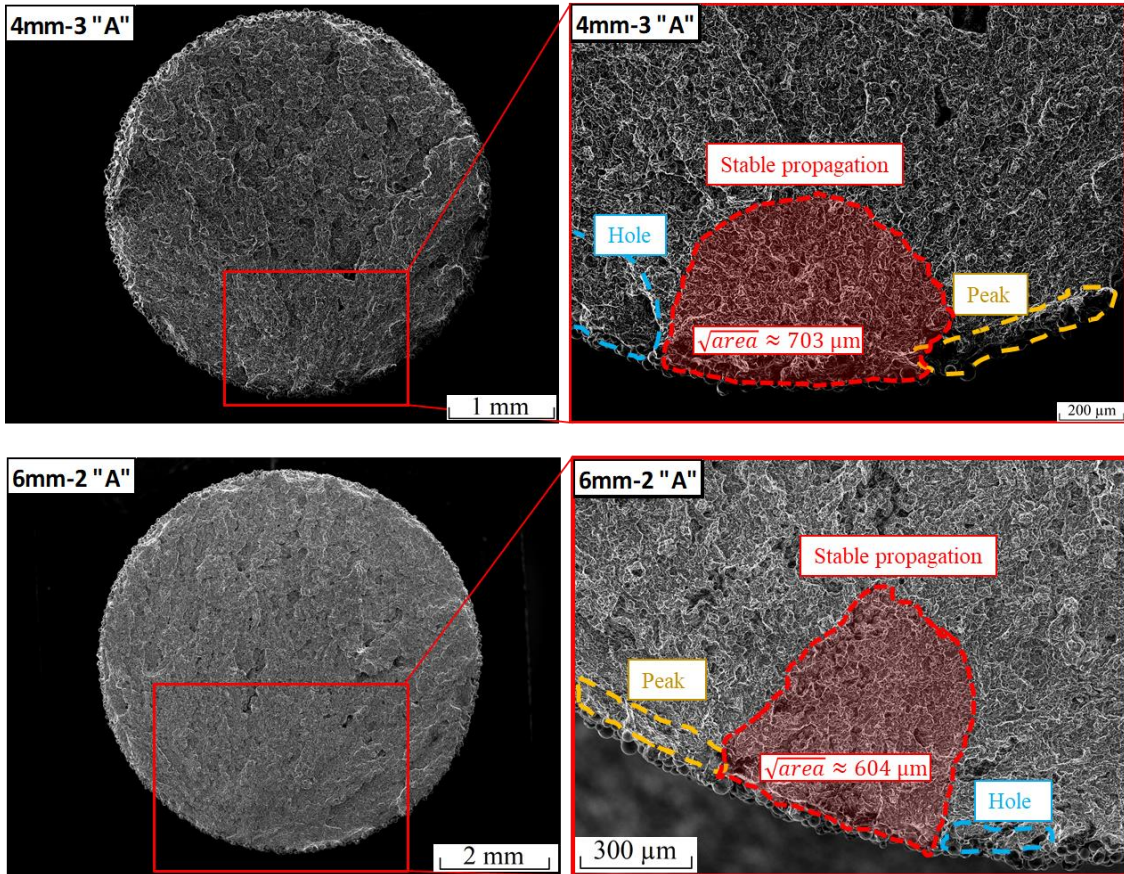


Fig. 3-11 Schematic of the measurement of the square root of the stable propagation area of the crack (\sqrt{area}) via fracture surface morphology in 4-mm (up) and 6-mm (down) round bar specimens.

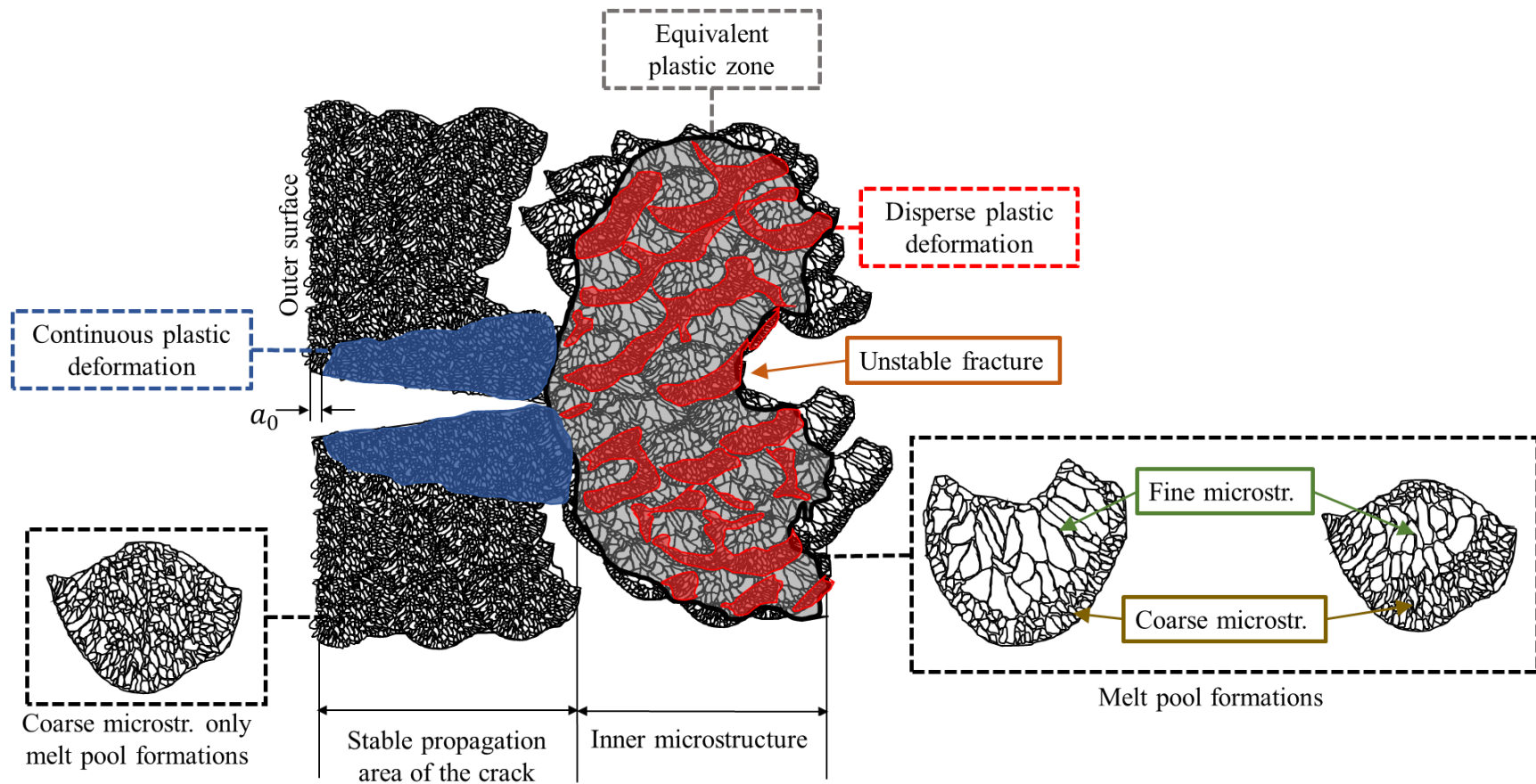


Fig. 3-12 Fracture mechanism in SLM products. The equivalent plastic zone in SLM products is much larger than the plastic zone in homogeneous materials. Schemes of the melt pool formations at the outer microstructure (irregular coarse microstructure) and inner microstructure (melt pool formations) in SLM products are also shown.

CHAPTER 4.- FRACTURE TOUGHNESS CALCULATION OF SLM PRODUCTS: MURAKAMI'S THEORY APPLICATION USING ARTIFICIALLY INTRODUCED DRILL HOLES

4.1 Introduction

The nature of the fracture mechanism of as-built specimens fabricated by SLM was evaluated in the previous chapters and indicates that the stable crack propagation induces a stress concentration source that is large enough to cause fracture when it is suddenly interrupted by microstructural changes in its distribution.

Although it was concluded that the length of the stable crack propagation is an intrinsic defect, it is difficult to comprehend and/or visualize a crack length that cannot be seen before stress is applied. In addition, a crack measured by fracture surface morphology can be a deceptive task since different researchers can provide different regions where a stable fracture transitions to an unstable fracture, especially when defects coalesce with each other. In short, if measuring a defect is based on any subjective perspective, the results could be different from what is expected or even biased.

To circumvent this problem, a solution that allows a precise measurement of a defect responsible for fracture in SLM products while at the same time corroborating to the fracture toughness results calculated in Chapter 3 is needed. Therefore, the author considered introducing drill holes of different depth and diameter in the center of the round-bar specimens at the outer surface. The experimental process is quite simple. An artificially introduced drill hole is a stress concentration source. If the drill hole has a smaller depth compared to the stable propagation area of the crack, then fracture will occur at the stable propagation area of the crack following the fracture mechanism explained in Chapters 2 and 3. On the other hand, if the drill hole has a larger depth compared to the stable propagation area of the crack, then fracture will occur at the drill hole. The resumed hypothesis can be observed in Fig. 4-1. With this method, the stress

concentration where the stable propagation area of the crack will be validated, and at the same time the visible drill holes in the fracture surface can provide a reliable crack size to use in Murakami's Theory and calculate fracture toughness using equation (3 – 1) [1]. Subsequently, the fracture toughness calculated in specimens with introduced artificial defects can be compared to the fracture toughness of SLM products in as-built conditions. If the results are similar, it is safe to conclude that the fracture toughness is correct.

Furthermore, strong evidence of a stable crack propagation due to a continuous plastic strain can be observed in Fig. 3-9, but it is unclear at what point does the crack start to propagate. Stress-strain diagrams of the specimens in Figs. 2-3 and 3-5 show the characteristic curve of ductile materials in the plastic region, but no necking was observable during testing, thus suggesting some way of crack propagation after yielding. To verify crack propagation after yielding, a specimen submitted to tensile testing will interrupt the load application at 80% of the UTS value. Since fracture initiation is linked to coarse microstructure at the outer surface, it is difficult to determine the exact point where fracture will occur. Therefore, an artificial drill hole can be inserted to induce fracture and then, after the tensile test is interrupted, a crack propagation should be observed. Additionally, since the whole specimen is under the applied load, theoretically the whole specimen should be yielded. However, the local strain at the crack tip is much larger than the strain measured in the gauge length. In a non-homogeneous SLM product, dislocation flow cannot be regular because the microstructure is not regular. As a result, other crack initiation points besides the drill hole should form in the outer surface.

In this chapter, five different drill holes with sizes of 100, 400, 600, 800, and 1000 μm were introduced individually into several 6-mm round bar specimens. Five specimens for each drill hole size were produced using SLM. Subsequently, the specimens were subjected to tensile testing, and the fracture surface was observed. The stable propagation area of the crack was measured, and the fracture toughness was calculated. In this manner, a method to precisely define the stable propagation area of a crack required to use Murakami's Theory could be useful to help determine a constant fracture toughness value, which in turn serves as a tool to predict the strength of the material and enhance the reliability of SLM products. An additional 6-mm round bar specimen with a 400 μm drill

hole was submitted to tensile testing, and then the load application was interrupted at 80% of the UTS value. Then, the drill hole and the outer surface were observed to identify crack propagation sources.

4.2 Experimental procedure

Twenty-five tensile test specimens with the same geometry were fabricated using the EOS M100 SLM machine shown in Fig. 2-1. The raw material was AZX912 Mg alloy powder with the same composition as in Table 1-1. The particle size distributions were the same as shown in Section 1.4. Laser irradiation parameters are shown in Table 2-1. The round bar specimens were carried out using the scanning strategy shown in Fig. 2-2 a). Fig. 4-2 shows the geometrical configuration of the 6-mm round bar specimens in as-built conditions.

Drill holes were introduced into the specimens by using a 002107-type Levin micro-drilling machine at a fixed speed rotation of 1700 rpm. In the case of drill holes with sizes of 600, 800, and 1000 μm , a mechanically equivalent system using two adjacent holes with equal diameters was used [2]. The schematics of the drill holes are shown in Fig. 4-3. A code was assigned to each specimen with a drill hole. The codes and depths of all the drill holes measured from the outer surface are given in Table 4-1.

Tensile testing was performed using a Shimadzu AG-50kNXD universal electromechanical testing machine, with a strain rate of 0.0011 $[\text{s}^{-1}]$ in accordance with the Japanese Industrial Standard JIS Z 2241:2011 (Method of Tensile Test for Metallic Materials). Tensile testing was conducted along the building direction of the round bar specimens at ambient temperature. All tests were performed using screw-type grips set with spherical bearings to ensure that no misalignment or bending occurs during testing. The elongation was measured using a Shimadzu SG25-100 extensometer. The fracture surfaces were observed using a JEOL JSM-IT300 scanning electron microscope (SEM) and were the basis to determine the defect that can be used in Murakami's Theory and subsequently calculate fracture toughness.

4.3 Results

4.3.1 Tensile tests results

Fig. 4-4 shows an example of the stress–strain diagram for each drill hole size. The results indicate that mean values of the yield strength (at 0.2% offset) and Young’s Modulus were 253 MPa and 45 GPa respectively. The ultimate strength values for all the tested specimens are shown in Fig. 4-5. The fracture initiation point for each specimen was identified and are also identified in Fig 4-5. It was observed that the drill holes were the fracture initiation points when the depth of the holes was equal to or larger than 600 μm . In specimens with drill holes of a smaller diameter, the fracture initiation point was located elsewhere.

4.3.2 Fractography results and determination of stable propagation area of the crack

The results enable the specimens to be classified into a non-damaged specimen and a specimen where fracture initiates at the drill hole. The location of the fracture initiation is also depicted in Table 4-1. For both cases, a similar method for determining the stable propagation area of the crack by fracture surface observation was used. First, the fracture initiation point was determined. Subsequently, the limits of the stable propagation area of the crack were defined by considering the peak–peak or hole–hole morphology corresponding to a ductile fracture and the peak–hole morphology corresponding to a brittle fracture [3], as previously shown in Chapter 2. It is worth noting that while unstable fracture occurs due to crack deflection [4, 5], the stable fracture is enabled by void formation in the form of layer detachment [6], since the grains crystallized where stable fracture occurs have a lower hardness in comparison to the center as shown in Fig. 2-15 and Fig. 5-6, thus enabling dislocation movement. Finally, with the limits established, an approximate arc-shaped crack that originates from the outer surface was drawn and measured. The arch-shaped area corresponded to the stable propagation area of the crack in the case of non-damaged specimens, and the enclosed drill hole in accordance with Murakami’s Theory for the remaining specimens. An example of using this method for a specimen in which fracture did not initiate at the drill hole (non-damaged specimen) is shown in Fig. 4-6, whereas the use of the same method for a specimen in which the drill hole is the fracture initiation point is illustrated in Fig. 4-7.

Fig. 4-8 shows the 400 μm drill hole before load was applied and after the load was interrupted at 80% of the UTS value. A small crack propagation can be observed from the drill hole largest stress concentration source. Fig. 4-9 shows other crack propagation evidence found in other regions in the gauge length of the specimens.

4.3.3 Fracture toughness results

Once the size stable propagation area of the crack was defined for each case, the corresponding area could be measured. Because the UTS values are known, the fracture toughness can be easily determined if Murakami's approach [7] is used. To determine the fracture toughness of a structure with a regular crack that originated at the surface, the square root of the effective area parameter is used as a parameter in the previously mentioned Murakami equation (3 – 1):

$$K_{IC} = 0.65\sigma_C\sqrt{\pi\sqrt{area}}$$

where K_{IC} is the fracture toughness and is expressed in $[\text{MPa}\sqrt{\text{m}}]$, σ_C is the UTS obtained via tensile testing (in $[\text{MPa}]$). \sqrt{area} is the square root of the stable propagation area of the crack or the drill hole projected onto the plane perpendicular to the applied stress direction (expressed in $[\text{m}]$). The results of the fracture toughness for all specimens are shown in Fig. 4-10. The determined maximum stress was 350 MPa, the average fracture toughness value was $K_{IC} = 10.3 \text{ MPa}\sqrt{\text{m}}$, and the potential energy release rate was $\varphi_C = 1.9 \text{ kJ/m}^2$. φ_C was calculated by using the following equation [8]:

$$\varphi_C = (1 - \nu^2) \frac{K_{IC}^2}{E} \quad (4 - 1)$$

where Poisson's ratio $\nu = 0.3$ and Young's modulus $E = 45 \text{ GPa}$ were used.

4.4 Discussion

4.4.1 Strength variation and constant fracture toughness

It is important to note that all the specimens used in this study had the same geometry and were fabricated using the same parameters. Even so, a slight variation in the UTS results was noted, especially in the case of the non-damaged specimens. This phenomenon can be explained by the stable propagation area of the crack. In Chapter 2,

it was established that the size of the stable propagation area of the crack is defined by the size of the chunks of coarse microstructure in the outer surface. However, the size of the coarse microstructure region is a parameter that cannot be systematically controlled, and therefore, a small strength variation is expected. On the other hand, the specimens that fracture at the drill hole have a larger area than the stable propagation of the crack, which also translates into a considerably lower UTS value, which can be verified in Fig. 4-5. The hypothesis that considers stable propagation area of the crack as a non-visible defect can also be confirmed by observing the fracture surfaces of all the tested non-damaged specimens. In all these cases, the fracture initiated at the outer surface; moreover, all the visible defects had similar sizes and did not exhibit any relation with the UTS. The presence of coarse microstructure in the outer surface of SLM products has been previously confirmed by direct observation of the microstructure in Chapter 2. Nevertheless, to consider K_{IC} as a material property, small-scale yielding (SSY) conditions have to be assumed, meaning that the dispersed plastic zone is small enough it can be neglected, which is unclear at the time being. In addition, considering that the specimens undergo brittle fracture due to the absence of necking, plain-strain conditions are assumed, meaning that the size of the stable propagation of the crack is small enough in comparison to the specimen's width. It is known that in the plain-strain regime K_{IC} is constant. Therefore, it can be safely assumed that regardless of the size of the coarse grain region and the UTS, the fracture toughness will remain constant in as-built conditions; a result that can be verified in Fig. 4-10.

However, the different mechanical state between a surface crack and a drill hole comes to mind. Specifically, the stress intensity factor (or K value) for each case is different because the crack has the stress singularity at the crack tip and the drill hole has a known stress concentration factor at the extremes. Thus, similar K_{IC} results for no-damage specimens and specimens where fracture occurred at the drill hole could be considered as a coincidence. To circumvent this problem, Murakami stated that the K value of a drill hole and a surface crack can be considered equal depending on the fracture mechanism. For instance, in the case of fatigue life prediction, a crack emanates non-propagation cracks from both the drill hole and the surface crack before unstable fracture occurs. As a result, Murakami concluded that using the \sqrt{area} parameter enclosing the

drill hole or the surface crack before the emanation of the non-propagation cracks to calculate stress intensity factors allowed for approximately equal results (with a $\pm 10\%$ error variation) when the hole diameter is a circle [9], as can be seen in Fig. 4-11. In the case of SLM products, the drill hole undergoes propagation as shown in Fig. 4-8, and then is suddenly interrupted and the plastic strain disperses. Therefore, the \sqrt{area} parameter enclosing the sudden interruption of the stable propagation of the crack same before plastic strain dispersion is considered a mechanically equivalent system to Murakami's, as shown in Fig. 4-11. As a result, it is safe to assume that the drill hole diameter has a similar K_{IC} value compared to the stable propagation area of the crack. At the same time, the K_{IC} results in Fig. 4-10 show a slight increase when the specimens fractured at the drill hole. However, the increase is located within the $\pm 10\%$ error variation estimated by Murakami, thus validating the result. Additionally, according to Murakami, a valid approximation of the \sqrt{area} can be made when the length of a crack (l) is much larger compared to its depth (c). The expression that consolidates this is $\sqrt{area} = \sqrt{10}c$, where c is the depth of the crack [10]. The value of c was determined by extreme value statistics of the microstructure in Section 2.3.2, and was 430 μm for a 4-mm round bar specimen and 600 μm for a 6-mm round bar specimen according to Fig. 2-13. Accordingly, $\sqrt{10}c = 1360 \mu\text{m}$ for 4-mm and 1900 μm for 6-mm. These values are far too large compared to the values shown in Fig. 3-11 (4-mm) and Fig. 4-6 (6-mm). However, this can be explained because Murakami requires that $l/c > 10$, a condition that is not satisfied because the coarse microstructure region at the outer surface is not continuous.

Finally, the validation of the K_{IC} results needs to be performed. Particularly, if the SSY condition is satisfied or not. For example, ASTM E399 standard validates the value K_{IC} once the testing results satisfy a series of conditions that guarantee the SSY condition in plain strain. However, the microstructure duality of SLM products does not allow for the ASMT to go through, since it makes the material non-homogeneous. For that reason, the K_{IC} result obtained in this chapter and that will be referred to in the following chapters, is a temporary solution that enhances the reliability of the SLM process. An indicator for validation of K_{IC} using this method remains a prospect for future research, and a step towards that direction will be analyzed in Chapter 7.

4.4.2 Influence of drill hole

It was observed that the UTS tended to be constant when the fracture of the specimens initiated from the drill hole, particularly in the case of specimens having a drill hole with a diameter of 600 μm or larger. These results are valuable because in all the 6-mm round bar specimens, the largest visible defects located in the fracture surfaces such as porosities or, in a few cases, lack-of-fusion defects, had a maximum size of approximately 70 μm . Therefore, according to traditional fracture mechanics, a drill hole larger than 70 μm must be the fracture initiation point due to its stress concentration. However, even with a drill hole size of 400 μm , after the application of stress, the fracture initiation point was located elsewhere, and no visible defect larger than 400 μm was observed on the fracture surface. This finding indicates that the drill hole size exerts no influence on both the fracture mechanism and specimen strength. This phenomenon can also be explained by the coarse microstructure size, as the fracture initiates at the point at which the size of the coarse microstructure region is maximum. This affirmation is particularly obvious with the fracture surface of specimen AD400-01, which can be observed in Fig. 4-12. The fracture process seemed to have started at the drill hole, but then the largest stress concentration source was located elsewhere. The magnified images shown in Fig. 4-12 (b) show no visible defect in the fracture initiation point, leaving as an only explanatory cause the microstructural changes occurring when the outer microstructure transitions into the inner microstructure.

Furthermore, in Chapter 2, by observing the microstructure of a 6-mm round bar specimen, the size of the coarse microstructure region was determined to be approximately 600 μm . In addition, another factor that indicates that microstructure-related defects have the highest stress concentration can be clarified by considering the result of specimen AD800-5. The fracture surface of this specimen is shown in Fig. 4-13. Although the UTS for this specimen has a similar value as that of other cases, it can clearly be seen that the 800 μm drill hole is not the fracture initiation point; instead, it is located in a rectangular shape indicating an irregular fusion of the powder. The irregular fusion can be attributed to the fumes formed at the beginning of the scan track, which, as determined in previous studies, is the location in which fusion-related defects are most likely to occur during processing [11, 12]. Furthermore, Mg alloys are highly volatile [13],

and thus, fumes are likely to be generated.

As for a fracture mechanism, non-damaged specimens follow the exact same mechanism as described in Fig. 3-12. The artificial drill hole has no influence in the strength of the specimen, and at the same time, experimentally confirms the effects of a non-visible defect from the outersurface as the weakest point instead of a visible artificial drill hole. On the contrary, the drill hole as the weakest point for fracture means that the drill hole size is larger than the stable propagation area of the crack. Therefore, strength should be slightly lower, as can be evidenced in the UTS results presented in Fig. 4-5. However, it is important to notice that, regardless of the weakest point location or strength value, fracture toughness tends to be constant with an average value of $10.3 \text{ MPa}\sqrt{\text{m}}$, a result consistent with the value of $10.8 \text{ MPa}\sqrt{\text{m}}$ obtained in section 3.3.4. Thus, strength reliability can be enhanced in SLM products considering fracture toughness as a mechanical property and at the same time the stable propagation area of the crack has a more accurate approximation. Further research is recommended to determine the influence of the localization of an artificial defect in a specific type of microstructure. According to the obtained results, it is expected that a defect located inside the coarse microstructure is more likely to fracture than a defect of the same size located inside the fine microstructure.

4.5 Conclusions

In previous chapters, a non-visible defect known as stable propagation area of the crack was categorized as the defect responsible for fracture in SLM products; however, its definition method using fracture surface morphology could have been debated or even biased. After introducing several artificial defects of different depths in various round bar specimens to overcome this problem, the following conclusions were derived in this study:

- The effects of the non-visible defect known as the stable propagation area of the crack were verified, and they are more critical than a large visible artificial defect.
- If a visible defect from the outer surface is smaller than the size of the stable propagation area of the crack, then the visible defect has no influence in the strength

or in the fracture mechanism of the specimen. On the other hand, if the visible defect is larger than the stable propagation of the crack, it becomes the weakest point for fracture and will influence the strength at failure.

- Microstructure related defects such as lack-of-fusion porosities or irregularly melted areas are critical to the mechanical properties of the specimen and should be avoided.
- For the non-combustible Mg alloy products in this study, the determined maximum stress was 350 MPa, the average fracture toughness value was $K_{IC} = 10.3 \text{ MPa}\sqrt{\text{m}}$, and the potential energy release rate of the fracture was $\varphi_C = 1.9 \text{ kJ/m}^2$.

4.6 References

- [1] Y. Murakami, S. Kodama, S. Konuma, Quantitative evaluation of effects of non-metallic inclusions on fatigue strength of high strength steels. I: Basic fatigue mechanism and evaluation of correlation between the fatigue fracture stress and the size and location of non-metallic inclusions, *International Journal of Fatigue*, 11 (1989) 291-298. [https://doi.org/10.1016/0142-1123\(89\)90054-6](https://doi.org/10.1016/0142-1123(89)90054-6).
- [2] W.D. Pilkey, *Formulas for Stress, Strain, and Structural Matrices*, Wiley, 1994.
- [3] D. Wang, W. Dou, Y. Yang, Research on Selective Laser Melting of Ti6Al4V: Surface Morphologies, Optimized Processing Zone, and Ductility Improvement Mechanism, *Metals*, 8 (2018). [10.3390/met8070471](https://doi.org/10.3390/met8070471).
- [4] A. Sapora, P. Cornetti, A. Carpinteri, V. Mantič, Crack deflection in brittle materials by Finite Fracture Mechanics, *Procedia Structural Integrity*, 2 (2016) 1975-1982. <https://doi.org/10.1016/j.prostr.2016.06.248>.
- [5] X. Zeng, Y. Wei, Crack deflection in brittle media with heterogeneous interfaces and its application in shale fracking, *Journal of the Mechanics and Physics of Solids*, 101 (2017) 235-249. <https://doi.org/10.1016/j.jmps.2016.12.012>.
- [6] N.T. Aboulkhair, I. Maskery, C. Tuck, I. Ashcroft, N.M. Everitt, The microstructure and mechanical properties of selectively laser melted AlSi10Mg: The effect of a conventional T6-like heat treatment, *Materials Science and Engineering: A*, 667 (2016) 139-146. <https://doi.org/10.1016/j.msea.2016.04.092>.
- [7] Y. Murakami, Analysis of stress intensity factors of modes I, II and III for inclined surface cracks of arbitrary shape, *Engineering Fracture Mechanics*, 22 (1985) 101-114. [https://doi.org/10.1016/0013-7944\(85\)90163-8](https://doi.org/10.1016/0013-7944(85)90163-8).
- [8] D. Broek, *Elementary Engineering Fracture Mechanics*, Springer, Dordrecht, Netherlands, 1982.
- [9] Y. Murakami, Cracks at Stress Concentrations, in: E.S. Ltd. (Ed.) *Metal Fatigue*:

- Effects of Small Defects and Nonmetallic Inclusions, 2002, pp. 20-21.
- [10] Y. Murakami, Effective 'area' for Particular Cases, in: E.S. Ltd. (Ed.) Metal Fatigue: Effects of Small Defects and Nonmetallic Inclusions, 2002, pp. 18.
- [11] C. Bruna-Rosso, A.G. Demir, B. Previtali, Selective laser melting finite element modeling: Validation with high-speed imaging and lack of fusion defects prediction, *Materials & Design*, 156 (2018) 143-153. <https://doi.org/10.1016/j.matdes.2018.06.037>.
- [12] A. Ladewig, G. Schlick, M. Fisser, V. Schulze, U. Glatzel, Influence of the shielding gas flow on the removal of process by-products in the selective laser melting process, *Additive Manufacturing*, 10 (2016) 1-9. <https://doi.org/10.1016/j.addma.2016.01.004>.
- [13] H. Watarai, Chapter 7: Trend of Research and Development for Magnesium Alloys, in: P.D.U. Kainer (Ed.) *Science & Technology Trends*, 2006, pp. 84-97.

4.7 List of tables

Table 4-1 Specimen codification and depth of the drill holes

Drill diameter [μm]	Code	Depth [μm]	Fracture Initiation	Drill diameter [μm]	Code	Depth [μm]	Fracture Initiation
100	AD100-1	90	Elsewhere	400	AD400-1	400	Elsewhere
	AD100-2	105	Elsewhere		AD400-2	400	Elsewhere
	AD100-3	130	Elsewhere		AD400-3	415	Elsewhere
	AD100-4	120	Elsewhere		AD400-4	400	Elsewhere
	AD100-5	85	Elsewhere		AD400-5	400	Elsewhere

Drill diameter [μm]	Code	Depth [μm]	Fracture Initiation	Drill diameter [μm]	Code	Depth [μm]	Fracture Initiation
600	AD600-1	620	Drill hole	800	AD800-1	800	Drill hole
	AD600-2	600	Drill hole		AD800-2	800	Drill hole
	AD600-3	600	Drill hole		AD800-3	795	Drill hole
	AD600-4	620	Drill hole		AD800-4	800	Drill hole
	AD600-5	600	Drill hole		AD800-5	800	Elsewhere

Drill diameter [μm]	Code	Depth [μm]	Fracture Initiation
1000	AD1000-1	1000	Drill hole
	AD1000-2	1010	Drill hole
	AD1000-3	1000	Drill hole
	AD1000-4	1030	Drill hole
	AD1000-5	1000	Drill hole

4.8 List of figures

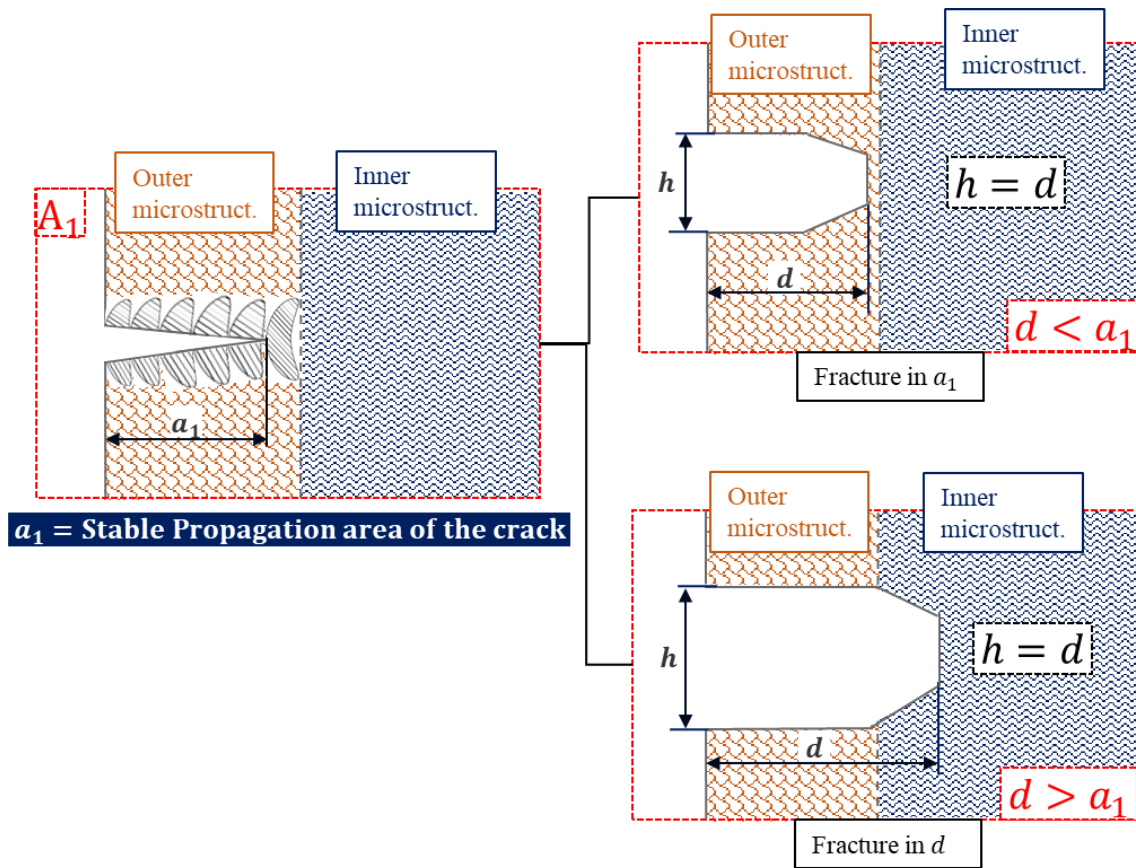


Fig. 4-1 Schematic of the hypothesis where a_1 is the stable propagation area of the crack, h is the drill hole diameter and d is the drill hole depth.

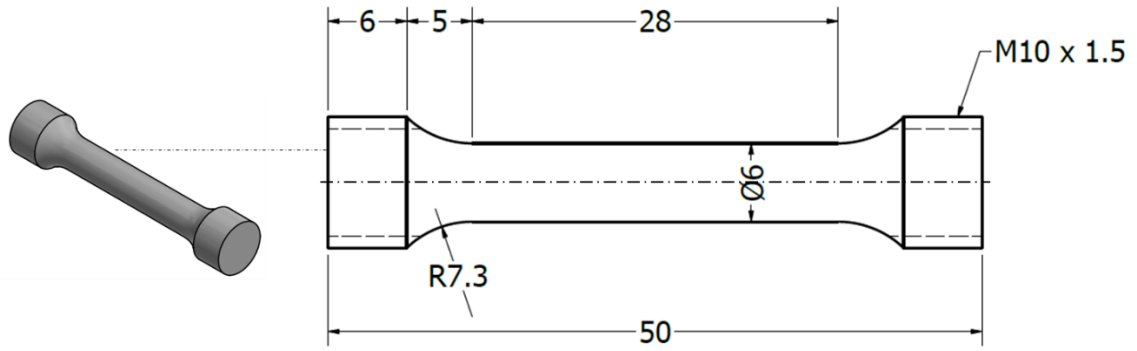


Fig. 4-2 Shape and dimensions for the 6-mm round bar tensile test specimens (Units: mm).

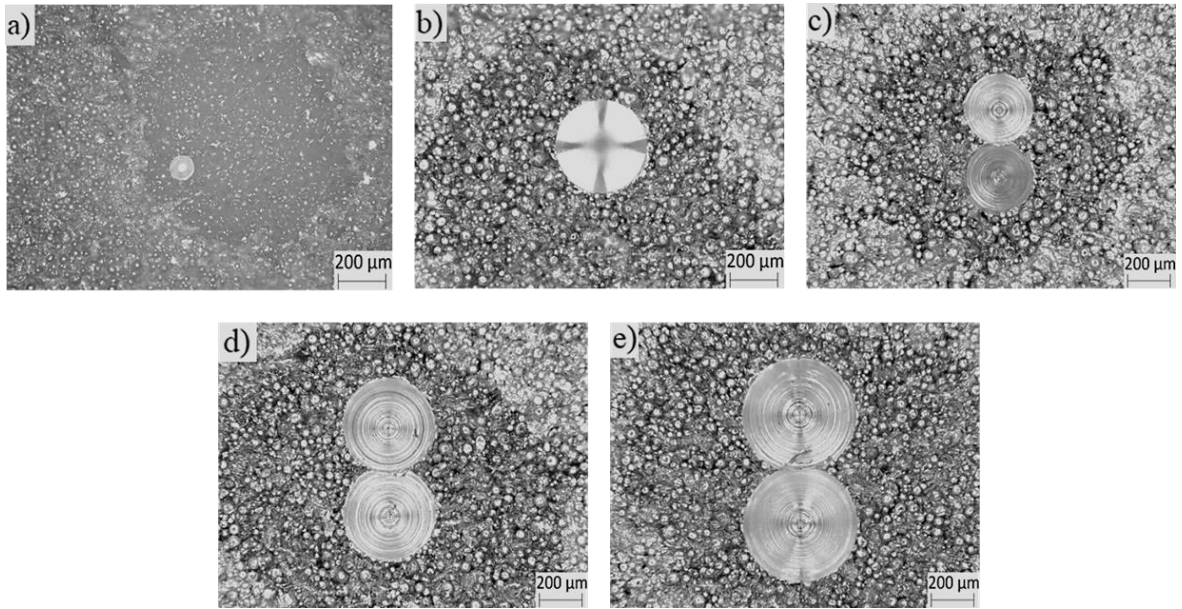


Fig. 4-3 Images of the drill holes for: a) 100 μm , b) 400 μm , c) 600 (300x2) μm , d) 800 (400x2) μm and e) 1000 (500x2) μm . Depths of the drill holes are shown in Table 4-3.

The red spot marks the center of the specimen.

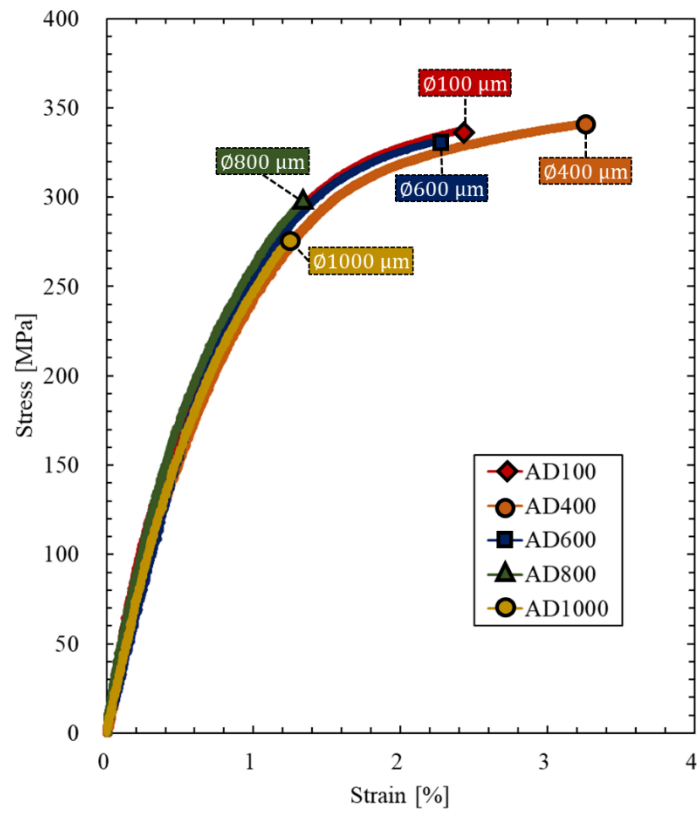


Fig. 4-4 Stress-strain diagrams for the specimens with introduced drill holes.

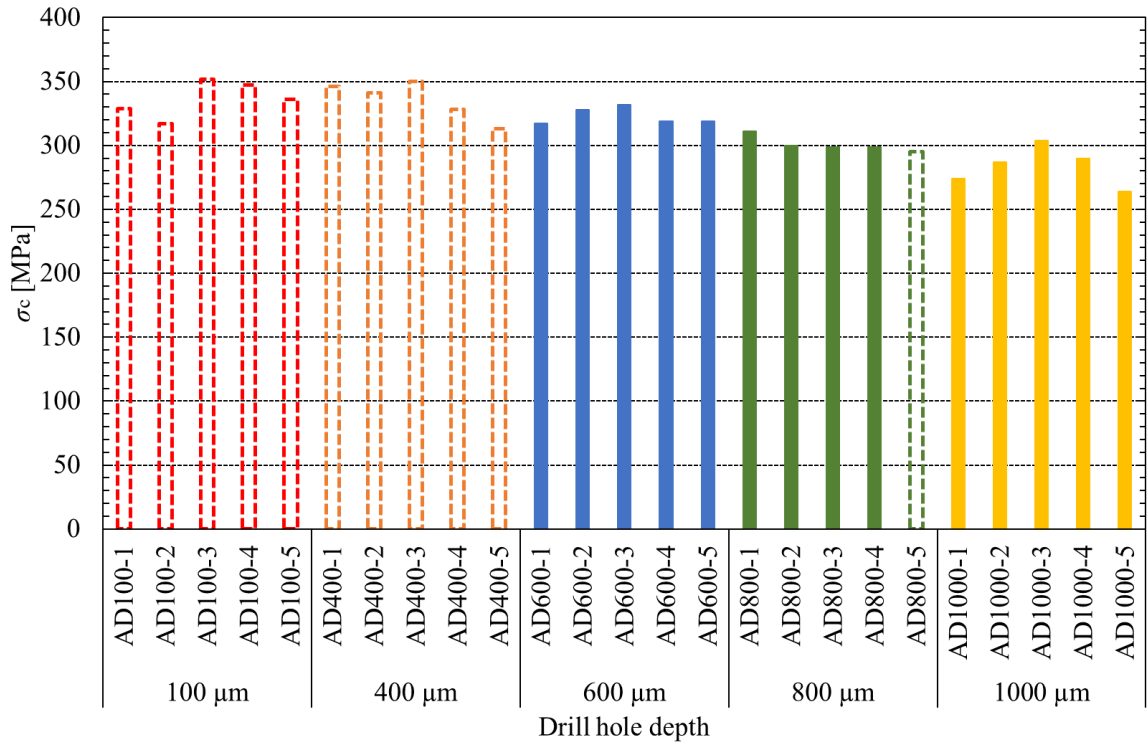


Fig. 4-5 Ultimate tensile strength (σ_c) for all the 6 mm round bar specimens with different drill hole sizes. Specimen with dashed bars fractured elsewhere than the drill hole (non-damaged specimens) and specimens with filled bars fractured in the drill hole.

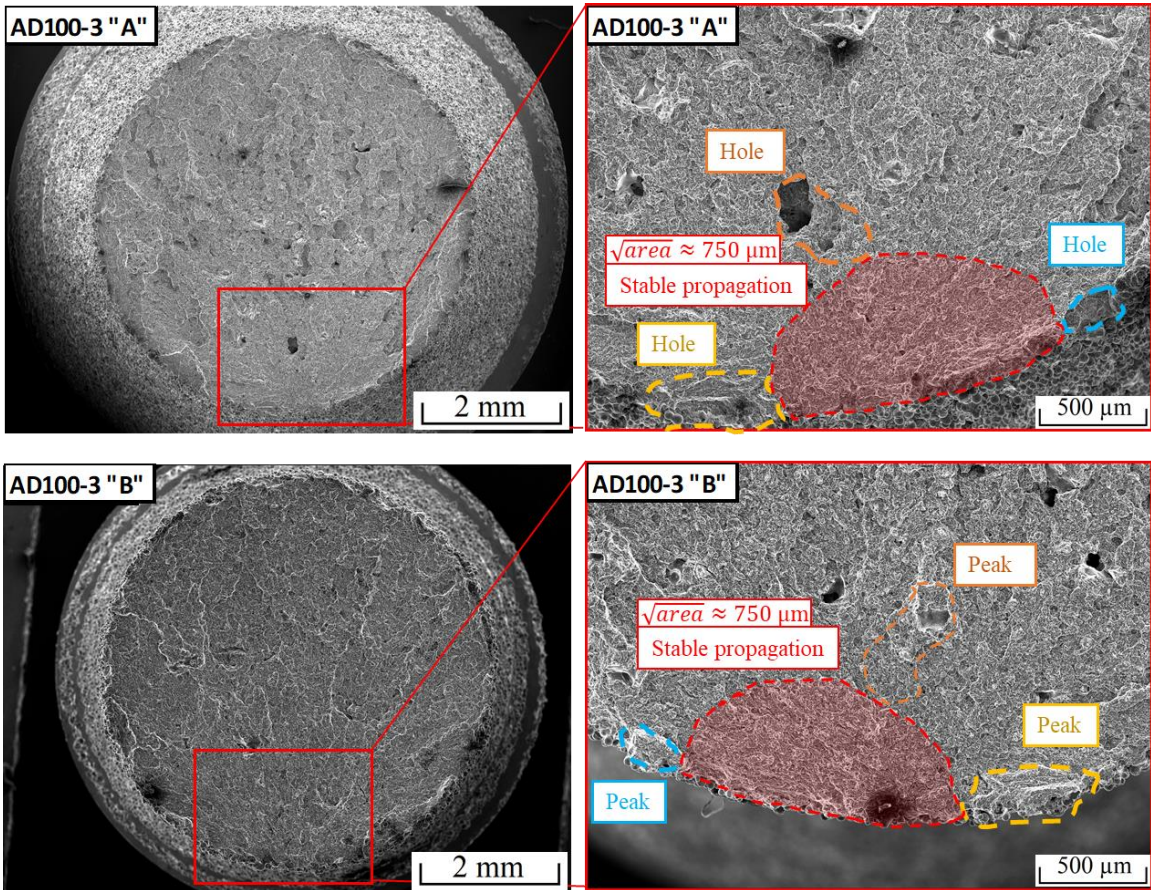


Fig. 4-6 Method to define the stable propagation area of the crack for a specimen where the drill hole is not the initiation point (non-damaged specimen), defined by fracture surface morphology.

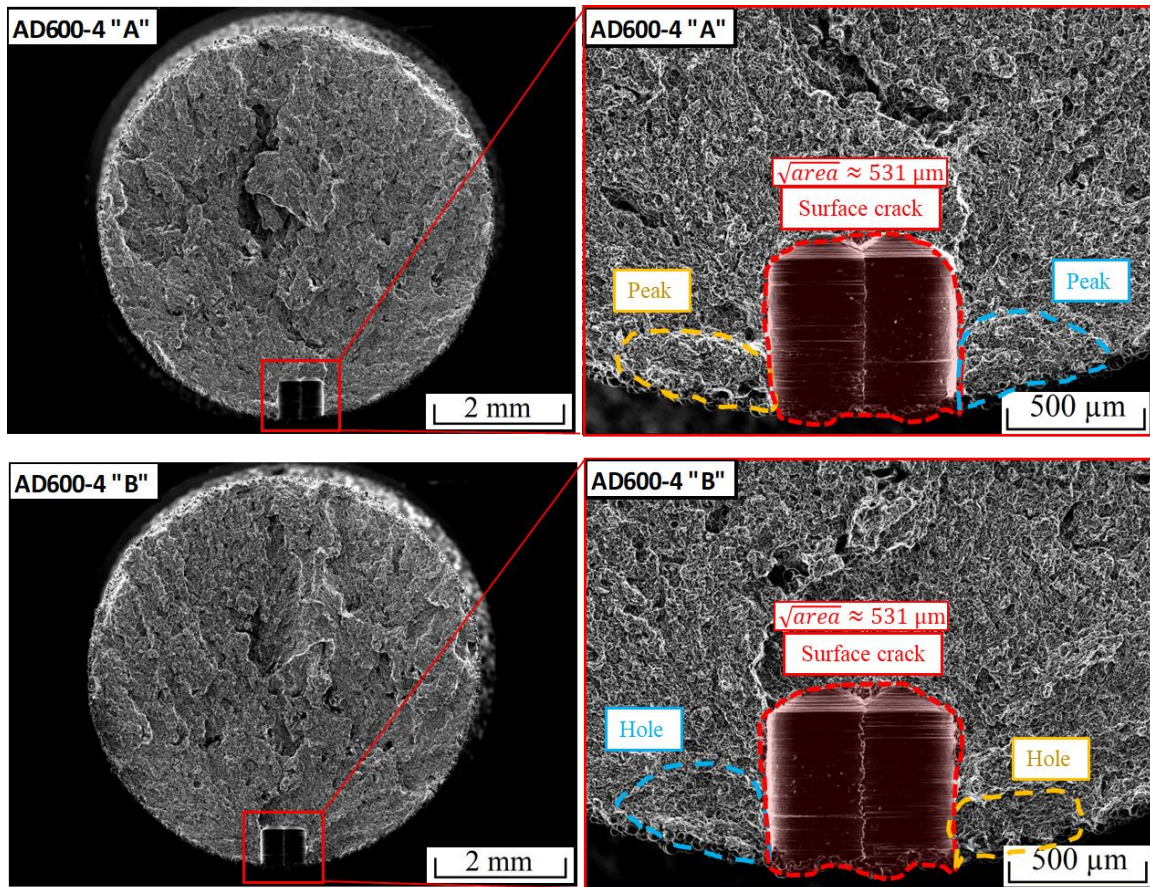


Fig. 4-7 Method to define the stable propagation area of the crack for a specimen where the drill hole is the initiation point, defined by fracture surface morphology.

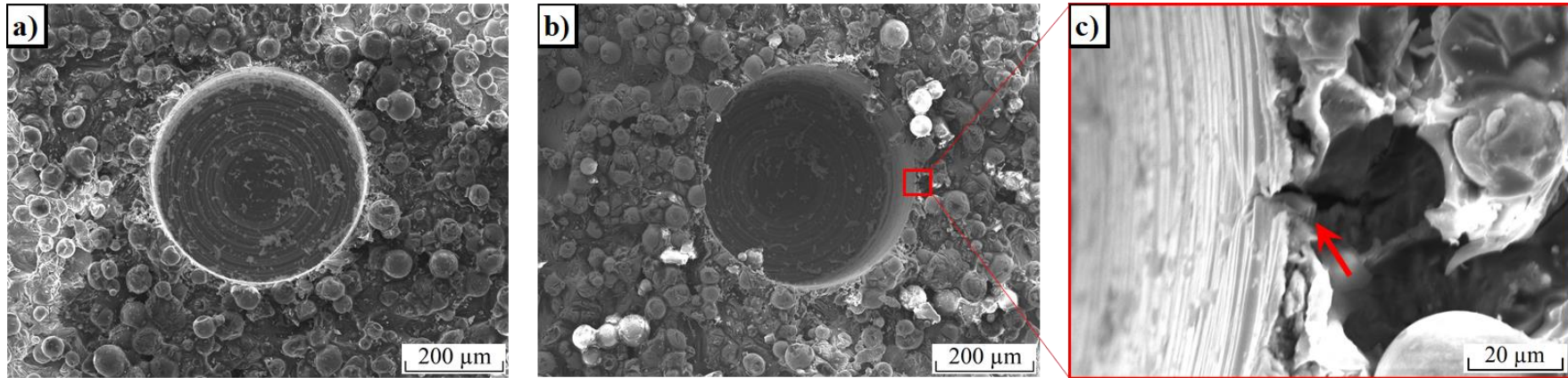


Fig. 4-8 SEM images of the 400 μm drill hole: a) before tensile testing; b) after load interruption at 80% of the UTS; and c) crack propagation from the drill hole.

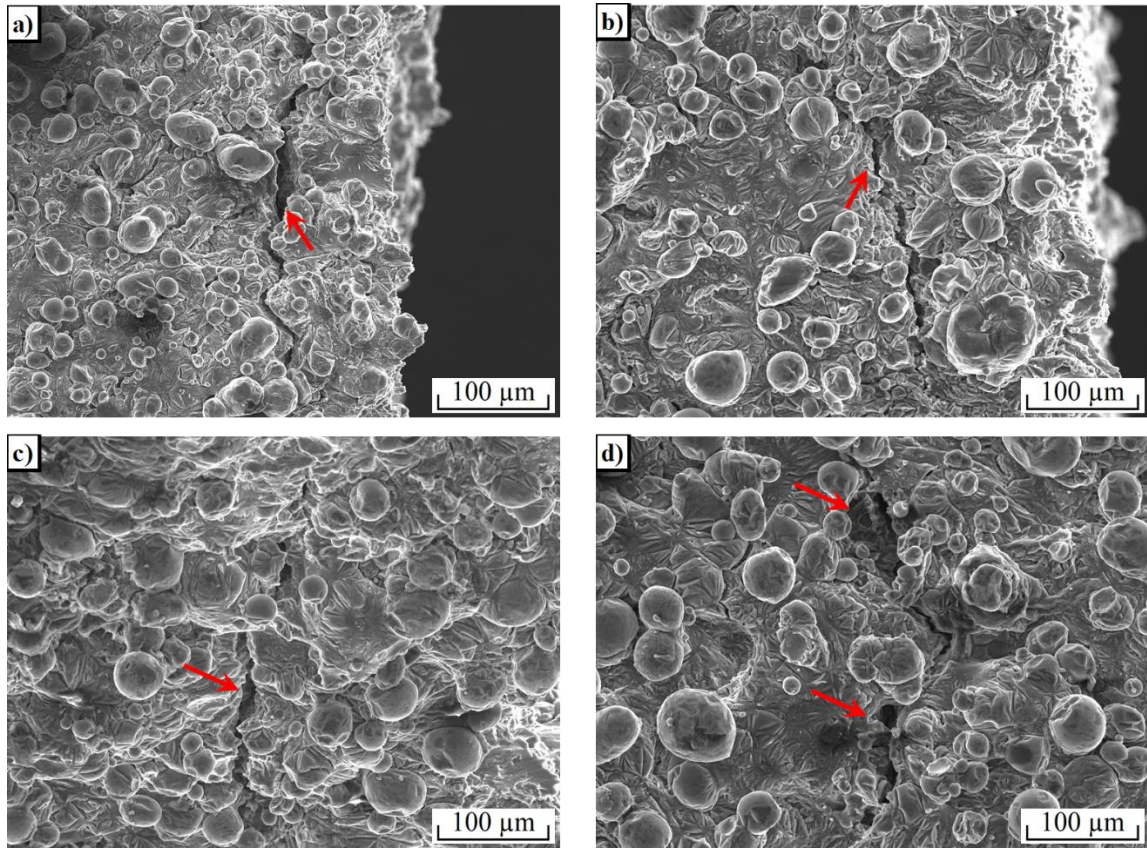


Fig. 4-9 SEM images of crack propagation evidence in: a) near the fracture surface of a 600 μm drill hole specimen; b) near the fracture surface of an 800 μm drill hole specimen; and c) and d) in the outer surface of the interrupted tensile test specimen besides the 400 μm drill hole.

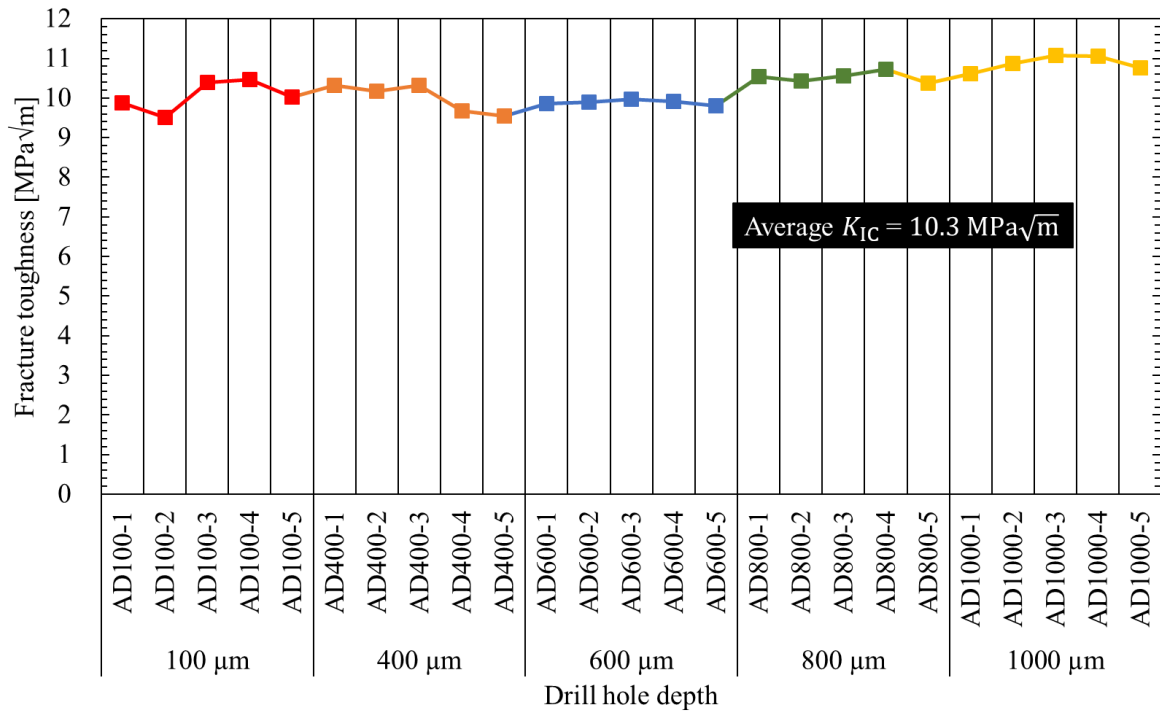


Fig. 4-10 Fracture toughness results for all the 6-mm round bar specimens with different drill hole sizes.

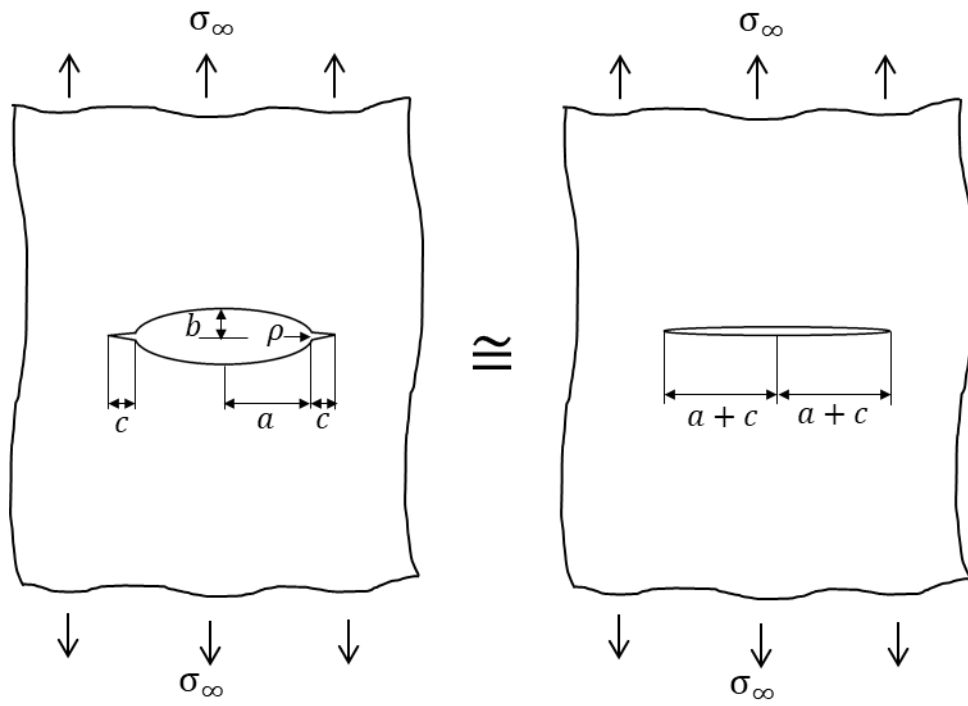


Fig. 4-11 Cracks emanating from an elliptical hole and its equivalent crack according to Murakami.

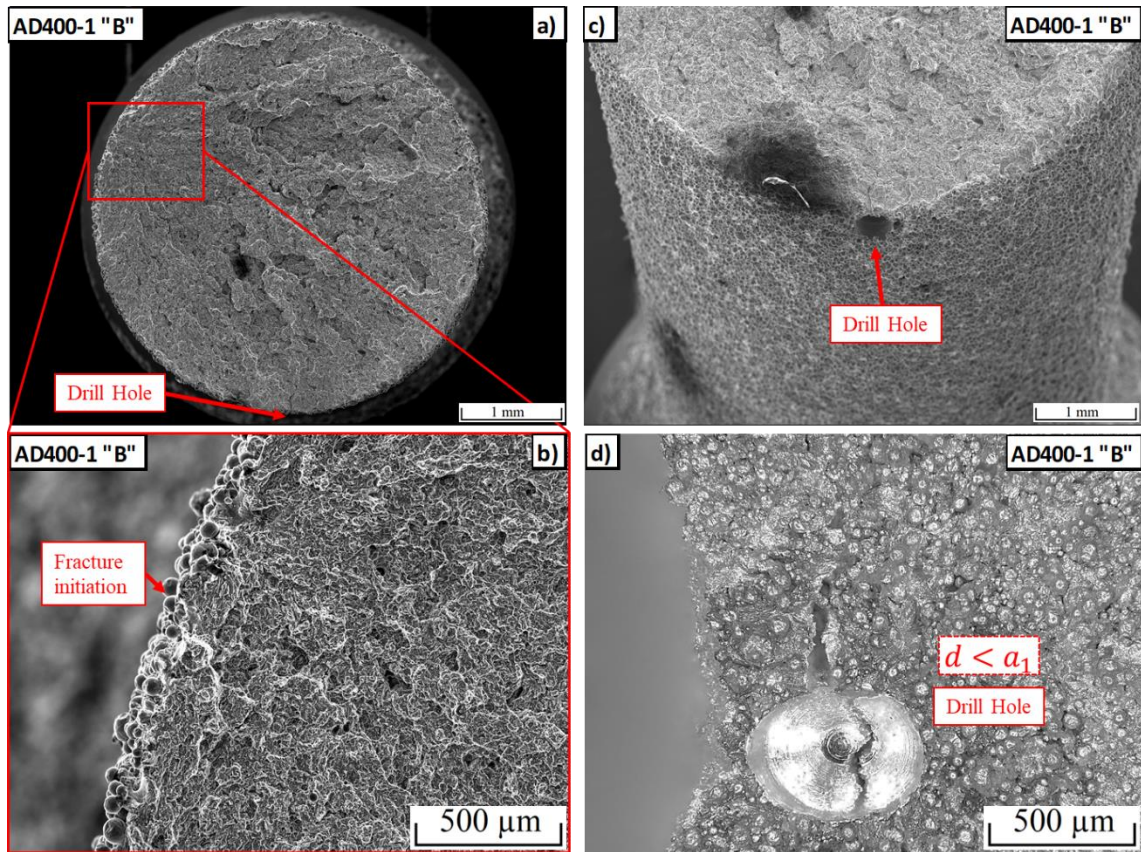


Fig. 4-12 Fracture surface of the AD400-1 specimen showing: a) SEM image of the fracture surface and the position of the 400 μm drill hole; b) SEM magnification of the fracture initiation point where no visible defects are present; c) SEM image of the surroundings of the fracture surface showing the position of the drill hole; and d) microscopical image of the drill hole after the specimen was fractured.

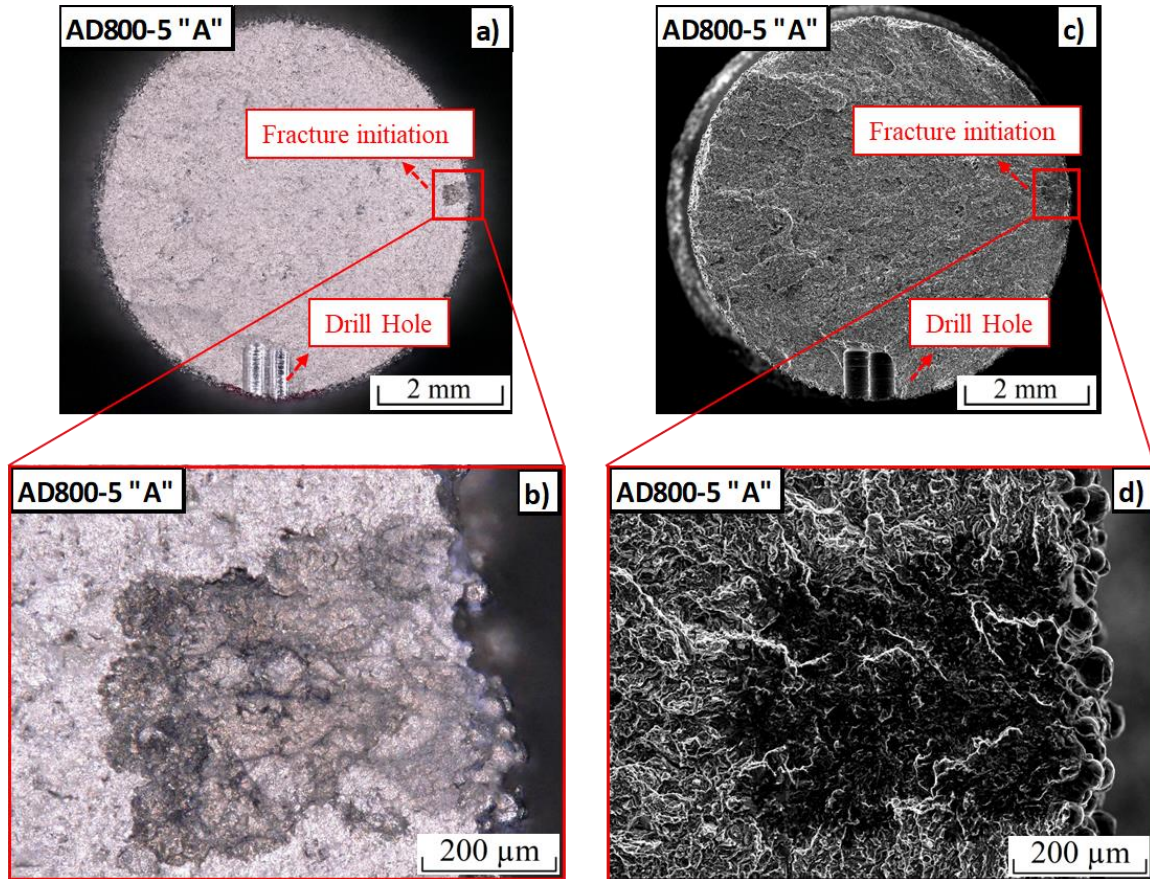


Fig. 4-13 Fracture surface of the AD800-5 showing: a) Microscopical image of the fracture surface showing the fracture initiation point and the microstructural defect; b) microscopical magnification of the microstructural defect; c) SEM image of the fracture surface showing the fracture initiation point and the microstructural defect; and d) SEM magnification of the microstructural defect.

CHAPTER 5.- MICROSTRUCTURE HOMOGENIZATION VIA HEAT TREATMENT: THE INFLUENCE OF ANNEALING IN SLM PRODUCTS

5.1 Introduction

In this chapter, the potential impact of post-processing in SLM products is considered. Since the largest stress concentration source responsible for fracture is attributed to microstructural changes between the outer surface and the inner body of SLM products in as-built conditions, it makes sense that the mechanical engineer would like to focus on the impact that heat treatments have on the microstructure and, consequentially, on the mechanical properties. In addition, owing to the intrinsic nature of melting and cooldown rates, heat treatments are also beneficial for relaxing the residual stresses, which are known to be high in SLM processes.

Although breakthrough innovations in processing resulted in a decrease of geometrical defects [1-4], the strength reliability of SLM products is low. This can be attributed partly to the fact that their mechanical properties are highly dependent on several parameters, such as the scanning speed, energy density, laser power, and scanning strategy [5, 6]. One of the most notable characteristics of SLM products is their non-homogeneous microstructure that results from the molten powder solidification process and the formation of a heat-affected zone during sintering [7, 8]. Furthermore, low cooling rates produce a soft and coarse microstructure that are located at the melt pool borders, whereas faster cooling rates induce a harder and finer microstructure concentrated toward the center of each melt pool [9], thereby inducing a microstructure duality intrinsic to the SLM process. Owing to the complexity of the microstructure under as-built conditions and the presence of residual stresses, some studies have analyzed the possibility of homogenization of the microstructure via heat treatment and/or machining [10-13]. However, it was proved through Chapters 2, 3, and 5 that the outer surface of

SLM products under as-built conditions is governed by the coarse microstructure owing to its proximity to the unmelted powder when solidification occurs. Consequently, under as-built conditions, a crack is initiated on the surface and propagated stably through the coarse microstructure, and the ductile crack propagation ceases at the boundary with the internal microstructure (a collection of melt pool formations consisting of coarse and fine microstructures). Because brittle fracture occurs with a subsequent increase in load, the fracture toughness value is an effective material strength characteristic that increases the reliability of the predicted ultimate tensile strength (UTS). However, the boundary between the surface and the internal microstructure is expected to disappear when heat treatment is performed. Therefore, the fracture process of heat-treated SLM products compared to that under as-built conditions and the effective strength evaluation parameter are yet to be clarified and consequently need further research attention. It is important to note that previous studies have analyzed the impact of a heat treatment in an SLM product [10, 14-18], and the changes and microstructure and mechanical properties have been noted. In particular, ductility increase and UTS decrease of the SLM product is a common result in the literature. However, the distinction between as-built and heat treated has not been brought into a sharp focus to date, specially from a plastic strain distribution point of view. Additionally, an indicator of when unstable fracture occurs in heat treated specimens has not been discussed yet.

It is common knowledge that a completely fractured piece would have undergone stable and unstable fractures [19, 20] before being separated into two parts. In principle, when a particular specimen presents a larger stable fracture region on the fracture surface than another specimen, the latter is considered more ductile. Therefore, the fracture surface of a heat-treated specimen should have a larger stable fracture region than that of a specimen under as-built conditions, as shown in the previous images of the fracture surfaces. Furthermore, the depth at which the stable propagation of the crack is interrupted is considered an intrinsic defect of the SLM process, thereby determining the precise point at which a stable fracture will transition into an unstable fracture even before stresses are loaded. However, because the microstructure gets homogenized when subjected to heat-treatment, the plastic strain is expected to continue propagation until the stable fracture transitions into an unstable fracture at some point. Consequently, the plastic strain and

crack propagation mechanisms are different between as-built and heat-treated specimens, and their validity while using traditional fracture mechanics remains to be explained. For instance, if stable crack propagation in a heat-treated specimen is no longer interrupted by different microstructural regions, the concept of energy release at the crack front during stable propagation until plastic instability is achieved can be easily explained by the R-curve.

For this study three 6-mm-diameter and 50-mm-long round bar specimens and three 6-mm-side length cubic specimens were fabricated by SLM process. Two round bar specimens and two cubic specimens were subjected to heat treatment at different temperatures for varying durations. All the round bar specimens were subjected to tensile testing while the fracture surfaces were observed closely, and the stable fracture regions were identified. Subsequently, the specimens were cut into adjacent planes for electron backscatter diffraction (EBSD) analysis. All cubic specimens were subjected to microstructural observations, and plastic strain manifestation was observed as dislocation accumulation under the as-built conditions and after heat treatment. Therefore, a crack propagation mechanism could be determined, and a clear explanation for the stress-strain (S–S) curve behavior for both scenarios could be obtained from a fracture mechanics perspective.

5.2 Experimental procedure

The raw material was AZX912 Mg alloy powder with the same composition as in Table 1-1. The particle size distributions were the same as shown in Section 1.4. Laser irradiation parameters are shown in Table 2-1. The round bar and cubic specimens were carried out using the EOS M100 SLM machine shown in Fig. 2-1, and the printing strategy shown in Fig. 2-2. Fig. 5-1 shows the geometry of the round bar tensile test specimens with a 6 mm diameter and 50 mm length and the cubic specimens with 6 mm side lengths: three specimens of each geometry were fabricated. In addition, a contour parameter with the same laser power and scan speed as listed in Table 2-1 was performed for increased surface quality. Besides, flat specimens were not considered because of the presence of high residual stresses and the low ultimate strength values, which often result in cracking after processing.

The annealing heat treatment strategy was selected for the analysis, considering its effects on residual stresses and low impact on the microstructure change rate [11, 21, 22], which was performed in a Koyo KBF1150°C box furnace. One pair of specimens consisting of a round bar and a cubic specimen remained under the as-built condition; another pair of specimens was annealed at 250°C for 3 h, and the last pair was annealed at 350°C for 10 h. The specimens were inserted into the heat-treatment furnace after it was preheated to the desired temperature, and the specimens were left inside the furnace until the predetermined treatment time was completed and allowed to cool gradually to a room temperature range of 21-22°C. Fig. 5-2 shows the annealing temperature-time diagrams. Surface roughness of the tensile test specimen in as-built conditions and the specimen annealed at 350°C for 10 h was measured using a LEXT OLS4500 Nano Search Microscope. Micro-hardness testing was performed using an HMV-FA Series Shimadzu Micro-Hardness Tester at a force of 10 g.

Tensile tests were performed using a Shimadzu AG-50kNXD universal electromechanical testing machine set at a strain rate of 0.0011 s^{-1} in conformance with the Japanese Industrial Standard JIS Z 2241:2011 (Method of Tensile Test for Metallic Materials). Tensile testing was performed along the building direction of the round-bar specimens at a room temperature range of 21-22°C. All tests were performed using a screw-type grip set with spherical bearings to ensure that no misalignment or bending occurred during testing. Elongation was measured using a Shimadzu SG25-100 extensometer with a gauge length of 25 mm. Scanning electron microscopy (SEM) and EBSD analyses were performed on a Hitachi High-Tech Low Vacuum Analysis SU6600 machine. The fractured parts of the specimens selected for observation were cut in horizontal and longitudinal cross-sections, and their inner surfaces were polished until a diamond-finish fineness was obtained. The cut surfaces were polished mechanically using an ion milling machine to obtain a mirror-finish surface with a Hitachi High-Tech IM-3000 machine at 2 kV.

For microstructure observation, the specimens were mirror-polished using the emery papers up to P4000 and a final pass with $0.2 \mu\text{m}$ fumed silica. To obtain clear images, the specimens were etched using an oxalate aqueous solution (oxalate: 0.1 g and distilled water: 100 ml). Macroscopic and microscopic solidification structures were observed

using an optical microscope and field-emission SEM with an acceleration voltage of 15 kV.

5.3 Results

5.3.1 Surface roughness and microstructure observation

Surface roughness was measured along four scanned areas inside the gauge length of both the tensile test specimen in as-built conditions and the specimen annealed at 350 °C for 10 h. The scanned areas for surface measurement were carried out in a 400 x 400 μm area with a 2 μm resolution and a pitch of 60 nm. The average roughness value was $R_a = 13.9 \mu\text{m}$ for the specimen in as-built conditions and $R_a = 13.5 \mu\text{m}$ for the annealed specimen, showing that the annealing had no effect in the surface roughness.

Figs. 5-3 and 5-4 show the microstructure observation results, Fig. 5-3 shows the melt pools in the specimen center, and Fig. 5-4 shows the coarse microstructure near the specimen's outer surface. Figs. 5-3 (a) and (b) show that the internal microstructure is a collection of melt pool formations, and the melt pool consists of a mostly fine microstructure with a coarse microstructure surrounding it. Fig. 5-3 shows the microstructural changes that occurred at different annealing parameters as observed using an optical microscope, while Fig. 5-4 shows the microstructural changes at different annealing parameters as observed using the SEM. The microstructures of as-built specimens and specimens that were subjected to annealing at 250°C for 3 h were similar, whereas images of specimens that were subjected to annealing at 350°C for 10 h showed a dissipated melt pool border, owing to the coarsening of the microstructure due to the recovery and recrystallization of the annealing process. The melt pool boundaries were still visible, whereas the columnar dendrites had almost completely disappeared. These results are compatible with those obtained in previous studies that analyzed the effects of annealing on the microstructure [23].

5.3.2 Micro-hardness results

Several microhardness measurements were performed at 10 g force at the center and boundaries of the melt pool formations for the following three conditions: as-built, annealing at 250°C for 3 h, and annealing at 350°C for 10 h. A schematic of the

measurement setup is shown in Fig. 5-5. Under the as-built condition, the average hardness of the melt pool center (fine microstructure) was 116 *HV* and that at the melt pool boundaries (coarse microstructure) was 84 *HV*. Further, the microhardness results for the specimen annealed at 250°C for 3 h presented similar average results with 112 *HV* for the melt pool center and 83 *HV* for the melt pool boundaries. It is important to note that the micro-hardness results for the as-built specimen and the specimen annealed at 250°C for 3 h are identical. This result was expected since the SEM images of the in Fig. 5-4 do not show any particular change of the microstructure. On the other hand, the microhardness results for the specimen annealed at 350°C for 10 h presented an average hardness of 75 *HV* at the melt pool center and 66 *HV* at the melt pool boundaries. The micro-hardness results of the specimen annealed at 350°C for 10 h does not only decrease considerably, but the difference between melt pool border and center also tend to disappear, serving as strong evidence that the microstructure is homogenizing. The microhardness test results for all the above specimens are depicted in Fig. 5-6.

5.3.3 Tensile tests results

Tensile tests were performed to the three round bar specimens until fracture occurred, and the S–S diagrams of the fractured specimens are presented in Fig. 5-7. Although the specimens that were subjected to annealing at 250°C for 3 h had a slightly lower UTS value and a considerable decrease in elongation than that of the as-built specimens, the author concluded that their yield strength, UTS, and elongation values were within a similar range in comparison with the results obtained in the previous chapters. For example, there is a UTS and elongation variation in Figs. 2-5 and 3-5 within different diameters. Additionally, there is a variation in UTS and elongation within specimens in as-built conditions of the same diameter that will be analyzed in Chapter 7. Moreover, the microstructure observation and microhardness results were similar to those under the as-built conditions; hence, it can be concluded that annealing at 250°C for 3 h is still considered within the recovery stage for non-combustible Mg alloys, and therefore had a negligible impact on the specimens.

The fractured specimens under as-built conditions and those annealed at 250°C for 3 h yielded the following mean values: an ultimate strength of 343 MPa, a yield strength of

256 MPa (0.2% proof strength), and an elongation of 3.0%. These results are consistent with the results obtained in other previous studies that used similar alloys [10, 24].

The specimen annealed at 350°C for 10 h exhibited the following values: an ultimate strength of 311 MPa, a yield strength of 253 MPa (0.2% proof strength), and an elongation of 4.6%. The behavior of the S-S curve is consistent with that of the other studies where annealing and other heat treatments were performed on SLM products [10, 11, 21, 23].

5.3.4 Fractography results

The fracture surfaces of all fractured specimens were observed, and the fracture initiation points and stable fracture region limits were determined. All the fracture initiation points were located on the outer surface. This result is appropriate for as-built specimens and specimens annealed at 250°C for 3 h because of their association to the same fracture mechanism that was proposed in Fig. 3-12 in Chapter 3. Moreover, because the sintering parameters, equipment, and powder used for these specimens were the same, the coarse microstructure depth from the surface was approximately 600 μm as evaluated in section 2.3.2. Fig. 5-8 shows the size determination of a stable fracture, and the fractography of both fracture surfaces shows a peak-hole morphology where the fracture is unstable and a hole-hole morphology where the fracture is stable. Once the circumventing three peak-hole spots nearest to the fracture initiation point were found, a semicircle was drawn to identify a fair approximation of the stable fracture region. This procedure is also supported by Murakami's theory of a crack located on the outer surface of a round body [25], and the results are consistent with those of the other studies where the same principle was used [26, 27].

The same method was also used to determine the stable fracture region limits of the specimens that were annealed at 250°C for 3 h and 350°C for 10 h: the results are shown in Fig. 5-9. Significantly, the specimens that were annealed at 350°C for 10 h showed a considerably stretched stable fracture in comparison to the other fracture surfaces. A consistent result can also be attributed to the increased ductility and lower UTS of the S-S curve. Notably, the fracture starts from the outer surface, which can be attributed to the high surface roughness of the specimen.

Although some geometrical defects such as pores and lack-of-fusion could be

observed on the fracture surfaces, they are located outside the stable fracture region, and hence, neither influenced the fracture mechanism nor the mechanical properties of any specimen.

5.3.5 EBSD analysis

The fractured specimens were cut and molded for EBSD observations, as shown in Fig. 5-10. Because the objective of this study is to determine the different fracture processes of the specimens under as-built and annealed conditions, it is of significant interest to observe the manifestation of plastic strain near the fracture surface, particularly where the melt pool formations have a clear coarse and fine microstructure duality.

Figure 5-11 shows the polished surface of the as-built specimen. The EBSD mapping consists of SEM imaging, and the morphology of coarse and fine microstructures can be identified using image quality (IQ) maps; crystal orientation and twinning deformations can be detected via inverse pole figure (IPF) maps, and the plastic strain can be observed using kernel average misorientation (KAM) maps. Fig. 5-12 shows the same mapping results mentioned above for the specimen annealed at 350°C for 10 h.

5.4 Discussion

5.4.1 Impact of the microstructure homogenization on the fracture process

Traditionally, the heat treatment of materials produced through conventional manufacturing processes aims to alter the mechanical properties to fit a specific requirement with no particular focus on the microstructure. Several studies have followed the same pattern by analyzing either the macro- or microscopic properties of additively manufactured products. For example, Aboulkhair et al. demonstrated that a regular T6 heat treatment softens AlSi10Mg products fabricated by SLM instead of hardening them [10]; Prashanth et al. reported that SLM-fabricated AlSi12 materials softened and the microstructure coarsened when annealing was performed [28]. Furthermore, according to Baek et al., T6 heat treatment decreases the fatigue performance of SLM AlSi10Mg alloys, whereas direct aging heat treatment improves their mechanical properties [15]. The aforementioned information questions the necessity of the conventional heat treatments in SLM products and their impact on the fracture process, which this chapter will focus

on answering.

To narrow such focus, an annealing heat treatment was performed owing to its performance simplicity and because it is a common alternative to reduce residual stresses, a phenomenon that cannot be neglected during sintering because of its high laser energy input and phase change during the solidification of the melted powder. In Chapter 2, it was established that the coarse microstructure in the melt pool borders enabled the dispersion of the plastic strain when stresses were applied. This affirmation is reinforced by the micro-hardness measurement results shown in Fig. 5-6, where the hardness difference between the microstructure at the melt pool borders (83 *HV*) and the center (112 *HV*) under the as-built conditions is considered substantial. Consequently, the plastic strain demonstrates a selective formation mechanism owing to the intrinsic microstructure duality of SLM products, which encloses the plastic strain from melt pool to melt pool and can be observed in the KAM maps of Fig. 5-11. The microstructure results in Figs. 5-3, 5-4(e), and 5-4(f) confirm the dissipation of the melt pool borders after the annealing of the AZX912 Mg alloy at 350°C for 10 h, and they are composed of coarse microstructures (dendrites). It could be observed that the barrier, which disperses the plastic strain under as-built conditions is removed, thereby allowing the plastic strain to form between melt pools, as illustrated in the KAM maps in Fig. 5-12. This phenomenon is particularly important because the author has previously confirmed in Chapters 2 and 3 that microstructure duality is responsible for fracture initiation under as-built conditions. Moreover, the micro-hardness results of the annealed material depicted in Fig. 5-6 show a hardness decrease (70 *HV*) in both the melt pool borders and center; significantly, the substantial hardness difference between them has also disappeared, thereby reinforcing the appearance of a continuous, non-localized plastic strain after annealing.

To further increase the validity of this discussion, a continuous plastic strain consequent to microstructure homogenization, as opposed to a dispersed plastic strain, can be translated into higher ductility and reduced UTS value. These results are consistent with those of other studies and can be observed in the S-S curve results shown in Fig. 5-7 [10, 21, 23]. Additionally, the fracture surface of the annealed specimen showed a wider, more elongated region of stable fracture compared to the fracture surface of the as-built specimen, as shown in Fig. 5-9. In conclusion, the microstructure homogenization of

SLM products induces the homogenization of the plastic strain during the fracture process, thereby enhancing elongation.

5.4.2 The R curve alternative

Under as-built conditions, the microstructure duality induced an intrinsic defect known as the stable propagation area of the crack that is defined by the coarse microstructure distributed irregularly at the outer surface. The fracture process of the SLM products under as-built conditions involves a sudden crack propagation interruption when the coarse microstructure chunks on the outer surface finishes, and the distance between the outer surface and such an interruption can be considered as an invisible crack. Because crack length is a known variable and can be used in Murakami's Theory, the fracture toughness value is a critical parameter for predicting strength. Consequently, the mechanical properties of SLM products and their overall reliability under as-built conditions can be increased.

However, when the microstructure is homogenized by annealing, the crack propagation is not interrupted and Murakami's theory for strength prediction using the fracture toughness value is no longer valid. Therefore, a new parameter is required to determine the point at which unstable fractures occur in heat-treated specimens. To circumvent this problem, it is important to consider that the plastic strain during the fracture process of the annealed specimen is homogenous and satisfies small-scale yielding (SSY) conditions. When stresses are applied, a crack starts to propagate from the outer surface owing to the high surface roughness of SLM products. During crack propagation, on the one hand, energy is released from the crack tip, while on the other hand, the material resists crack growth. If the energy release rate, crack growth resistance, and crack growth length is denoted by φ , R , and Δa , respectively, the three sequential steps undergone by the fracture process can be described as follows. First, the crack is propagated stably at a steady φ . Thereafter, as the stresses increase further, the φ value tends to approximate the R value until the crack propagation reaches its critical state and ceases further propagation. Finally, when the condition $\varphi = R$ is satisfied, an unstable fracture occurs. Fig. 5-13 depicts the fracture process, for both the as-built as well as the after-annealing conditions, using the proposed energy criterion and the behavior of R ,

otherwise known as the R -curve. Importantly, the conditions under which the criterion $\varphi = R$ is satisfied depends on the critical energy release rate φ_C , and it can be drawn as a constant line for either plot in Fig. 5-13 that applies to all materials that are used for manufacturing SLM products and undergo the same heat treatment. For example, when compared to the annealed specimen, the φ_C of the specimens under as-built conditions (Fig. 5-13(a)) is slightly inclined to the left owing to the crack growth interruption of the coarse grain region on the outer surface and slightly increased microhardness, thereby causing a slight decrease in the Δa at which the unstable fracture occurs; this, in turn, decreases ductility but increases the UTS. The determination of the φ_C of SLM products subjected to different heat treatments can be established in future research studies on material testing. For instance, the annealing effect influences the microstructure mostly in hardness rather than grain size, as can be verified in the micro-hardness results shown in Fig. 5-6 and the IPF maps in Figs. 5-11 and 5-12. Therefore, besides microstructure homogenization, the SLM product that undergoes annealing can either become harder or softer depending on the annealing conditions [13]. Regardless of the change in overall hardness of the SLM product after annealing, the microstructure has been homogenized and the fracture mechanism shown in Fig. 5-13 (b) enables the use of traditional fracture mechanics. In that manner, annealed SLM products can be submitted to fracture toughness determination using standards such as ASTM E399, and then the critical energy release rate can be calculated by its relation to the fracture toughness given a two-dimensional loading mode in plain strain, and SSY conditions are satisfied under equation (4 – 1) [29]:

$$\varphi_C = \frac{K_{IC}^2}{E} (1 - \nu^2)$$

where φ_C is the critical energy release rate, K_{IC} is the fracture toughness, E is Young's Modulus and ν is the Poisson's ratio.

5.5 Conclusions

This chapter aims to determine the effects of annealing on the microstructure duality of SLM products and its influence on the plastic strain manifestation once tensile stresses are loaded. The findings of this study led to the following conclusions:

- Annealing coarsens the microstructure at the melt pool boundaries, dissipating the columnar dendrites and enabling dislocations to move freely once the crack starts to propagate stably. Consequently, the plastic deformation at the crack tip becomes large and homogeneous.
- The microstructure duality under the as-built conditions interrupts the stable crack propagation that originates from the outer surface. When annealing or, in principle, when any heat treatment is performed, the crack continues to propagate stably without interruption.
- The interruption of the stable propagation of the crack under as-built conditions disperses the plastic strain, which enables crack cessation and explains the high UTS value of SLM products compared to the heat-treated or casting counterparts. Conversely, heat treatment disables the interruption and allow crack propagation to continue stably in the specimens, thereby increasing the ductility. Additionally, the decrease in the micro-hardness enables the reduction of the ultimate strength.
- When annealing is performed, the critical energy release rate and the R curve could be a valid indicator for determining when unstable fracture will occur.

5.6 References

- [1] N.T. Aboulkhair, N.M. Everitt, I. Ashcroft, C. Tuck, Reducing porosity in AlSi10Mg parts processed by selective laser melting, *Additive Manufacturing*, 1-4 (2014) 77-86. <https://doi.org/10.1016/j.addma.2014.08.001>.
- [2] F. Klocke, C. Wagner, F. Klocke, Coalescence Behaviour of Two Metallic Particles as Base Mechanism of Selective Laser Sintering, *CIRP Annals*, 52 (2003) 177-180. [https://doi.org/10.1016/S0007-8506\(07\)60559-9](https://doi.org/10.1016/S0007-8506(07)60559-9).
- [3] M. Yakout, M.A. Elbestawi, S.C. Veldhuis, A study of thermal expansion coefficients and microstructure during selective laser melting of Invar 36 and stainless steel 316L, *Additive Manufacturing*, 24 (2018) 405-418. <https://doi.org/10.1016/j.addma.2018.09.035>.
- [4] G. Strano, L. Hao, R.M. Everson, K.E. Evans, Surface roughness analysis, modelling and prediction in selective laser melting, *Journal of Materials Processing Technology*, 213 (2013) 589-597. <https://doi.org/10.1016/j.jmatprotec.2012.11.011>.
- [5] W. Schneller, M. Leitner, S. Pomberger, F. Grün, S. Leuders, T. Pfeifer, O. Jantschner, Fatigue strength assessment of additively manufactured metallic structures considering

- bulk and surface layer characteristics, *Additive Manufacturing*, 40 (2021) 101930. <https://doi.org/10.1016/j.addma.2021.101930>.
- [6] T. Larimian, M. Kannan, D. Grzesiak, B. AlMangour, T. Borkar, Effect of energy density and scanning strategy on densification, microstructure and mechanical properties of 316L stainless steel processed via selective laser melting, *Materials Science and Engineering: A*, 770 (2020) 138455. <https://doi.org/10.1016/j.msea.2019.138455>.
- [7] J.P. Kruth, G. Levy, F. Klocke, T.H.C. Childs, Consolidation phenomena in laser and powder-bed based layered manufacturing, *CIRP Annals*, 56 (2007) 730-759. <https://doi.org/10.1016/j.cirp.2007.10.004>.
- [8] L. Thijs, F. Verhaeghe, T. Craeghs, J.V. Humbeeck, J.-P. Kruth, A study of the microstructural evolution during selective laser melting of Ti-6Al-4V, *Acta Materialia*, 58 (2010) 3303-3312. <https://doi.org/10.1016/j.actamat.2010.02.004>.
- [9] H.K. Rafi, N.V. Karthik, H. Gong, T.L. Starr, B.E. Stucker, Microstructures and Mechanical Properties of Ti6Al4V Parts Fabricated by Selective Laser Melting and Electron Beam Melting, *Journal of Materials Engineering and Performance*, 22 (2013) 3872-3883. [10.1007/s11665-013-0658-0](https://doi.org/10.1007/s11665-013-0658-0).
- [10] N.T. Aboulkhair, I. Maskery, C. Tuck, I. Ashcroft, N.M. Everitt, The microstructure and mechanical properties of selectively laser melted AlSi10Mg: The effect of a conventional T6-like heat treatment, *Materials Science and Engineering: A*, 667 (2016) 139-146. <https://doi.org/10.1016/j.msea.2016.04.092>.
- [11] B. Vrancken, L. Thijs, J.-P. Kruth, J. Van Humbeeck, Heat treatment of Ti6Al4V produced by Selective Laser Melting: Microstructure and mechanical properties, *Journal of Alloys and Compounds*, 541 (2012) 177-185. <https://doi.org/10.1016/j.jallcom.2012.07.022>.
- [12] V. Cain, L. Thijs, J. Humbeeck, B. Hooreweder, R. Knutsen, Crack propagation and fracture toughness of Ti6Al4 V alloy produced by selective laser melting, 5 (2014) 68-76. [10.1016/j.addma.2014.12.006](https://doi.org/10.1016/j.addma.2014.12.006).
- [13] J. Fiochi, A. Tuissi, P. Bassani, C.A. Biffi, Low temperature annealing dedicated to AlSi10Mg selective laser melting products, *Journal of Alloys and Compounds*, 695 (2017) 3402-3409. <https://doi.org/10.1016/j.jallcom.2016.12.019>.
- [14] F. Alghamdi, X. Song, A. Hadadzadeh, B. Shalchi-Amirkhiz, M. Mohammadi, M. Haghshenas, Post heat treatment of additive manufactured AlSi10Mg: On silicon morphology, texture and small-scale properties, *Materials Science and Engineering: A*, 783 (2020) 139296. <https://doi.org/10.1016/j.msea.2020.139296>.
- [15] M.-S. Baek, R. Kreethi, T.-H. Park, Y. Sohn, K.-A. Lee, Influence of heat treatment

- on the high-cycle fatigue properties and fatigue damage mechanism of selective laser melted AlSi10Mg alloy, *Materials Science and Engineering: A*, 819 (2021) 141486. <https://doi.org/10.1016/j.msea.2021.141486>.
- [16] M. Deng, H.-z. Li, S.-N. Tang, H.-J. Liao, X.-p. Liang, R.-M. Liu, Effect of Heat Treatment on Fracture Toughness of As-Forged AZ80 Magnesium Alloy, *Journal of Materials Engineering and Performance*, 24 (2015) 1953-1960. [10.1007/s11665-015-1490-5](https://doi.org/10.1007/s11665-015-1490-5).
- [17] L. Girelli, M. Tocci, M. Gelfi, A. Pola, Study of heat treatment parameters for additively manufactured AlSi10Mg in comparison with corresponding cast alloy, *Materials Science and Engineering: A*, 739 (2019) 317-328. <https://doi.org/10.1016/j.msea.2018.10.026>.
- [18] W. Li, S. Li, J. Liu, A. Zhang, Y. Zhou, Q. Wei, C. Yan, Y. Shi, Effect of heat treatment on AlSi10Mg alloy fabricated by selective laser melting: Microstructure evolution, mechanical properties and fracture mechanism, *Materials Science and Engineering: A*, 663 (2016) 116-125. <https://doi.org/10.1016/j.msea.2016.03.088>.
- [19] V. Tvergaard, J.W. Hutchinson, The relation between crack growth resistance and fracture process parameters in elastic-plastic solids, *Journal of the Mechanics and Physics of Solids*, 40 (1992) 1377-1397. [https://doi.org/10.1016/0022-5096\(92\)90020-3](https://doi.org/10.1016/0022-5096(92)90020-3).
- [20] S. Morel, E. Bouchaud, J. Schmittbuhl, G. Valentin, R-curve behavior and roughness development of fracture surfaces, *International Journal of Fracture*, 114 (2002) 307-325. [10.1023/A:1015727911242](https://doi.org/10.1023/A:1015727911242).
- [21] P. Ma, K.G. Prashanth, S. Scudino, Y. Jia, H. Wang, C. Zou, Z. Wei, J. Eckert, Influence of Annealing on Mechanical Properties of Al-20Si Processed by Selective Laser Melting, *Metals*, 4 (2014). [10.3390/met4010028](https://doi.org/10.3390/met4010028).
- [22] L.F. Wang, J. Sun, X.L. Yu, Y. Shi, X.G. Zhu, L.Y. Cheng, H.H. Liang, B. Yan, L.J. Guo, Enhancement in mechanical properties of selectively laser-melted AlSi10Mg aluminum alloys by T6-like heat treatment, *Materials Science and Engineering: A*, 734 (2018) 299-310. <https://doi.org/10.1016/j.msea.2018.07.103>.
- [23] M. Wang, B. Song, Q. Wei, Y. Zhang, Y. Shi, Effects of annealing on the microstructure and mechanical properties of selective laser melted AlSi7Mg alloy, *Materials Science and Engineering: A*, 739 (2018). [10.1016/j.msea.2018.10.047](https://doi.org/10.1016/j.msea.2018.10.047).
- [24] Z. Dong, X. Zhang, W. Shi, H. Zhou, H. Lei, J. Liang, Study of Size Effect on Microstructure and Mechanical Properties of AlSi10Mg Samples Made by Selective Laser Melting, *Materials (Basel)*, 11 (2018) 2463. [10.3390/ma11122463](https://doi.org/10.3390/ma11122463).
- [25] Y. Murakami, Analysis of stress intensity factors of modes I, II and III for inclined

- surface cracks of arbitrary shape, *Engineering Fracture Mechanics*, 22 (1985) 101-114. [https://doi.org/10.1016/0013-7944\(85\)90163-8](https://doi.org/10.1016/0013-7944(85)90163-8).
- [26] H. Masuo, Y. Tanaka, S. Morokoshi, H. Yagura, T. Uchida, Y. Yamamoto, Y. Murakami, Effects of Defects, Surface Roughness and HIP on Fatigue Strength of Ti-6Al-4V manufactured by Additive Manufacturing, *Procedia Structural Integrity*, 7 (2017) 19-26. <https://doi.org/10.1016/j.prostr.2017.11.055>.
- [27] Y. Yamashita, T. Murakami, R. Mihara, M. Okada, Y. Murakami, Defect Analysis and Fatigue Design Basis for Ni-based Superalloy 718 manufactured by Additive Manufacturing, *Procedia Structural Integrity*, 7 (2017) 11-18. <https://doi.org/10.1016/j.prostr.2017.11.054>.
- [28] K.G. Prashanth, S. Scudino, H.J. Klauss, K.B. Surreddi, L. Löber, Z. Wang, A.K. Chaubey, U. Kühn, J. Eckert, Microstructure and mechanical properties of Al-12Si produced by selective laser melting: Effect of heat treatment, *Materials Science and Engineering: A*, 590 (2014) 153-160. <https://doi.org/10.1016/j.msea.2013.10.023>.
- [29] G.C. Sih, B. Macdonald, Fracture mechanics applied to engineering problems-strain energy density fracture criterion, *Engineering Fracture Mechanics*, 6 (1974) 361-386. [https://doi.org/10.1016/0013-7944\(74\)90033-2](https://doi.org/10.1016/0013-7944(74)90033-2).

5.7 List of figures

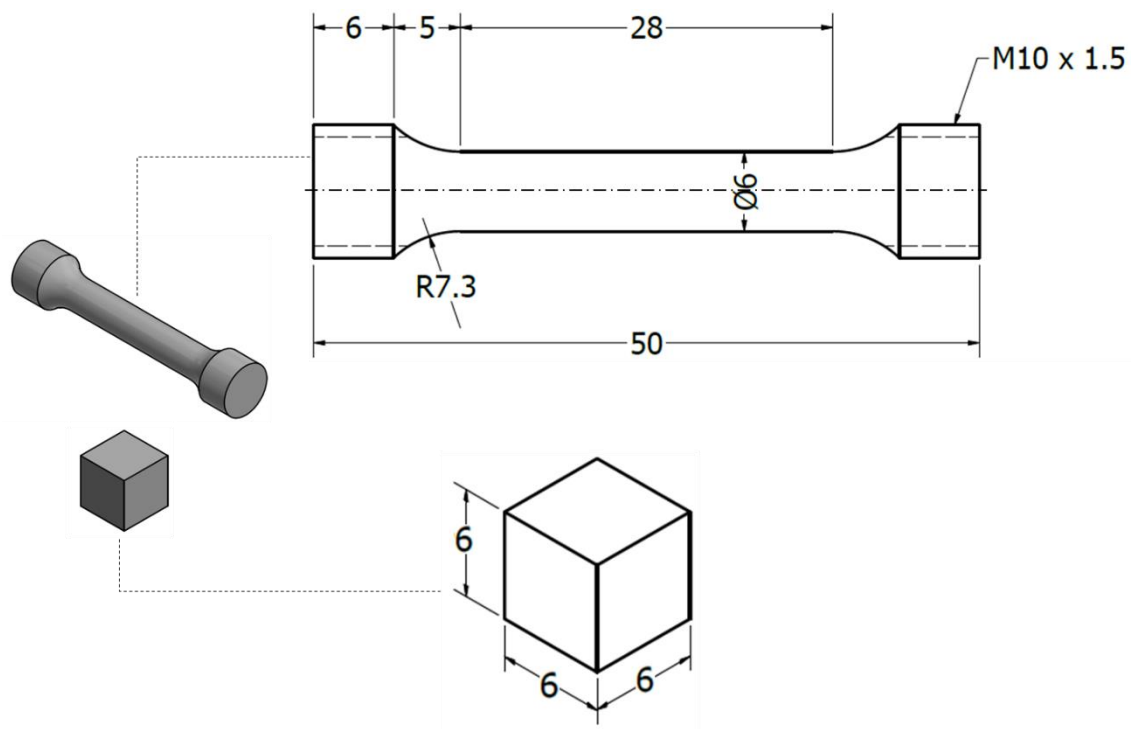


Fig. 5-1 Shapes and dimensions for the tensile test and cubic specimens (Unit: mm).

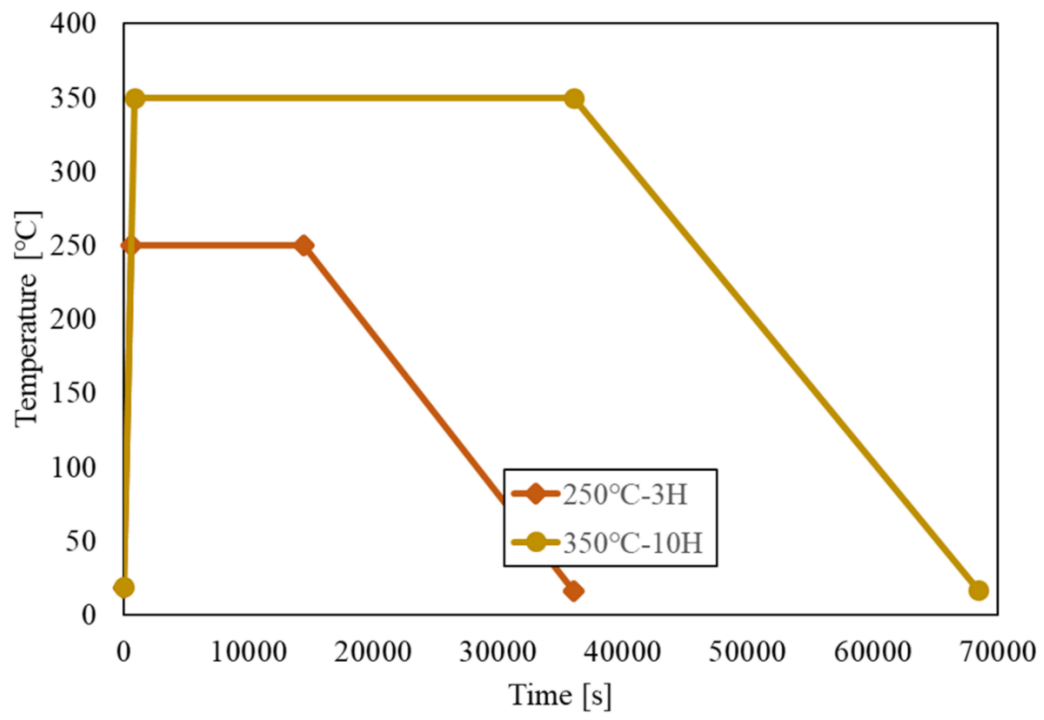


Fig. 5-2 Temperature-Time (T-T) diagram of the annealing process.

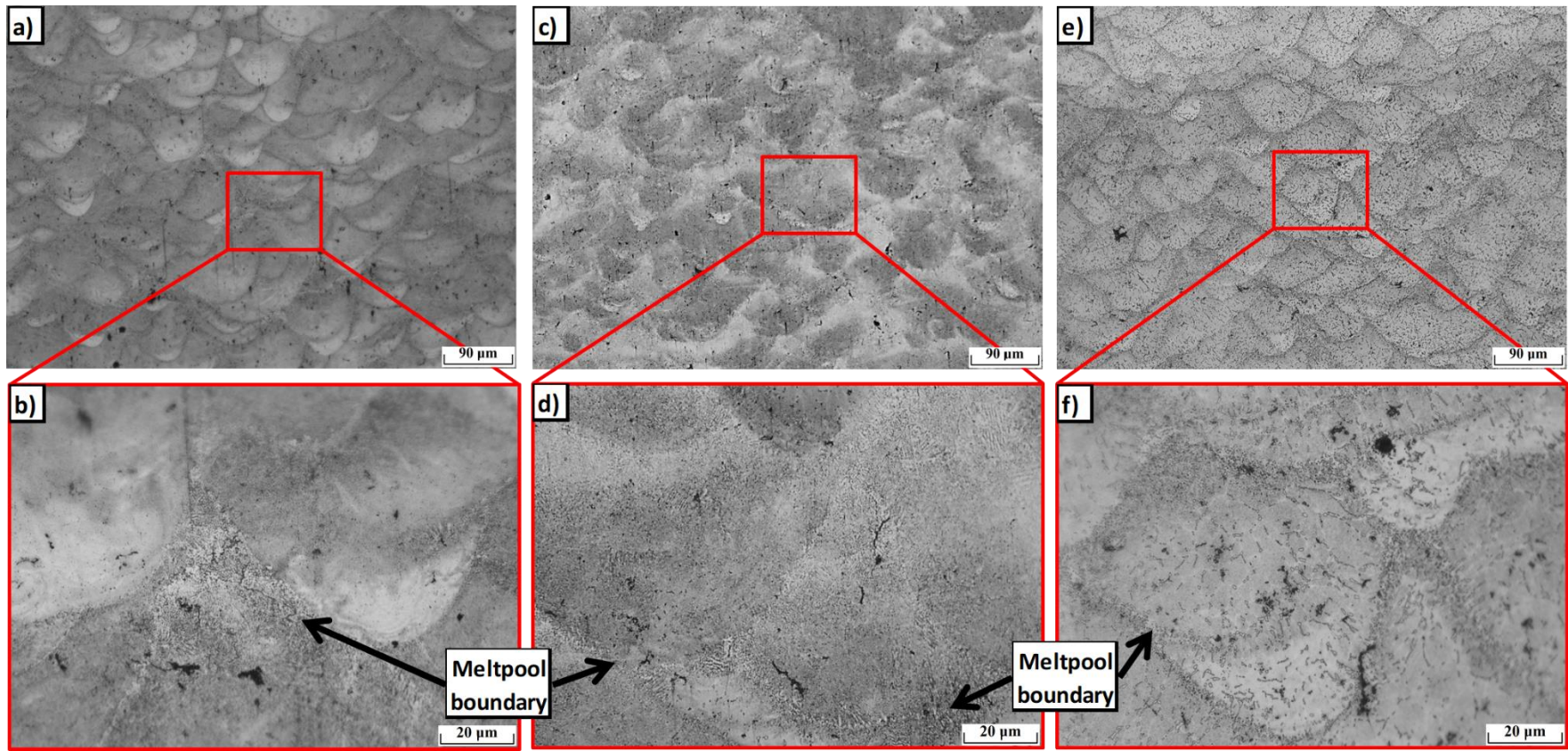


Fig. 5-3 Optical microscope images of the microstructure: a), b) in as-built conditions; c), d) after annealing at 250°C-3 h; e), f) after annealing at 350°C-10 h.

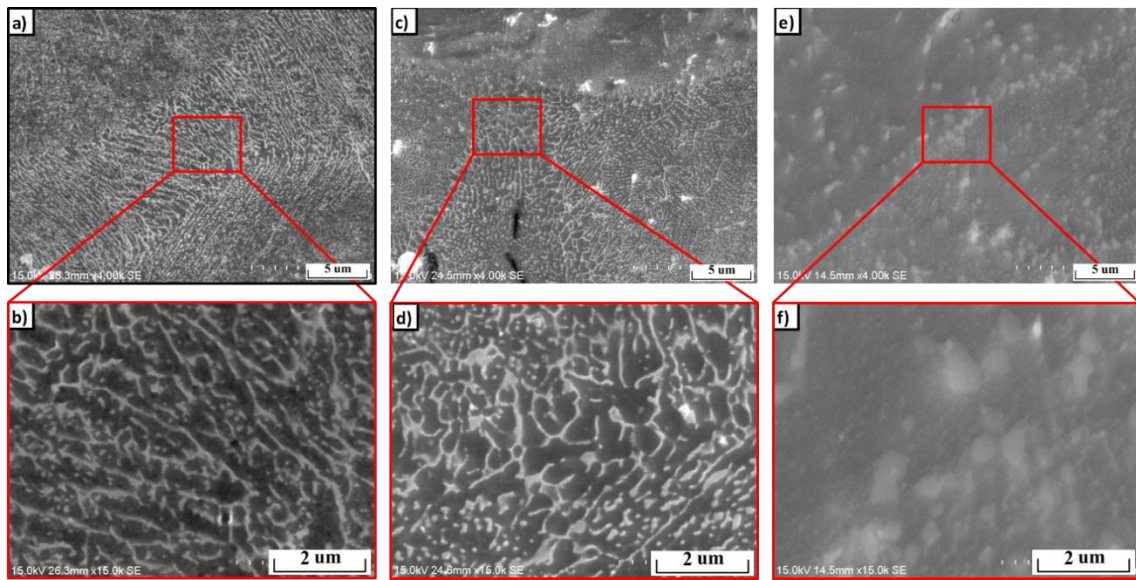


Fig. 5-4 SEM images of the microstructure: a), b) in as-built conditions; c), d) after annealing at 250°C-3 h; e), f) after annealing at 350°C-10 h.

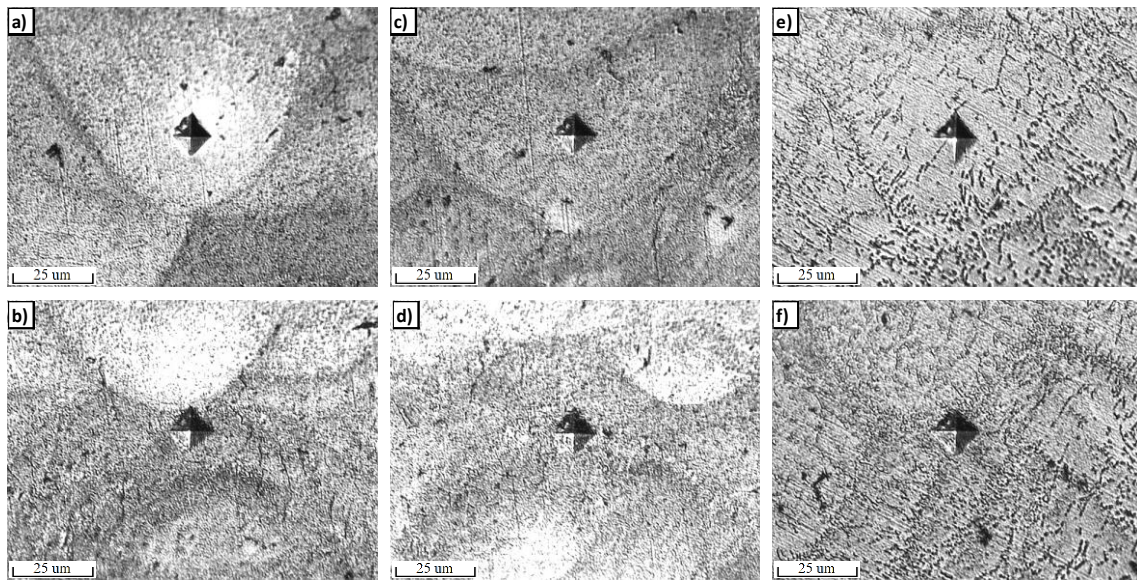


Fig. 5-5 Representative images of the micro-hardness indentation measurements: a), b) in as-built conditions; c), d) after annealing at 250°C-3 h; e), f) after annealing at 350°C-10 h.

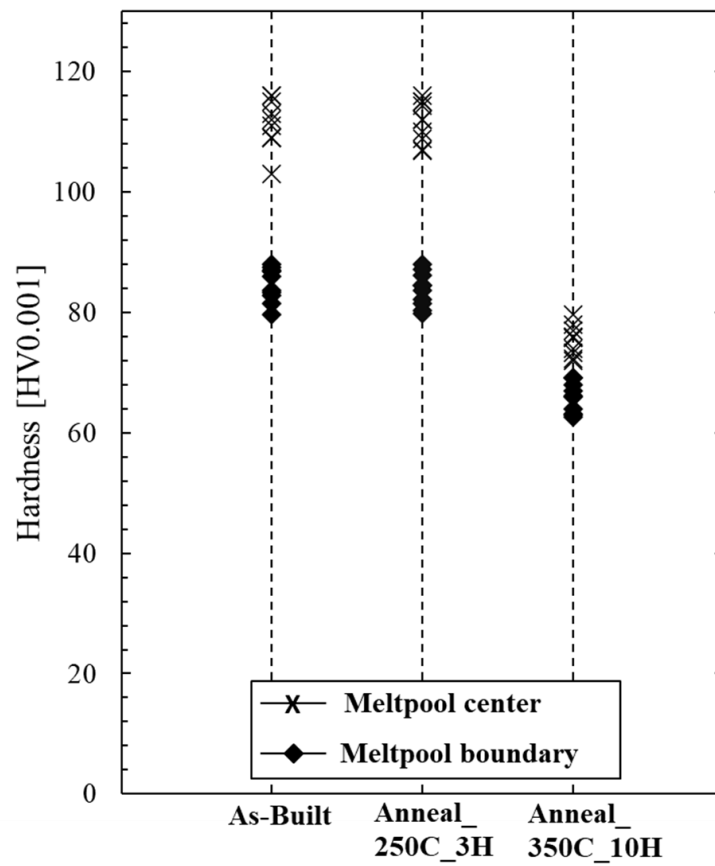


Fig. 5-6 Micro-hardness results of all the specimens.

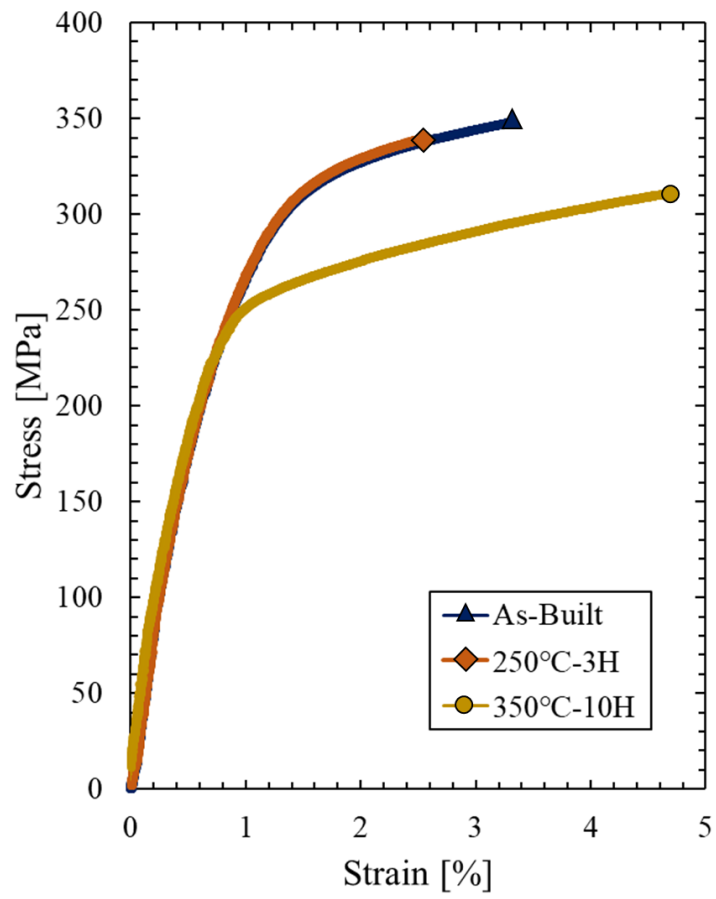


Fig. 5-7 Stress-strain diagrams for all the fractured specimens.

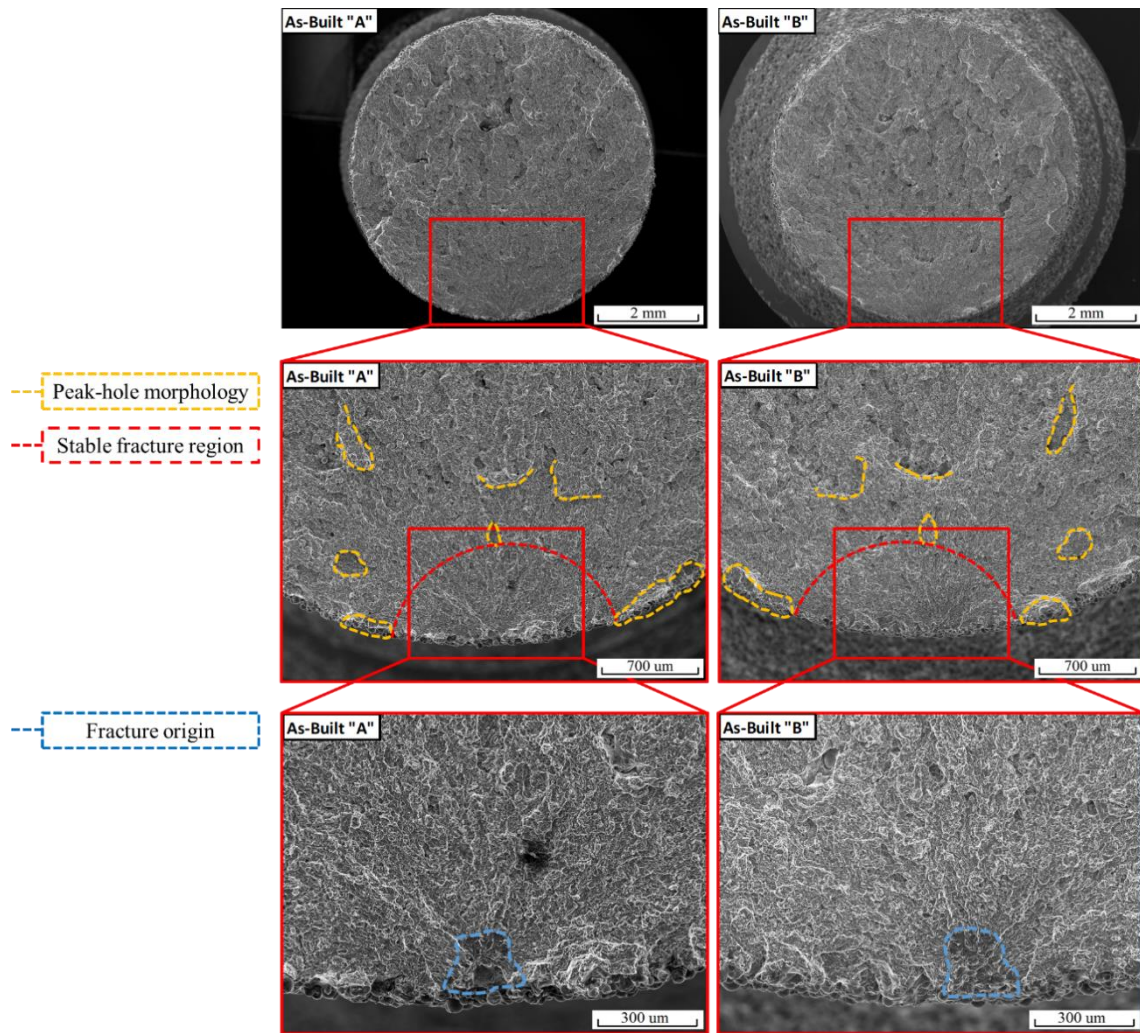


Fig. 5-8 SEM images of the fracture surfaces of the fractured parts of the specimen showing: fracture initiation point (blue dashed line); peak-hole morphology of unstable fracture (orange dashed line); definition of the stable fracture region (red dashed line).

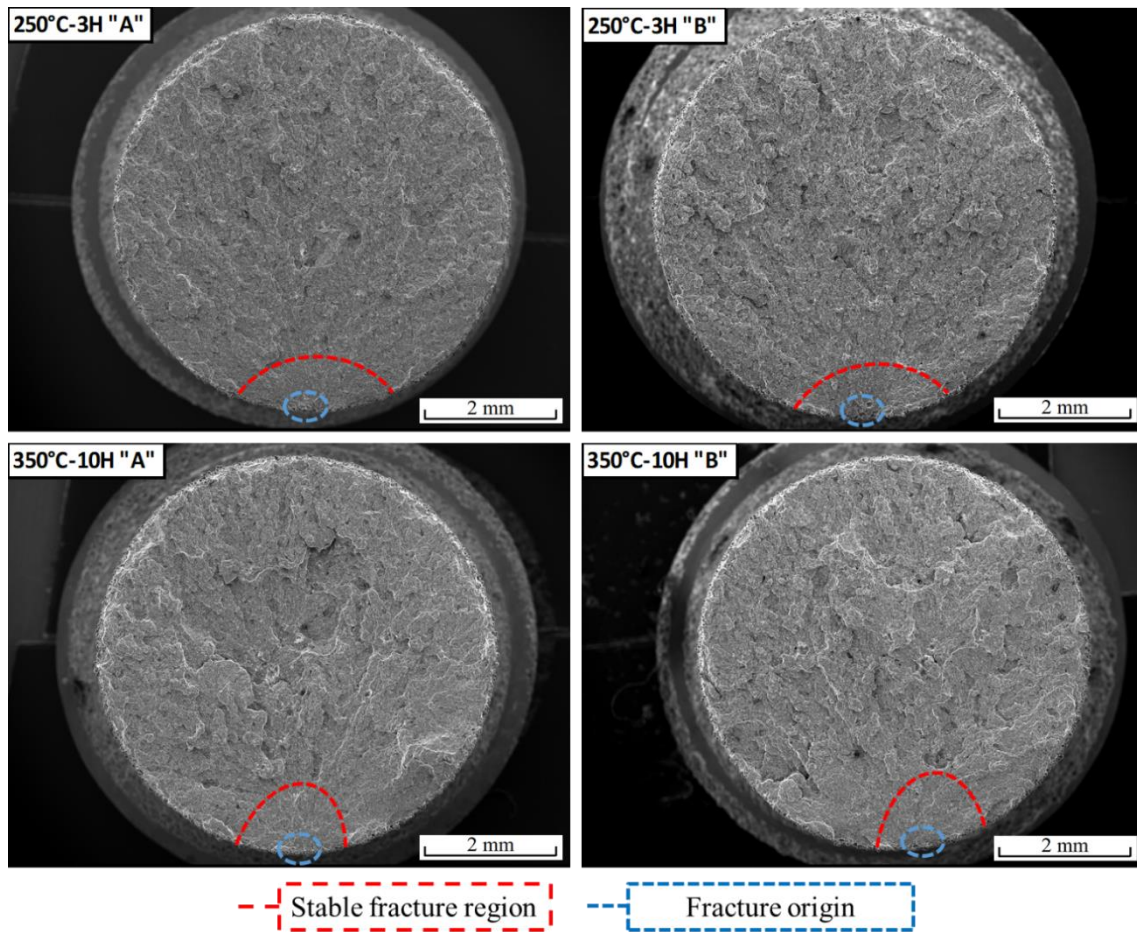


Fig. 5-9 SEM images of the fracture surfaces from the remaining fractured specimens showing the approximate stable fracture region (red dashed line) and the fracture initiation point (blue dashed line). Determination method was the same as that shown in

Fig. 5-8.

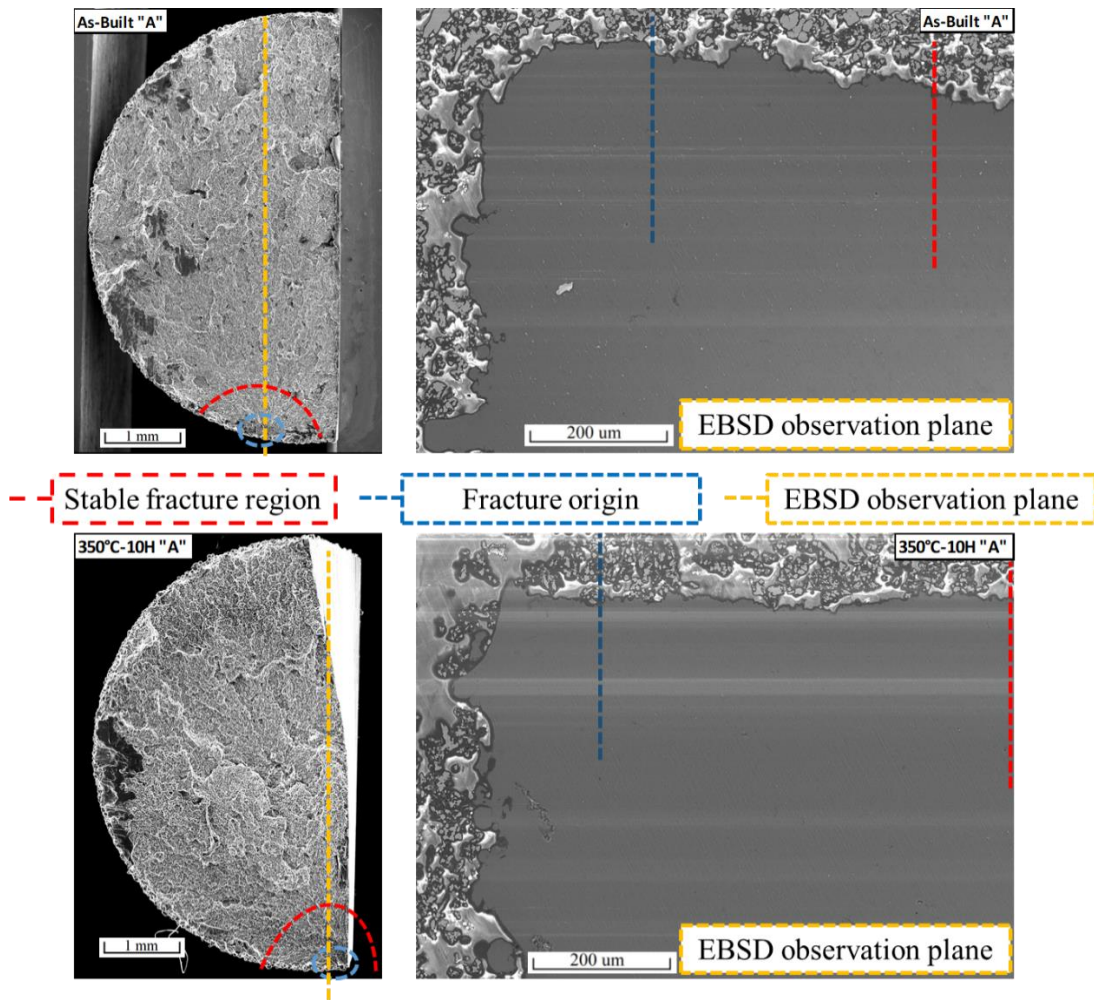


Fig. 5-10 SEM images of the cut and polished fractured specimens for EBSD observation of the specimen in as-built conditions (upper) and after annealing at 350 °C-10 h (lower).

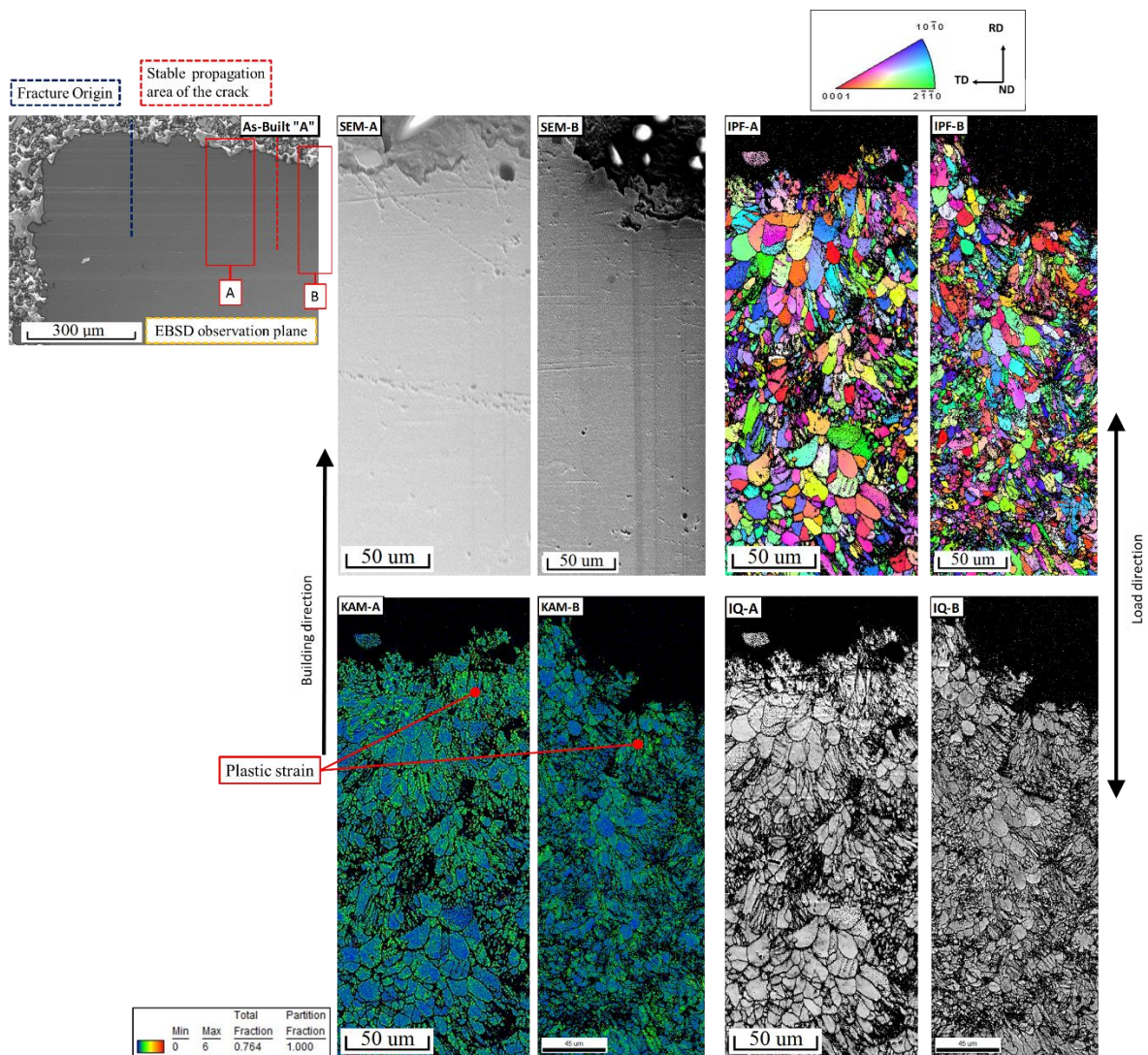


Fig. 5-11 EBSD analysis near the fracture surface of the specimen under as-built conditions with SEM images (Upper left), IPF map (Upper right), KAM map (Lower left), and IQ map (Lower right). Twinning deformation characteristic of Mg alloys (HCP crystalline structure) can be seen in the IPF map. Coarse microstructure is located at the melt pool borders. Light green areas in the KAM map show the plastic deformation inside the stable fracture region (A) and after the stable fracture region (B).

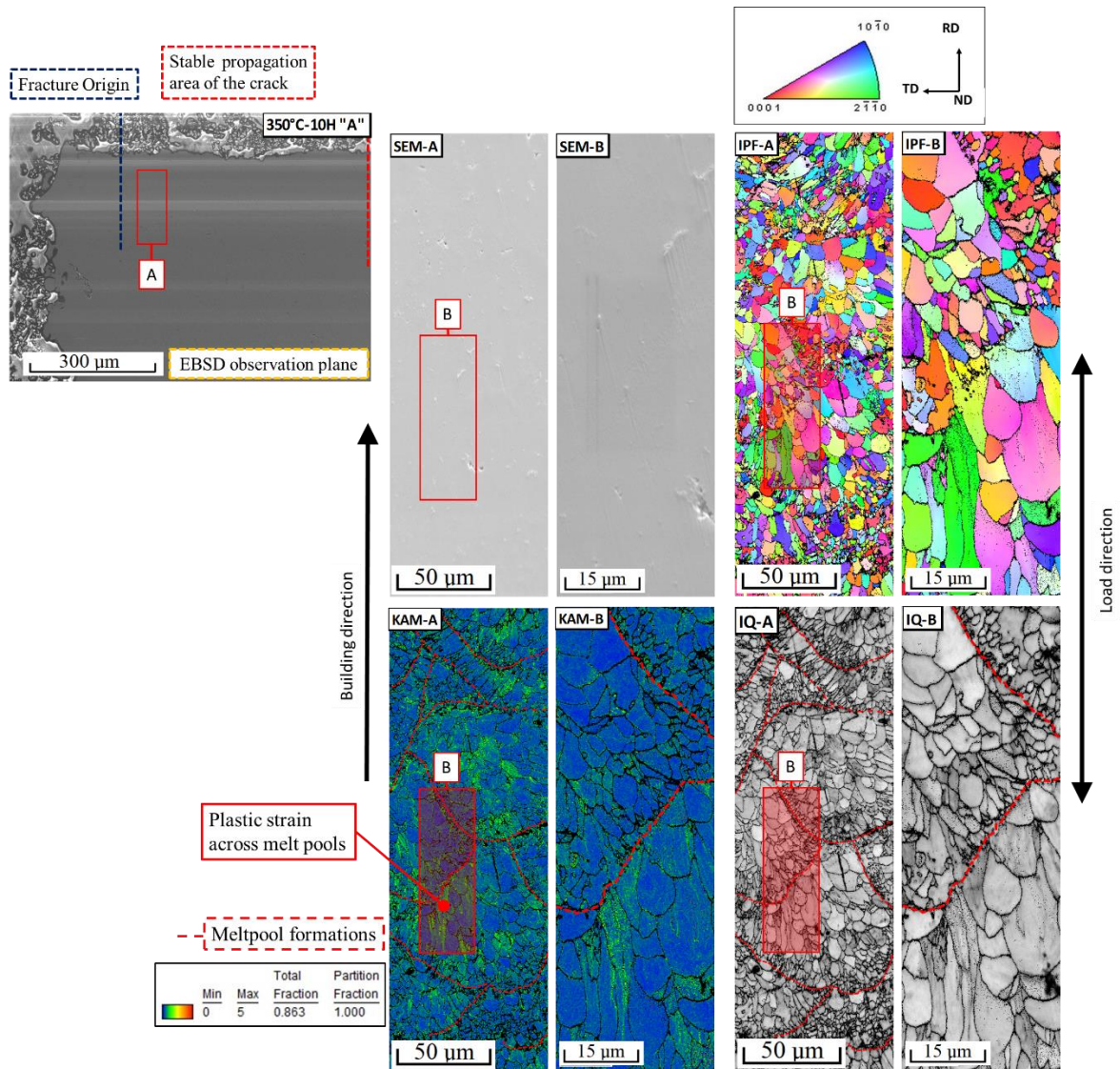


Fig. 5-12 EBSD analysis near the fracture surface of the annealed specimen at 350 °C-10 h with SEM images (Upper left), IPF map (Upper right), KAM map (Lower left), and IQ map (Lower right). Twinning deformation characteristic of Mg alloys (HCP crystalline structure) can be seen in the IPF map. Coarse microstructure dissipates at the melt pool borders. Light green areas in the KAM map show a homogenizing plastic deformation.

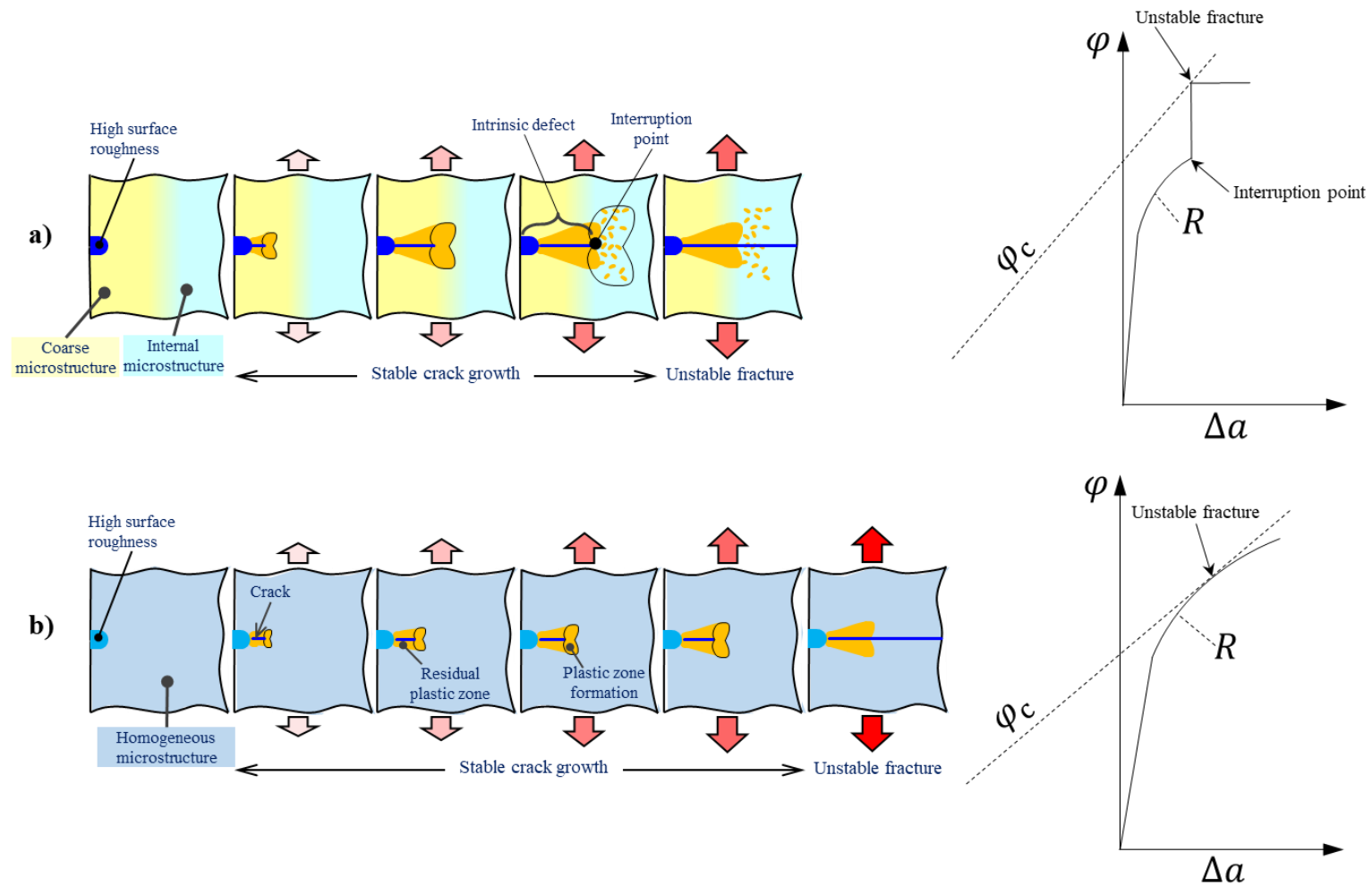


Fig. 5-13 Schematic image showing the fracture process and the R -curve using energy criterion for a specimen under as-built conditions (upper) and after annealing at 350 °C-10 h (lower).

CHAPTER 6.- IDEAL TENSILE STRENGTH OF A METALLIC SLM PART: EXAMPLE OF A NON-COMBUSTIBLE MAGNESIUM ALLOY

6.1 Introduction

Chapter 5 started the analysis on post-processing of SLM products focusing on the defects responsible for fracture in accordance with the fracture mechanism proposed in Chapters 2 and 3. Since it was concluded that microstructural changes are the critical defects that enable the largest stress concentration sources responsible for fracture in SLM products, particularly the irregular coarse microstructure at the outer surface, it makes sense that the mechanical engineer would consider using post-processing to influence this specific area.

To overcome this problem, many studies have performed post-processing machining and/or microstructure homogenization via heat treatment to provide a more reliable mechanical properties evaluation [1-5]. However, throughout the modification process of the as-built conditions, the natural characteristics of the SLM technology, particularly its unique microstructure qualities, disappear. For instance, microstructural changes presented in Section 5.3.1 showed that the homogenization of the microstructure via annealing increases the ductility of the specimens but reduces its UTS value considerably. Moreover, the indicators for finding the true potential of SLM products also disappear. Therefore, the next step is to use a post-processing technique that mechanically removes the defect responsible for fracture without altering the microstructure duality formed during sintering. It is worth noting that machining of SLM products is a common process when destined for material testing. For example, Hadadzadeh et. al machined a round bar specimen from a Al alloy cylinder fabricated by SLM to compare the tensile test results to the a sample of the same material made by casting [6], Leuders et. al machined Ti alloy round bar specimens for tensile testing and concluded that defects are critical in fatigue behavior [7], and Schuch et. al machined Al alloy rods to form round bar specimens and compare different loading conditions and microstructural states after heat treatments [8].

However, as pointed out in the introduction, results from as-built and post-processed specimens show different results and necessary distinction has not been pointed out to date. In addition, by removing the critical defect responsible for fracture in as-built specimens, the ideal strength and the evaluation parameters of the fracture process of SLM products can be determined.

Common knowledge dictates that a sufficiently high load and a stress concentration source are required for fracture to occur. In addition, the highest stress concentration sources are located in the abnormalities within a specimen. Depending on the material, these abnormalities can range from dislocation sources in crystallographic borders to large visible defects. Since SLM can be considered as a micro-casting, micro-welding process, defects similar to that of pores and lack-fusion defects are expected to appear along high stress concentration sources [9-12]. In addition, conclusions in Chapter 2 consider the coarse microstructure in the outer surface of a specimen fabricated by SLM as a defect, which is responsible for fracture in as-built conditions. As a result, in the fracture process, a crack is generated in the outer surface, and a transition from a stable to unstable crack propagation occurs, thus defining the UTS in a parameter known as fracture toughness, which in turn enhances the predictability and reliability of the mechanical properties of SLM products. However, the fracture process for the case in which all of the above-mentioned defects disappear and only the inner microstructure in the melt pool formations remains, is yet to be explained. Considering that: (1) a melt pool formation has a dominant fine microstructure at the center surrounded by a narrow coarse microstructure at the melt pool border, and (2) the fine microstructure has a higher hardness compared to the coarse microstructure [8, 13, 14], three crucial phenomena are expected to occur during the fracture process of the ideal specimen. First, ductile fracture is enabled by void coalescence, which occurs between the fine and coarse microstructure of the melt pool formations. Second, the higher hardness of the dominant fine microstructure increases the stress required for the formation of plastic strain compared to the microstructure in as-built conditions, thus enhancing the UTS value. Third, a uniformly distributed plastic strain throughout the void coalescence of the ductile fracture dominated by Plastic Instability Theory will significantly increase the elongation at break of the specimen. Furthermore, Plastic Instability Theory can be a useful tool to predict

the ideal strength of SLM products and provide a concrete explanation for the potential of SLM.

In this chapter, a method for making small ideal SLM specimens is proposed. Next, all the specimens are subjected to tensile testing and the fracture surfaces were closely analyzed to determine fracture initiation points and ductile fracture regions. Additionally, the fractured specimens are cut into adjacent planes for EBSD analysis. As a result, a fracture mechanism can be determined and a clear ideal target of UTS value from the stress-strain (S-S) curve can be obtained from the perspective of fracture mechanics.

6.2 Method proposal for fabrication of the ideal SLM specimen

6.2.1 Presence of geometrical defects

First, it is important to point out the remarks under which this study considers an SLM specimen as ideal. Since gas pores and lack-of-fusion defects are expected to appear during sintering, the less presence they have, the closer they are to the ideal state. A common rule of thumb is that the smaller the specimen is, the smaller the number of defects that will be present [15]. Nevertheless, it is also of great importance to consider the sintering parameters for each material. Although there is a considerable amount of literature on the matter, another rule of thumb is to find a balance between the energy input to reduce the amount of gas pores, and the scan speed to guarantee melt pool binding mechanisms between layers and avoid lack-of-fusion pores [16-18]. The specific materials and sintering parameters for this study will be described in detail in Section 6.4.

6.2.2 Mechanical removal of the outer surface

Several objectives can be achieved with the mechanical removal of the outer surface of as-built specimens. First, products fabricated by SLM have the notorious characteristic of having a considerably high surface roughness that can influence the mechanical properties and fracture mechanism [12, 19-21]. Therefore, the surface roughness was reduced via computer numerical control (CNC) machining. Second, the author has previously stated that irregular regions of coarse microstructure, which are formed at the outer surface as a product of slow cooldown due to the low heat transfer conductivity of the powder located next to the specimen, are a critical defect in as-built conditions. Using

extreme value statistics theory, it was concluded in Section 2.3.2 that increasing the diameter of the round bar specimens leads to an increase in the size of the irregular coarse grain regions at the outer surface. Specifically, 4-mm round bar specimens have an approximate coarse microstructure depth of 430 μm , and 6-mm round bar specimens have an approximate coarse microstructure depth of 600 μm . Therefore, the mechanical removal of the outer surface is to guarantee that the irregular coarse microstructure at the outer surface disappears. In addition, machining marks were removed by mechanical polishing and a smooth outer surface was achieved. Auxiliary components such as larger lengths of body have the purpose of easier manipulation of the specimens during mechanical removal. Finally, when the specimens are ready to be subjected to tensile testing, the auxiliary components can be cut using a fine cutter.

6.2.3 Flow chart of the proposed method

Figure 6-1 shows the flow chart describing the proposed method. It should be noted that heat treatments were not considered in this study due to their high influence on the resultant microstructure [22-24]. As a result, this study considers ideal SLM specimens as smooth specimens consisting of melt pool formations characteristic of SLM processes with the least amount of gas pores and lack-of-fusion defects, and at the same time do not have the irregular coarse microstructure at the outer surface.

6.3 Experimental procedure

The raw material was AZX912 Mg alloy powder with the same composition as in Table 1-1. The particle size distributions were the same as shown in Section 1.4. Laser irradiation parameters are shown in Table 2-1. The round bar specimens were carried out using the EOS M100 SLM machine shown in Fig. 2-1, and the printing strategy is shown in Fig. 2-2. Figure 6-2 shows the geometry of the round bar specimens with different geometrical configurations that have a diameter of either 4 or 6-mm, and a length of either 50 or over 60-mm in as-built conditions. Three specimens were fabricated for each machined specimen geometry, along with three additional 6-mm round bar specimens to test in as-built conditions for results comparison. After machining, the specimens had a gauge length of either 10 or 25-mm. Flat specimens were not considered owing to the

presence of high residual stresses and the low ultimate strength values, which often result in cracking after processing.

The outer surface mechanical machining of the specimens was performed using a Takisawa TSL-360 CNC machine. Figure 6-2 shows also shows a schematic of the geometrical configuration for the machined specimens. Specimens programmed to have a final diameter of 4 or 3-mm were entirely machined along the surface, while the specimens with a final diameter of 2.5 or 2-mm were machined sectionally along the gauge length only. Once the machining was complete, the machining marks were smoothed by mechanical polishing using P1200, P2400 and P4000 emery sandpapers. For easier maneuvering during machining, the 2-mm specimen had an auxiliary round bar extended component at its end, which was removed using a Struers Minitom low speed saw machine after the mechanical polishing.

A total of 15 tensile tests were performed using a Shimadzu AG-50kNXD universal electromechanical testing machine set at a strain rate of 0.0011 s^{-1} for all diameters in conformance with the Japanese Industrial Standard JIS Z 2241:2011 (Method of Tensile Test for Metallic Materials). All tests were performed at an approximate room temperature range of 21-22 °C using a screw-type grip set with spherical bearings to ensure that no misalignment or bending occurred during testing. Elongation for the 6, 4 and 3-mm round bar specimens was measured using a Shimadzu SG25-100 extensometer with a gauge length of 25 mm, whereas, for the 2.5 and 2-mm round bar specimens, a Shimadzu SG10-100 extensometer with a gauge length of 10 mm was used. Fractography images were taken using a JEOL JSM IT-300 scanning electron microscope (SEM) and EBSD analyses were performed on a Hitachi High-Tech Low Vacuum Analysis SU6600 machine. The fractured parts of the specimens selected for observation were cut in horizontal and longitudinal cross-sections using a Struers Minitom low speed saw, and their inner surfaces were mechanically polished using emery sandpapers up to P4000 and a final pass with 0.2 μm fumed silica. Subsequently the surfaces were polished using a Hitachi High-Tech IM-3000 ion milling machine at 2 kV to obtain a mirror-finish fineness.

6.4 Results

6.4.1 Mechanical removal of the outer surface

Figure 6-3 shows a schematic of the resulting roughness during the mechanical removal process. Figure 6-3(a) shows the state of the round bar specimens in as-built conditions, Fig. 6-3(b) shows the machining marks after the mechanical removal using the CNC machine, and Fig. 6-3 (c) shows the smoothed outer surface after P4000 mechanical polishing was performed. A smooth outer surface was preferred to avoid any stress concentration sources in potential geometrical abnormalities located at the outer surface. Figure 6-3 (d) shows the outer microstructure of the as-built specimens while Fig. 6-3 (e) shows the inner microstructure of the specimens. Important distinctions of the microstructure will be explained in detail in Section 6.6.

6.4.2 Tensile tests results

All specimens were submitted to tensile testing until the occurrence of fracture. Figure 6-4 shows a schematic of engineering stress-strain diagrams for each diameter. The comparison also includes a typical result of the specimen in as-built conditions. To avoid any confusion in specimen recognition, codes were assigned to each specimen configuration and are listed in Table 6-1, where “AB” stands for “as-built” and “MS” stands for “machined specimen”. Figure 6-5 represents all the stress and elongation at failure data.

The fractured 6-mm round bar specimens under as-built conditions yielded the following mean values: an ultimate strength of 344 MPa, a yield strength of 231 MPa (0.2% proof strength), and an elongation of 3.3%. These results are consistent with the results obtained in the previous studies by the authors, and other studies that used similar alloys [15, 25, 26].

The machined specimens exhibited the following mean values: an ultimate strength of 371 MPa, a yield strength of 257 MPa (0.2% proof strength), and an elongation of 4.4%. Although the UTS value and elongation at failure increased considerably compared to the as-built conditions, there is a higher variation of the stress-elongation at failure of the machined specimens. The detailed discussion regarding the behavior of the S-S diagrams is provided in Section 6.6.

6.4.3 Fractography results

The fracture surfaces of all the fractured pieces were observed and a clear difference between the fractography morphologies of the as-built and machined specimens is found. Figure 6-6 shows the typical fracture surface of a 6-mm round bar specimen in as-built state. It consists of: (1) a fracture initiation point at the outer surface, (2) a stable fracture region and (3) an unstable fracture region, all components that resonate with the results of previous chapters. In contrast, Fig. 6-7 shows the fracture surface of a 6-mm diameter specimen machined into 4-mm. Although a fracture initiation point is difficult to determine, the presence of lack-of-fusion defects has influenced the fracture process. It is worth noting that all the specimens were sintered with the same fabrication parameters in the same production bulk. Additionally, AB06 and MS04 specimens were found to have the same geometrical configuration after 3D printing was completed. However, in as-built conditions, the lack-of-fusion defects are not present in the fracture surface while after machining they become critical and appear in a significantly irregular fracture surface. The reasoning behind this phenomenon is explained in detail during the discussion in Section 6.6.

Figures 6-8, 6-9 and 6-10 show the fracture surface of the specimens machined into 3, 2.5 and 2-mm round bar specimens, respectively. In these results, the fracture initiation point is clearly observed, and again a stable fracture region and an unstable fracture region can be recognized. However, it is important to remark that the MS2.5 and MS02 specimens are machined from a selective laser melted 4-mm round bar specimen as shown in Fig. 6-2, a result attributed to the fact that sintering specimens with smaller diameter have a smaller number of defects. Furthermore, compared to the AB06 specimens, the difference between the fracture surface of MS2.5 and MS02 specimens lies in the fracture initiation point. The machined specimens approaching the ideal state have a fracture initiation point in a visible defect such as a small gas pore or a single lack-of-fusion defect located at the outer surface, which are easily observable and can be easily understood. On the other hand, as-built specimens also have the fracture initiation point at the outer surface; moreover, it is also recognizable; however, evidently no defect could be localized. This result can be attributed to the irregular coarse microstructure regions explained in

Chapter 2. The differences between the two fracture processes and the reasoning behind them will be explained in detail in Section 6.6. Additionally, the remaining fracture surfaces of the 2-mm round bar specimens can be observed in Fig. 6-11, where an increase in the gas porosities is shown.

6.4.4 Void formation and coalescence observation

Observation of void formation and coalescence is divided into two sections: (1) Observation at the fracture surface, and (2) observation below the fracture surface. Figure 6-12 shows a compilation of void formations and coalescence inside the stable fracture region of the fracture surface for the machined specimens. To perform EBSD analyses and void coalescence observation below the fracture surface, a cross-sectional plane, which was cut using the Struers Minitum low speed saw, was required. Figure 6-13 shows the cutting and polishing planes destined for observation, where the stable and unstable fracture morphologies can be clearly distinguished. Figure 6-14 shows the SEM images of void formations and coalescence underneath the fracture surface on the cross-sectional plane. Void formations have a mean maximum size of 10 μm , and they are distributed along the stable fracture region.

6.4.5 EBSD analysis

Figure 6-15 shows the EBSD analyses results. A continuous plastic strain can be observed in the Kernel Average Misorientation (KAM) map of the stable fracture region (Fig. 6-15, KAM-A) followed by the plastic strain being shortly interrupted and dispersed (Fig. 6-15, KAM-B). Accordingly, several twin deformations can be observed in the Inverse Polar Figure (IPF) maps under the fracture surface, a characteristic of plastic deformation of HCP crystalline structures.

6.5 Discussion

6.5.1 Fracture mechanism in small, ideal specimens

For a clear understanding of the fracture process, it is crucial to understand the role of the microstructure. Accordingly, findings of Chapter 2 have recorded two types of microstructures: coarse and fine microstructures. These findings are consistent with the

other studies that have analyzed the microstructure for other ferrous and non-ferrous materials where coarse microstructure is a result of slow solidification, thus being located at the boundaries of the melt pool formations. In contrast, fine microstructure is a result of a faster solidification, consequently located at the center of the melt pool formations [6, 27-29]. To better describe the fracture mechanism, the microstructure distribution has been classified into two regions: the outer microstructure and the inner microstructure. The former consists of melt pool formations with large and irregular regions of coarse microstructure that can be observed at the outer surface of the as-built specimens in Fig. 6-3 (d), while the latter consists only of melt pool formations as can be seen in Fig. 6-3 (e). The irregular coarse microstructure in the outer microstructure is attributed to the slow cooldown at the beginning of the laser scan track due to its proximity to the metallic powder, which has a low heat transfer coefficient. The length of the outer microstructure was calculated previously in Section 2.3.2 using statistics of extreme values, resulting in an approximate 430 μm for a 4-mm round bar specimen and 600 μm for a 6-mm round bar specimen.

As-built specimens consist of both inner and outer microstructure. Previous studies from the authors have defined a crack initiation at the outer microstructure that propagates stably until it reaches the inner microstructure, where stable fracture transitions into unstable fracture. The total length of the stable propagation of the crack is considered as a critical defect due to the sudden interruption of the plastic strain, and according to Murakami's Theory, the \sqrt{area} parameter of the defect can be used in fracture toughness (K_{IC}) to predict the strength of the material. Fracture surface observation of the as-built specimens in this paper shown in Fig. 6-6 confirm the same results, thus the same fracture mechanism occurs, which is described in Fig. 6-16 for an as-built state.

However, once the outer microstructure is mechanically removed, the critical defect disappears, and the fracture mechanism remains unexplained. In this case, fracture initiates from a visible defect such as a gas pore or lack-of-fusion defect located at the outer surface, since it is geometrically easier for a crack to propagate from a defect in the outer surface compared to a defect located at the center of the specimen [30]. Next, there is a stable fracture region, which can be evidenced in Figs. 6-8, 6-9 and 6-10. However, the stable fracture of the inner microstructure is different from the outer microstructure in

two main aspects: First, propagation is enabled by void formation and coalescence owing to stress triaxiality when load is applied [31, 32]. Voids are formed between the boundary and the center of the melt pool formations and can be evidenced clearly at the fracture surface in Fig. 6-12 and below the fracture surface in Fig. 6-14. Second, stable crack propagation occurs in the fine microstructure of the melt pool formations. This phenomenon will be explained in detail in Section 6.6.2. The fracture mechanism for the machined specimens can also be observed in Fig. 6-16.

To contrast the difference between both fracture mechanisms, a comparison between Figs. 6-6 and 6-7 can be made. The results for both the fracture surfaces originally come from a 6-mm round bar specimen. In as-built state, there are lack-of-fusion pores present in the specimen; however, they do not influence the fracture mechanism because the maximum defect is in the outer microstructure. Nevertheless, once the outer microstructure is removed mechanically, as shown in Fig. 6-3 (e), several lack-of-fusion defects appear in the fracture surface because they are relevant to the fracture mechanism for the machined state, as described in Fig. 6-16.

6.5.2 Microstructural factors that affect the UTS value and critical \sqrt{area} size of the defect

As discussed in Section 6.6.1, the impact of change in the distribution ratio of coarse and fine microstructure on the UTS value of the as-built specimens is evident. After the mechanical removal of the outer microstructure, the fine microstructure volume ratio increases to a significantly higher proportion compared to the coarse microstructure, consequently changing the fracture mechanism, as explained in Fig. 6-16. In addition, in Fig. 6-4, the clear increase in the yield strength of the machined specimens, which is shown in the S-S diagrams, can be explained by stable crack propagation through the fine microstructure in the machined specimens, since fine microstructure has a higher hardness compared to coarse microstructure. This result is consistent with other studies where increasing the martensite volume percentage changes the fracture mechanism in dual-phase steel materials and has a highly similar S-S behavior [33-35].

As a result, both as-built and machined specimens manifest different stable propagation of the crack mechanisms, however, at the same time, both stable fractures

reach a critical value before transitioning into unstable fracture. Consequently, both fracture mechanisms can be covered by the same fracture toughness concept. According to Murakami's equation [30], the stress intensity factor K_I can be considered with the remote stress σ_∞ and the size \sqrt{area} of a defect in the following relation:

$$K_I = 0.65\sigma_\infty\sqrt{\pi\sqrt{area}} \quad (6 - 1)$$

where the stable fracture region is included with a defect in the \sqrt{area} parameter. Assuming a K_{IC} value of $10 \text{ MPa}\sqrt{\text{m}}$ for Mg alloys fabricated by SLM (determined in Chapters 3 and 4), a UTS- \sqrt{area} graph can be defined until an ideal UTS (σ_{ci}) value of 430 MPa (see Appendix) is reached. For that purpose, the theoretical UTS- \sqrt{area} line is drawn using a range of UTS values (σ_C) that start at the ideal UTS of 430 MPa and then decrease gradually as per Murakami's equation [30]. Then, the experimental \sqrt{area} size of the stable fracture region for the as-built and machined specimens is measured via fracture surface observation, as shown in Fig. 6-17. The experimental UTS values are obtained through the tensile test results. Subsequently, the experimental \sqrt{area} and UTS values of the fractured specimens are included in the UTS- \sqrt{area} graph along with the theoretical results for comparison, as shown in Fig. 6-18. To increase the quantity of results, all the \sqrt{area} and UTS values of round bar specimens with different diameters in as-built conditions tested for previous papers were also considered and are shown in Fig. 6-18 [36-38]. For the ideal calculated UTS in the Appendix, the critical defect size ($\sqrt{area_C}$) of the defect is approximately 410 μm . This indicates that even if a defect responsible for fracture is small enough, a stable propagation of the crack will still occur via void coalescence that will reach at least a $\sqrt{area_C}$ of 410 μm . A result that is mathematically evident with the fracture surface results of Figs. 6-8, 6-9 and 6-10, where the fracture initiation points can be observed to have a considerable variation in size, however, the stable fracture region has a similar size, which results in a similar UTS value.

Finally, Fig. 6-5 shows some scattering in the elongation values amongst machined specimens of the same diameter. For example, the 2-mm machined specimens present a variation in elongation that ranges from 5% to 7%. The reasoning behind this phenomenon is the presence of gas porosities in the fracture surfaces of the lowest elongation, as can be seen in Fig. 6-11. The fracture initiation is at a visible defect located at the outer surface. However, the increase of the gas porosity population serves as

evidence of how sensitive the SLM product to the presence of small defects when the stable propagation area of the crack enabled by the outer microstructure is removed by mechanical machining.

6.6 Conclusions

This chapter proposes a new mechanical method to remove the critical defects of SLM products and obtain a round bar specimen with a sufficiently small volume to approach its ideal state. All the results obtained are displayed and analyzed as a foundation to determine the ideal UTS of SLM products and unravel the true potential of AM technologies. The findings of this study led to the following conclusions:

- The ideal specimen obtained in this study is defined as a smooth specimen without the irregular coarse microstructure at the outer surface known as outer microstructure, leaving only an inner microstructure (melt pool formations) characteristic of SLM processes with the least amount of gas pores and lack-of-fusion defects.
- Owing to the presence of the irregular coarse microstructure at the outer surface, SLM products in as-built conditions have a higher tolerance to the number of defects present throughout the volume. However, when the outer microstructure is removed and the surface is smoothed, the specimen becomes much more sensitive to the presence of defects, which greatly affects the mechanical properties.
- When the specimen is machined and the microstructure approaches the ideal conditions (melt pool formations only) the dominant microstructure is mostly fine grain, which has a higher hardness. As a result, the yield strength of the machined specimens increases.
- The ideal strength of non-combustible Mg alloys is controlled by the microstructure. Void formation occurs between the melt pool center (fine microstructure) and melt pool boundary (coarse microstructure) and their coalescence enables a stable propagation.
- The ideal UTS for non-combustible Mg alloys was found to be approximately 431 MPa, with a critical \sqrt{area} size of 410 μm , which includes the stable propagation

of the crack via void coalescence. The calculation method involved plastic instability theory and the determination of the strain hardening coefficient “n”, which has an average value of 0.131.

6.7 References

- [1] B. Vrancken, L. Thijs, J.-P. Kruth, J. Van Humbeeck, Heat treatment of Ti6Al4V produced by Selective Laser Melting: Microstructure and mechanical properties, *Journal of Alloys and Compounds*, 541 (2012) 177-185. <https://doi.org/10.1016/j.jallcom.2012.07.022>.
- [2] N. Takata, H. Kodaira, K. Sekizawa, A. Suzuki, M. Kobashi, Change in microstructure of selectively laser melted AlSi10Mg alloy with heat treatments, *Materials Science and Engineering: A*, 704 (2017) 218-228. <https://doi.org/10.1016/j.msea.2017.08.029>.
- [3] R. Seede, B. Zhang, A. Whitt, S. Picak, S. Gibbons, P. Flater, A. Elwany, R. Arroyave, I. Karaman, Effect of heat treatments on the microstructure and mechanical properties of an ultra-high strength martensitic steel fabricated via laser powder bed fusion additive manufacturing, *Additive Manufacturing*, 47 (2021) 102255. <https://doi.org/10.1016/j.addma.2021.102255>.
- [4] X. Yu, L. Wang, T6 heat-treated AlSi10Mg alloys additive-manufactured by selective laser melting, *Procedia Manufacturing*, 15 (2018) 1701-1707. <https://doi.org/10.1016/j.promfg.2018.07.265>.
- [5] C. Zhang, H. Zhu, H. Liao, Y. Cheng, Z. Hu, X. Zeng, Effect of heat treatments on fatigue property of selective laser melting AlSi10Mg, *International Journal of Fatigue*, 116 (2018) 513-522. <https://doi.org/10.1016/j.ijfatigue.2018.07.016>.
- [6] A. Hadadzadeh, B.S. Amirkhiz, S. Shakerin, J. Kelly, J. Li, M. Mohammadi, Microstructural investigation and mechanical behavior of a two-material component fabricated through selective laser melting of AlSi10Mg on an Al-Cu-Ni-Fe-Mg cast alloy substrate, *Additive Manufacturing*, 31 (2020) 100937. <https://doi.org/10.1016/j.addma.2019.100937>.
- [7] S. Leuders, M. Thöne, A. Riemer, T. Niendorf, T. Tröster, H.A. Richard, H.J. Maier, On the mechanical behaviour of titanium alloy TiAl6V4 manufactured by selective laser melting: Fatigue resistance and crack growth performance, *International Journal of Fatigue*, 48 (2013) 300-307. <https://doi.org/10.1016/j.ijfatigue.2012.11.011>.
- [8] M. Schuch, T. Hahn, M. Bleckmann, The mechanical behavior and microstructure of additively manufactured AlSi10Mg for different material states and loading conditions, *Materials Science and Engineering: A*, 813 (2021) 141134.

- <https://doi.org/10.1016/j.msea.2021.141134>.
- [9] N. Sanaei, A. Fatemi, Defects in additive manufactured metals and their effect on fatigue performance: A state-of-the-art review, *Progress in Materials Science*, 117 (2021) 100724. <https://doi.org/10.1016/j.pmatsci.2020.100724>.
- [10] M. Dallago, B. Winiarski, F. Zanini, S. Carmignato, M. Benedetti, On the effect of geometrical imperfections and defects on the fatigue strength of cellular lattice structures additively manufactured via Selective Laser Melting, *International Journal of Fatigue*, 124 (2019) 348-360. <https://doi.org/10.1016/j.ijfatigue.2019.03.019>.
- [11] H. Gong, K. Rafi, H. Gu, G.D. Janaki Ram, T. Starr, B. Stucker, Influence of defects on mechanical properties of Ti–6Al–4V components produced by selective laser melting and electron beam melting, *Materials & Design*, 86 (2015) 545-554. <https://doi.org/10.1016/j.matdes.2015.07.147>.
- [12] H. Masuo, Y. Tanaka, S. Morokoshi, H. Yagura, T. Uchida, Y. Yamamoto, Y. Murakami, Effects of Defects, Surface Roughness and HIP on Fatigue Strength of Ti-6Al-4V manufactured by Additive Manufacturing, *Procedia Structural Integrity*, 7 (2017) 19-26. <https://doi.org/10.1016/j.prostr.2017.11.055>.
- [13] J. Wu, X.Q. Wang, W. Wang, M.M. Attallah, M.H. Loretto, Microstructure and strength of selectively laser melted AlSi10Mg, *Acta Materialia*, 117 (2016) 311-320. <https://doi.org/10.1016/j.actamat.2016.07.012>.
- [14] L. Thijs, F. Verhaeghe, T. Craeghs, J.V. Humbeeck, J.-P. Kruth, A study of the microstructural evolution during selective laser melting of Ti–6Al–4V, *Acta Materialia*, 58 (2010) 3303-3312. <https://doi.org/10.1016/j.actamat.2010.02.004>.
- [15] Z. Dong, X. Zhang, W. Shi, H. Zhou, H. Lei, J. Liang, Study of Size Effect on Microstructure and Mechanical Properties of AlSi10Mg Samples Made by Selective Laser Melting, *Materials (Basel)*, 11 (2018) 2463. [10.3390/ma11122463](https://doi.org/10.3390/ma11122463).
- [16] C. Tang, J.L. Tan, C.H. Wong, A numerical investigation on the physical mechanisms of single track defects in selective laser melting, *International Journal of Heat and Mass Transfer*, 126 (2018) 957-968. <https://doi.org/10.1016/j.ijheatmasstransfer.2018.06.073>.
- [17] A.B. Spierings, K. Dawson, P.J. Uggowitzer, K. Wegener, Influence of SLM scan-speed on microstructure, precipitation of Al₃Sc particles and mechanical properties in Sc- and Zr-modified Al-Mg alloys, *Materials & Design*, 140 (2018) 134-143. <https://doi.org/10.1016/j.matdes.2017.11.053>.
- [18] W. Xiong, L. Hao, Y. Li, D. Tang, Q. Cui, Z. Feng, C. Yan, Effect of selective laser melting parameters on morphology, microstructure, densification and mechanical properties of supersaturated silver alloy, *Materials & Design*, 170 (2019) 107697.

- <https://doi.org/10.1016/j.matdes.2019.107697>.
- [19] K. Solberg, S. Guan, S.M.J. Razavi, T. Welo, K.C. Chan, F. Berto, Fatigue of additively manufactured 316L stainless steel: The influence of porosity and surface roughness, *Fatigue & Fracture of Engineering Materials & Structures*, 0 (2019). [10.1111/ffe.13077](https://doi.org/10.1111/ffe.13077).
- [20] E. Beevers, A.D. Brandão, J. Gumpinger, M. Gschweidl, C. Seyfert, P. Hofbauer, T. Rohr, T. Ghidini, Fatigue properties and material characteristics of additively manufactured AlSi10Mg – Effect of the contour parameter on the microstructure, density, residual stress, roughness and mechanical properties, *International Journal of Fatigue*, 117 (2018) 148-162. <https://doi.org/10.1016/j.ijfatigue.2018.08.023>.
- [21] G. Strano, L. Hao, R.M. Everson, K.E. Evans, Surface roughness analysis, modelling and prediction in selective laser melting, *Journal of Materials Processing Technology*, 213 (2013) 589-597. <https://doi.org/10.1016/j.jmatprotec.2012.11.011>.
- [22] F. Alghamdi, X. Song, A. Hadadzadeh, B. Shalchi-Amirkhiz, M. Mohammadi, M. Haghshenas, Post heat treatment of additive manufactured AlSi10Mg: On silicon morphology, texture and small-scale properties, *Materials Science and Engineering: A*, 783 (2020) 139296. <https://doi.org/10.1016/j.msea.2020.139296>.
- [23] B. Amir, E. Grinberg, Y. Gale, O. Sadot, S. Samuha, Influences of platform heating and post-processing stress relief treatment on the mechanical properties and microstructure of selective-laser-melted AlSi10Mg alloys, *Materials Science and Engineering: A*, 822 (2021) 141612. <https://doi.org/10.1016/j.msea.2021.141612>.
- [24] W. Li, S. Li, J. Liu, A. Zhang, Y. Zhou, Q. Wei, C. Yan, Y. Shi, Effect of heat treatment on AlSi10Mg alloy fabricated by selective laser melting: Microstructure evolution, mechanical properties and fracture mechanism, *Materials Science and Engineering: A*, 663 (2016) 116-125. <https://doi.org/10.1016/j.msea.2016.03.088>.
- [25] N.T. Aboulkhair, I. Maskery, C. Tuck, I. Ashcroft, N.M. Everitt, The microstructure and mechanical properties of selectively laser melted AlSi10Mg: The effect of a conventional T6-like heat treatment, *Materials Science and Engineering: A*, 667 (2016) 139-146. <https://doi.org/10.1016/j.msea.2016.04.092>.
- [26] R. Karunakaran, S. Ortgies, A. Tamayol, F. Bobaru, M.P. Sealy, Additive manufacturing of magnesium alloys, *Bioactive Materials*, 5 (2020) 44-54. <https://doi.org/10.1016/j.bioactmat.2019.12.004>.
- [27] X. Liu, C. Zhao, X. Zhou, Z. Shen, W. Liu, Microstructure of selective laser melted AlSi10Mg alloy, *Materials & Design*, 168 (2019) 107677. <https://doi.org/10.1016/j.matdes.2019.107677>.
- [28] E. Santos, K. Osakada, M. Shiomi, Y. Kitamura, F. Abe, Microstructure and

- mechanical properties of pure titanium models fabricated by selective laser melting, *Proceedings of the Institution of Mechanical Engineers Part C Journal of Mechanical Engineering Science*, 218 (2004) 711-719. [10.1243/0954406041319545](https://doi.org/10.1243/0954406041319545).
- [29] J.G. Santos Macías, T. Douillard, L. Zhao, E. Maire, G. Pyka, A. Simar, Influence on microstructure, strength and ductility of build platform temperature during laser powder bed fusion of AlSi10Mg, *Acta Materialia*, 201 (2020) 231-243. <https://doi.org/10.1016/j.actamat.2020.10.001>.
- [30] Y. Murakami, S. Kodama, S. Konuma, Quantitative evaluation of effects of non-metallic inclusions on fatigue strength of high strength steels. I: Basic fatigue mechanism and evaluation of correlation between the fatigue fracture stress and the size and location of non-metallic inclusions, *International Journal of Fatigue*, 11 (1989) 291-298. [https://doi.org/10.1016/0142-1123\(89\)90054-6](https://doi.org/10.1016/0142-1123(89)90054-6).
- [31] R. Casati, J. Lemke, M. Vedani, Microstructure and Fracture Behavior of 316L Austenitic Stainless Steel Produced by Selective Laser Melting, *Journal of Materials Science & Technology*, 32 (2016) 738-744. <https://doi.org/10.1016/j.jmst.2016.06.016>.
- [32] D.D. Ben, Y.R. Ma, H.J. Yang, L.X. Meng, X.H. Shao, H.Q. Liu, S.G. Wang, Q.Q. Duan, Z.F. Zhang, Heterogeneous microstructure and voids dependence of tensile deformation in a selective laser melted AlSi10Mg alloy, *Materials Science and Engineering: A*, 798 (2020) 140109. <https://doi.org/10.1016/j.msea.2020.140109>.
- [33] Q. Lai, O. Bouaziz, M. Gouné, L. Brassart, M. Verdier, G. Parry, A. Perlade, Y. Bréchet, T. Pardoen, Damage and fracture of dual-phase steels: Influence of martensite volume fraction, *Materials Science and Engineering: A*, 646 (2015) 322-331. <https://doi.org/10.1016/j.msea.2015.08.073>.
- [34] Q. Lai, L. Brassart, O. Bouaziz, M. Gouné, M. Verdier, G. Parry, A. Perlade, Y. Bréchet, T. Pardoen, Influence of martensite volume fraction and hardness on the plastic behavior of dual-phase steels: Experiments and micromechanical modeling, *International Journal of Plasticity*, 80 (2016) 187-203. <https://doi.org/10.1016/j.ijplas.2015.09.006>.
- [35] N. Nakada, K.-i. Ikeda, H. Shuto, T. Yokoi, T. Tsuchiyama, S. Hata, H. Nakashima, S. Takaki, Quantification of Large Deformation with Punching in Dual Phase Steel and Change of its Microstructure –Part II: Local Strain Mapping of Dual Phase Steel by a Combination Technique of Electron Backscatter Diffraction and Digital Image Correlation Methods, *ISIJ International*, 56 (2016) 2077-2083. [10.2355/isijinternational.ISIJINT-2016-310](https://doi.org/10.2355/isijinternational.ISIJINT-2016-310).
- [36] B. Proaño, H. Miyahara, T. Matsumoto, S. Hamada, H. Sakai, K. Ogawa, Suyalatu, H. Noguchi, Weakest region analysis of non-combustible Mg products fabricated by

- selective laser melting, *Theoretical and Applied Fracture Mechanics*, 103 (2019) 102291. <https://doi.org/10.1016/j.tafmec.2019.102291>.
- [37] B. Proaño, H. Miyahara, T. Matsumoto, S. Hamada, H. Sakai, K. Ogawa, Suyalatu, H. Noguchi, Plastic Strain Distribution throughout the Microstructure Duality during the Fracture Process of Non-Combustible Mg Products Fabricated by Selective Laser Melting, *Theoretical and Applied Fracture Mechanics*, (2020) 102805. <https://doi.org/10.1016/j.tafmec.2020.102805>.
- [38] B.S. Proaño, T. Yamaguchi, H. Miyahara, T. Matsumoto, S. Hamada, H. Sakai, K. Ogawa, Suyalatu, H. Noguchi, Weakest Region Analysis and Size Effects on the Nature and Distribution of Defects and their Influence on the Strength of Non-combustible Mg Products, in: *First European Conference on Structural Integrity of Additively Manufactured Materials (ESIAM19)*, Trondheim, Norway, 2019, pp. 88.

6.8 List of tables

Table 6-1 Specimen codification.

SPECIMEN CODE	Gauge diameter [mm]	Gauge length [mm]	Geometry configuration		
AB06-01	6	25			
AB06-02					
AB06-03					
MS04-01	4		25		
MS04-02					
MS04-03					
MS03-01	3			25	
MS03-02					
MS03-03					
MS2.5-01	2.5	10			
MS2.5-02					
MS2.5-03					
MS02-01	2		10		
MS02-02					
MS02-03					

6.9 List of figures

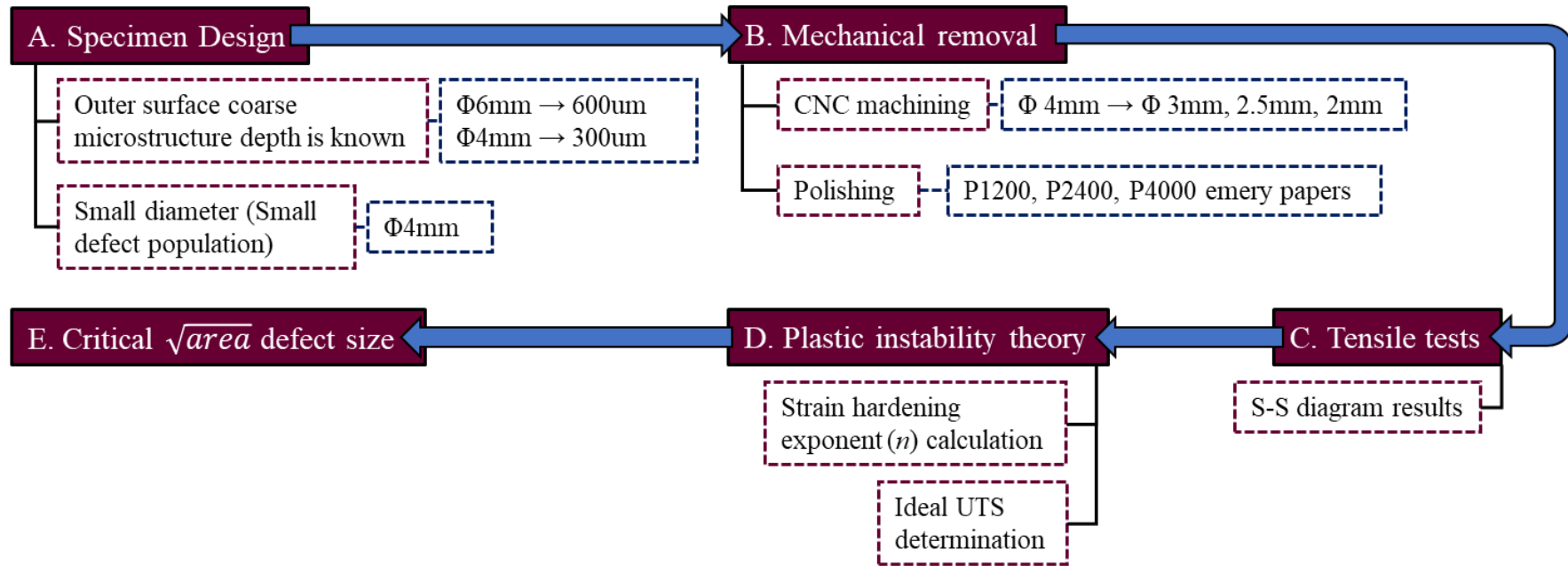


Fig. 6-1 Flow chart of the method for obtaining ideal SLM specimens.

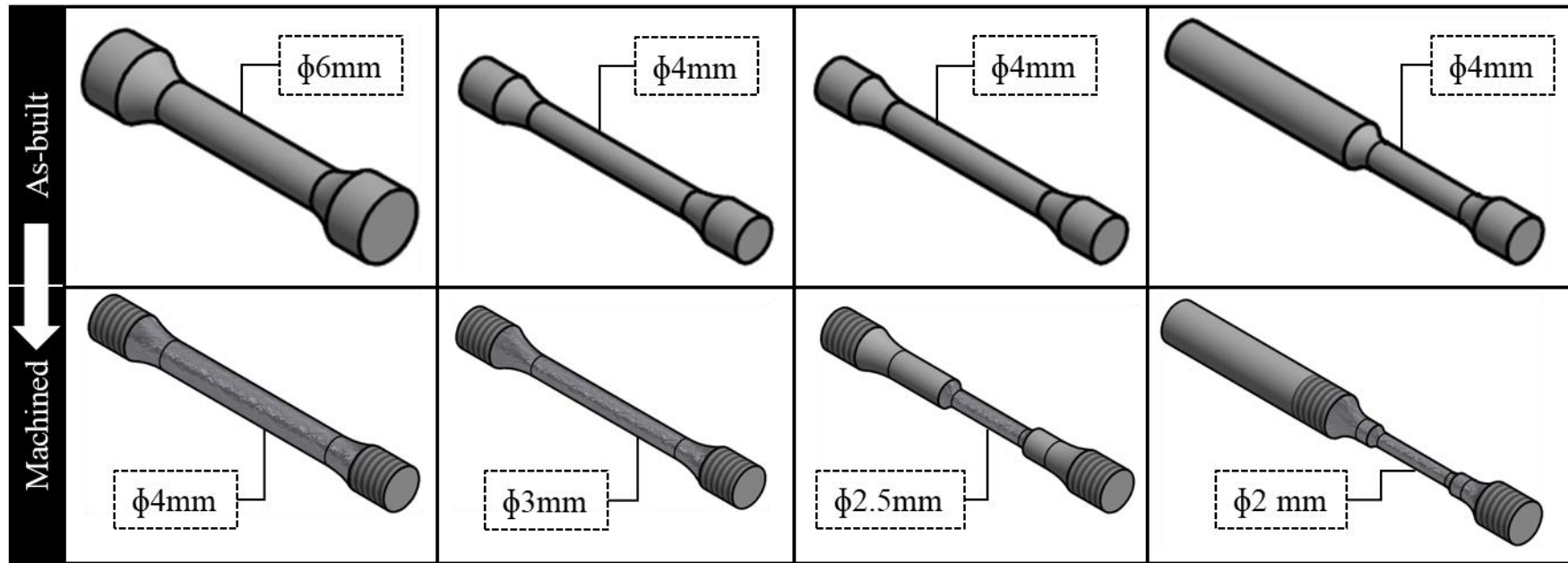


Fig. 6-2 Shapes for the round bar tensile test specimens in as-built state (up) and after machining (down).

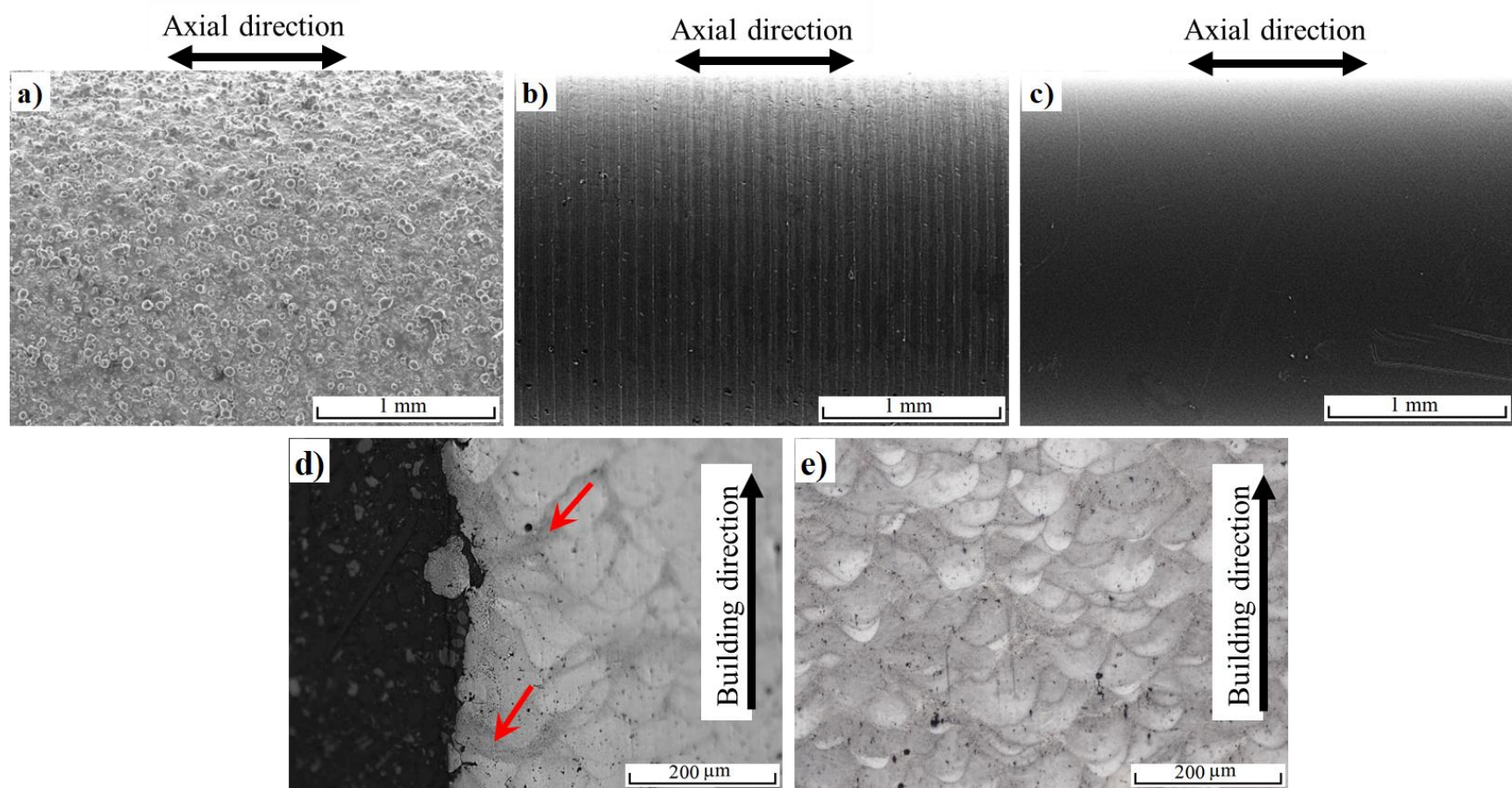


Fig. 6-3 Outer surface roughness of the round bar specimens a) in as-built conditions, b) after machining and c) after mechanical polishing with P4000 emery paper. Cross-section of the d) external microstructure with irregular coarse microstructure (red arrows) and e) internal microstructure with melt pool formations.

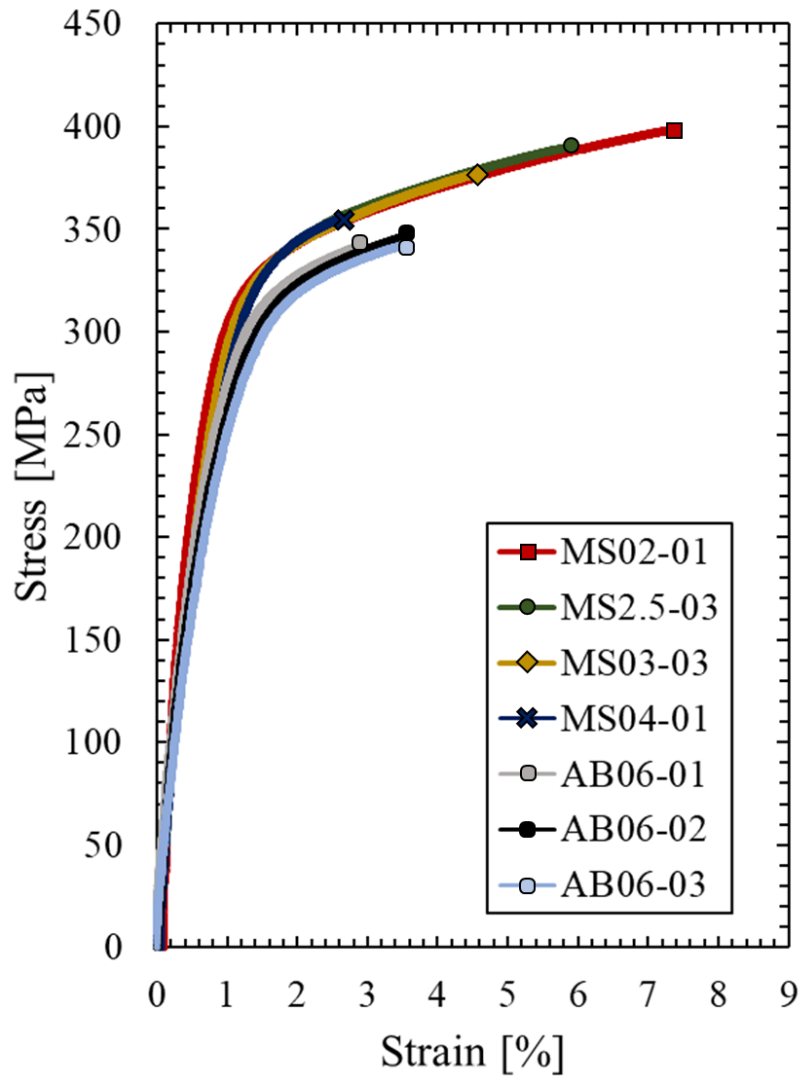


Fig. 6-4 Stress-strain diagram results for each diameter in as-built and after machining state. (MS02 – AB06 are defined in Table 6-2)

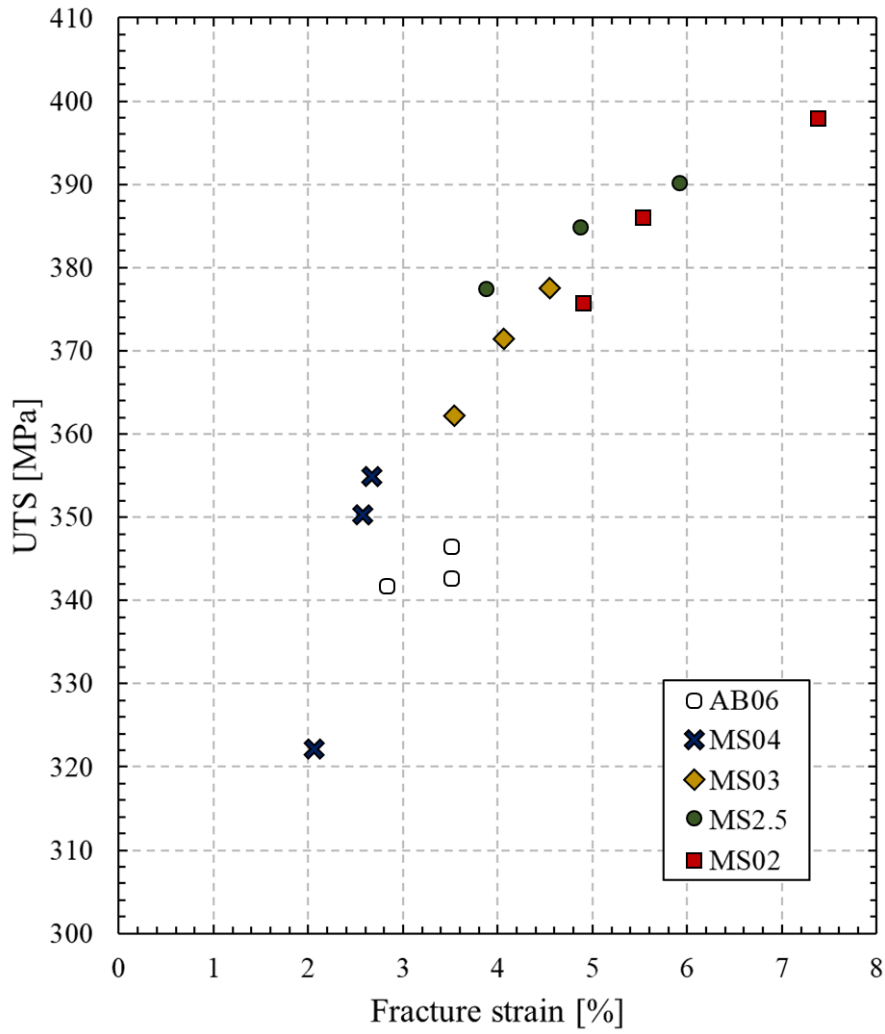


Fig. 6-5 Stress and elongation at failure results for all the fractured specimens. (MS02 – AB06 are defined in Table 6-2)

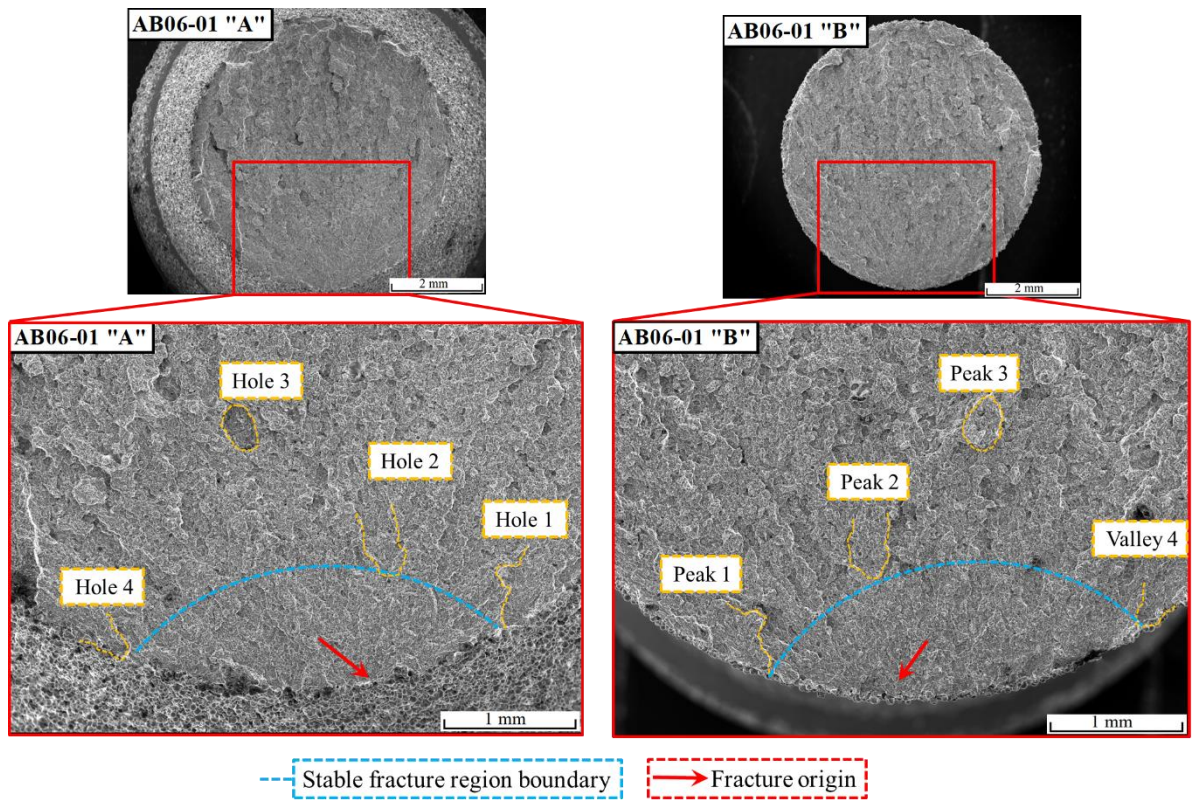


Fig. 6-6 SEM images of the fracture surfaces of a 6-mm round bar specimen in as-built conditions. The images show the fracture origin (red arrow) and definition of the stable fracture region (blue dashed line) by peak-hole fracture surface morphology. (AB06 is defined in Table 6-2)

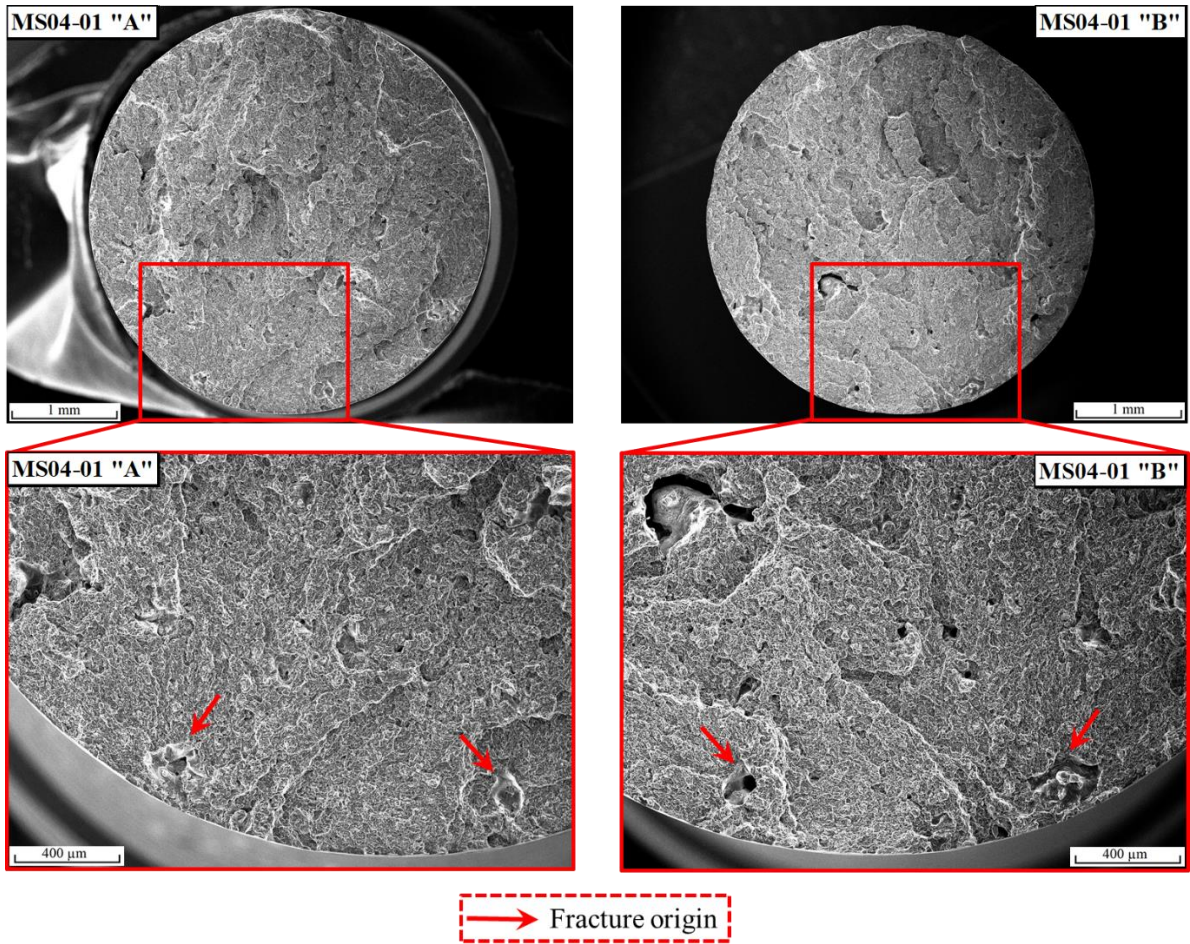


Fig. 6-7 SEM images of the fracture surfaces of a 4-mm round bar specimen after machining was performed. The images show the fracture origin (red arrow) and a significant number of lack-of-fusion defects. (MS04 is defined in Table 6-2)

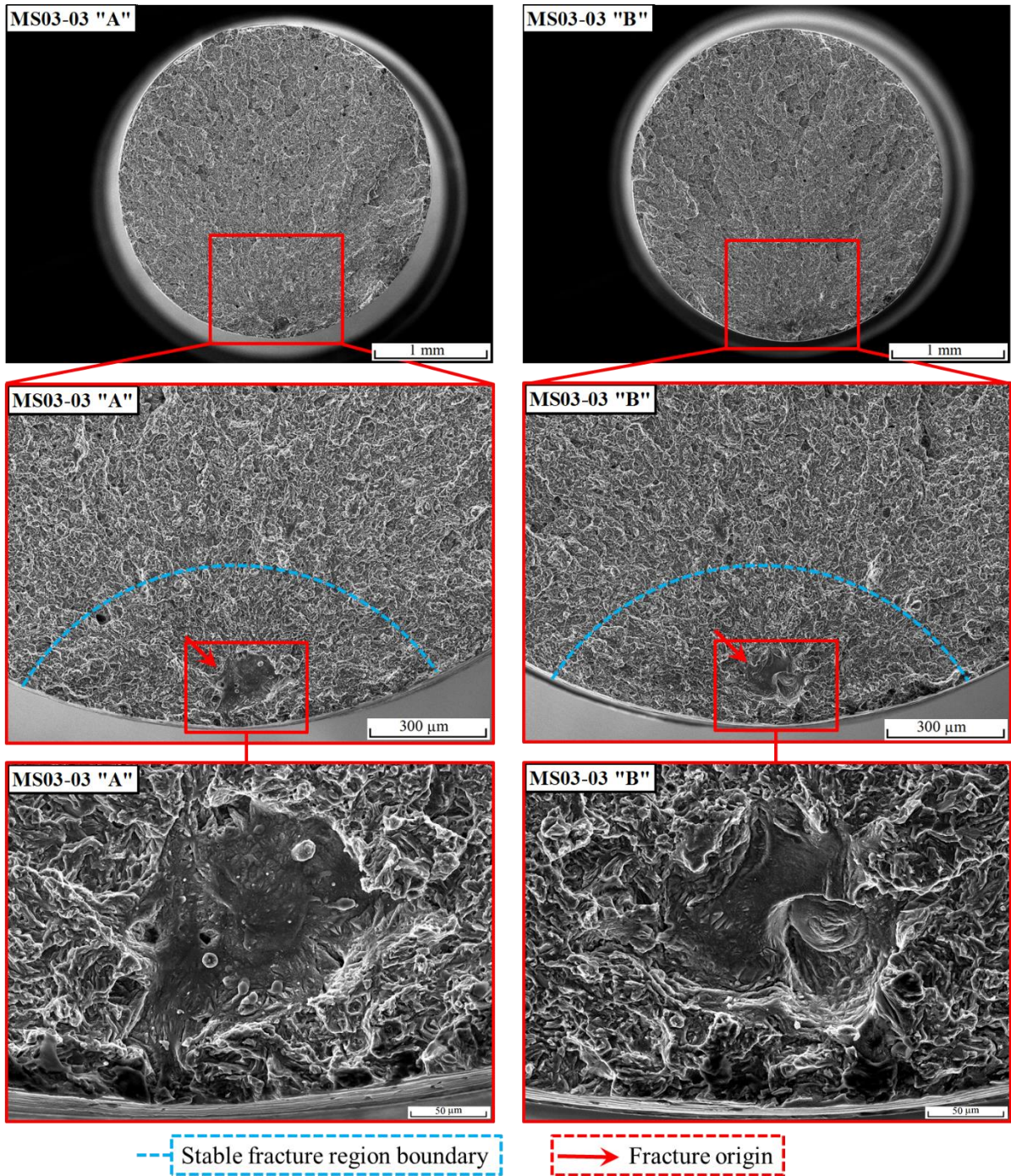


Fig. 6-8 SEM images of the fracture surfaces of a 3-mm round bar specimen after machining was performed. The images show the fracture origin (red arrow) and a definition of the stable fracture region (blue dashed line) by the same method shown in Fig. 6-6. (MS03 is defined in Table 6-2)

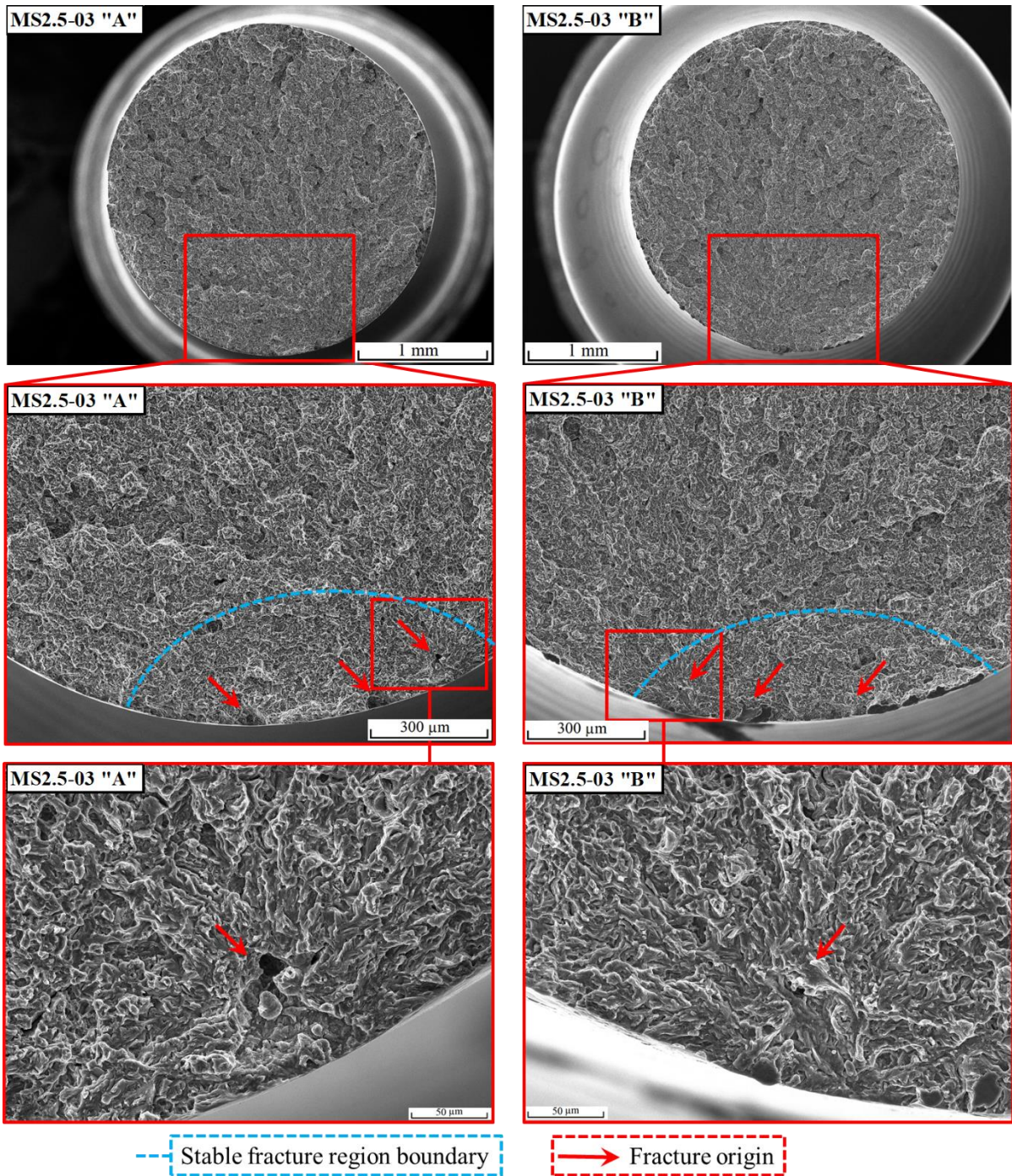


Fig. 6-9 SEM images of the fracture surfaces of a 2.5-mm round bar specimen after machining was performed. The images show the fracture origin (red arrow) and a definition of the stable fracture region (blue dashed line) by the same method shown in Fig. 6-6. (MS2.5 is defined in Table 6-2)

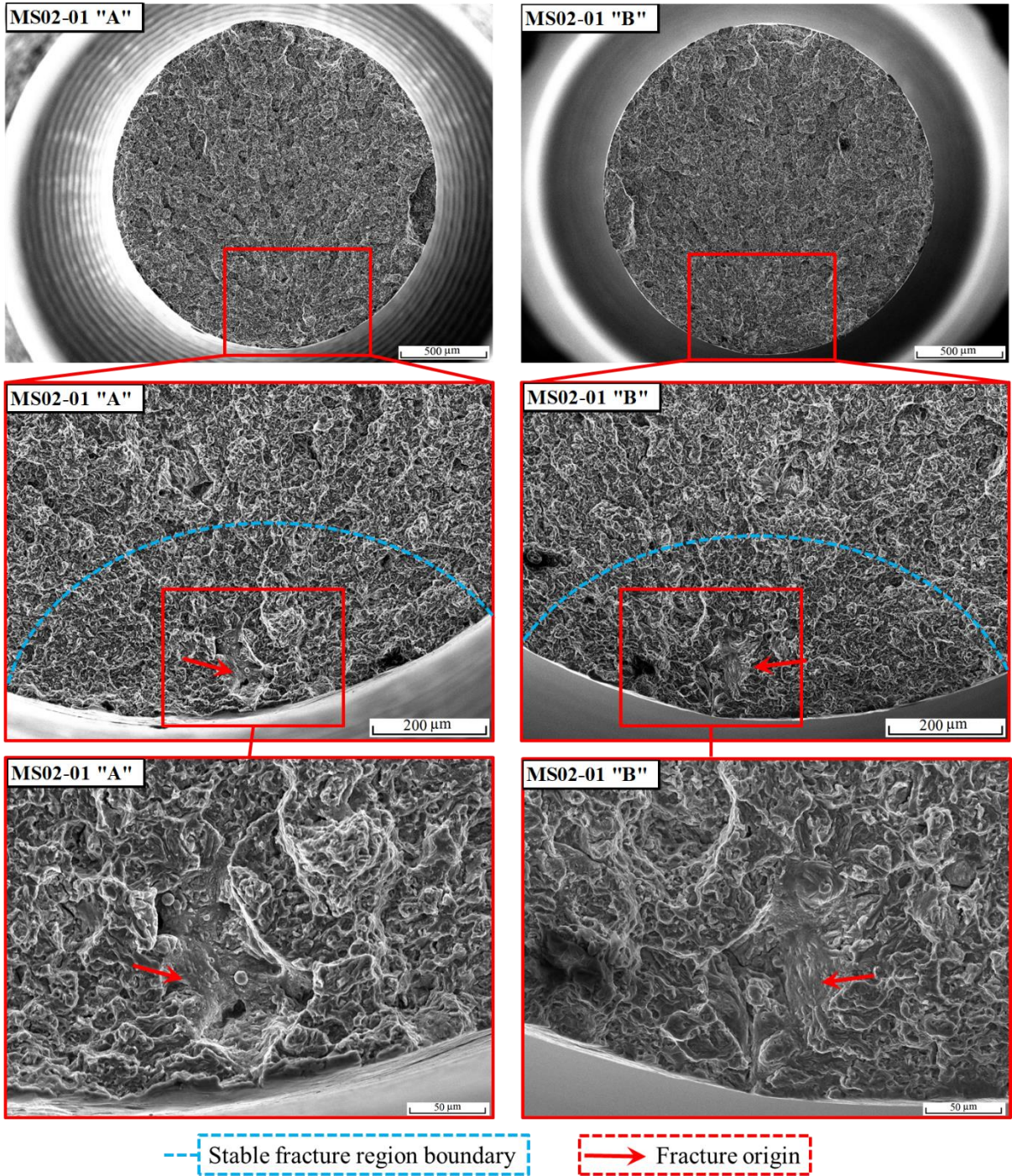


Fig. 6-10 SEM images of the fracture surfaces of a 2-mm round bar specimen after machining was performed. The images show the fracture origin (red arrow) and a definition of the stable fracture region (blue dashed line) by the same method shown in Fig. 6-6. (MS02 is defined in Table 6-2)

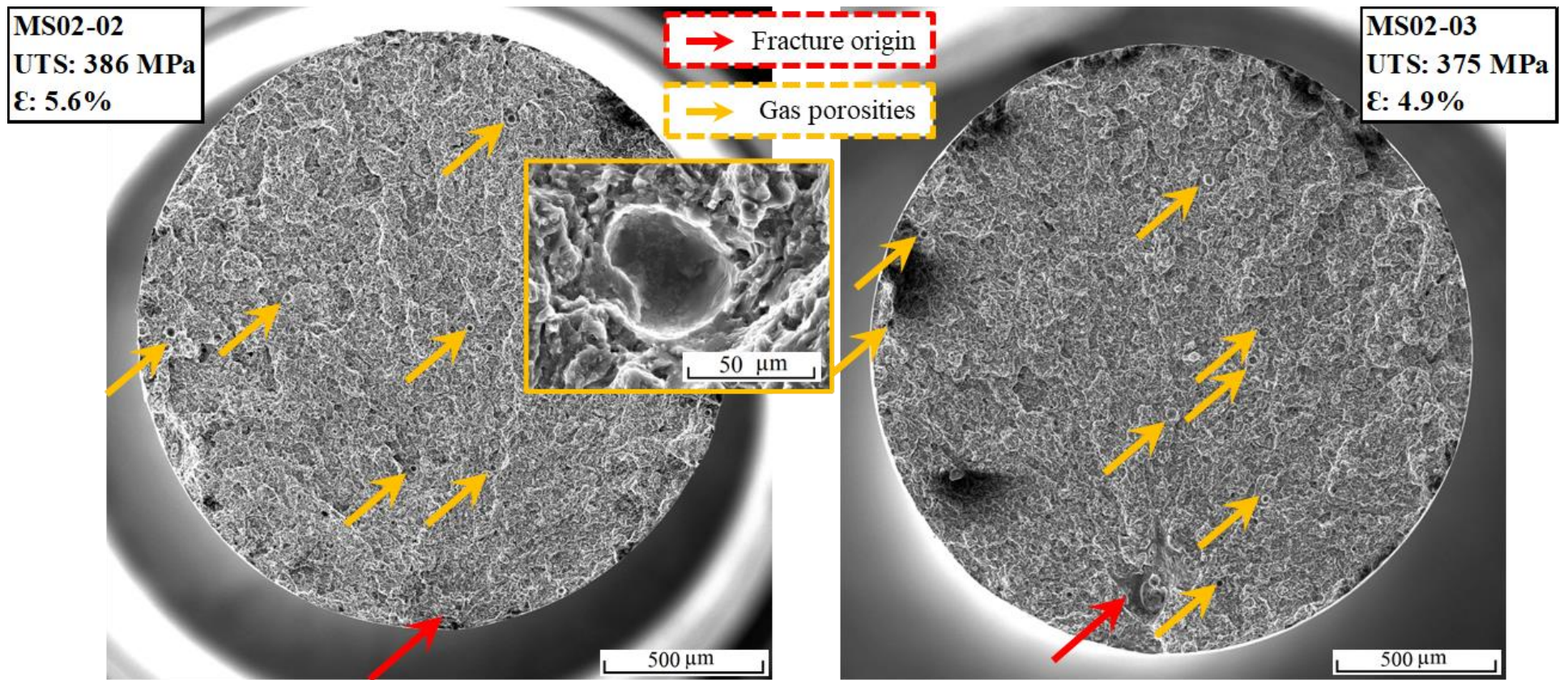


Fig. 6-11 SEM images of the rest of the fracture surfaces of the MS02 specimens. Gas porosity defect population can be observed.

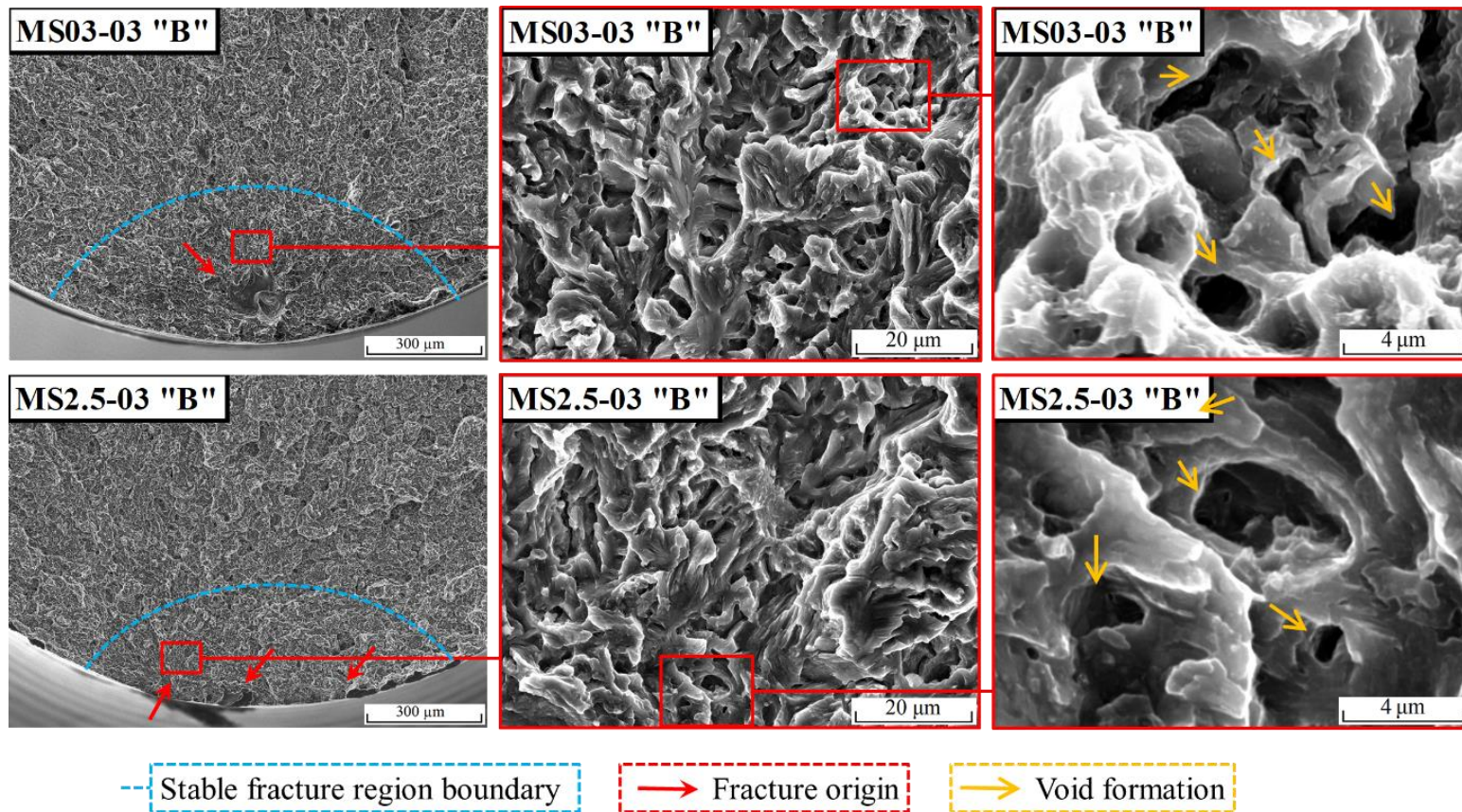


Fig. 6-12 SEM images of the void formations and void coalescence inside the stable fracture region at the fracture surface of the machined specimens. (MS03 and MS2.5 are defined in Table 6-1)

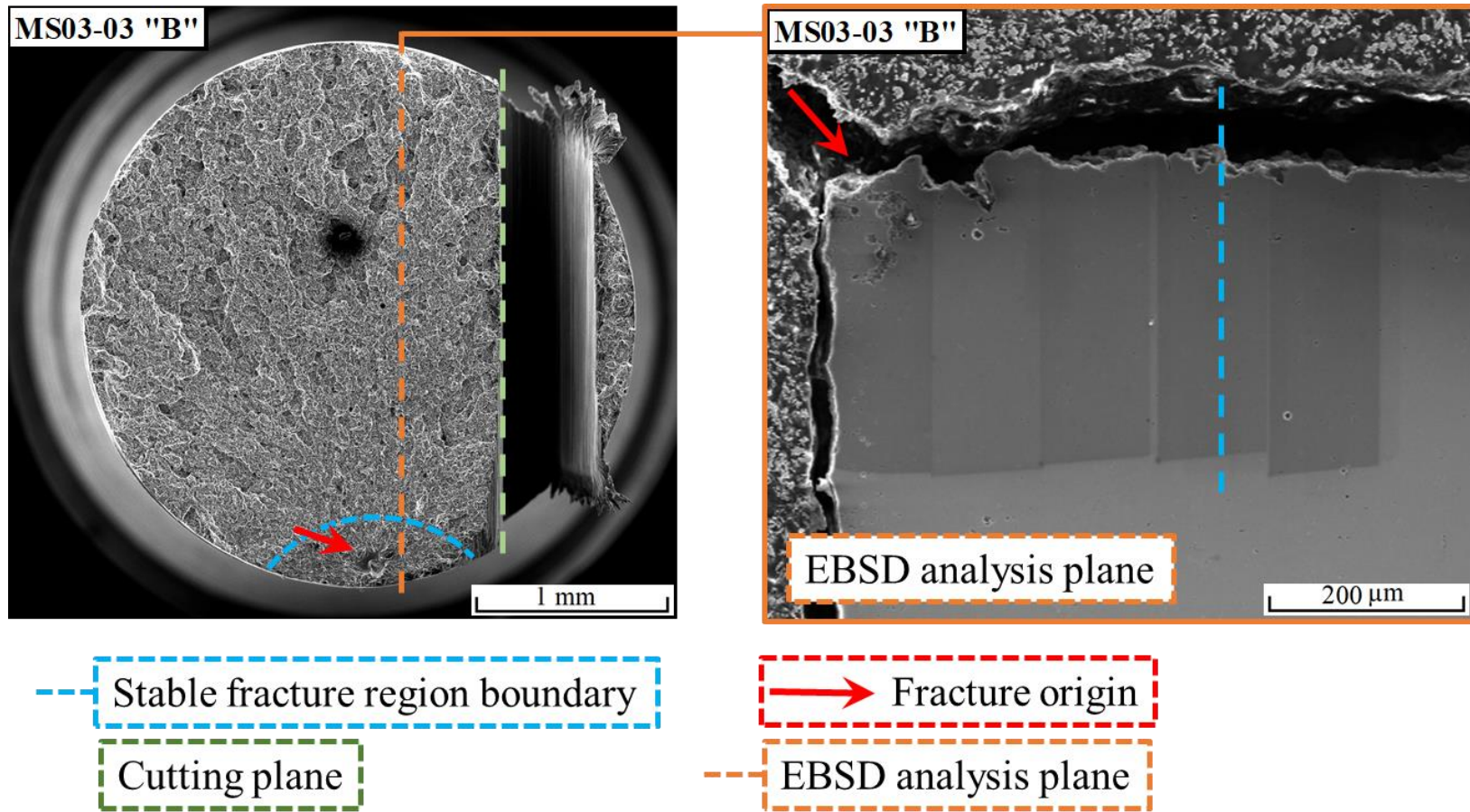
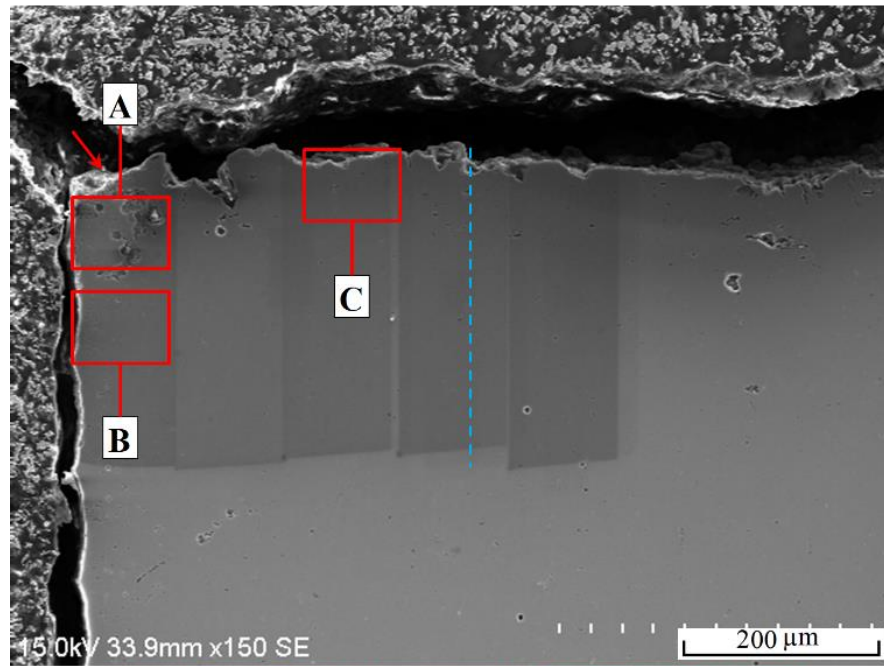


Fig. 6-13 Cross-section preparation for void observation and EBSD analysis. (MS03 is defined in Table 6-1)



-- Stable fracture region boundary → Fracture origin
 → Void formation

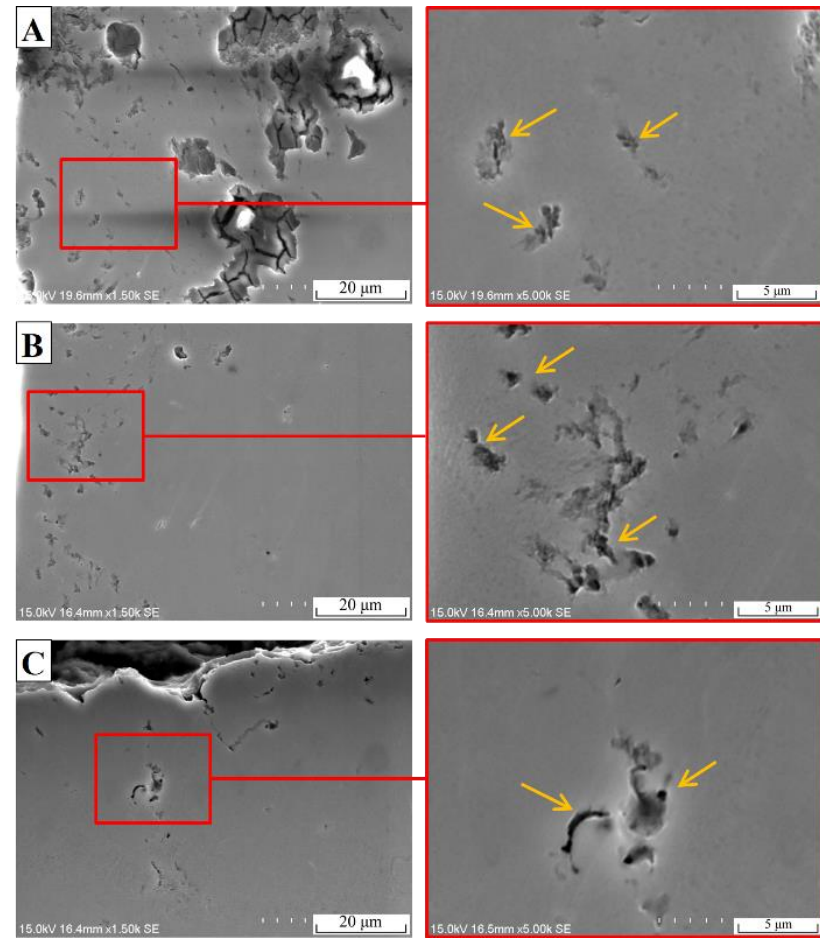


Fig. 6-14 SEM images of the void formations and coalescence inside the stable fracture region below the fracture surface of the machined specimens in Fig. 6-12.

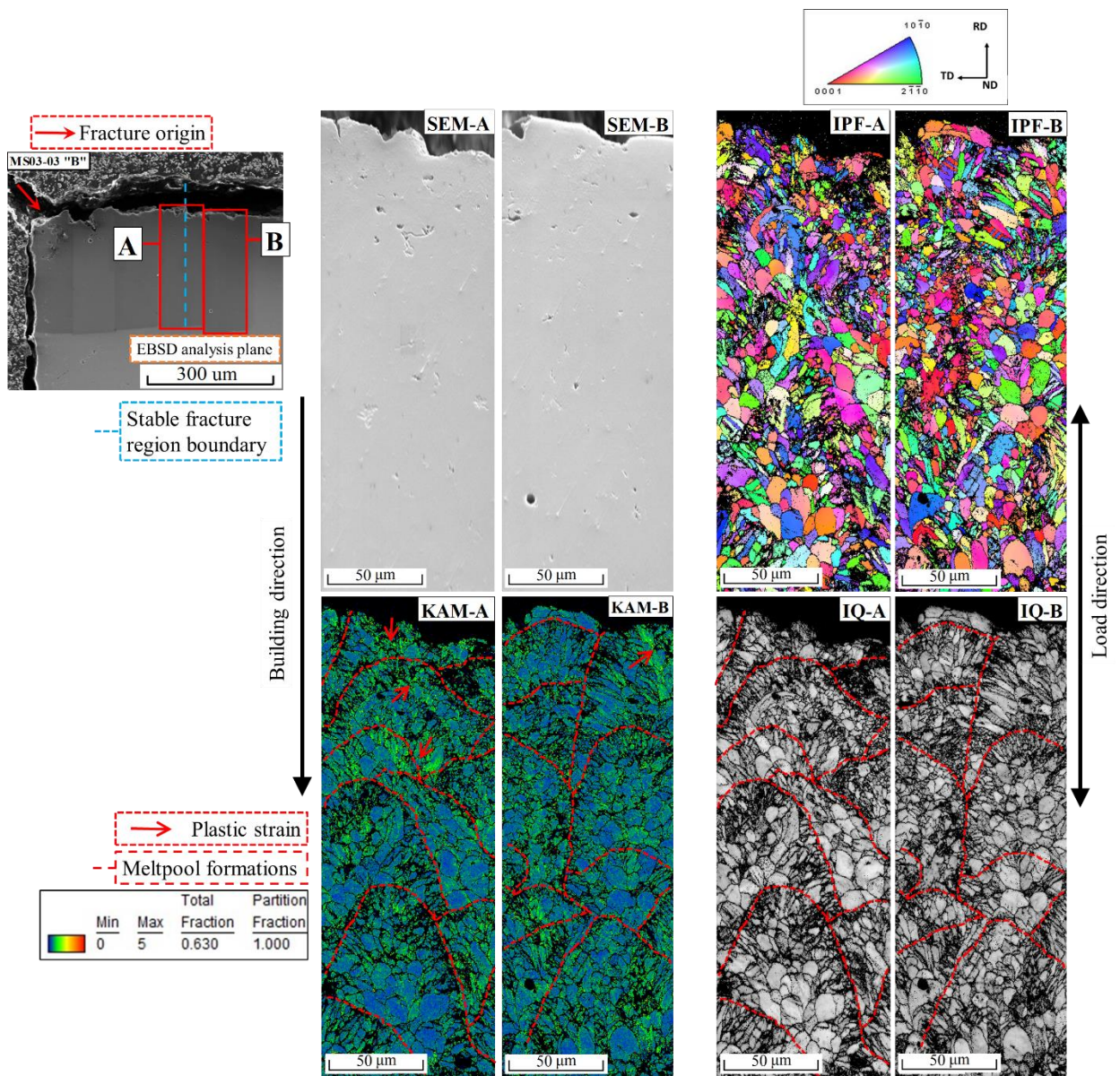


Fig. 6-15 EBSD analysis at the fracture surface of the machined specimen with SEM images (Upper left), IPF map (Upper right), KAM map (Lower left), and IQ map (Lower right). The images correspond to the stable fracture region boundary (A) and in the unstable fracture region (B). Light green areas in the KAM map show plastic deformation.

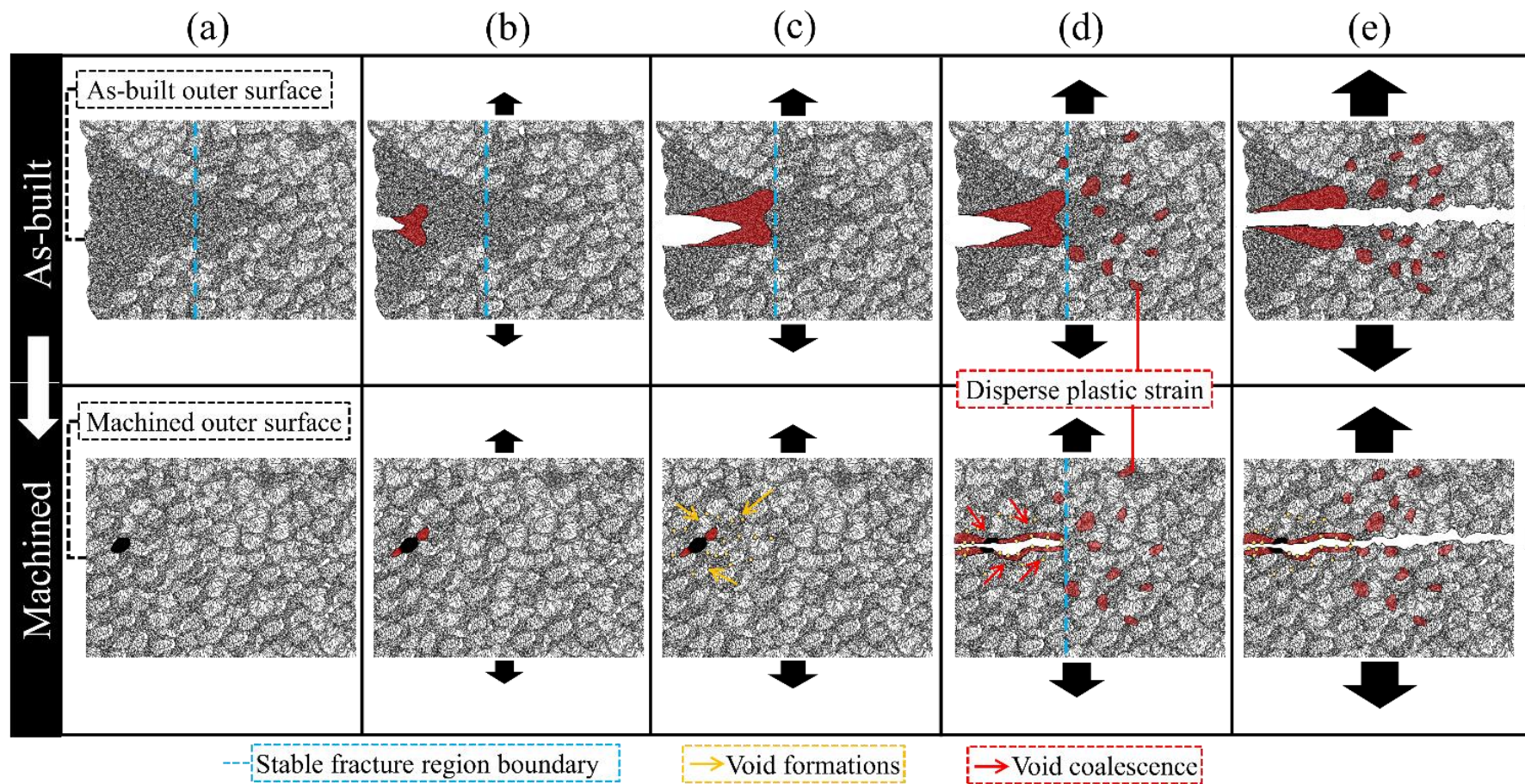


Fig. 6-16 Schematic images of the fracture mechanism for the specimens in as-built (up) and machined states (down).

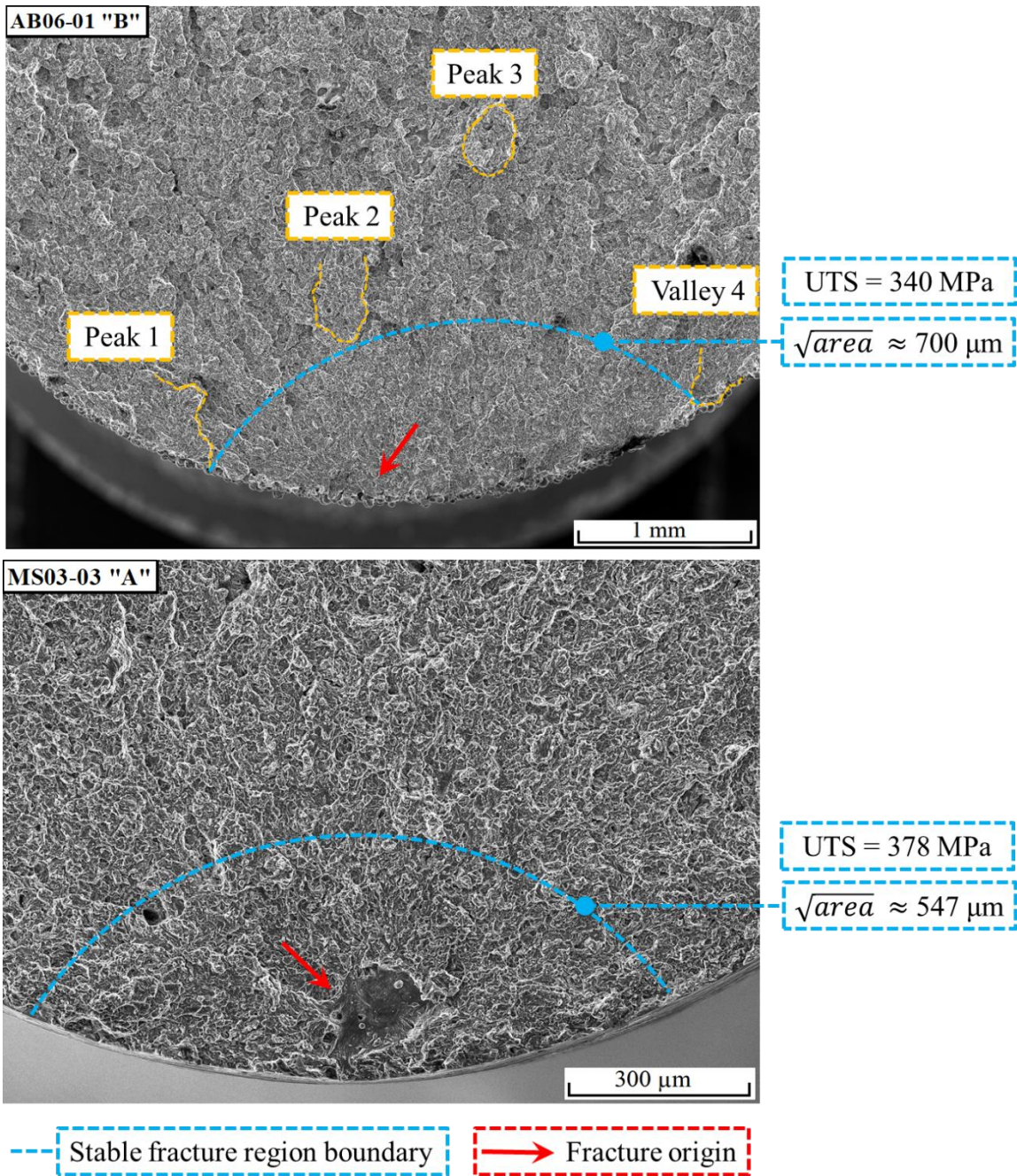


Fig. 6-17 Schematic images of the \sqrt{area} size measured via fracture surface observation of the specimens in as-built state (up) and in machined state (down).

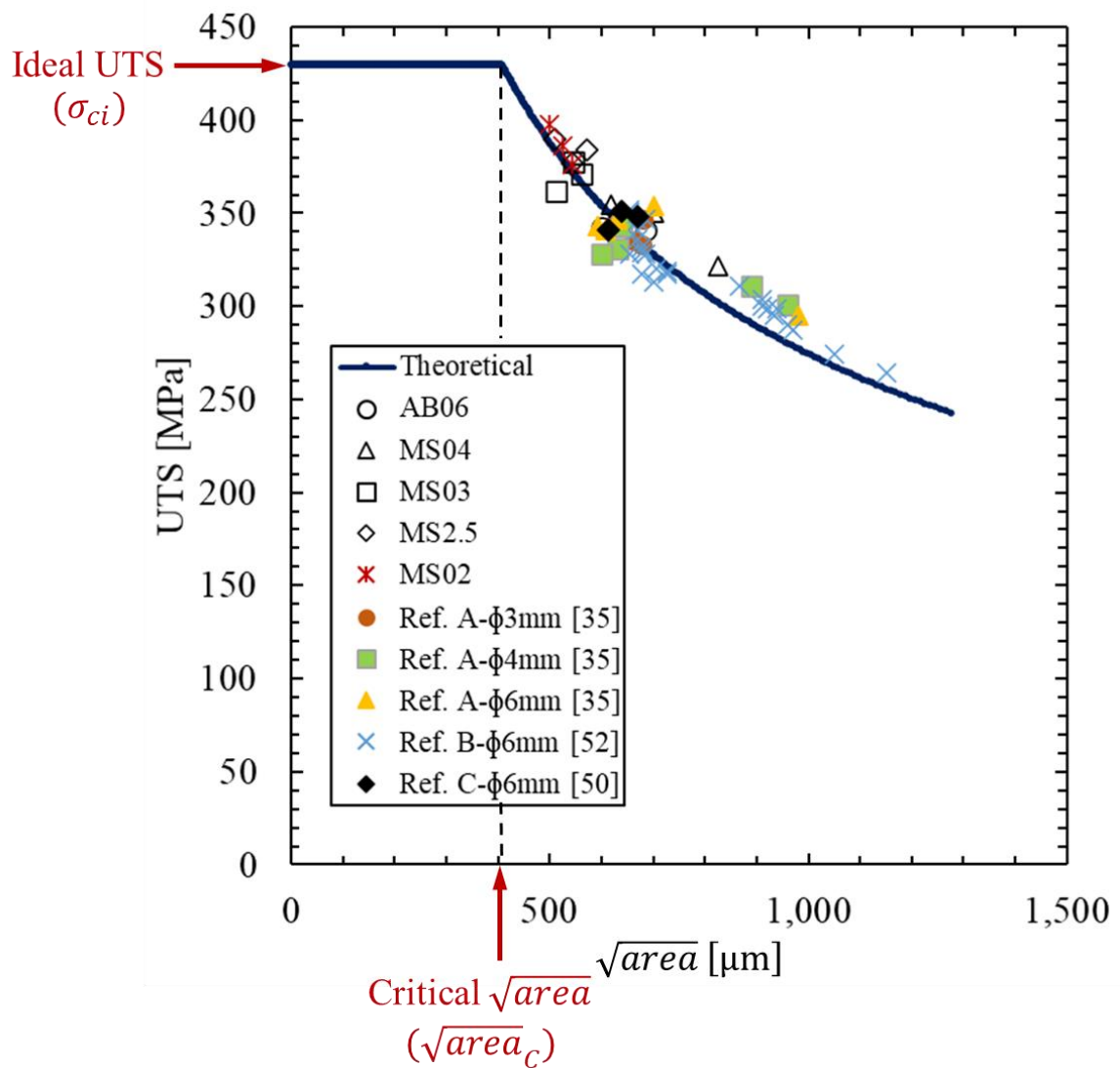


Fig. 6-18 UTS- \sqrt{area} graph shows the mathematical results considering the assumption, $K_{IC} = 10 \text{ MPa}\sqrt{\text{m}}$, and demonstrates the experimental results using Murakami's theory. The critical \sqrt{area} size was determined by the ideal UTS.

APPENDIX

A.1 Appendix A

A.1.1 Plastic instability condition and ideal UTS determination of SLM products

Since the fracture mechanisms have already been explained in Section 6.6.1 and the machined specimens are approximated to ideal conditions, the ideal UTS value of SLM products can be determined. The elastic region of the S-S diagrams can be determined by Hooke's Law using Young's modulus:

$$\sigma = E \varepsilon_{el} \quad \text{Eq. (A.1)}$$

where σ is the stress, E is Young's modulus and ε_{el} is the strain. The flow curve of the stress-strain diagram in the uniform plastic region is governed by the general Power Law equation [1]:

$$\sigma = K \varepsilon_{pl}^n \quad \text{Eq. (A.2)}$$

where n is the strain-hardening exponent, K is the strength coefficient and ε_{pl} is the plastic strain in the plastic region. In addition, assuming work hardening during plastic deformation in a nonlinear manner and void coalescence, both the Voce hardening law and the Nonlinear Power Law can be used to form the nonlinear isotropic hardening power law, governed by Gurson's model in the following equation [2]:

$$\frac{\sigma_Y}{\sigma} = \left(\frac{\sigma_Y}{\sigma} + \frac{3G}{\sigma} \varepsilon_{pl} \right)^n \quad \text{Eq. (A.3)}$$

where σ_Y is the yield strength, and G is the shear modulus that depends on E and Poisson's ratio ν in accordance to the following relation [3]:

$$G = \frac{E}{2(1+\nu)} \quad \text{Eq. (A.4)}$$

Assuming a Poisson's ratio of 0.3 and a $\sigma_Y = 300$ Mpa, and considering that σ can be obtained from the experimental data as well as $E = 42$ GPa, the flow curve can be approximated to the experimental results of the machined specimens by calculating ε_{pl} in Eq. (A.3) followed by subsequently calculating the total strain ε by simply adding the elongation in both the elastic and plastic regions using the following equation:

$$\varepsilon = \varepsilon_{el} + \varepsilon_{pl} \quad \text{Eq. (A.5)}$$

Moreover, the flow curve graph is determined by fitting it to the experimental results by

adjusting the value of n . For example, considering the S-S curve of the machined specimen MS03-03, the fitting of the flow curve with a value of $n = 0.129$, gives the results shown in Fig. A.1.

Furthermore, plastic instability theory affirms that the UTS value of a ductile material is defined by the moment where plastic strain reaches the plastic instability condition, or in other words, the immediate moment before necking occurs. Such condition is represented in the following equation [4]:

$$\hat{\varepsilon}_{pl} = n \quad \text{Eq. (A.6)}$$

which means that the plastic instability condition is reached when the strain hardening coefficient is equal to the value of the plastic strain $\hat{\varepsilon}_{pl}$. Therefore, in the same example mentioned above, the plastic instability condition is reached when Eq. (A.6) is satisfied, resulting in a value plastic strain:

$$\hat{\varepsilon}_{pl} = 0.129 \quad \text{Eq. (A.7)}$$

for the machined specimen MS03-03. At this value of $\hat{\varepsilon}_{pl}$, the calculated value of σ according to Eq. (A-3) is:

$$\sigma_{ci} = 429 \text{ MPa} \quad \text{Eq. (A.8)}$$

At the same time, for that value of σ and using Eq. (A.1), the elongation $\hat{\varepsilon}_{el}$ at which the plastic instability condition is satisfied results in:

$$\hat{\varepsilon}_{el} = 0.01 \quad \text{Eq. (A.9)}$$

Thus, giving a total elongation $\hat{\varepsilon}$ at the plastic instability condition in accordance to Eq. (A.5):

$$\hat{\varepsilon} = \hat{\varepsilon}_{el} + \hat{\varepsilon}_{pl} = 0.139 \quad \text{Eq. (A.10)}$$

Finally, the ideal UTS that satisfies the plastic instability condition is the value of σ that corresponds to $\hat{\varepsilon} = 0.139 = 13.9\%$. In the same example in Fig. A.1, the ideal UTS value is determined to be 429 MPa.

Following the same method as shown in Fig. A.1, the strain hardening coefficients of all the machined specimens are shown in Table A.1, giving the average n and ideal UTS values of 0.131 and 431 MPa, respectively, for AZX912 Mg alloys fabricated by SLM.

A.2 References

- [1] J.H. Hollomon, Tensile deformation, Trans. AIME, 162 (1945) 268-290.
- [2] A.L. Gurson, Continuum Theory of Ductile Rupture by Void Nucleation and Growth:

- Part I—Yield Criteria and Flow Rules for Porous Ductile Media, *Journal of Engineering Materials and Technology*, 99 (1977) 2-15. [10.1115/1.3443401](https://doi.org/10.1115/1.3443401).
- [3] L.D. Landau, L.P. Pitaevskii, A.M. Kosevich, E.M. Lifshitz, *Theory of Elasticity*, Vol. 7, in: *Course of Theoretical Physics*, Pergamon Press, Oxford, 1970, pp. 13.
- [4] G.E. Dieter, *Instability in Tension*, in: M. EDITIONS (Ed.) *Mechanical Metallurgy*, McGraw-Hill, 1989, pp. 290.

A.3 List of tables

Table A-1 Ideal strain hardening coefficient “ n ” in Eq. (A.3) and UTS values.

	n Value	Ideal UTS [MPa]
MS04-01	0.133	435
MS04-02	0.131	431
MS04-03	0.131	431
MS03-01	0.132	432
MS03-02	0.130	430
MS03-03	0.129	429
MS2.5-01	0.130	431
MS2.5-02	0.131	430
MS2.5-03	0.132	433
MS02-01	0.133	432
MS02-02	0.130	430
MS02-03	0.128	427
Average	0.131	431

A.4 List of figures

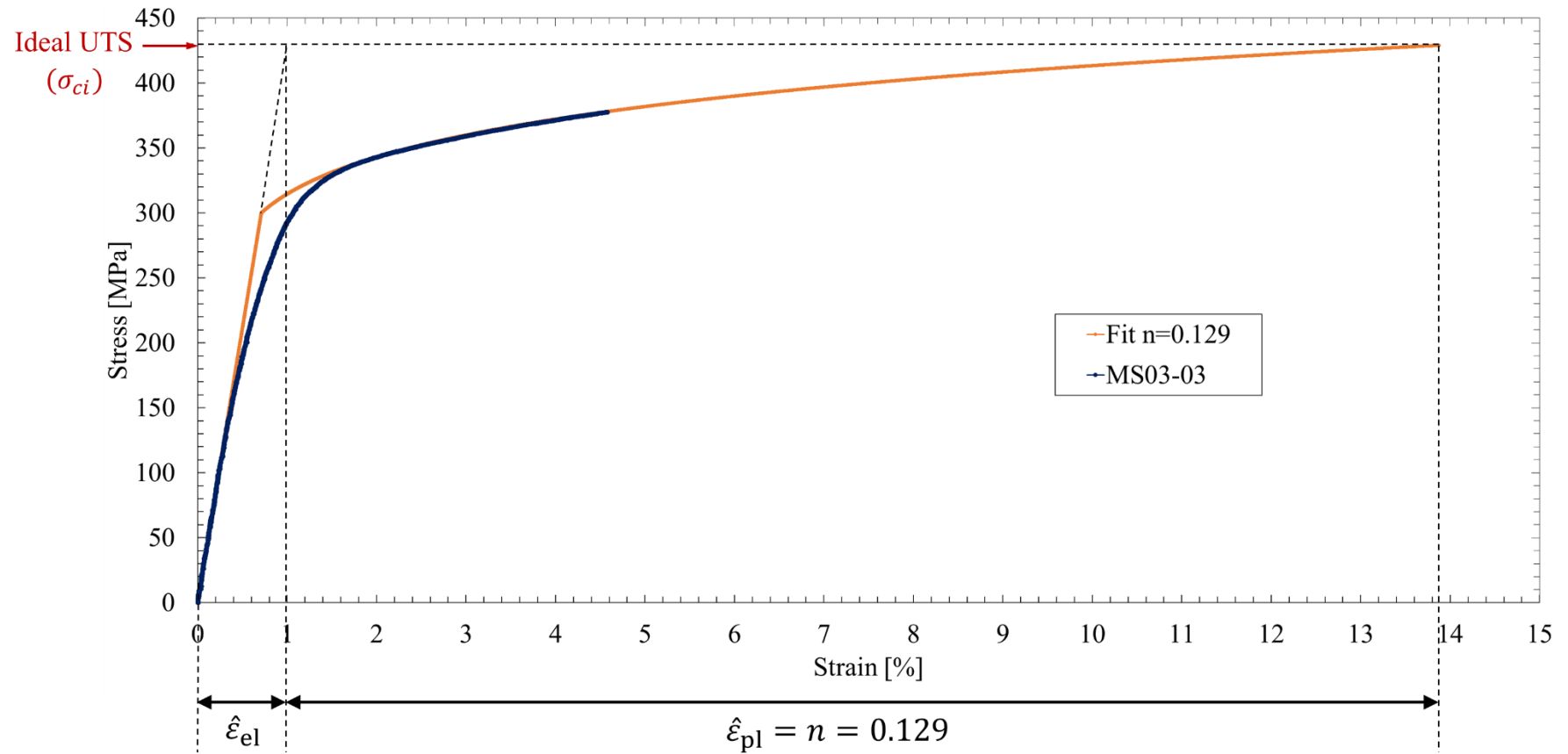


Fig. A.1 S-S diagrams showing the experimental results and its approximation using Gurson's model in the nonlinear isotropic hardening law. Ideal UTS was determined by the plastic instability condition.

CHAPTER 7.- THEORETICAL EVALUATION OF MATERIAL INDEX FOR FRACTURE TOUGHNESS VARIATION IN SLM PRODUCTS

7.1 Introduction

According to the analysis and results provided until Chapter 4, it was concluded that non-combustible Mg alloys fabricated by SLM have a fracture toughness of $K_{IC} = 10.3 \text{ MPa}\sqrt{\text{m}}$, following the surface crack approximation to the $\sqrt{\text{area}}$ parameter proposed by Murakami's Theory. Its use was justified owing to the sudden interruption of the stable crack propagation, which induces large stress concentrations. However, if equation (3 – 1) is used to calculate fracture toughness, then small scale yielding conditions are implied. This means that the plastic zone formed at the crack tip an instant before unstable fracture occurs is small enough to be neglected and the only factors that change the fracture toughness value are either the UTS or the $\sqrt{\text{area}}$ size of the defect. Nevertheless, it was shown in Chapter 2 that the microstructure is not homogeneous, and in Chapter 3, particularly in Fig. 3-12, it was shown that plastic strain disperses because of that non-homogeneity. Furthermore, Chapter 5 discussed the use of the *R* curve and it was established in Fig. 5-13 that, compared to a homogeneous strain, more energy is required for the dispersion of the plastic strain of SLM products in as-built conditions, thus K_{IC} value is enhanced. In short, the microstructural differences that allow plastic strain dispersion to occur could be an additional factor that influences the fracture toughness value. Therefore, this chapter will focus on determining what microstructure controls fracture toughness.

Since plastic strain manifests in the melt pool borders and at the same time is the reason it disperses when it reaches the inner microstructure, it makes sense that the coarse microstructure at the melt pool borders needs to be quantitatively evaluated. In addition, it was established that more energy is needed to disperse the plastic strain. Therefore, if the plastic strain dispersion is widened, more energy is required, thus K_{IC} value is enhanced, and the result is that UTS value is increased. With this affirmation, small

variations in the UTS and ductility values of as-built specimens in a single production bulk can also be explained. In principle, if defects such as gas porosities or lack-of-fusion pores are not present, the only mechanism to enlarge the dispersion area of plastic strain is to reduce the coarse microstructure distribution in a single melt pool. Thus, the coarse microstructure distribution needs to be confirmed in a quantitative manner. Then, further research can be applied for purposely reduce or increase the coarse microstructure by altering the laser sintering parameters or even changing the geometry of the melt pool. In addition, the role of microstructural differences in the mechanical properties could be the foundation for future Finite Element Method (FEM) simulations of SLM products.

In this chapter, four 6-mm round bar specimens were fabricated by SLM in a single production bulk and the same laser sintering parameters. Subsequently, the specimens were submitted to tensile testing and fracture surface observation. Then, the specimen with the highest UTS result and the lowest UTS result were cut in longitudinal and cross-sectional planes for microstructure observation. In addition, the coarse microstructure in a single melt pool was quantitatively evaluated to find a co-relation between the coarse microstructure distribution and the material properties.

7.2 Experimental procedure

The raw material was AZX912 Mg alloy powder with the same composition as in Table 1-1. The particle size distributions were the same as shown in Section 1.4. The round bar specimens were carried out using the EOS M100 SLM machine shown in Fig. 2-1. The geometrical configuration of the round bar specimens is the same one as shown in Fig. 4-2. The specimens had a gauge length of 25 mm and were fabricated using the same scanning strategy shown in Fig. 2-2. The laser-irradiation processing parameters are the same ones as listed in Table 2-1. In addition, a contour parameter with the same laser power and scan speed as listed in Table 2-1 was performed for increased surface quality. Besides, flat specimens were not considered because of the presence of high residual stresses and the low ultimate strength values, which often result in cracking after processing.

Tensile tests were performed using a Shimadzu AG-50kNXD universal electromechanical testing machine set at a strain rate of 0.0011 s^{-1} in conformance with

the Japanese Industrial Standard JIS Z 2241:2011 (Method of Tensile Test for Metallic Materials). Tensile testing was performed along the building direction of the round-bar specimens at a room temperature range of 21-22 °C. All tests were performed using a screw-type grip set with spherical bearings to ensure that no misalignment or bending occurred during testing. Elongation was measured using a Shimadzu SG25-100 extensometer with a gauge length of 25 mm. Fracture surfaces were observed using a JEOL JSM-IT300 scanning electron microscope.

The fractured parts of the specimens selected for microstructure observation were cut in horizontal and longitudinal cross-sections using a Struers Minitum low speed saw, and their inner surfaces were mechanically polished using emery sandpapers up to P4000 and a final pass with 0.2 µm fumed silica. Subsequently the surfaces were polished using a Hitachi High-Tech IM-3000 ion milling machine at 2 kV to obtain a mirror-finish fineness. To obtain clear images, the specimens were etched using an oxalate aqueous solution (oxalate: 0.1 g and distilled water: 100 ml). Macroscopic and microscopic solidification structures were observed using a Hitachi High-Tech Low Vacuum Analysis SU6600 scanning electron microscope with an acceleration voltage of 15 kV.

7.3 Results

7.3.1 Tensile tests and fractography results

Tensile tests were performed to the all the round bar specimens until fracture occurred, and the S–S diagrams of the fractured specimens are presented in Fig. 7-1. Results exhibited the following values: an ultimate strength of 347 MPa, a yield strength of 256 MPa (0.2% proof strength), and an elongation of 3.4%. The behavior of the S-S curve is consistent with the results of 6-mm round bar specimens from Chapters 2 through 5. It is worth mentioning that three of the specimens had very similar UTS and elongation values, yet one specimen had a similar UTS value but reduced ductility despite being from the same production bulk. The reasoning behind this phenomenon will be discussed in section 7.4.

For fracture surface and microstructure observation, the specimens with the highest and lowest tensile test results (6mm-1 and 6mm-3 in Fig. 7-1, respectively) were selected. Fracture surfaces of both specimens marking the fracture initiation point, stable

propagation area of the crack and the transition from stable fracture into unstable fracture region are shown in Fig. 7-2. In consistence with what was established in previous chapters, fracture always started from the outer surface.

7.3.2 Microstructure observation and distribution

Fig. 7-3 shows a schematic of the cuts performed to the fracture surfaces of the specimens for microstructure observation. Figs. 7-4 and 7-5 shows a schematic of the melt pool formations near the fracture surface for both specimens. Fracture initiation points are marked, where irregular coarse microstructure bundles can be observed. In addition, melt pool formations with coarse microstructure at the borders can be observed. Fig. 7-6 show the sample areas chosen for measuring microstructure distribution in each specimen. The areas were chosen at approximately 600 μm from the outer surface, since this was the length where plastic strain disperses before unstable fracture occurs. The melt pool formations were marked, and the coarse microstructure ratio was calculated as shown in Fig. 7-7. Results of the coarse microstructure distribution in relation with the melt pool size are shown in Fig. 7-8., where the specimen with the highest tensile test results has a slightly decreased coarse microstructure distribution in a single melt pool.

7.4 Discussion

Previously, the author classified the microstructure distribution macroscopically by outer microstructure and inner microstructure. The former consists of irregular coarse microstructure bundles formed in the outer surface owing to the proximity of the metallic powder, while the latter consists of melt pool formations that have coarse microstructure at the borders. From a microscopic point of view, it makes sense to classify the microstructure distribution in a single melt pool. The importance of the microscopic distribution relies on the dispersion of the plastic strain before unstable fracture occurs. In principle, a larger coarse microstructure region means a larger plastic strain in a single melt pool. Thus, plastic strain will homogenize approximating the conditions to the heat treatment results showed in Chapter 5, where the energy required for stable fracture to occur tends to be constant. On the other hand, if the coarse microstructure region is small in a single melt pool, the plastic strain before unstable fracture disperses more, requiring

more energy for unstable fracture to occur and enhancing the fracture toughness value. The theoretical evaluations using the *R* curve behavior and its correspondent plastic strain distribution are shown in Fig. 7-9.

Results of the microstructure distribution in Fig. 7-8 are consistent with such affirmation. For instance, specimen 6mm-3 has a lower ductility value, which implies a less dispersed plastic strain in a single melt pool compared to specimen 6mm-1, results that can be verified in Fig. 7-8. However, it is important to note that all the specimens were fabricated in the same bulk production with the same laser irradiation parameters shown in Table 2-1. As a result, a variation in coarse microstructure distribution owing to SLM fabrication parameters is not likely since same irradiation parameters on two specimens with the same geometry should mean same microstructure distribution. If that is the case, a reasonable explanation for the coarse microstructure distribution results can be attributed to the scanning technique. Since the scanning direction was rotated 67° when a single layered finished sintering, it makes sense that the melt pool size is not constant in one direction only. Thus, irregular coarse microstructure bundles in two specimens with the same geometry and same irradiation parameters are a circumstantial factor explained by the laser direction rotation at each layer. This affirmation is also confirmed with the results shown in Fig. 7-8, since the melt pool size and the coarse microstructure distribution should be similar in a single track, and the results show variation when measured from a single plane. Although the microstructure results are non-conclusive due to the 67° rotation, it is a starting point to determine if SSY conditions can be assumed with future research.

In addition, even though the variation shown in Fig. 7-8 is quite small, the results provide an insight into the influence of coarse microstructure distribution in the mechanical properties. From here a wide opportunity for research is opened. For example, evaluate the mechanical properties by altering the laser sintering parameters focusing on changing the microstructure distribution of a single melt pool. Another option is to alter the melt pool size and/or geometry by modifying the laser diameter and irradiation parameters as well. Coarse microstructure distribution in percentage could be the same for a certain set of fabrication parameters, but if a larger melt pool is formed with a larger coarse microstructure at its borders, the amount of energy required for dispersion is

unclear. By evaluating the mechanical properties of the tested specimens with different melt pool sizes can be determined if the dispersed plastic strain depends on coarse microstructure distribution in a single melt pool or simply depends on the size of the coarse microstructure regions after the stable crack propagation occurs in as-built conditions. Finally, from a finite element method (FEM) perspective, setting the above-mentioned conditions of the melt pool formations in a simulation analysis and extrapolate them can provide an insight on the range at which the plastic strain is dispersed and the conditions where plastic strain is considered homogeneous, thus increasing the reliability of SLM products even further.

7.5 Conclusions

The focus on this chapter is to evaluate the microstructure distribution of the dispersed plastic strain before unstable fracture occurred and determine its role on the fracture process and the mechanical properties. The findings of this study led to the following conclusions:

- An increase in the coarse microstructure distribution of a single melt pool induces a less dispersed plastic strain before unstable fracture occurs.
- The microstructure distribution results are not constant in a plane surface area when the scanning method for the specimens involves a rotation at every layer owing to the melt pool size being dependent on the direction of the scan track.
- A less dispersed plastic strain means it is more homogenized, thus approximating its evaluation to small scale yielding conditions and the use of traditional fracture mechanics is justified. A more dispersed plastic strain means more energy is required for dispersion, thus enhancing fracture toughness, which increases UTS and elongation at failure.

7.6 List of figures

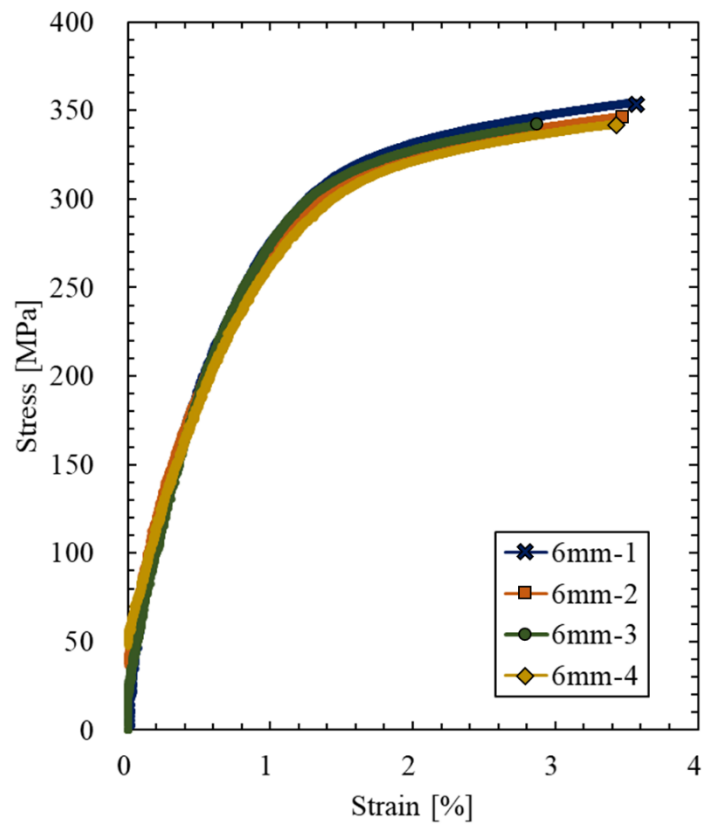


Fig. 7-1 Stress-strain diagrams of the 6-mm round bar specimens.

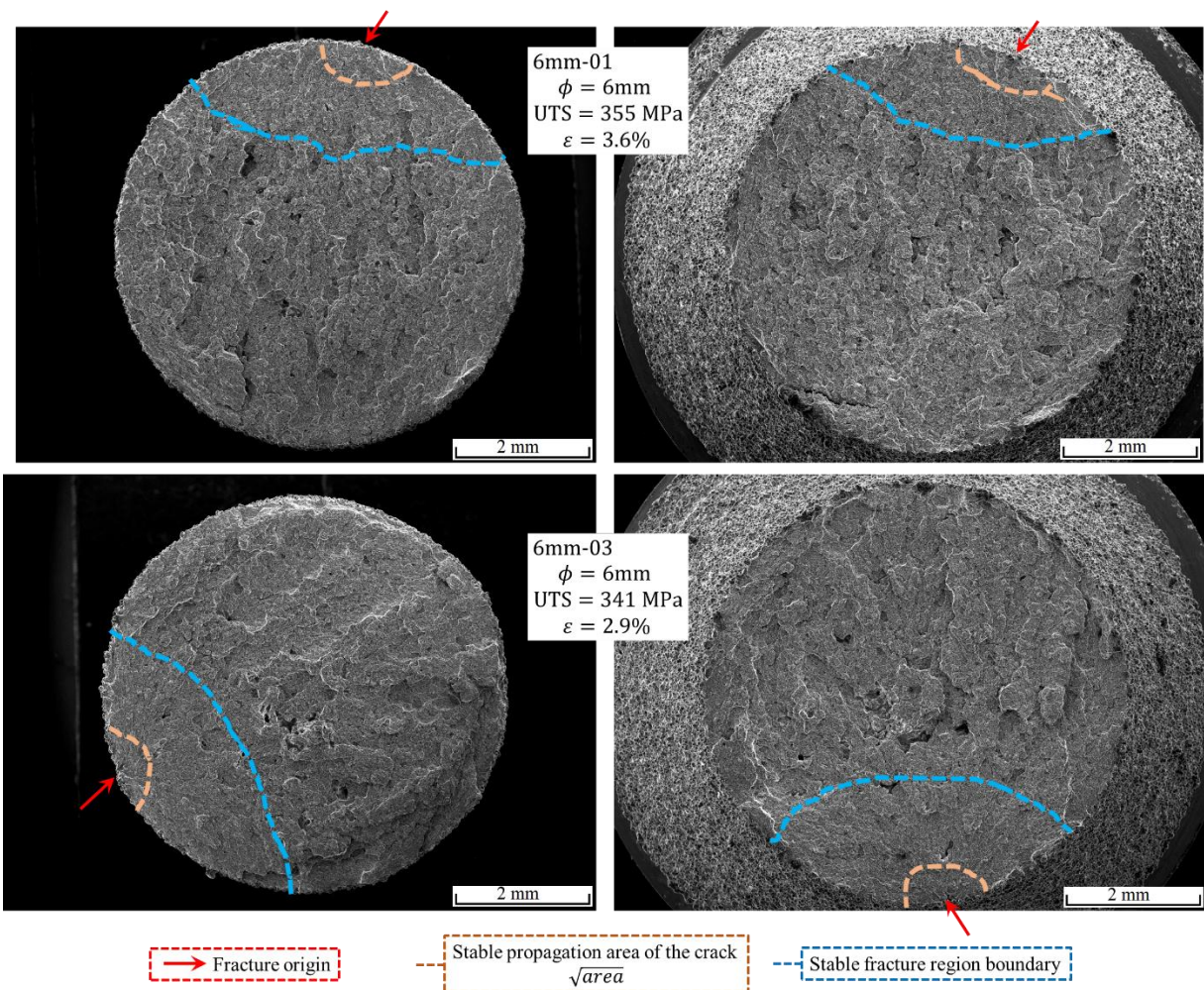


Fig. 7-2 Fracture surfaces of the specimen with highest UTS and elongation at failure (6mm-1, up) and the specimen with lowest UTS and elongation at failure (6mm-3, down) chosen for observation.

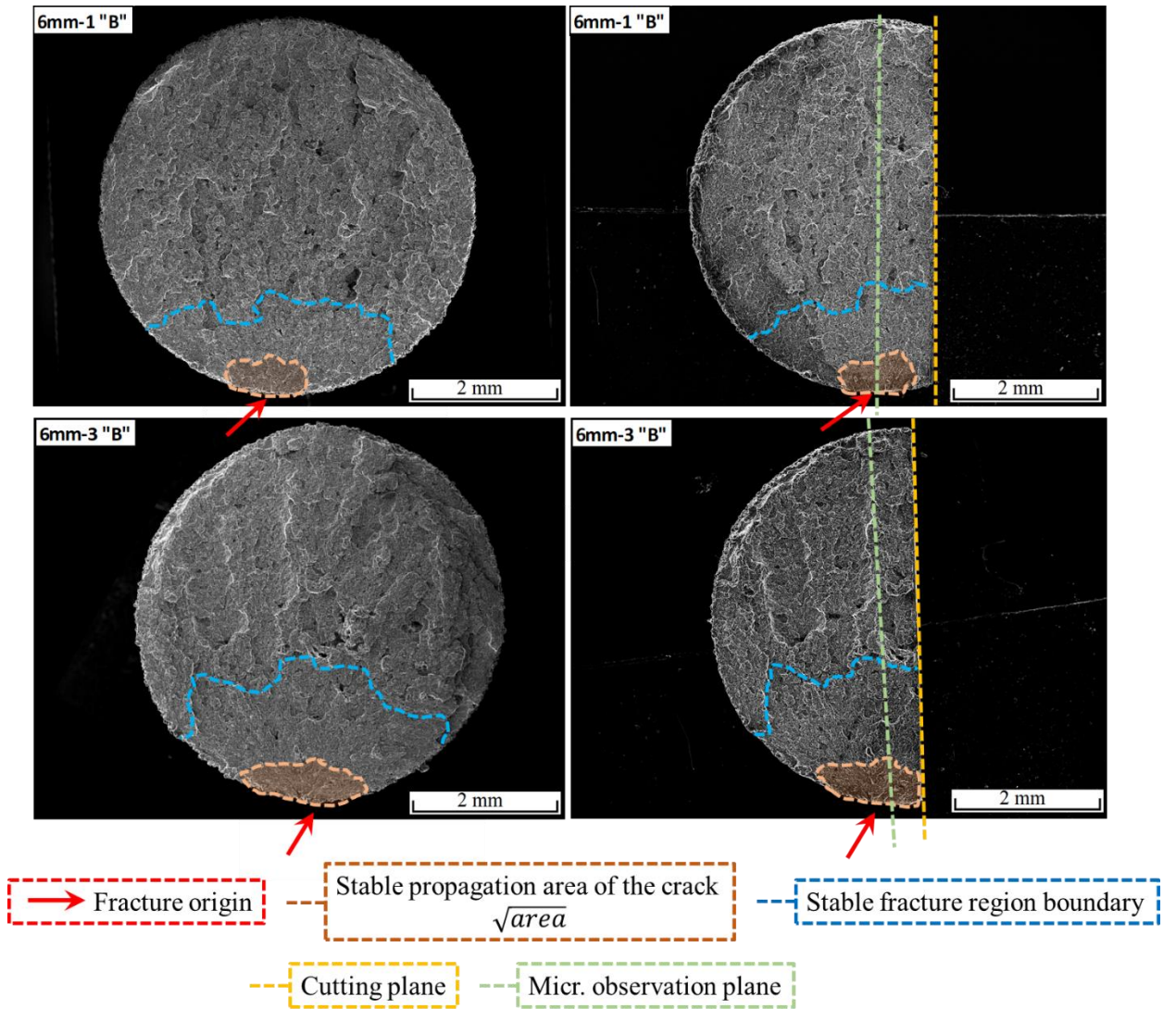


Fig. 7-3 Schematic of the cuts performed for microstructure observation of the specimens.

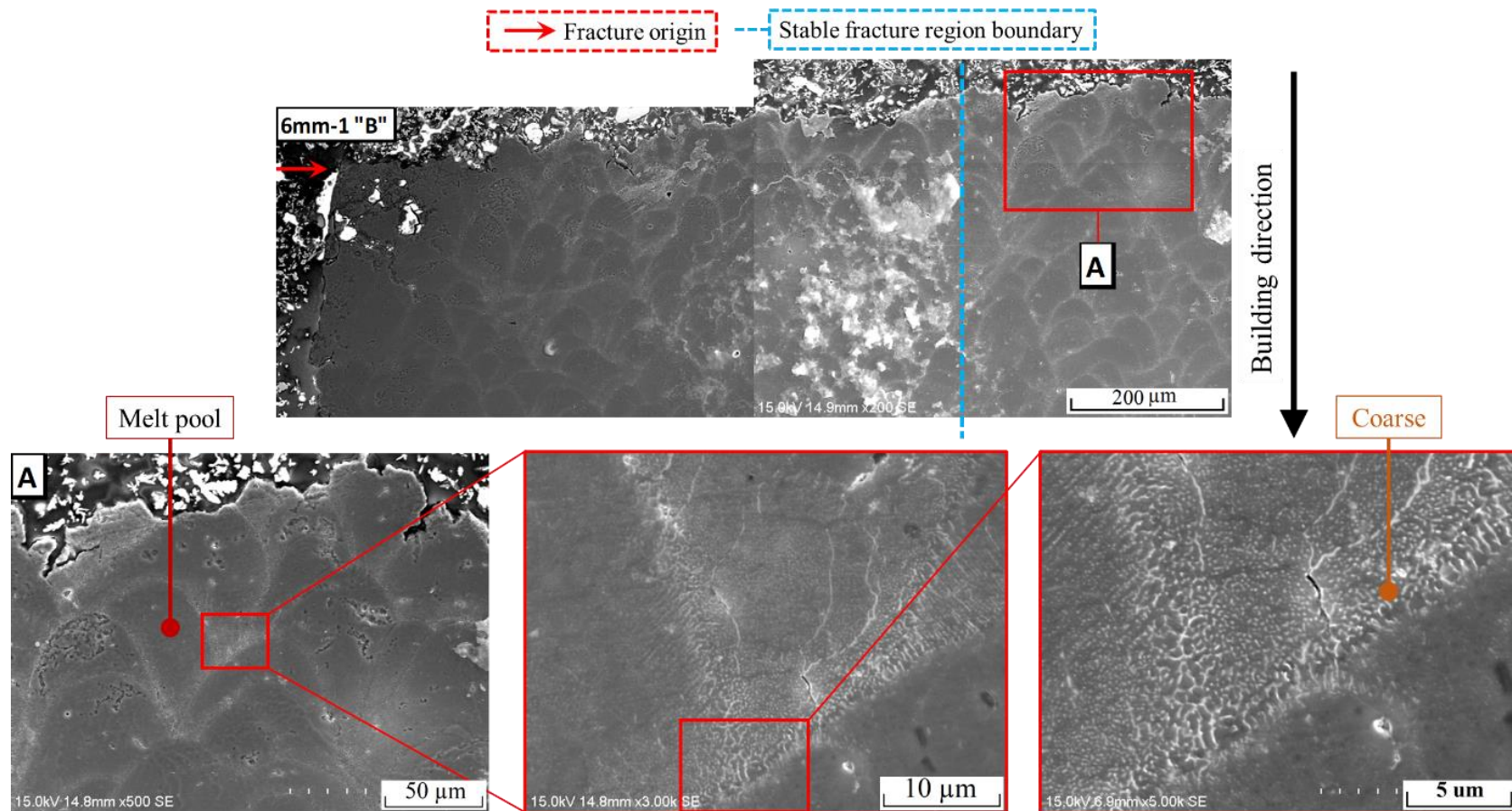


Fig. 7-4 SEM images of the microstructure observation plane of the specimen with the highest UTS and elongation at failure (6mm-01).

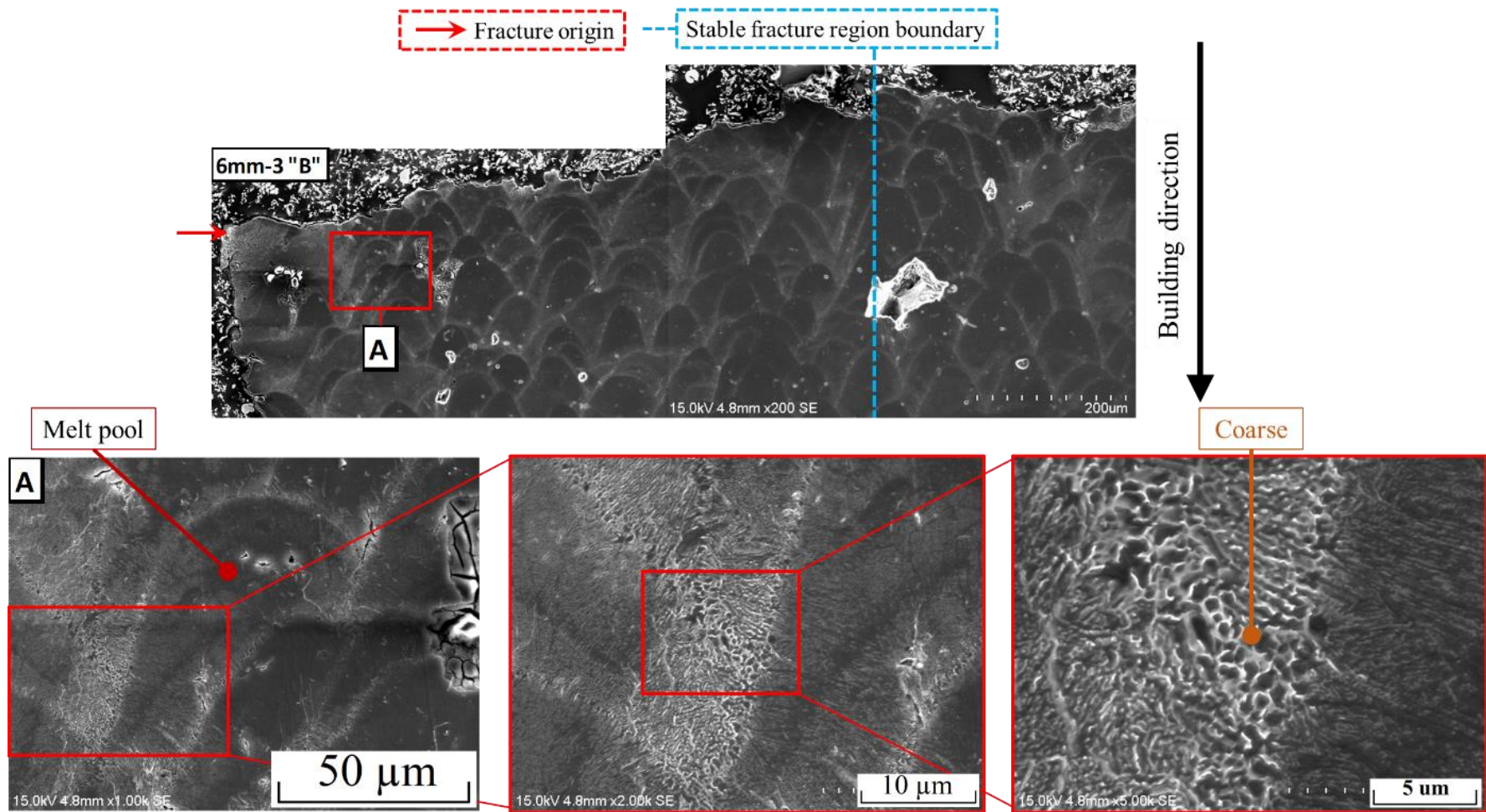


Fig. 7-5 SEM images of the microstructure observation plane of the specimen with the highest UTS and elongation at failure (6mm-01).

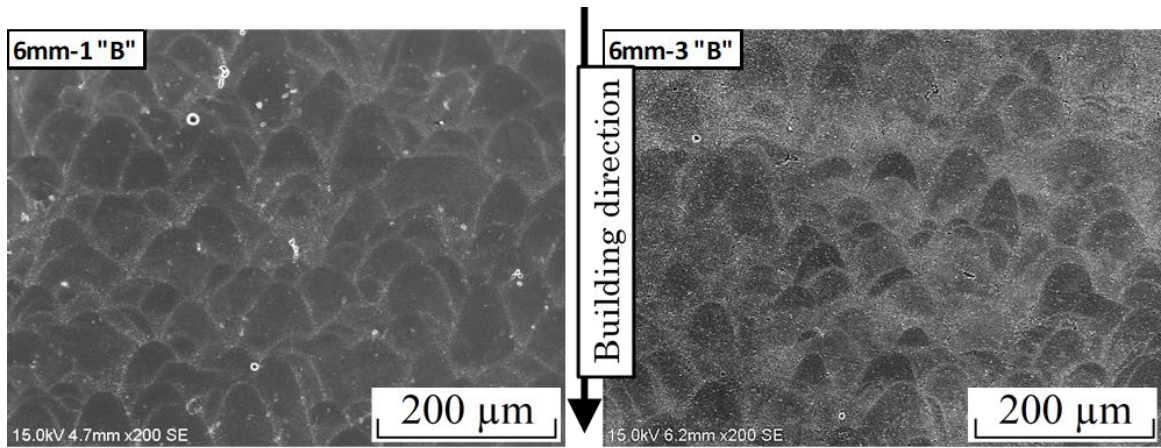


Fig. 7-6 SEM images of the microstructure observation used for measuring the microstructure distribution in 6mm-01 (Left) and 6mm-03 (Right).

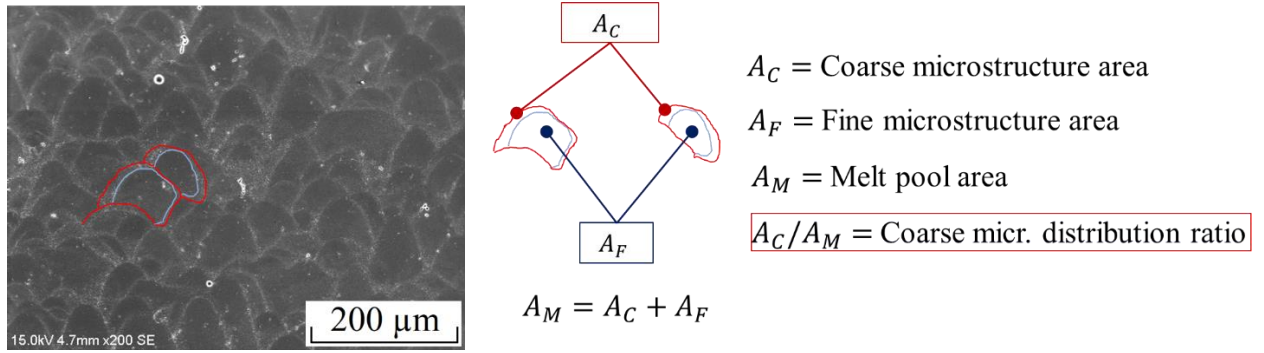


Fig. 7-7 Schematic of the method used to calculate the coarse microstructure distribution in a single melt pool for both specimens.

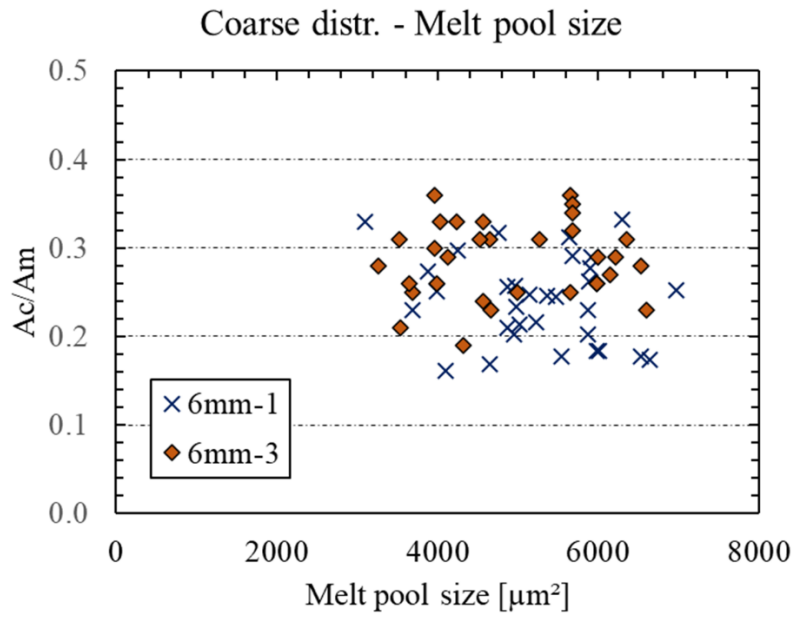


Fig. 7-8 Results of the coarse microstructure distribution of a single melt pool for both specimens.

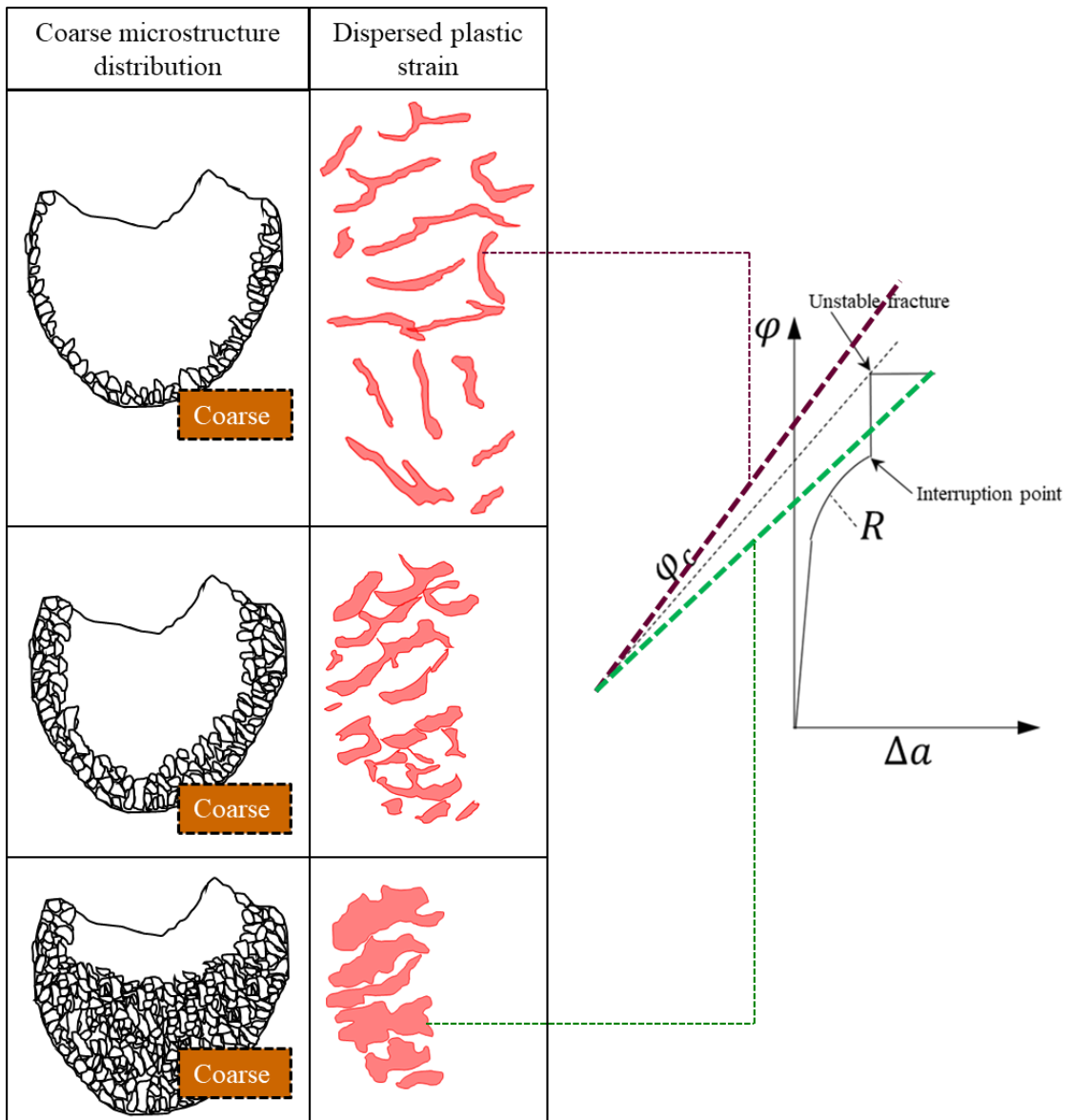


Fig. 7-9 Schematic of the plastic strain dispersion according to the coarse microstructure distribution along with its influence on the behavior of the R curve.

CHAPTER 8.- CONCLUDING REMARKS

In the current study, the reliability of the mechanical properties of SLM products in as-built conditions was enhanced with the following steps. A microstructure distribution analysis allowed the determination of a fracture mechanism. Subsequently, the defect responsible for fracture in SLM products under as-built conditions was determined. It was named the stable propagation area of the crack and its size was used in fracture toughness according to Murakami's Theory to predict the strength at failure, thus increasing the reliability. In addition, post-processing to directly influence the stable propagation of the crack and enhance the mechanical properties of SLM products was performed. First, the microstructure was homogenized via annealing heat treatment. Results showed an increased ductility, but a considerable decrease in the UTS value. Consequently, the stable propagation area of the crack was mechanically removed. The results showed a considerable increase in yield strength, UTS value and ductility if the presence of defects is reduced to a minimum; thus, allowing the quantitative evaluation of the ideal strength for SLM products. The findings of the study lead to the following conclusions:

There are two types of microstructures in SLM products. A coarse microstructure is associated to a long cooldown, and a fine microstructure associated with a fast cooldown. Melt pool formations have a coarse microstructure in the borders, and fine microstructure in the center. SLM products in as-built conditions have an outer microstructure distribution, composed of irregular chunks of coarse microstructure, and an inner microstructure distribution, composed of mostly fine grain regularly distributed through the melt pool formations.

The transition from outer microstructure to inner microstructure enables a stable crack propagation that is suddenly interrupted and creates large stress concentration sources. The length from the outer surface to such interruption is called stable propagation area of the crack and is a non-visible defect responsible for fracture in SLM products under as-built conditions. Since it is a surface crack, Murakami's Theory for fracture toughness calculation can be used to predict the strength at failure, thus enhancing the reliability of the process.

The validity of the non-visible defect known as the stable propagation area of the

crack in fracture toughness results was evaluated with artificially introduced drill holes. Accordingly, if a visible defect is smaller than the stable propagation area of the crack, it can be neglected. But if the defect is larger than the stable propagation area of the crack, then fracture will occur at the drill hole. Regardless of the fracture initiation point, fracture toughness according to Murakami's Theory was verified. In non-combustible Mg alloys, the average fracture toughness value is approximately $10.2 \text{ MPa}\sqrt{\text{m}}$.

The homogenization of the microstructure of SLM products via heat treatment alters the fracture mechanism. The stable crack propagation is no longer interrupted by microstructural differences; thus, the plastic deformation is continuous and homogeneous. As a result, heat treated specimens show a considerable increase in ductility but a decrease in UTS. If fracture toughness is an indicator for the transition from stable fracture to unstable fracture in SLM products under as-built conditions, then the indicator for the same transition in heat treated specimens is the R curve.

The mechanical removal of the outer microstructure also means the removal of the stable propagation area of the crack. Therefore, the fracture mechanism is altered. The fracture initiation point of a machined specimen is a visible defect that propagates stable through void coalescence that initiates at the melt pool borders. As a result, the yield strength increases and a higher UTS is achieved. However, mechanical properties are sensitive to the changes in size of the defects. Nevertheless, the potential of SLM products was quantitatively evaluated by plastic instability theory and resulted in a maximum UTS value of approximately 430 MPa with a critical \sqrt{area} defect size of 410 μm in non-combustible Mg alloys fabricated by SLM.

Finally, a clear distinction between the as-built conditions and post-processing state was reached from the perspective of fracture mechanisms. Although such distinction might seem shallow on the surface and the concept of post-processing of SLM products is not new, this study served as a basis in three critical areas. First, the critical defect known as the stable propagation area of the crack is introduced. Second, the strength predictability using the \sqrt{area} parameter was tested and helped as a reliability enhancing factor. And thirdly, the maximum achievable potential of SLM products using fracture mechanics was evaluated. With these conclusions as a basis, it is interesting to visualize what further research might bring in the future.

ACKNOWLEDGEMENTS

Coming to Japan has been a long-time dream throughout my life, and finally being here completing my Doctorate's Thesis has been nothing less than fulfilling. I would like to deeply thank Prof. Noguchi and Prof. Hamada, since their trust in me and roles as well as guides were key for my growth, both scientifically and personally. I wish to express a grateful sentiment to Prof. Matsunaga and Prof. Toda, who provided a critical insight into the usefulness of this study in the engineering industry and technological society. Also, of course, the wonderful staff and colleagues of the Solid Mechanics Laboratory in Kyushu University who have been extremely helpful and also are responsible for the friendly and supportive environment of the laboratory.

I cannot express enough my gratitude to my loved ones. My dear family in Ecuador consisting of my father, Santiago, my mother Monica, and my sister Samantha, who always put a smile on my face. And my present family, Yanina, who has been at my side through all tough moments before and now. Her kind love has inspired me endlessly. And to all my relatives, who have expressed pride and happiness for me and my achievements.

I would like to gratefully acknowledge the financial support provided by the Ministry of Education, Culture, Sports, Science and Technology (MEXT) of Japan. Additionally, this study was supported by the Adaptable and Seamless Technology transfer Program through Target-driven R&D (A-STEP) from Japan Science and Technology Agency (JST), Grant Number JPMJTR202A.

Finally, a great thanks to all my friends. In Ecuador, to my long-time trusted friends for keeping me posted on how things are at home. To my Japanese friends, for sharing culture with me, which will fascinatingly not end. And to my friends from all over the world, in my band, in my neighborhood, in my class, since their day-to-day life has given me such joy. A heartfelt thank you to you all.

“Obstacles are those frightful things you see when you take your eyes off your goal”

- Henry Ford (1863 -1947)